

ACTUATION FATIGUE PROPERTIES OF NITI-BASED HIGH TEMPERATURE
SHAPE MEMORY ALLOYS

A Dissertation

by

OMER KARAKOC

Submitted to the Office of Graduate and Professional Studies of
Texas A&M University
in partial fulfillment of the requirements for the degree of

DOCTOR OF PHILOSOPHY

Chair of Committee,	Ibrahim Karaman
Committee Members,	Dimitris C. Lagoudas
	Raymundo Arroyave
	Ankit Srivastava
Head of Department,	Ibrahim Karaman

August 2019

Major Subject: Materials Science and Engineering

Copyright 2019 Omer Karakoc

ABSTRACT

Since the addition of Hf or Zr provides a cost-effective alternative to NiTi alloyed with Pd, Pt and Au, due to the high cost of the latter, NiTiHf and NiTiZr alloys have recently attracted considerable attention [1]. In Ni-rich NiTiHf and NiTiZr alloys, it is possible to form nano-scale Ni-rich precipitates upon heat treatment, which strengthen the matrix by acting as barriers against plastic deformation [2-6]. The increase in strength due to precipitation also permits reversible martensitic transformation at higher stress levels [2, 3, 7, 8]. Furthermore, nano-precipitation in Ni-rich NiTiHf and NiTiZr alloys allows for precise control of transformation temperatures through the change in Ni content of the matrix as a function of precipitate volume fraction [4]. Consequently, the possibility to tailor these properties through nano-precipitation make the Ni-rich NiTiHf SMAs promising candidates for practical applications that involve elevated temperatures and high stresses. Despite the aforementioned advantages brought about by nano-precipitation, many of the envisaged applications also require a stable fatigue response and long fatigue lives, and thus, it is of utmost importance to assess the cyclic deformation response of NiTiHf and NiTiZr high temperature SMAs (HTSMAs) at elevated temperatures.

Even though numerous studies have been conducted on superelastic fatigue properties of SMAs [9-13], only a very few reports are available in the literature addressing their actuation fatigue response [14-17], and to the best of the authors' knowledge, none on the actuation fatigue response of HTSMAs. The current study was undertaken with the

motivation of addressing these problems, and thereby establishing a thorough understanding of the effect of microstructure, upper cycle temperature, applied stress level on thermo-mechanical cyclic behavior and fatigue response of $\text{Ni}_{50.3}\text{Ti}_{29.7}\text{Hf}_{20}$ and $\text{Ni}_{50.3}\text{Ti}_{29.7}\text{Zr}_{20}$ alloys

Overall, the current findings constitute the first systematically obtained set of results demonstrating the microstructure dependence of actuation strain, irrecoverable strain, thermal hysteresis, transformation temperatures and fatigue performance of the Ni-rich $\text{Ni}_{50.3}\text{Ti}_{29.7}\text{Hf}_{20}$ and $\text{Ni}_{50.3}\text{Ti}_{29.7}\text{Zr}_{20}$ HTSMAs, demonstrating the importance of controlling H-phase precipitate size. Furthermore, the work presented herein focused on the roles of UCT and applied stress levels on the actuation fatigue performance of the Ni-rich $\text{Ni}_{50.3}\text{Ti}_{29.7}\text{Hf}_{20}$ $\text{Ni}_{50.3}\text{Ti}_{29.7}\text{Zr}_{20}$ HTSMAs. The experimental results reported herein not only revealed the optimum UCT and applied stress levels for desired high-temperature actuation fatigue performance, but also constitute the first set of data towards building a comprehensive database for HTSMA actuation performance to guide the efforts in designing durable and stable HTSMA actuators with the maximum possible work output.

DEDICATION

To my family: my father Huseyin Gazi Karakoc, my mother Muzaffer Karakoc, my wife Kubra Karakoc, my little daughter Beril Elif Karakoc and my sister Halime Ozen for their great support and motivation at all times

ACKNOWLEDGEMENTS

I would like to express my special thanks of gratitude and my respect to my advisor, Prof. Ibrahim Karaman and giving me golden opportunity of obtaining a doctoral degree. During my six years of research and education, he helped me in doing a lot of research and I came to know about so many new things I am really thankful to him.

I would like to thank my committee members, Prof. Dimitris C. Lagoudas, Prof. Raymundo Arroyave and Dr. Ankit Srivastava for their guidance and support throughout the course of this research.

Mr. Jim H. Mabe from Boeing Corporation and Dr. Ronald D. Noebe, Dr. Othmane Benafan from NASA Glenn Research Center, Structural Materials Division, this research would not have successful without your help. I owe a great debt of gratitude to your guidance and valuable comments on this research.

I would like to express my sincere gratitude to Dr. Demircan Canadinc for helping me writing my papers, always listening and giving me words of encouragement. I cannot write my papers without your help and your encouragement.

I would like to express my deepest gratitude Dr. Ruben Santamarta and Dr. Shujuan Wang. This study would have had successful transmission electron microscopy analysis without your experience and help.

And finally, I would like to thank all my close friends (MESAM Research Group). You have all encouraged and believed in me. You have all helped me to focus on what has been hugely rewarding and enriching process. Dr. Anup Kbandyopadhyay, Dr. Kadri Can Atli, Ceylan Hayrettin, Ebubekir Dogan, Alper Evirgen, Joel Sam, Matthew

Vaughan, William Trehern, Hande Ozcan, Ji Ma, Brian Franco, Taymaz Jo, Nick Barta,
Li Wei Tseng, Liangfa Hu, Ankush Kothalkar, Michael Bass, Sezer Picak, Alex
Demblon, Tejas Umale, Daniel Salas, Benjamin Young.

CONTRIBUTORS & FUNDING SOURCES

This study was supported by the US Air Force Office of Scientific Research, under Grant no. FA9550-15-1-0287, the National Science Foundation under Grant no. CMMI-1534534, and the NASA University Leadership Initiative Grant Number NNX17AJ96A. RS acknowledges the support from Spanish MINECO and FEDER under Project Number MAT2014-56116-C4-1-R and the grant by the Salvador de Madariaga Program (PRX15/00549).

NOMENCLATURE

A_f	Austenite finish
A_s	Austenite start
BSE	Back-scattered electron
CC	Clasius-Clapeyron
CSS	Critical shear stress
CVP	Corresponding variant pair
DSC	Differential scanning calorimetry
EDM	Electrical discharge machining
EDS	Energy-dispersive spectroscopy
EDX	Energy-dispersive X-ray
ϵ_{irr}	Irrecoverable strain
ϵ_{act}	Actuation strain
FC	Furnace cooling
HRTEM	High resolution transmission electron microscopy
HTSMA	High temperature shape memory alloy
LIS	Lattice invariant shear
M_f	Martensite finish
M_p	Martensite peak
M_s	Martensite start
MT	Martensite transformation

SADP	Selected area diffraction pattern
SE	Superelasticity
SEM	Scanning electron microscopy
SHT	Solution heat treated
SIMT	Stress induced martensitic transformation
SMA	Shape memory alloy
SME	Shape memory effect
σ_{SIM}	Critical stress to induce martensite
TEM	Transmission electron microscopy
TRIP	Transformation induced plasticity
TTs	Transformation temperatures
TWSME	Two way shape memory effect
TWSMS	Two way shape memory strain
XRD	X-ray diffraction
WQ	Water quenched

TABLE OF CONTENTS

	Page
ABSTRACT	ii
DEDICATION	iv
ACKNOWLEDGEMENTS	v
CONTRIBUTORS & FUNDING SOURCES	vii
NOMENCLATURE.....	viii
TABLE OF CONTENTS	x
LIST OF FIGURES.....	xiii
LIST OF TABLES	xxiii
CHAPTER I INTRODUCTION	1
1.1 Motivation and Significance	1
1.2 Objectives	6
CHAPTER II BACKGROUND.....	10
2.1 Martensitic Transformations	10
2.1.1 Shape Memory Effect and Superelasticity	12
2.2. High Temperature Shape Memory Alloys	16
2.3 NiTiHf and NiTiZr Alloys	18
2.4 Two-Way Shape Memory Effect in High-Temperature Shape Memory Alloys ...	22
2.5 Actuation Fatigue Properties of High Temperature Shape Memory Alloys.....	25
2.6 Stress-induced Pseudoelastic Fatigue of SMAs	27
2.7 Temperature-induced Actuation Fatigue of SMAs	28
CHAPTER III EXPERIMENTAL METHODS.....	31
3.1 Materials Fabrication.....	31
3.2 Actuation Fatigue Processing.....	31
3.3 Two-Way Shape Memory Effect Procedure	34
3.3.1 Annealing Process	36
3.4 Microstructural Characterization.....	37

3.4.1 Microstructure and Compositional Analysis	37
3.4.2 Nanoindentation Hardness Testing	38
3.4.3 Calorimetry.....	38
3.4.5 Isothermal Monotonic Loading Tests.....	38
CHAPTER IV ROLE OF MICROSTRUCTURE ON THE ACTUATION FATIGUE PERFORMANCE OF NI-RICH NITIHF HIGH TEMPERATURE SHAPE MEMORY ALLOYS	40
4.1 Microstructure and Martensitic Transformation Characteristics of the Precipitation Hardened Ni _{50.3} Ti _{29.7} Hf ₂₀ HTSMA	44
4.2. Actuation Fatigue Experiments.....	49
4.3. Post-Mortem Martensitic Transformation Characteristics.....	52
4.4. Fracture Surface Analysis	54
4.5. Role of Microstructure on the Cyclic Evolution of Actuation Strain, Fatigue Life and Work Output	56
4.6. Effect of Microstructure on the Cyclic Evolution of Irrecoverable Strain.....	65
4.7. Evolution of Martensitic Transformation Temperatures.....	67
4.8. Fractography and Fracture Modes.....	68
4.9. Summary and Conclusions.....	69
CHAPTER V ROLE OF APPLIED STRESS LEVEL ON THE ACTUATION FATIGUE BEHAVIOR OF NITIHF HIGH TEMPERATURE SHAPE MEMORY ALLOYS	73
5.1 Initial Material Properties.....	75
5.2 Actuation Fatigue Experiments.....	77
5.3 Post-Mortem Analysis- DSC and SEM Results.....	81
5.4 Discussion of The Results	83
5.5 Effects of Stress Level on Irrecoverable Strain.....	91
5.6 Calorimetric Results and Phase Transformation Behavior	92
5.7 Failure Mechanisms	95
5.8 Summary and Conclusions.....	95
CHAPTER VI EFFECTS OF UPPER CYCLE TEMPERATURE ON THE THERMOMECHANICAL FATIGUE PERFORMANCE OF NITIHF HIGH TEMPERATURE SHAPE MEMORY ALLOYS	99
6.1. Initial Material Properties	100
6.2. Thermo-Mechanical Fatigue Experiments.....	101
6.3. Post-Mortem Characterization – DSC Results.....	105
6.4. Post-Mortem Characterization – SEM and TEM Results	106
6.5. Cyclic Evolution of Actuation Strain.....	107
6.6. Cyclic/Dimensional Stability	117
6.7. Calorimetric Results and Phase Transformation Behavior	119

6.8. Microstructural Evolution	121
6.9. Summary and Conclusions.....	125
CHAPTER VII ON THE ROLE OF APPLIED STRESS LEVEL ON THE ACTUATION FATIGUE PERFORMANCE OF NITIZR HIGH TEMPERATURE SHAPE MEMORY ALLOYS	128
CHAPTER VIII EFFECTS OF UPPER CYCLE TEMPERATURE ON THE ACTUATION FATIGUE PERFORMANCE OF NITIZR HIGH TEMPERATURE SHAPE MEMORY ALLOYS	136
CHAPTER IX COMPARISON OF ACTUATION FATIGUE PERFORMANCE FOR NI-RICH NITIHf AND NITIZR HIGH TEMPERATURE SHAPE MEMORY ALLOYS	144
9.1. Stress-Free Martensitic Transformation Temperature and Thermal Stability	145
9.2. Microstructure of NiTiHf and NiTiZr Alloys	148
9.3. Strain vs. Temperature of NiTiHf and NiTiZr alloys.....	149
9.4. Actuation Fatigue Properties of NiTiHf and NiTiZr alloys	150
9.5. Stress-Strain Behaviour of NiTiHf and NiTiZr Alloys.....	154
9.6. Stress-Free Transformation Heat and Temperatures of Failed Samples.....	155
9.7. Work-Based Model	158
9.8. Conclusions	161
CHAPTER X TWO-WAY SHAPE MEMORY EFFECT IN THE NITIHf AND NITIZR HIGH TEMPERATURE SHAPE MEMORY ALLOYS	163
10.1. Calorimetric results of Ni-rich Ni _{50.3} Ti _{29.7} Hf ₂₀ and Ni _{50.3} Ti _{29.7} Zr ₂₀ alloys	165
10.2. Electron microscopy results	167
10.3. Isothermal Monotonic Stress-Strain Response	169
10.4. Evolution of the Actuation Strain and Generation of TWSME	170
10.5. Thermomechanical training and evolution of actuation strain and TWSME....	172
10.6. Effect of annealing on the stability and magnitude of TWSMS	176
10.7. Summary and conclusions.....	178
CHAPTER XI MAIN CONCLUSIONS AND FUTURE DIRECTIONS.....	181
REFERENCES.....	186

LIST OF FIGURES

	Page
Figure 2.1 Simple illustration of one-way shape memory effect and two-way shape memory effect. In one way shape memory effect, martensite returns back to self-accommodated structure upon cooling from austenite, while martensite returns to single variant orientation in the two-way shape memory effect. Internal stresses favor certain habit plane variants, resulting in shape changes after cooling from austenite state [1].	11
Figure 2.2 (a) Schematic illustration of the actuation fatigue loading cycles on a stress-temperature phase diagram, and (b) a representative strain-temperature response describing how the relevant shape memory characteristics of the HTSMA actuator are determined from this kind of response. M_f : martensite finish, M_s : martensite start, A_s : austenite start, A_f : austenite finish temperatures [50]......	13
Figure 2.3 Schematic illustration of how transformation temperatures are determined using DSC curve.	14
Figure 2.4 (a) Schematic representation of superelasticity using a σ -T phase diagram. Austenite transforms fully detwinned martensite when sufficient stress is applied at temperature slight above A_f . (b) illustration of superelasticity on strain (ϵ) vs. stress (σ) [1].	15
Figure 2.5 Increase in transformation temperatures of NiTi alloys with addition of Pd, Pt, Au, Hf and Zr elements [69].	17
Figure 2.6. Change in the transformation temperatures of NiTi alloys as a function of Hf addition [1].	19
Figure 2.7. Change in the transformation temperatures of NiTi alloys as a function of Zr addition [1]......	21
Figure 2.8. Change in martensitic peak temperature as a function of Ni content [1].	22
Figure 2.9 (a) EDS scan carried out on a H-phase precipitate (H) and martensite matrix (M) (b) compositional line scan from H-phase precipitate to matrix phase [124]......	25
Figure 3.1 Dimensions of the dog-bone shaped fatigue samples of the nano-precipitation hardened $Ni_{50.3}Ti_{29.7}Hf_{20}$ HTSMAs used in this study [161]......	32

Figure 3.2 Experimental set-up utilized for the actuation fatigue testing of nano-precipitation hardened Ni _{50.3} Ti _{29.7} Hf ₂₀ HTSMAs. See text for details [161].....	34
Figure 3.3 Training procedure to obtain TWSME followed by an annealing treatment to evaluate the thermal stability of TWSME right after thermo-mechanical training for nano-precipitation hardened Ni _{50.3} Ti _{29.7} Hf ₂₀ and Ni _{50.3} Ti _{29.7} Zr ₂₀ alloys.....	36
Figure 4.1 DSC results of the Ni _{50.3} Ti _{29.7} Hf ₂₀ HTSMA specimens in as-extruded condition and after different aging treatments. Three DSC cycles are shown for each sample. " Reprinted with permission from [164]. "	45
Figure 4.2 Bright-field TEM images of the Ni _{50.3} Ti _{29.7} Hf ₂₀ HTSMA specimens exhibiting different sizes and distribution of H-phase precipitates within martensite variants after aging at (a) 550°C-3h, (b) 600°C-10h and after (c) furnace cooling from 700°C to 100°C in 48h, where the precipitates that are interfering the martensite growth are marked with red dashed ellipsoids. " Reprinted with permission from [164]. "	47
Figure 4.3 Thermal cyclic response of nano-precipitation hardened Ni _{50.3} Ti _{29.7} Hf ₂₀ HTSMA subjected to 300 MPa. The specimens were exposed to different aging treatments before the tests and then tested up to different UCT: (a) 550°C-3h, 300°C UCT, (b) 550°C-3h, 350°C UCT, (c) 600°C-10h, 300°C UCT, (d) 600°C-10h, 350°C UCT, (e) FC from 700°C to 100°C in 48h, 300°C UCT, and (f) FC from 700°C to 100°C in 48h, 350°C UCT. FC: Furnace Cooling, UCT: Upper Cycle Temperature. " Reprinted with permission from [164]. "	48
Figure 4.4 Evolution of strain in austenite (i.e. irrecoverable strain), strain in martensite, and actuation strain until failure during thermal cycling tests under constant stress level of 300 MPa for nano-precipitation hardened Ni _{50.3} Ti _{29.7} Hf ₂₀ HTSMA. The specimens were exposed to different aging treatments before the tests and then tested up to different UCT: (a) 550°C-3h, 300°C UCT, (b) 550°C-3h, 350°C UCT, (c) 600°C-10h, 300°C UCT, (d) 600°C-10h, 350°C UCT, (e) FC from 700°C to 100°C in 48h, 300°C UCT, and (f) FC from 700°C to 100°C in 48h, 350°C UCT. FC: Furnace Cooling, UCT: Upper Cycle Temperature. " Reprinted with permission from [164]. "	51
Figure 4.5 A comparison of the work output vs. fatigue life responses of Ni ₅₅ Ti ₄₅ [158], Ni ₅₀ Ti ₅₀ [128], Ti ₅₀ Ni ₄₀ Cu ₁₀ [130], Ti ₄₀ Ni ₅₀ Cu ₁₀ [47] and Ni _{50.3} Ti _{29.7} Hf ₂₀ HTSMA heat treated at different aging times and temperatures. The Ti ₅₀ Ni ₄₀ Cu ₁₀ specimens were in the form of wires whereas all others were in form of flat dog-bone shaped specimens. " Reprinted with permission from [164]. "	52

- Figure 4.6 Post-mortem DSC results of the nano-precipitation hardened $\text{Ni}_{50.3}\text{Ti}_{29.7}\text{Hf}_{20}$ HTSMA specimens with different aging heat treatments, exhibiting the change in the transformation temperatures and heat of transformation after the actuation fatigue experiments. The figures organized in such a way that (a) and (b) are from the samples aged at 550°C for 3h, (c) and (d) are from the samples aged at 600°C for 10h, and (e) and (f) are from the samples furnace cooled from 700°C to 100°C in 48h. (a), (c), and (e) are for cooling and (b), (d), and (f) are for heating cycles. The numbers in parentheses correspond the fatigue life of those particular samples tested. UCT: Upper Cycle Temperature. " Reprinted with permission from [164].53
- Figure 4.7 Evolution of the M_s temperatures of the actuation fatigue tested $\text{Ni}_{50.3}\text{Ti}_{29.7}\text{Hf}_{20}$ HTSMA specimens with different aging heat treatments as a function of the number of cycles to failure, relative to that of the untested samples (with the same aging heat treatments). $\Delta M_s = M_{s\text{pro} - \text{fatigue}} - M_{s\text{pre} - \text{fatigue}}$. " Reprinted with permission from [164]. "54
- Figure 4.8 SEM micrographs of the fracture surfaces of $\text{Ni}_{50.3}\text{Ti}_{29.7}\text{Hf}_{20}$ HTSMA samples following the failure after the actuation fatigue experiments. The specimens were exposed to different aging treatments before the tests and then tested up to different UCT: (a) 550°C-3h, 300°C UCT, (b) 550°C-3h, 350°C UCT, (c) 600°C-10h, 300°C UCT, (d) 600°C-10h, 350°C UCT, (e) FC from 700°C to 100°C in 48h, 300°C UCT, and (f) FC from 700°C to 100°C in 48h, 350°C UCT. FC: Furnace Cooling, UCT: Upper Cycle Temperature. " Reprinted with permission from [164]. "55
- Figure 4.9 Fatigue cracks on the side surface of the failed specimens of $\text{Ni}_{50.3}\text{Ti}_{29.7}\text{Hf}_{20}$ HTSMA samples for different aging treatments/ UCT: (a) 550°C-3h, 300°C UCT, (b) 550°C-3h, 350°C UCT, (c) 600°C-10h, 300°C UCT, (d) 600°C-10h, 350°C UCT, (e) FC from 700°C to 100°C in 48h, 300°C UCT, and (f) FC from 700°C to 100°C in 48h, 350°C UCT. FC: Furnace Cooling, UCT: Upper Cycle Temperature. " Reprinted with permission from [164]. "58
- Figure 4.10 Effect of microstructure, obtained with different aging heat treatments, on the actuation fatigue response of the nano-precipitation hardened $\text{Ni}_{50.3}\text{Ti}_{29.7}\text{Hf}_{20}$ HTSMA, thermally cycled up to different Upper Cycle Temperatures (UCT) under 300 MPa: (a) 300°C UCT and (b) 350°C UCT. " Reprinted with permission from [164]. "60
- Figure 4.11 Role of microstructure on the evolution of irrecoverable strain (strain in austenite, see Figure 2. 2 (b)) during thermal cycling under 300 MPa for nano-precipitation hardened $\text{Ni}_{50.3}\text{Ti}_{29.7}\text{Hf}_{20}$ HTSMA under different upper

cycle temperatures (UCT): (a) 300°C UCT and (b) 350°C UCT. " Reprinted with permission from [164]. "62

Figure 4.12 Summary of the important actuation fatigue characteristics such as the average actuation strain, work output, and fatigue life of nano-precipitation hardened Ni_{50.3}Ti_{29.7}Hf₂₀ HTSMAs aged at 550°C for 3h, 600°C for 10h and FC from 700 to 100°C in 48h. Patterned and solid bars represent the average actuation strain and work output, respectively. FC: Furnace Cooled. UCT: Upper Cycle Temperature. " Reprinted with permission from [164]. " .65

Figure 5.1 (a) Initial DSC results of the Ni_{50.3}Ti_{29.7}Hf₂₀ specimen in as extruded and heat treated (HT) at 550°C for 3 hours conditions before the actuation fatigue tests, (b) the corresponding bright field TEM image of the microstructure, showing H-phase nano-precipitates, and (c) representative carbide size and distribution in the microstructure for the same Ni_{50.3}Ti_{29.7}Hf₂₀ sample. White particles in (c) are the hafnium carbides. " Reprinted with permission from [50]. "76

Figure 5.2 Evolution of strain vs. temperature responses with the number of cycles to failure for the nano-precipitation hardened Ni_{50.3}Ti_{29.7}Hf₂₀ HTSMA, heat treated (HT) at 550°C for 3 hours, under (a) 200MPa, (b) 300 MPa, (c) 400 MPa, and (d) 500 MPa tensile stresses. Only one representative case for each condition is shown. " Reprinted with permission from [50]. "78

Figure 5.3 Evolution of the martensite strain, total irrecoverable strain, and actuation strain as a function of the number of thermal cycles until failure for the nano-precipitation hardened Ni_{50.3}Ti_{29.7}Hf₂₀ HTSMA, heat treated (HT) at 550°C for 3 hours, under (a) 200 MPa, (b) 300 MPa, (c) 400 MPa and (d) 500 MPa tensile stress levels. " Reprinted with permission from [50]. "80

Figure 5.4 Evolution of martensitic transformation temperatures as a function of stress level in the first and last cycles of the actuation fatigue experiments for the nano-precipitation hardened Ni_{50.3}Ti_{29.7}Hf₂₀ HTSMA demonstrating large shifts in M_s and A_f temperatures while almost constant M_f and A_s temperatures. " Reprinted with permission from [50]. "80

Figure 5.5 Post-mortem DSC results exhibiting changes in transformation heat and martensitic transformation temperatures of the fatigue failed specimens as compared to the initial nano-precipitation hardened Ni_{50.3}Ti_{29.7}Hf₂₀ HTSMA samples: (a) heating and (b) cooling DSC curves of the samples before and after fatigue failure under different stress levels, and (c) the corresponding evolution of M_s temperatures of these fatigue specimens relative to that of an untested specimen. $\Delta M_s = M_{s \text{ after fatigue}} - M_{s \text{ before fatigue}}$. " Reprinted with permission from [50]. "83

Figure 5.6 Backscattered scanning electron micrographs of the fracture surfaces of the nano-precipitation hardened Ni _{50.3} Ti _{29.7} Hf ₂₀ HTSMA specimens after failure during the actuation fatigue experiments under (a) 200 MPa, (b) 300 MPa, (c) 400 MPa and (d) 500 MPa. Cracks detected in the interior sections of the failed specimens for (e) 200 MPa and (f) 500 MPa. The arrows in (e) and (f) indicate the loading direction of the specimens. " Reprinted with permission from [50]. "	85
Figure 5.7 Effect of constant tensile stress level on the evolution of actuation strain as a function of the number of thermal cycling in the Ni _{50.3} Ti _{29.7} Hf ₂₀ HTSMA samples aged at 550°C for 3 hrs during the actuation fatigue experiments. Lower and upper cycling temperatures were 40 °C and 300 °C, respectively. The results from two different samples are presented here to demonstrate the relatively small sample to sample variation in actuation strains and fatigue lives. " Reprinted with permission from [50]. "	86
Figure 5.8 Comparison of the average actuation strains, average work output levels, and fatigue lives as a function of the applied tensile stress levels during actuation fatigue experiments on nano-precipitation hardened Ni _{50.3} Ti _{29.7} Hf ₂₀ HTSMA, heat treated at 550°C for 3 hrs. The error bars represent the sample to sample variations. " Reprinted with permission from [50]. "	88
Figure 5.9 A comparison of the work output vs. fatigue life results obtained from Ti ₅₀ Ni ₄₀ Cu ₁₀ wires [130], bulk Ni ₅₀ Ti ₅₀ [128], bulk Ni ₆₀ Ti ₄₀ [184], Ti ₄₀ Ni ₅₀ Cu ₁₀ wires [47], and bulk nano-precipitation hardened Ni _{50.3} Ti _{29.7} Hf ₂₀ HTSMAs. The solid lines and the equations next to them are the best fit lines of the data presented to the power-law relationship $\sigma_{act\epsilon act} = aNf - b$. " Reprinted with permission from [50]. "	89
Figure 5.10 Effect of applied stress level on the evolution of the irrecoverable strain until failure upon thermal cycling of the nano-precipitation hardened Ni _{50.3} Ti _{29.7} Hf ₂₀ HTSMA heat treated at 550°C for 3 hrs. " Reprinted with permission from [50]. "	94
Figure 6.1. (a) DSC result for the Ni _{50.3} Ti _{29.7} Hf ₂₀ specimen heat treated at 550°C for 3 hours and (b) the corresponding TEM image showing H-phase precipitates. HT:Heat Treatment. " Reprinted with permission from [161]. "	101
Figure 6.2. Strain vs. temperature curves for the nano-precipitation hardened Ni _{50.3} Ti _{29.7} Hf ₂₀ HTSMA heat treated at 550°C for 3 hours under (a) 300 MPa with the UCT of 300°C and (b) 400MPa with the UCT of 350°C. UCT: Upper Cycle Temperature. " Reprinted with permission from [161]. "	102

- Figure 6.3. Effect of upper cycle temperature (UCT) on the actuation fatigue response of the nano-precipitation hardened $\text{Ni}_{50.3}\text{Ti}_{29.7}\text{Hf}_{20}$ HTSMA heat treated at 550°C for 3 hours under (a) 300 MPa and (b) 400 MPa constant stress levels. HT: Heat Treatment. " Reprinted with permission from [161]. " 104
- Figure 6.4. Evolution of the irrecoverable strain upon thermo-mechanical cycling of nano-precipitation hardened $\text{Ni}_{50.3}\text{Ti}_{29.7}\text{Hf}_{20}$ HTSMA (heat treated at 550°C for 3 hours) for the four stress - UCT combinations employed in the current experiments. " Reprinted with permission from [161]. " 105
- Figure 6.5. Post-mortem DSC results of nano-precipitation hardened $\text{Ni}_{50.3}\text{Ti}_{29.7}\text{Hf}_{20}$ HTSMA specimens, demonstrating the change in the transformation temperatures and heat of transformation after the thermo-mechanical fatigue experiments: (a) heating and (b) cooling DSC curves of pre- and post-fatigue samples, and (c) the corresponding evolution of M_s temperatures of these fatigue specimens relative to that of an untested specimen: $\Delta M_s = M_{s\text{pro}} - \text{fatigue} - M_{s\text{pre}} - \text{fatigue}$. The numbers in parentheses in (a) and (b) correspond the fatigue lives of those particular samples tested. " Reprinted with permission from [161]. " 107
- Figure 6.6. SEM micrographs of the fracture surfaces of nano-precipitation hardened $\text{Ni}_{50.3}\text{Ti}_{29.7}\text{Hf}_{20}$ HTSMA specimens following failure after the thermo-mechanical fatigue experiments under (a) 300 MPa with 300°C UCT, (b) 300 MPa with 350°C UCT, (c) 400 MPa with 300°C UCT, and (d) 400 MPa with 350°C UCT. Detected fatigue cracks on the side surface of the failed samples are demonstrated for (e) 300 MPa with 300°C UCT and (f) 400 MPa with 350°C UCT cases. The arrows in (e) and (f) show the loading direction of the samples. " Reprinted with permission from [161]. " 109
- Figure 6.7. Bright field TEM images exhibiting size, volume, and morphology of precipitates in nano-precipitation hardened $\text{Ni}_{50.3}\text{Ti}_{29.7}\text{Hf}_{20}$ HTSMA specimens: (a) the sample heat treated at 550°C for 3 hours prior to fatigue testing, (b) failed sample under 300 MPa stress and an UCT of 300°C , and (c) the failed specimen under 400 MPa stress and an UCT of 350°C . All images were captured at room temperature. " Reprinted with permission from [161]. " 111
- Figure 6.8. Average precipitate size along the long and short axes based on the TEM observations carried out on the $\text{Ni}_{50.3}\text{Ti}_{29.7}\text{Hf}_{20}$ HTSMA samples prior to and following thermo-mechanical cyclic experiments. The error bars indicate the range of the measured lengths for each case. Minimum 20 different TEM images from different locations and more than 500 precipitates were analyzed for each case. " Reprinted with permission from [161]. " 113

Figure 6.9. (a) Crack opens in the martensite state and (b) closes in the austenite state during thermomechanical cycling. NiTiHf sample was thermally cycled between 50°C-300°C under 545 N [190].	114
Figure 6.10 (a) An exemplary bright field TEM image of two variants of (001) compound twins observed in the matrices of all failed specimens, (b) the corresponding SAD pattern evidencing the compound twins observed in tested samples, (c) an exemplary bright field TEM image of {011} Type I twins observed in all failed samples, and (d) the corresponding SAD pattern demonstrating two martensite variants on the (011) _{B19'} type I twin plane along the [100] _{B19'} zone axis, and precipitates. " Reprinted with permission from [161]. "	116
Figure 6.11. Summary of the average actuation strains and actuation fatigue lives observed in the thermo-mechanical fatigue experiments carried out on nano-precipitation hardened Ni _{50.3} Ti _{29.7} Hf ₂₀ HTSMAs heat treated at 550°C for 3 hours, for the four stress - UCT combinations considered in this work. The error bars were obtained based on the companion experiments conducted for each case. " Reprinted with permission from [161]. "	118
Figure 6.12. A comparison of the work output vs. number of cycles to failure responses of Ni ₆₀ Ti ₄₀ [192], Ni ₅₀ Ti ₅₀ [128], Ti ₅₀ Ni ₄₀ Cu ₁₀ [193] and nano-precipitation hardened Ni _{50.3} Ti _{29.7} Hf ₂₀ HTSMA. The Ti ₅₀ Ni ₄₀ Cu ₁₀ samples were in form of wires whereas all others were in form of dog-bone shaped samples. " Reprinted with permission from [161]. "	120
Figure 6.13. Effect of UCT on the actuation fatigue response of the nano-precipitation hardened Ni _{50.3} Ti _{29.7} Hf ₂₀ HTSMA samples heat treated at 550°C for 3 hours under 300 MPa. The experiment with 250°C UCT did not result in failure of specimen, and the experiment was stopped at about 31,000 cycles. " Reprinted with permission from [161]."	122
Figure 7.1 (a) Nano-precipitates within the matrix after aging 550°C-3h, temperature vs. strain evolution of nano-precipitation hardened Ni _{50.3} Ti _{29.7} Zr ₂₀ alloys until failure under stress level of (b) 200MPa, (c) 400MPa, and effect of applied stress levels on (d) the evolution of actuation (e) work-output of Ni _{50.3} Ti _{29.7} Zr ₂₀ .	129
Figure 7.2 (a) Effect of applied stress levels on the evolution of the irrecoverable strain for nano-precipitation strengthened Ni _{50.3} Ti _{29.7} Zr ₂₀ alloy (b) stress vs. strain graph of Ni _{50.3} Ti _{29.7} Zr ₂₀ aged at 550°C-3h obtained through servo-hydraulic MTS test frame, and fracture surface of specimens failed at stress level of (c) 200MPa and (d) 400MPa.	131

Figure 7.3 (a) Stress-free DSC measurements over ten thermal cycles prior to fatigue testing for $\text{Ni}_{50.3}\text{Ti}_{29.7}\text{Zr}_{20}$ alloy in the as-extruded condition and aged at 550°C -3h, (b) decrease in the M_s for two conditions (c) post-mortem heating DSC curve of pre- and post-fatigue specimens.....	132
Figure 7.4. Grain size images of failed $\text{Ni}_{50.3}\text{Ti}_{29.7}\text{Zr}_{20}$ samples (a) 200MPa, (b) 400MPa and (c) grain size distribution plots of 200MPa and 400MPa.....	134
Figure 8.1. Initial material properties of nano-precipitation hardened $\text{Ni}_{50.3}\text{Ti}_{29.7}\text{Zr}_{20}$ alloy before the actuation fatigue testing (a) transformation temperatures of specimens in as-extruded condition and aged at 550°C -3h, (b) decrease in the M_s of specimen as a function of DSC cycles under stress free conditions for as-extruded condition and aged at 550°C -3h, (c) bright field TEM micrograph of microstructure after aging at 550°C -3h, (d) grain size analysis in the optical microscopy for sample aged at 550°C -3h.....	137
Figure 8.2 Effect of UCT levels on the actuation fatigue performance of nano-precipitation hardened $\text{Ni}_{50.3}\text{Ti}_{29.7}\text{Zr}_{20}$ alloys, temperature vs. strain vs evolution until failure of specimens at (a) 250°C UCT, (b) 400°C UCT and evolution of (c) actuation strain and (d) irrecoverable strain for various UCT levels.....	138
Figure 8.3. Post- mortem analysis through DSC after failure of samples (a) heat of transformation of failed samples at different UCT levels as compared to untested sample in the stress free condition during cooling, (b) evolution of M_s temperature of failed samples relative to an untested sample. $\Delta M_s = M_{s\text{after fatigue}} - M_{s\text{before fatigue}}$	141
Figure 8.4. Secondary electron images of the fracture surfaces of nano-precipitation hardened $\text{Ni}_{50.3}\text{Ti}_{29.7}\text{Zr}_{20}$ HTSMA specimens after failure at (a) 250°C -UCT and (b) 400°C -UCT, backscattered electron micrographs of microstructure examined in the interior section of broken samples at (c) 250°C -UCT and (d) 400°C -UCT.....	142
Figure 9.1. Comparison of transformation temperatures for $\text{Ni}_{50.3}\text{Ti}_{29.7}\text{Hf}_{20}$ and $\text{Ni}_{50.3}\text{Ti}_{29.7}\text{Zr}_{20}$ alloys in the condition of (a) As-Extruded (b) 550°C -3h and (c) both As-Extruded and 550°C -3h.....	145
Figure 9.2. Decrease in the M_s temperatures of $\text{Ni}_{50.3}\text{Ti}_{29.7}\text{Hf}_{20}$ and $\text{Ni}_{50.3}\text{Ti}_{29.7}\text{Zr}_{20}$ alloys due to stress free thermal cycling through DSC in the condition of (a) As-Extruded (b) 550°C -3h and (c) both As-Extruded and 550°C -3h.....	146
Figure 9.3. Comparison of morphology, size and distribution of precipitates after aging at 550°C -3h for (a) $\text{Ni}_{50.3}\text{Ti}_{29.7}\text{Hf}_{20}$ (b) $\text{Ni}_{50.3}\text{Ti}_{29.7}\text{Zr}_{20}$ and (c)	

comparison of size of precipitates along long axis and short axis for Ni _{50.3} Ti _{29.7} Hf ₂₀ and Ni _{50.3} Ti _{29.7} Zr ₂₀ alloys.	147
Figure 9.4. Strain vs. temperature response of nano-precipitation hardened Ni _{50.3} Ti _{29.7} Hf ₂₀ loaded at (a) 200MPa, (b) 400MPa and Ni _{50.3} Ti _{29.7} Zr ₂₀ loaded at (c) 200MPa, (d) 400MPa.....	148
Figure 9.5. Evolution of actuation strain until failure of specimens for nano-precipitation hardened Ni _{50.3} Ti _{29.7} Hf ₂₀ and Ni _{50.3} Ti _{29.7} Zr ₂₀ materials under (a) 200MPa, (b) 300MPa and (c) 400 MPa.	149
Figure 9.6. Effect of stress levels on the evolution of actuation strain for nano-precipitation hardened (a) Ni _{50.3} Ti _{29.7} Hf ₂₀ and (b) Ni _{50.3} Ti _{29.7} Zr ₂₀ alloys.	150
Figure 9.7. Evolution of irrecoverable strain until failure of specimens for nano-precipitation hardened Ni _{50.3} Ti _{29.7} Hf ₂₀ and Ni _{50.3} Ti _{29.7} Zr ₂₀ materials under (a) 200MPa, (b) 300MPa and (c) 400 MPa.	151
Figure 9.8. Effect of stress levels on the evolution of irrecoverable strain for nano-precipitation hardened (a) Ni _{50.3} Ti _{29.7} Hf ₂₀ and (b) Ni _{50.3} Ti _{29.7} Zr ₂₀ alloys.	152
Figure 9.9. Comparison of uniaxial stress vs. strain curves of Ni _{50.3} Ti _{29.7} Hf ₂₀ and Ni _{50.3} Ti _{29.7} Zr ₂₀ material aged at 550°C-3h.....	153
Figure 9.10. Comparison of work-output vs. number of cycles to failure of (a) Ni _{50.3} Ti _{29.7} Hf ₂₀ vs. Ni _{50.3} Ti _{29.7} Zr ₂₀ alloys and (b) high temperature shape memory alloys (HTSMAs) vs. low temperature shape memory alloys (LTSMAs) including Ti ₄₀ Ni ₅₀ Cu ₁₀ wires, bulk Ni ₅₀ Ti ₅₀ , Ti ₅₀ Ni ₄₀ Cu ₁₀ wires, bulk Ni ₆₀ Ti ₄₀ . The equations and solid lines are obtained through power-law relationship $\sigma_{act\epsilon act} = aNf - b$	154
Figure 9.11. Changes in the transformation temperatures and transformation heat of the fatigue failed Ni _{50.3} Ti _{29.7} Hf ₂₀ and Ni _{50.3} Ti _{29.7} Zr ₂₀ samples during heating at different stress levels as compared to the untested and aged Ni _{50.3} Ti _{29.7} Hf ₂₀ and Ni _{50.3} Ti _{29.7} Zr ₂₀ samples at 550°C-3h.	155
Figure 9.12. Post-mortem DSC results demonstrating evolution of the M _s temperatures of the fatigue failed specimens as compared to the untested nano-precipitation hardened (a) Ni _{50.3} Ti _{29.7} Hf ₂₀ (b) Ni _{50.3} Ti _{29.7} Zr ₂₀ (c) both Ni _{50.3} Ti _{29.7} Hf ₂₀ and Ni _{50.3} Ti _{29.7} Zr ₂₀ . $\Delta M_s = M_{s\text{ after fatigue}} - M_{s\text{ before fatigue}}$	156
Figure 9.13. Comparison of nano-precipitation hardened Ni _{50.3} Ti _{29.7} Hf ₂₀ and Ni _{50.3} Ti _{29.7} Zr ₂₀ materials at different stress levels in terms of (a) fatigue life (b) work output.	158

Figure 10.1 DSC results of Ni _{50.3} Ti _{29.7} Hf ₂₀ and Ni _{50.3} Ti _{29.7} Zr ₂₀ alloys aged at 550°C-3h (a) transformation temperatures and transformation heat (b) decrease in the M _s temperature representing cyclic instability of materials during stress-free thermal cycling across martensite and austenite phases.	166
Figure 10.2 Bright field TEM images after aging at 550°C for 3h (a) Ni _{50.3} Ti _{29.7} Hf ₂₀ (b) Ni _{50.3} Ti _{29.7} Zr ₂₀ and (c) comparison of size of precipitates along long axis and short axis for Hf- and Zr- based alloys.	167
Figure 10.3 Comparison of uniaxial stress vs. strain curves of nano-precipitation hardened Ni _{50.3} Ti _{29.7} Hf ₂₀ and Ni _{50.3} Ti _{29.7} Zr ₂₀ HTSMAs.	169
Figure 10.4 Evolution of actuation strain during thermomechanical training procedure employed in this study and subsequent effect of annealing treatment on the actuation strain of material previously trained for 2000-cycles isobaric thermal cycling. The results are for nano-precipitation hardened Ni _{50.3} Ti _{29.7} Hf ₂₀ and Ni _{50.3} Ti _{29.7} Zr ₂₀ alloys.	170
Figure 10.5 Evolution of strain vs. temperature response at 1 st , 1000 th and 2000 th training cycles for nano-precipitation hardened Ni _{50.3} Ti _{29.7} Hf ₂₀ under (a) 50MPa, (b) 300MPa and Ni _{50.3} Ti _{29.7} Zr ₂₀ under (c) 50MPa, (d) 300MPa.	171
Figure 10.6 Evolution of actuation strain as a function of applied stress levels at various training cycles for nano-precipitation hardened Ni _{50.3} Ti _{29.7} Hf ₂₀ and Ni _{50.3} Ti _{29.7} Zr ₂₀	172
Figure 10.7 Evolution of actuation strain as a function of number of cycles under various applied stress levels for nano-precipitation hardened Ni _{50.3} Ti _{29.7} Hf ₂₀ and Ni _{50.3} Ti _{29.7} Zr ₂₀	173
Figure 10.8 Effect of annealing treatment on the evolution of actuation strain and TWSMS stored after 2000 th training cycles.	175
Figure 10.9 Change in the TWSMS obtained right after 2000 th training cycles as a function of annealing treatment for nano-precipitation hardened (a) Ni _{50.3} Ti _{29.7} Hf ₂₀ and (b) Ni _{50.3} Ti _{29.7} Zr ₂₀	176

LIST OF TABLES

	Page
Table 4.1 Martensitic transformation temperatures and transformation heats, determined using DSC, before and after the actuation fatigue tests, with two different upper cycle temperatures (UCT), of the $\text{Ni}_{50.3}\text{Ti}_{29.7}\text{Hf}_{20}$ HTSMA samples, precipitation heat treated (HT) at three different conditions before the tests. M_s and M_f : Martensite start and finish temperature; A_s and A_f : Austenite start and finish temperatures. FC: Furnace Cooled. Stress-free represents the sample before the fatigue testing. " Reprinted with permission from [164]. "	42
Table 4.2 Transformation temperatures and thermal hysteresis in the first and last thermo-mechanical cycles of the actuation fatigue experiments, extracted from the strain vs temperature curves of $\text{Ni}_{50.3}\text{Ti}_{29.7}\text{Hf}_{20}$ HTSMAs heat treated (HT) at different aging times and temperatures. M_s and M_f : Martensite start and finish temperature; A_s and A_f : Austenite start and finish temperatures. $\Delta M_s = M_s^{\text{first}} - M_s^{\text{last}}$, $\Delta A_f = A_f^{\text{first}} - A_f^{\text{last}}$. UCT: Upper Cycle Temperature. " Reprinted with permission from [164]. "	43
Table 5.1 First and last cycle transformation temperatures obtained from the strain-temperature responses of the $\text{Ni}_{50.3}\text{Ti}_{29.7}\text{Hf}_{20}$ HTSMA specimens, heat treated at 550°C for 3 hours, for different stress levels during the actuation fatigue experiments. " Reprinted with permission from [50]. "	74
Table 5.2 Change in martensitic transformation temperatures and the transformation heat of the $\text{Ni}_{50.3}\text{Ti}_{29.7}\text{Hf}_{20}$ HTSMA heat treated at 550°C for 3 hours after failure in the actuation fatigue experiments under different stress levels. DSC was utilized for measuring the transformation temperatures, and the results represent the average of the measurements carried out on two different failed specimens. " Reprinted with permission from [50]. "	75
Table 6.1. Evolution of transformation temperatures and enthalpies of nano-precipitation hardened $\text{Ni}_{50.3}\text{Ti}_{29.7}\text{Hf}_{20}$ HTSMAs following failure in the thermo-mechanical fatigue experiments. The measurements were conducted using DSC. The average values from two or three different failed fatigue samples are provided. DSC samples were cut from a region near the fracture surface. " Reprinted with permission from [161]. "	100

CHAPTER I

INTRODUCTION

The focus of this study is centered on development of functionally durable, reliable and thermally stable NiTiHf and NiTiZr high temperature shape memory alloys (HTSMAs) to be utilized as a solid state actuator in many engineering applications. Reliability and durability of these materials are significant criteria before any commercial use. The precipitation strengthening mechanism is employed to improve their functional and thermal stability and actuation fatigue performance. The objectives of the present study are undertaken with addressing these issues.

1.1 Motivation and Significance

Shape memory alloys (SMAs) have the capability to recover large deformations upon heating through reversible martensitic transformations from low symmetry, low temperature martensitic state to higher symmetry, higher temperature austenitic state [1, 18]. Nickel-titanium (NiTi) SMAs are the most commonly used ones in applications, and they frequently find use in actuators, especially in automotive, robotic and aerospace industries, mainly owing to their high work output, acceptable durability, and corrosion resistance [18, 19]. However, the utility of NiTi SMAs is restricted to relatively low temperatures ($< 100^{\circ}\text{C}$) and applied stresses below 500 MPa, which prevents them from being employed in applications involving elevated temperatures and requiring high strengths [1, 18-21]. Furthermore, NiTi SMAs exhibit dimensional instability during thermo-mechanical cycling due to the accumulation of a large amount of irrecoverable strains [22, 23].

In order to address these shortcomings, NiTi has been alloyed with ternary elements, including Au, Hf, Pd, Pt, and Zr, with the intent of increasing the martensitic transformation temperatures and improving their shape memory properties through solid solution hardening. Over the last ten years, the martensitic transformation behavior and thermo-mechanical response of such ternary alloys have been extensively studied [2, 24-33] . Since the addition of Hf or Zr provides a cost-effective alternative to NiTi alloyed with Pd, Pt and Au, due to the high cost of the latter, NiTiHf and NiTiZr alloys have recently attracted considerable attention [1].

Despite the favorable increase in transformation temperatures, the addition of Hf to NiTi has been shown to introduce few issues related to shape memory response, such as lower actuation strains as compared to binary NiTi, and fast degradation of the reversibility of transformation during thermal and mechanical cycling [24, 34-36]. However, the latter issue is mostly observed in NiTiHf alloys that have near-stoichiometric or Ni-lean chemical compositions (containing 50 at.% or less Ni) [7]. The main reasons for thermo-mechanical instability during martensitic transformation upon cyclic loading in these alloys are the significant incompatibility between austenite and martensite phases (more pronounced than in binary NiTi) [37], the change in martensite twinning modes with the addition of Hf (more compound twins instead of conventional Type I and Type II twin formation in martensite) [37, 38], and low strength against dislocation plasticity that accompanies the transformation in order to accommodate the incompatibility between the transforming phases [2, 24, 25, 34, 39].

In Ni-rich NiTiHf and NiTiZr alloys, on the other hand, it is possible to form nano-scale Ni-rich precipitates upon heat treatment, which strengthen the matrix by acting as barriers against plastic deformation [2-6]. The increase in strength due to precipitation also permits reversible martensitic transformation at higher stress levels [2, 3, 7, 8]. Furthermore, nano-precipitation in Ni-rich NiTiHf and NiTiZr alloys allows for precise control of transformation temperatures through the change in Ni content of the matrix as a function of precipitate volume fraction [4]. Consequently, the possibility to tailor these properties through nano-precipitation make the Ni-rich NiTiHf and NiTiZr SMAs promising candidates for practical applications that involve elevated temperatures and high stresses.

Despite the aforementioned advantages brought about by nano-precipitation, many of the envisaged applications also require a stable fatigue response and long fatigue lives, and thus, it is of utmost importance to assess the cyclic deformation response of NiTiHf and NiTiZr high temperature SMAs (HTSMAs) at elevated temperatures. In general, most of the current practical applications of SMAs, especially biomedical applications [40-42] rely on the superelastic behavior of these materials: when loaded, SMAs exhibit stress-induced martensitic transformation from austenite to martensite, followed by the reverse transformation back to austenite upon unloading. The aerospace and automotive applications, on the other hand, can take advantage of high energy densities of SMAs as actuator materials [43-45]. In such cases, initially deformed SMA actuators can do work against an external load upon heating, undergo large shape changes upon subsequent cooling under the same load due to forward martensitic transformation, and once heated,

recover their original shape due to reverse martensitic transformation, while still providing work against the same external load. Even though numerous studies have been conducted on superelastic fatigue properties of SMAs [9-13], only a very few reports are available in the literature addressing their actuation fatigue response [14-17], and to the best of the authors' knowledge, none on the actuation fatigue response of HTSMAs. Additionally, even though several studies are reported on two-way shape memory effect (TWSME) properties of Ni-rich NiTiHf alloy, there is no study in the literature about TWSME for Ni-rich NiTiZr alloy and its thermal stability at elevated temperature as well as comparison with its counterpart Ni-rich NiTiHf. So far, the experimental results on these aspects are rather limited, particularly in promising candidate Ni-rich NiTiZr alloy.

In general, fatigue lives and actuation fatigue performance as well as TWSME properties of SMAs are dictated by several material parameters, including chemical composition, surface finish, training cycles, microstructural changes as a result of various thermo-mechanical processing parameters, and operating temperatures [16, 17]. Recent studies on the actuation fatigue of NiTi and NiTiCu SMAs were conducted by Miller and co-workers [46, 47]. NiTiCu wire specimens aged at different heat treatments were thermo-mechanically cycled until failure under constant stress level. It is reported that actuation fatigue performance depends on heat treatment conditions and optimal heat treatment needs to be identified to utilize the SMA on a best effort basis. Thus, there is a need to understand optimum microstructure to attain best actuation fatigue performance of Ni-rich NiTiHf since recent studies indicated that nano-sized precipitates

upon heat treatment lead to precise control of transformation temperatures, outstanding shape memory response and high resistance to plastic deformation, as well as excellent superelastic shape recovery for Ni-rich $\text{Ni}_{50.3}\text{Ti}_{29.7}\text{Hf}_{20}$ [2, 3]. Furthermore, a notable observation regarding the operating temperatures of SMAs is that an increase in UCT above austenite finish temperature in NiTi SMAs leads to shorter fatigue lives under thermo-mechanical cyclic loading [20, 48]. However, the role of UCT and applied stress levels on the cyclic deformation response of Ni-rich NiTiHf and NiTiZr alloys have not been studied to date. Moreover, the transformation temperatures in most HTSMAs can be relatively high especially under applied stress (e.g., near $0.3T_H$ ¹ and higher), and diffusional mechanisms may accompany the phase transformation and negatively impact its reversibility. Transformation temperatures under stress can approach the temperatures at which new precipitates may form or existing ones may further grow during thermo-mechanical cycling. Additionally, to our knowledge, comprehensive study in NiTiHf and NiTiZr HTSMAs is still lacking in the literature. Available comparative studies are mostly limited to transmission electron microscopy (TEM) and calorimetry investigation.

The present work was undertaken with the motivation of addressing this issue and providing the first systematic study on the actuation fatigue response of HTSMAs, and more specifically, establishing a thorough understanding of the thermo-mechanical fatigue response of a nano-precipitation hardened NiTiHf and NiTiZr HTSMAs. In

¹ T_H : Homologous temperature

particular, for NiTiHf alloy, three heat treatments were selected to form different microstructures: 550°C-3h (corresponding precipitate size: <20nm in length), 600°C-10h (precipitate size: 40-80 nm), and furnace cooling from 700 to 100°C at 48h (precipitate size: 70-200nm). After failure of specimens, actuation fatigue performance of distinct microstructures was examined through microstructural characterization using differential scanning calorimetry (DSC), scanning electron microscopy (SEM) and transmission electron microscopy (TEM) to understand effect of heat treatments on failure mechanism, as well as evolution of shape memory response of material. Moreover, the effects of upper cycle temperature (UCT) and stress level on the thermo-mechanical cyclic response and actuation fatigue life of the Ni-rich Ni_{50.3}Ti_{29.7}Hf₂₀ and Ni_{50.3}Ti_{29.7}Zr₂₀ HTSMA were investigated, where nano-precipitates with sizes less than 50 nm lead to excellent reversibility of martensitic transformation and dimensional stability under thermo-mechanical loading [2-4, 26, 29]. The experimental results reported herein not only revealed the optimum UCT and applied stress levels for desired high-temperature actuation fatigue performance, but also constitute the first set of data towards building a comprehensive database for HTSMA actuation performance to guide the efforts in designing durable and stable HTSMA actuators with the maximum possible work output.

1.2 Objectives

Primary objective of the present study can be summarized as an intensive investigation on actuation fatigue performance and TWSME properties of Ni_{50.3}Ti_{29.7}Hf₂₀ and Ni_{50.3}Ti_{29.7}Zr₂₀ alloys to attain improved functional and cyclic

stability for high temperature actuator applications. Furthermore, this study establishes the fundamental understanding on the role of microstructure parameters on functional and cyclic stability during repeated transformations. $\text{Ni}_{50.3}\text{Ti}_{29.7}\text{Hf}_{20}$ and $\text{Ni}_{50.3}\text{Ti}_{29.7}\text{Zr}_{20}$ compositions are most widely investigated Ni-rich NiTiHf and NiTiZr alloys, having high transformation temperatures ($>100^\circ\text{C}$) after nano-precipitation with excellent shape memory characteristics.

The overall objectives of the present work are:

1. Investigation on the role of precipitates size, morphology and distribution on the cyclic response and actuation fatigue performance of $\text{Ni}_{50.3}\text{Ti}_{29.7}\text{Hf}_{20}$ HTSMA through thermo-mechanical testing, SEM, TEM and DSC.

- a. Optimum microstructure for extended actuation fatigue lives, durability and damage tolerance.
- b. Control of level of actuation strain, fatigue life and irrecoverable strain by controlling precipitates size.
- c. Fracture analysis and cracks density measurement of failed samples with different microstructures.
- d. Post-mortem analysis on transformation temperatures and heat of transformation prior to fatigue testing and after fatigue test is completed.

2. Evaluation of effect of upper cycle temperature on the actuation fatigue properties of $\text{Ni}_{50.3}\text{Ti}_{29.7}\text{Hf}_{20}$ and $\text{Ni}_{50.3}\text{Ti}_{29.7}\text{Zr}_{20}$ HTSMA through isobaric thermal cycling, SEM, TEM and DSC.

- a. Determination of UCT level on actuation fatigue life, irrecoverable strain and actuation strain for nano-precipitation hardened $\text{Ni}_{50.3}\text{Ti}_{29.7}\text{Hf}_{20}$ at 550°C -3h.
- b. Determination of stability of precipitates during thermo-mechanical cycling by comparing the precipitates size and morphology after failure of samples relative to those of untested samples.

3. Testing on the influence of applied stress level on the thermo-mechanical properties of $\text{Ni}_{50.3}\text{Ti}_{29.7}\text{Hf}_{20}$ and $\text{Ni}_{50.3}\text{Ti}_{29.7}\text{Zr}_{20}$ HTSMA through actuation fatigue testing, SEM, TEM and DSC.

- a. Understanding the effect of stress levels on actuation fatigue life, level of actuation strain and total irrecoverable strain.
- b. Speculated a universal empirical rule for describing the actuation fatigue response of shape memory alloys that determines suitability of material as an actuator.
- c. Understanding suitability of work-based model to predict actuation fatigue life of SMAs by relating work-output of samples with two empirical constants to number of cycles to failure.

4. Two-way shape memory characterization of $\text{Ni}_{50.3}\text{Ti}_{29.7}\text{Hf}_{20}$ and $\text{Ni}_{50.3}\text{Ti}_{29.7}\text{Zr}_{20}$ HTSMAs and investigation its cyclic stability at elevated temperatures.

- a. Generation of two-way shape memory strain (TWSMS) during thermo-mechanical cycling on nano-precipitation hardened $\text{Ni}_{50.3}\text{Ti}_{29.7}\text{Hf}_{20}$ and $\text{Ni}_{50.3}\text{Ti}_{29.7}\text{Zr}_{20}$ HTSMAs.

- b. Determination of stability TWSME of $\text{Ni}_{50.3}\text{Ti}_{29.7}\text{Hf}_{20}$ and $\text{Ni}_{50.3}\text{Ti}_{29.7}\text{Zr}_{20}$ HTSMAs through annealing treatment at elevated temperatures.

5. Comprehensive comparison of shape memory properties of $\text{Ni}_{50.3}\text{Ti}_{29.7}\text{Hf}_{20}$ and $\text{Ni}_{50.3}\text{Ti}_{29.7}\text{Zr}_{20}$ alloys.

- a. Evolution of transformation temperatures and thermal stability of Ni-rich NiTiHf and NiTiZr alloys.
- b. Precipitates size, morphology and distribution of Ni-rich NiTiHf and NiTiZr alloys after aging at 550°C -3h.
- c. Stress vs. strain behavior of Ni-rich NiTiHf and NiTiZr alloys after aging at 550°C -3h.
- d. Determination actuation fatigue properties of Ni-rich NiTiHf and NiTiZr alloys after aging at 550°C -3h.

The present study aims to establish fundamental understanding on actuation fatigue properties and two-way shape memory properties of Ni-rich NiTiHf and NiTiZr alloys for their potential application in the automotive, energy and aerospace industries. Additionally, the durability and actuation tests will be employed to develop parameters for damage models and actuator design tools and to evaluate them for applicability to life cycle predictions needs.

CHAPTER II

BACKGROUND

In this chapter, brief literature review will be conducted covering martensitic transformation and its two unique shape memory effect and superelastic properties, high temperature shape memory alloys (HTSMAs), NiTiHf and NiTiZr HTSMAs, H-phase precipitation hardening, as well as actuation fatigue properties of HTSMAs, work-based approach to predict fatigue life of SMAs and origins of two-way shape memory effect (TWSME).

2.1 Martensitic Transformations

Shape memory alloys (SMAs) exhibit two distinct crystal structures or phases, high symmetry and high temperature austenite phase and low symmetry and low temperature martensite phase [1]. SMAs flip back and forth between austenite and martensite solid crystalline states. SMAs take the form of austenite at higher temperature, which is relatively harder material and much more difficult to shape and deform while they transform into martensite at lower temperature, which is relatively plastic, soft, and easy to deform and shape [49]. Martensitic transformation (MT) is solid to solid phase transformations from high temperature austenite phase to low temperature martensite state upon cooling [1]. Due to difference in their crystal structure, it is possible to introduce macroscopic shape changes. Figure 2.1 demonstrates mechanism of one-way and two-way shape memory effect. Two-way shape memory effect will be discussed in the following chapter. In the one-way shape memory effect, self-accommodated martensite transforms to single-variant martensite in the presence of stress. Upon

heating, detwinned martensite transforms to austenite. Atoms maintain close relationship one another instead of diffusion of atoms. Martensitic transformation has two unique properties; shape memory effect and superelasticity which can be activated temperature, stress or magnetic field [1].

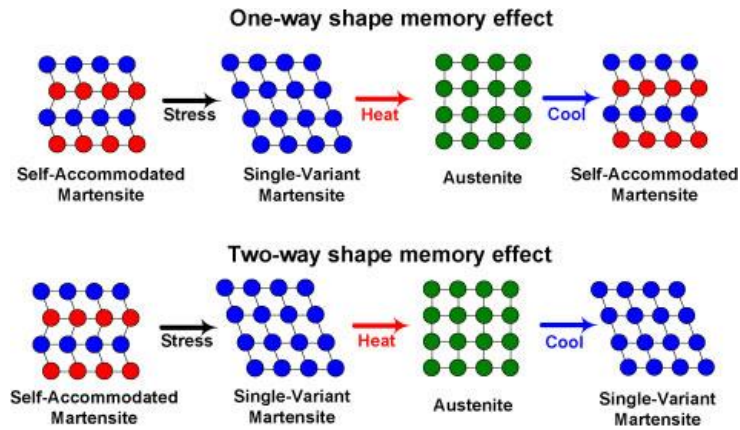


Figure 2.1 Simple illustration of one-way shape memory effect and two-way shape memory effect. In one way shape memory effect, martensite returns back to self-accommodated structure upon cooling from austenite, while martensite returns to single variant orientation in the two-way shape memory effect. Internal stresses favor certain habit plane variants, resulting in shape changes after cooling from austenite state [1].

Local strains occurring during transformation from austenite to martensite is so large that it is impossible to accommodate strains elastically. Large strains are only able to be accommodated by formation of twins in martensite state [1]. In the absence of stress, martensite lattice correspondence variants are formed with self-accommodated martensite. Crystallographic structure of two phases determines the number of martensite variants [1]. For example, there are 12 lattice variants between B19' monoclinic structure (martensite) and B2 body centered cubic structure (austenite) transformation [1]. There are no shape changes in the absence of stress due to formation

of a self-accommodated martensite structure. On the other hand, in the presence of stress, certain habit plane variants are energetically more favorable to form and grow at the expense of others called as the martensitic detwinning/reorientation. As a result of martensite detwinning/reorientation, large amount of recoverable strain takes place. Shape memory effect and superelasticity are a consequence of martensite detwinning/reorientation.

2.1.1 Shape Memory Effect and Superelasticity

Shape memory effect is phenomena where materials can restore the original shape of pre-deformed specimen after being heated shown in Figure 2.2 [50]. This phenomenon is consequence of a crystalline phase change called as “thermo-elastic martensitic transformation”. At lower temperature, SMAs take form of martensite, which their microstructure consists of “self-accommodating twins”. The martensitic state is soft and can be shaped and deformed easily by de-twinning. Detwinned martensite state undergoes austenite phase by recovering original shape upon heating. When this procedure is performed against biasing force, materials is able to produce work. Figure 2.2 shows the mechanism of shape memory effect [1]. Sample under load undergoes thermally-induced martensitic transformation across martensitic temperatures.

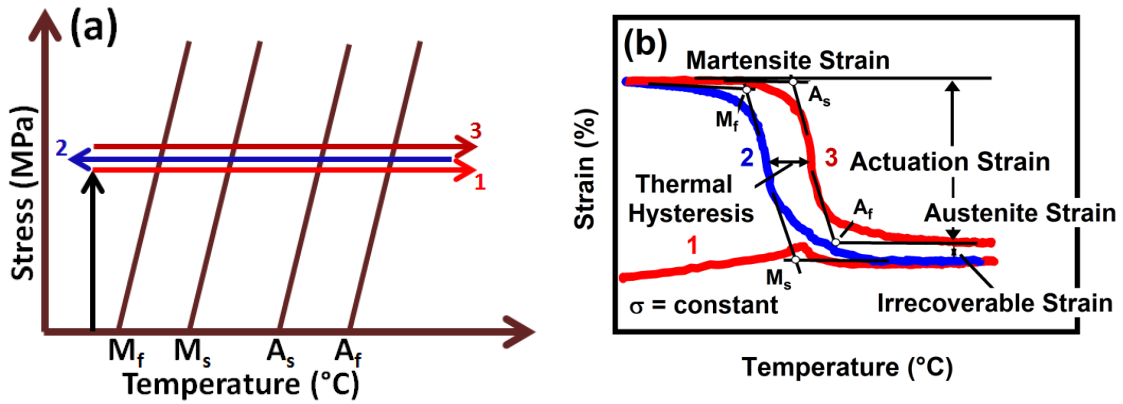


Figure 2.2 (a) Schematic illustration of the actuation fatigue loading cycles on a stress-temperature phase diagram, and (b) a representative strain-temperature response describing how the relevant shape memory characteristics of the HTSMA actuator are determined from this kind of response. M_f : martensite finish, M_s : martensite start, A_s : austenite start, A_f : austenite finish temperatures [50].

The forward transformation from austenite to martensite state and reverse transformation from martensite to austenite state do not occur at the same temperature. Figure 2.2 (b) demonstrates a typical strain vs. temperature transformation cycle for SMA sample under load. Plot of transformation cycle also shows how shape memory characteristics are determined such as transformation temperatures, austenite strain, martensite strain, thermal hysteresis, actuation strain and irrecoverable strain. The complete transformation cycle consists of martensite start temperature (M_s), martensite finish temperature (M_f), austenite start temperature (A_s) and austenite finish temperature (A_f). There is a dependency between applied stress level and transformation temperatures called as Clausius-Clapeyron relationship. As applied stress level increases, transformation temperatures of SMAs rise, resulting a constant $d\sigma/dT$ diagram as shown in Figure 2.2(a). Generally, transformation temperatures and heat of transformation of SMAs can be determined using differential scanning calorimetry (DSC) as shown in

Figure 2.3. Forward and reverse transformation temperatures are determined as M_s , M_f and A_s , A_f , respectively through tangent line method. Exothermic reaction occurs with transformation from austenite to martensite, while endothermic reaction takes place with transformation from martensite to austenite. The thermal hysteresis (ΔT) is determined as the difference in the A_f and M_s ($A_f - M_s$) under stress-free DSC thermal cycling.

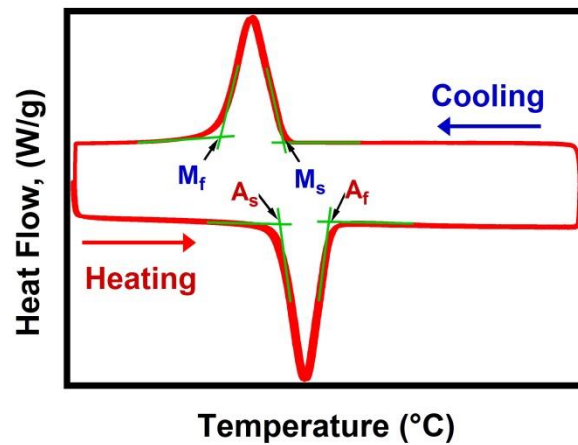


Figure 2.3 Schematic illustration of how transformation temperatures are determined using DSC curve.

Superelasticity (pseudoelasticity) is isothermal phenomena, whereby materials can recover large deformation induced by stress. SMAs exhibit superelasticity if deformed at a temperature which is slightly above A_f temperature [1]. This phenomena occurs due to stress-driven formation of martensite above its normal temperature. Since martensite is formed above its normal temperature, as soon as stress is removed, martensite reverts to undeformed austenite phase immediately. Superelastic behavior gives SMAs a springy and rubberlike elasticity. Martensite state requires less energy to be deformed than austenite state. Stress-induced transformation process can induce accommodation of

transformation strain up to 10%. If this procedure is applied to single crystal of specific alloys, it is possible to attain 25% pseudoelastic strain in specific directions. When applied stress is removed, material returns back into its pre-deformed shape. This phenomenon is known as transformational superelasticity or pseudoelasticity. As temperature increases above A_f , it becomes increasingly difficult to obtain stress-induced martensite state. Therefore, pseudoelastic (superelasticity) behavior can be obtained over a narrow temperature range. M_d is temperature where martensite can be no longer stress-induced. Above M_d , SMA material deforms similar to conventional and ordinary materials [51]. As mentioned, superelastic characteristics are determined through constant temperature loading and unloading tests at a temperature above A_f . Figure 2.4 demonstrates a superelastic cycle and superelastic properties such as stress required to induce SIMT (σ_{SIM}), recoverable strain (ϵ_{rec}), unrecoverable strain (ϵ_{irr}), super elastic strain (ϵ_{SE}), and elastic strain (ϵ_{el}).

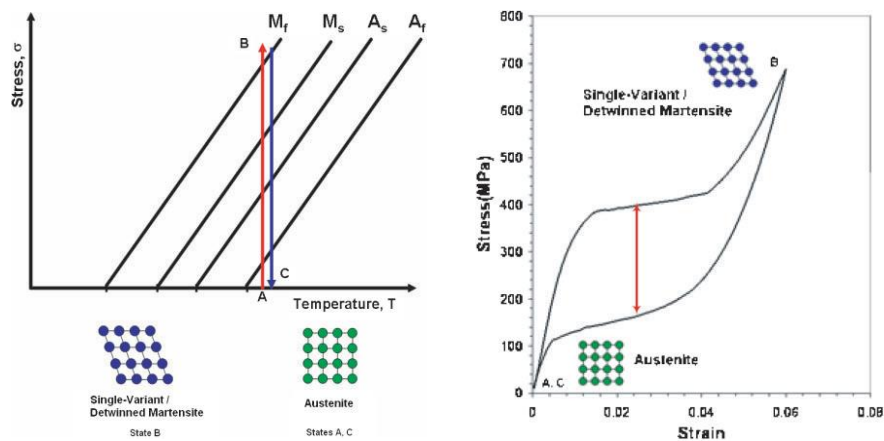


Figure 2.4 (a) Schematic representation of superelasticity using a σ - T phase diagram. Austenite transforms fully detwinned martensite when sufficient stress is applied at temperature slight above A_f . (b) illustration of superelasticity on strain (ϵ) vs. stress (σ) [1].

2.2. High Temperature Shape Memory Alloys

As mentioned previously, while NiTi continues to remain as the most widely studied SMA, due to its biocompatibility, large recoverable strain, and resistance to corrosion, its application is rather limited due to low transformation temperatures ($<100^{\circ}\text{C}$) [18, 19]. Many envisioned applications require higher temperature capability than 100°C , particularly in the automotive, energy and aerospace industries [1, 18-21]. There are some SMAs such as NiAl and CuAlNi which display high transformation temperatures yet exhibit microstructural instabilities [52]. Cu-based alloys decompose at intermediate temperatures whereas martensite of NiAl alloys decomposes to Ni_5Al_3 phase [53]. Ru- and Rh- based alloys also have high transformation temperatures [54]. However, due to cost of these alloys, they have not received great attention beyond some preliminary study. Thus, addition of ternary elements into NiTi binary alloy appears to be most promising and grandest technique to develop NiTiX materials with increased transformation temperatures.

If ternary alloying elements are below 10 at-%, transformation temperature remains unchanged or decrease. Addition of Cu or Mn has not remarkably changed the transformation temperature of NiTi alloys [1]. Alloys in the form of Ni-Ti-X where X: Pd, Pt, Au, Hf and Zr have been adopted to increase its transformation temperatures and strength [54]. Figure 2.5 demonstrates increase in transformation temperature (M_s or M_p) as a function of X: Pd, Au, Pt, Hf and Zr beyond 10 at-%. At same stoichiometry, addition of Hf and Zr are more effective in transformation temperatures than Pd and Au addition. Highest increase in TTs is observed with the addition of Pt element.

Ternary alloying has influence on the thermal hysteresis of NiTi materials since crystal structure of martensite experience a change. For instance, NiTiCu containing B19 martensite possesses 10-15°C of thermal hysteresis while NiTi alloy containing B19' exhibits 20-40°C of ΔT [54]. Nb addition increases ΔT to nearly 100°C [55].

Addition of ternary elements into NiTi was adopted to increase its transformation temperatures and strength, where Hf and Zr stand out among the other ternary element candidates, such as Pd, Au, and Pt, mainly due to their lower cost [1-4, 6, 24-29, 56-68]. In particular, the Ni-Ti-Hf/Zr system has shown significant improvement in the last half-decade, and we will focus on these alloys.

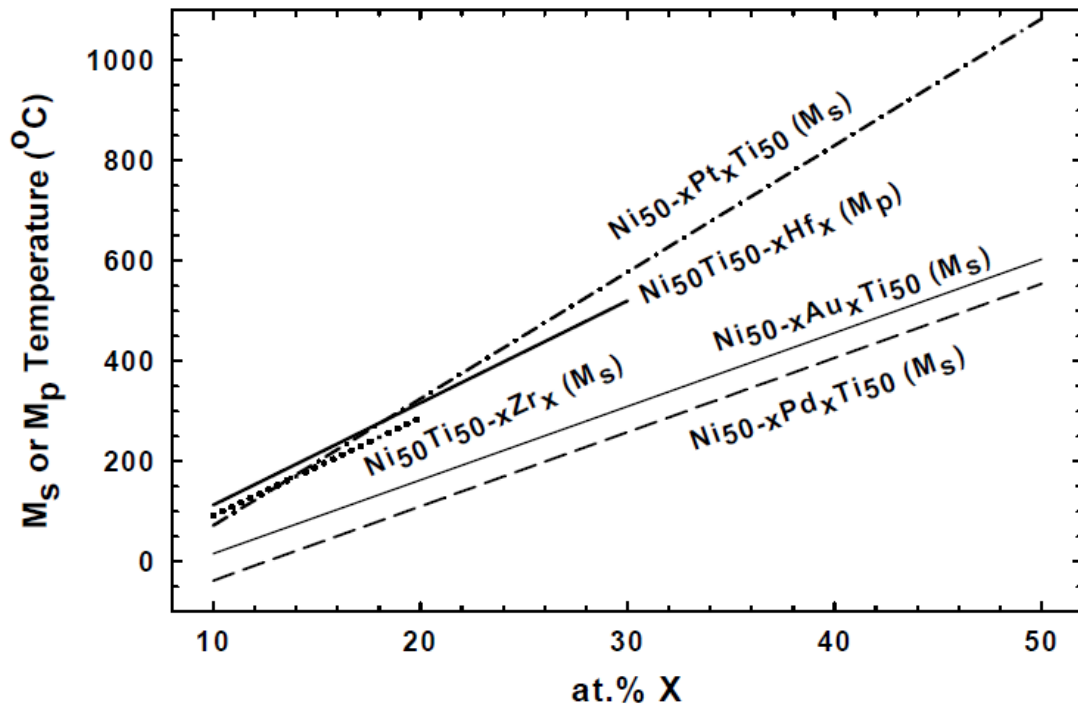


Figure 2.5 Increase in transformation temperatures of NiTi alloys with addition of Pd, Pt, Au, Hf and Zr elements [69].

2.3 NiTiHf and NiTiZr Alloys

Shape memory properties of NiTi(Hf,Zr) high temperature SMAs (HTSMAs) have been extensively studied, especially in the last 15 years [2-6, 24, 29, 34, 59, 61, 62, 66, 68, 70]. The Ni-Ti-Hf and Ni-Ti-Zr high temperature shape memory alloys have initially received great interest due to lower cost compared to alloys containing precious metals such as Pd, Pt and Au [1]. Addition of Hf and Zr elements into binary NiTi alloy at the expense of Ti achieves the temperature range of 100-400°C [71-73]. NiTiHf and NiTiZr alloys have a reversible martensitic transformation between an ordered cubic austenite (B2) phase and ordered monoclinic martensite (B19') phase [1, 74]. Figure 2.6 displays the change of the TTs of NiTiHf alloy with respect to hafnium content [24, 39, 75]. The martensite peak (M_p) temperature increases after 3 at-% Hf addition and Hf addition beyond 10 at-% results in rise M_p at a rate of 20°C/at-% [76]. Similarly, Figure 2.7 exhibits that increase in M_p begins beyond 10 at-% Zr addition and continues at a rate of 18°C/at-% until 20 at-% Zr [72]. Figure 2.8 indicates that, transformation temperatures experience sudden drop in the ternary NiTi-Hf/Zr alloys similar to binary NiTi when Ni content is above 50 at.% [72, 74, 76, 77].

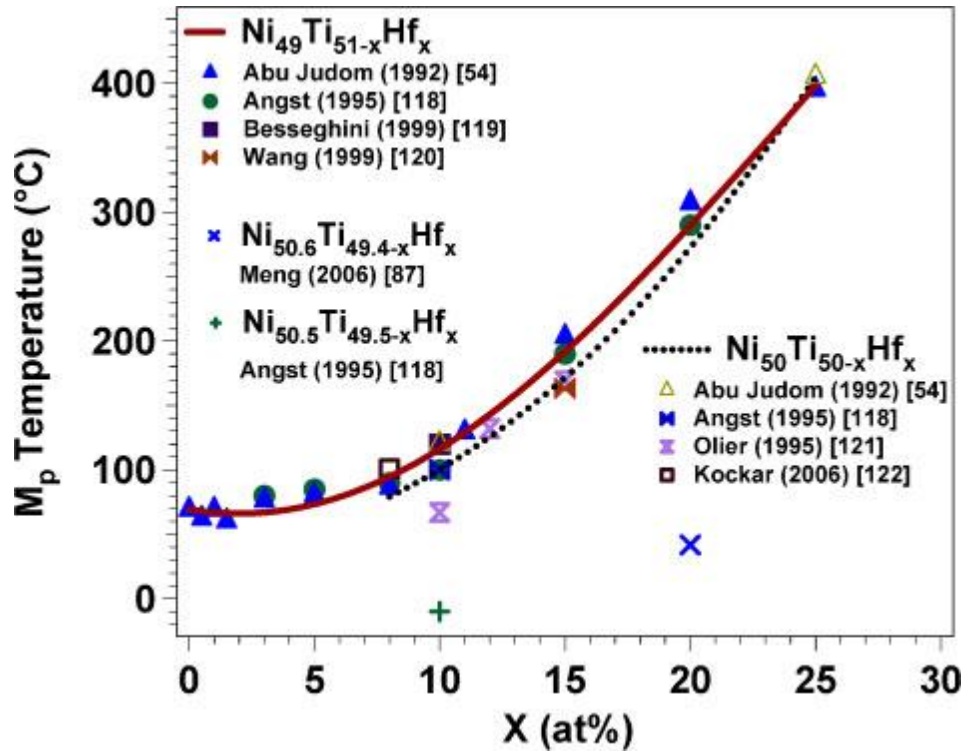


Figure 2.6. Change in the transformation temperatures of NiTi alloys as a function of Hf addition [1].

It has been demonstrated that the addition of Hf, replacing Ti, in the amount of 8 at.% [24, 78], 10 at.% [70], and 15 at.% [34, 39, 79] introduced new limitations, such as poor shape memory effect [34, 78], degradation of thermal and mechanical cyclic responses during reversible martensitic transformation [1, 24], and brittleness [1, 80, 81], which become prevalent when Ni content is stoichiometric or lower than 50 at.%. The majority of early works concentrated upon the (Ti, Hf/Zr)-rich side of the stoichiometry [39, 70, 71, 82-87]. In this composition range, (Ti, Hf/Zr)-rich second phases such as Hf₂Ni(Ti), Ti₄Ni₂O_x (x<1), and Ti₂Ni, HfNi(Ti) or (Ti,Hf)₂Ni were reported. Since the size of such second phases is generally large, their availability in matrix mostly worsens the strength of the alloys and shape memory properties [74, 85, 88, 89]. These second phases result

in poor workability and brittleness, contributing to poor reversibility, thermal, mechanical and cyclic stability as well as leading to low recoverable strains and large thermal hysteresis [85, 87-89]. These problems take place as a result of high detwinning/reorientation stress and low yield strength of austenite and martensite phases [24, 54]. In order to improve shape memory properties of HTSMAs, three methods have been proposed: (i) adding quaternary elements for solid solution hardening [25, 90-93], (ii) cold deformation followed by annealing, or warm deformation [24, 26, 80, 94], and (iii) precipitation hardening [2, 8, 34, 59, 62, 66, 68, 94-99]. It has been reported that first method does not improve the shape memory properties at a desired level [25, 90, 93], and the second method is not practical due to the brittleness of these materials [1, 24, 36, 80]. On the other hand, it was shown that precipitation hardening plays an important role in tailoring mechanical and shape memory properties of HTSMAs [2, 68, 97, 100]. Desirable precipitation hardening in NiTi(Hf,Zr) alloys requires Ni compositions higher than 50 at.%, however, the increase in Ni content beyond 50 at.% results in a significant decrease in transformation temperatures [2, 3, 6, 68]. It has recently been proven that proper precipitation heat treatments allow for higher martensitic transformation temperatures, by depleting the matrix from Ni, and improve mechanical and thermal cyclic stability of martensitic transformation in Ni-rich NiTiHf alloys [2, 4, 5, 29, 59, 68, 96-98, 101]. For instance, Bigelow *et al.* [59, 68, 96], Evirgen *et al.* [2, 4, 6], and Saghaian *et al.* [8, 97, 99] reported that a heat treatment of 550°C for 3 hours in the Ni_{50.3}Ti_{29.7}Hf₂₀ alloy leads to the formation of Ni- and Hf-rich coherent

nano-precipitates inside the matrix, providing thermal and mechanical cyclic stability for the martensitic transformation.

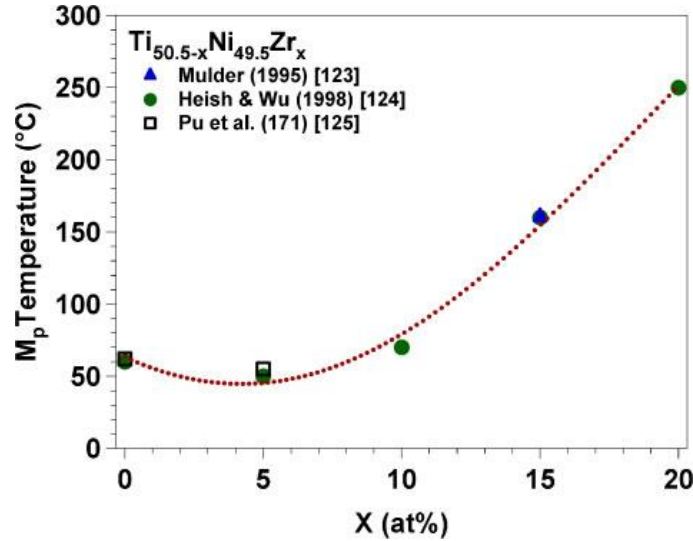


Figure 2.7. Change in the transformation temperatures of NiTi alloys as a function of Zr addition [1].

Recent studies have concentrated on the Ni-rich NiTiHf and NiTiZr alloys, where nanoprecipitation hardening is demonstrated to be far more effective in modifying transformation temperatures and enhancing shape memory characteristics [5, 102-104]. Coherent nano-precipitates after heat treatment give rise to excellent mechanical and thermal stability as well as outstanding shape recovery [2-6, 62, 102]. In the beginning, it was viewed that precipitates in Ni-rich NiTiHf and NiTiZr SMAs were $Ni_4(Ti, Hf/Zr)_3$ type phase similar to the Ni_4Ti_3 precipitates in NiTi alloys [102, 105]. On the other hand, recent investigations found a more complicated crystal structure called as “H-phase” (Figure 2. 9). The structure of H-phase is a face-centered orthorhombic lattice with a space group of $F 2/d 2/d 2/d$ with lattice parameters close to $a=12.56^\circ A$, $b=8.89^\circ A$, $c=26.02^\circ A$ [95]. H-phase precipitates are generally generated through heat treatments in

the range of 400°C to 700°C but it depends on composition. Generally, the size of H-phase precipitates are small relative to second phases: for instance, heat treatment at 450°C-10h results in precipitates size of 4-7 nm in the long axis in $\text{Ni}_{50.3}\text{Ti}_{34.7}\text{Zr}_{15}$, while precipitate size grows to 60-300 nm after aging at 600°C-10h [29]. Both Ni-rich NiTiHf and Ni-rich NiTiZr compositions are indicated to contain the same H-phase precipitates with the same crystal structure [29]. H-phase is rich in nickel and hafnium and lean in titanium relative to martensite matrix for all NiTi(Hf/Zr) alloys.

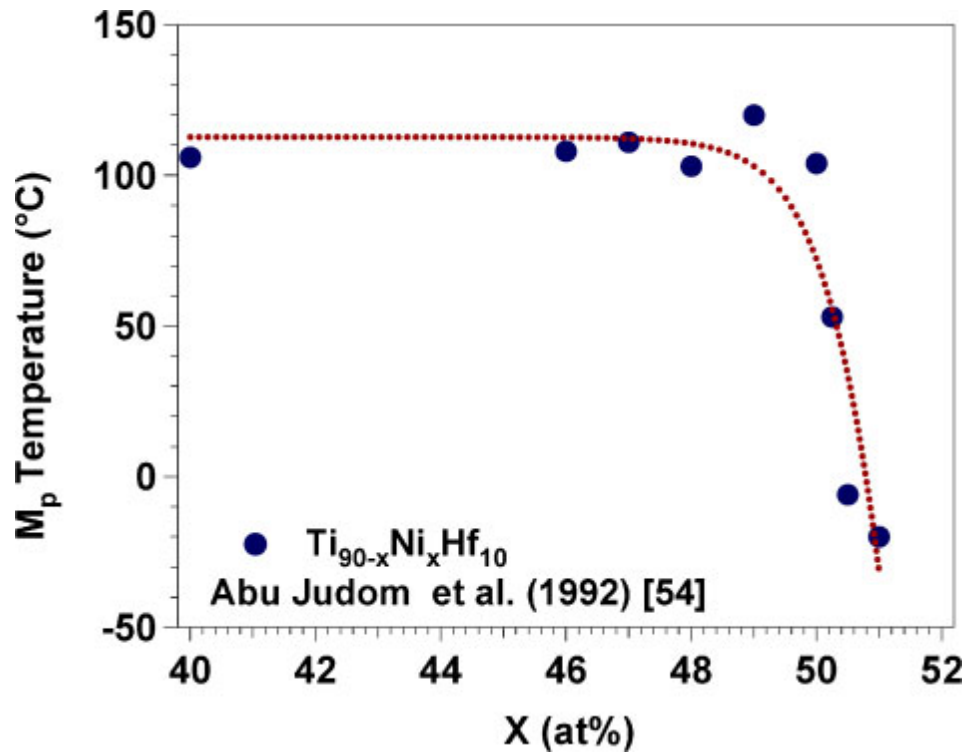


Figure 2.8. Change in martensitic peak temperature as a function of Ni content [1].

2.4 Two-Way Shape Memory Effect in High-Temperature Shape Memory Alloys

Even though numerous studies are available concerning on TWSME characterization of NiTi alloys and Cu-based SMAs, limited studies are present regarding TWSME

characterization of HTSMAs. TWSME requires specific training procedure and microstructural conditioning to form oriented internal stress fields since it is not an intrinsic property. Some of specific procedures to generate the microstructural conditioning are marforming [24, 34, 106] and mechanical deformation, following by annealing at low temperature [107, 108] as well as thermomechanical training [109, 110]. These techniques form oriented internal stress fields in the matrix which bias martensite variants during thermal cycling, led to actuation strain in the absence of external biasing force. Microstructural origin of internal stress fields is up to debate. However, the most accepted theory is generation of dislocation substructures; presence of remnant martensite or oriented precipitates to form remnant oriented stress field around precipitates [111-113]. Trained elements are mostly employed as solid actuator, where multiple motion cycles are applied to trained elements. From the application perspective, the functional stability during repeated employment is important criteria.

Although many experimental results have been reported regarding TWSME of NiTi SMAs in the literature [107, 114-118], limited studies are available on thermo-mechanical training and resulting TWSME in HTSMAs [5, 108, 110, 119]. TWSME in HTSMAs are low cycle tests, up to several hundred cycles, targeted to evaluate the formation of TWSM in HTSMA. The reason behind that is difficulty to acquire TWSME in HTSMAs due to their elevated transformation temperatures that can also result in modification and elimination microstructural characteristics which are origin of TWSME. Kockar et al. obtained TWSME in $\text{Ni}_{49.8}\text{Ti}_{42.2}\text{Hf}_8$ after investigation the influence of the severe plastic deformation on cyclic stability of shape memory

characteristics in $\text{Ni}_{49.8}\text{Ti}_{42.2}\text{Hf}_8$ [24]. Atli et. al reported the influence of Pd and Pt addition on TWSME in NiTi alloy [110, 120, 121]. Thermo-mechanical training rather than severe deformation is more effective in obtaining TWSME in NiTiHf since origin of TWSME is originated from oriented internal stress fields or oriented remnant martensite. Recently, Benafan et al. investigated effect of several parameters such as tube thicknesses, sizes and applied stress level on TWSME evolution of nano-precipitation hardened NiTiHf torque tubes [122]. Digital image correlation exhibited 6% actuation strain. TWSMS was obtained as 3% after 100 training cycles. Additionally, Benafan investigated the influence of loading configurations on evolution of TWSME of Ni-rich NiTiHf torque tubes [123]. Hayrettin et. al made research on the effects of the training parameters and geometric factors including thickness of tube walls, shear stress levels, training cycles on the evolution of TWSME of $\text{Ni}_{50.3}\text{Ti}_{29.7}\text{Hf}_{20}$ and its thermal stability at elevated temperature [119]. Even though several studies are reported on TWSME properties of Ni-rich NiTiHf alloy, there is no study in the literature on TWSME for Ni-rich NiTiZr alloy and its thermal stability at elevated temperature as well as comparison with its counterpart Ni-rich NiTiHf. So far, the experimental results on these aspects are rather limited, particularly in promising candidate Ni-rich NiTiZr alloy.

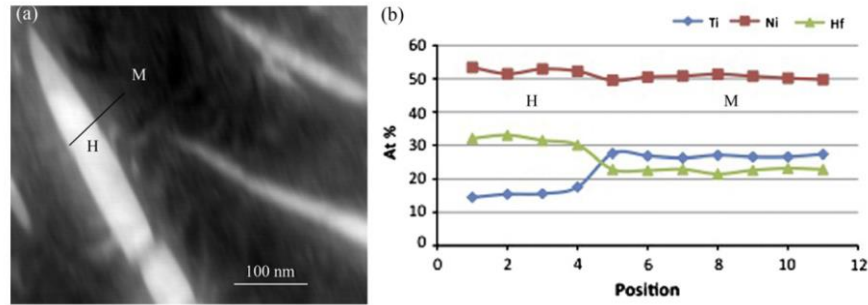


Figure 2. 9 (a) EDS scan carried out on a H-phase precipitate (H) and martensite matrix (M) **(b)** compositional line scan from H-phase precipitate to matrix phase [124].

2.5 Actuation Fatigue Properties of High Temperature Shape Memory Alloys

Many applications benefiting from SMAs involves cyclic loading in service, hence structural and functional fatigue are considered as the main failure mechanisms for SMAs in those applications [125]. As opposed to conventional metals, plastic deformation occurs in SMAs during repeated phase transformation even though applied stress level is often below the yield strength of the alloys [126]. Moreover, the fatigue performance of an SMA is strongly dependent on few parameters such as material composition, test temperatures, heat treatment procedures, and applied stress level [11, 127-135].

SMAs have found use as actuating materials with high energy densities in the aerospace and automotive industries. Actuators undergo thermally-driven transformation under load, generating macroscopic recoverable strains. Boeing Company has used SMAs in many applications such as Variable Geometry Chevron (VGC) and Variable Area Fan Nozzle [44, 136, 137]. VGC is designed and tested to change efficiency and noise characteristic of the engine of a Boeing 777. VGC uses SMA actuators to morph shape of chevrons on fan cowling on engine of airplane [44, 136, 137]. This design

permits for a quiet configuration during take-off and landing. Variable Area Fan Nozzle has also been developed to change the efficiency and noise characteristics of the engine.

As SMAs gain popularity for use as high energy actuators, in addition to cyclic stability and maximum recoverable strain, one constitutive parameter become increasingly significant is the actuation fatigue lives. Important criteria in determining their durability and reliability are to establish fundamental understanding influence of temperature induced transformation on actuation fatigue characteristics and integrity of actuator. Federal Aviation Administration (FAA) has strict rules and regulation for safe operation of SMA actuating materials on an aircraft.

Behavior of metal alloys under cyclic loading depends on the type of fatigue loading, the surface quality, strength, and microstructure [138]. As for SMAs, the fatigue behavior is classified under two main categories; namely structural fatigue and functional fatigue [11]. Structural fatigue refers to the failure of SMAs under high cyclic loads as in the case of other conventional metals. Functional fatigue, on the other hand, represents changes in shape memory characteristics, such as recoverable strain, irrecoverable strain, dissipated energy, transformation temperatures and thermal hysteresis during repeated martensitic transformation [139]. While few studies are available on functional fatigue of SMAs [13, 140-142] when specimens are thermally cycled between austenite and martensite, there are many works that reported on structural fatigue of SMAs, when specimens are subjected to varying stresses [143-146].

2.6 Stress-induced Pseudoelastic Fatigue of SMAs

After discovery of SMAs, fatigue behaviours of SMAs have remained untouched and unsolved until many years. Delaey and his co-workers performed first fatigue testing on CuZnAl samples in 1978 where specimens were cycled under load until fracture [147]. What they have done was similar to stress-based fatigue experiment being performed at the time on the ordinary and conventional metals. Mercier and Melton around similar time performed similar fatigue testing on almost same CuZnAl materials in 1979 [148]. At the same year, Mercier and Melton also performed some of first study on fatigue properties of NiTi alloys [149]. Pseudoelastic fatigue testing and fatigue crack growth were performed on NiTi wire samples. It was found that rates of fatigue crack growth were almost equivalent with conventional and ordinary metals. NiTi wire achieved 1,000 cycles tested with strain amplitude of 5%, while conventional metals were capable of producing 1,000 cycles tested with a strain amplitude of 1% [150].

Numerous researchers have primarily continued to study stress-driven fatigue properties as development of SMAs, specifically NiTi alloys, exhibited great potential in the variety of applications. Majority of pseudoelastic fatigue testing has been conducted through a rotating-bending apparatus to cycle samples until fracture [151-155]. SMA wires are firstly bended into a selected radius, rotating-bending testing is applied to the wires, producing a constant-amplitude cyclic strain. Conventional metals have not commonly utilized from this testing method, however it is quick and consistent way for SMA wires with a cycling rate of 100 – 1000c.p.m [154].

Recently, McKelvey and Ritchie performed testing to identify crack growth behavior and ultimate strength of NiTi SMAs in uniaxial tensions tests [156]. Four different temperatures were selected; stable austenite at 120°C, pseudoelastic austenite at 37°C and two in martensite -65°C and -177°C. Fastest crack growth rates associated with four temperature studied were observed with pseudoelastic austenite samples, followed by stable austenite, slowest rate of crack growth was associated with martensite.

2.7 Temperature-induced Actuation Fatigue of SMAs

Even though there are numerous studies concerning on the structural fatigue of SMAs through pseudoelastic cycling at constant temperatures, few studies are available in thermally-driven actuation cycling. Specifically, McNichols and Brookes performed one of the earliest structural fatigue experiments on NiTi SMAs undergoing thermal cycling in 1981 [14], where helical SMA wires were heated and thermo-mechanically cycled until fracture with the motivation of employing SMA wires in heat engine applications. Two key conclusions were reported from this study: there is a linear log-log relationship between fatigue life and strain amplitude, and NiTi alloy is able to produce recoverable strains an order of magnitude larger than conventional metals for a given fatigue life.

Morin and Bignon had performed on CuZnAl and NiTiCu wire specimens in 1996 undergoing repeated temperature-induced transformation under constant stress until fracture of samples [157]. Applied stress levels are within the range of 50MPa to 800MPa for NiTiCu samples, and 20MPa to 200MPa for the CuZnAl samples. Experimental results revealed that there was a correlation between applied stress level and fatigue lives of SMAs [147].

More recent studies on the actuation fatigue of NiTi and NiTiCu SMAs were conducted by Miller and co-workers [46, 47]. NiTiCu wire samples aged at different heat treatments were thermally cycled through partial and complete transformation until failure under constant nominal stresses. Primary objective of this study was to identify the influence of aging treatment and partial transformation on actuation fatigue lives. For partial transformation fatigue testing, same heat treatment was applied. Two stress levels were determined and samples at each stress level were tested with varying amounts of actuation strain which was adjusted by controlling cooling and heating time of samples. When level of actuation strain was maintained constant, there was a strong correlation between actuation fatigue life and applied stress level. It was also reported that actuation fatigue performance depends on the heat treatment conditions and an optimal heat treatment needs to be identified in order to utilize the SMAs in fatigue sensitive applications.

Bertacchini and his coworkers investigated as follow up study the influence of corrosion on number of cycles to failure of NiTiCu wires employed previously by Lagoudas, however different aging treatment [130]. Wires were thermally cycled under load until failure with partial and full transformation, which were described as thermally cycling from 25% of full actuation and 75 of full actuation. Solution used in the testing resulted in corrosion on the surface of sample as a brittle oxide layer. Incompatibility of the thermomechanical response of transforming core of sample and non-transforming oxide layer generates cracks.

Schick performed the earliest work of actuation fatigue of samples made of plate $\text{Ni}_{55}\text{Ti}_{45}$ (at-%) [158]. Samples were machined using an electro-discharge machining (EDM), which formed a recast layer on the sample surfaces. This study utilized $\text{Ni}_{55}\text{Ti}_{45}$ actuators since variable geometry chevron (VGC) used this actuating material. It is possible to generate high volume fraction of Ni_4Ti_3 and Ni_3Ti Ni-rich precipitates in the $\text{Ni}_{55}\text{Ti}_{45}$ alloy which enhance the cyclic and dimensional stability. All samples were thermally cycled under load until failure through complete transformation. Experimental results demonstrated that actuation fatigue life was shortened due to formation recast layer after EDM machining. Additionally, corrosive environment obtained through ethylene-glycol resulted in shorter actuation fatigue lives. SEM observation revealed that cracks were initiated in or around Ni-rich precipitates, which was likely result of incompatibility of shape memory response of non-transforming Ni_4Ti_3 and transforming core of materials.

Ramaiah et. al performed actuation fatigue tests on NiTi wire samples, focusing on the cracking properties [159]. Periodic cylindrical cracking was observed. Experimental investigations revealed that cracks initiated in the core of transforming matrix during repeated transformations but there is no preferential locations favoring crack formations.

CHAPTER III

EXPERIMENTAL METHODS

The objective of this chapter introduces details on fabrication and processing of the shape memory alloys (SMAs), actuation fatigue testing and characterization methods employed in this study.

3.1 Materials Fabrication

$\text{Ni}_{50.3}\text{Ti}_{29.7}\text{Hf}_{20}$ and $\text{Ni}_{50.3}\text{Ti}_{29.7}\text{Zr}_{20}$ (at. %) HTSMAs were vacuum induction melted under a partial argon atmosphere using a graphite crucible and high purity elemental constituents (99.98% Ni, 99.95% Ti, 99.9% Hf and 99.9% Zr) and subsequently cast into a 25.4 mm diameter by 102 mm long copper mold. The as-cast was homogenized at 1050 °C for 72h, followed by hot extrusion at 900 °C with a 7:1 area reduction. Dog-bone shaped tensile testing specimens with gauge dimensions of 40 mm x 2.5 mm x 1 mm were machined from the hot-extruded rods using wire electrical discharge machining (EDM). Specimens were aged at 550 °C for 3h followed by a water quench, an aging procedure which was proven to induce perfect superelastic behavior, near perfect functional stability and high work output in Ni-rich NiTiHf and NiTiZr HTSMAs through nano-precipitation [2, 160].

3.2 Actuation Fatigue Processing

Each specimen was heat treated at different temperatures and time, mostly at 550°C for 3 hours, followed by air cooling in order to precipitate out nano-particles with sizes below 20 nm. The parameters utilized in the current actuation fatigue experiments were UCT of 250, 300 and 350 °C. To investigate the role of stress levels, stress levels of 200,

300 and 400 and 500 MPa were applied. For instance, in order to reach stress levels of 300 MPa, the required dead weights (Figure 3.2) were calculated based on the dimensions of specimens (Figure 3.1). The samples were mechanically mounted onto the fatigue testing frame (Figure 3.2) and subjected to constant stresses of 200, 300, 400 and 500 MPa. All samples were thermally cycled under the constant stress until failure. Each experiment was repeated twice or three times on companion samples in order to ensure repeatability.

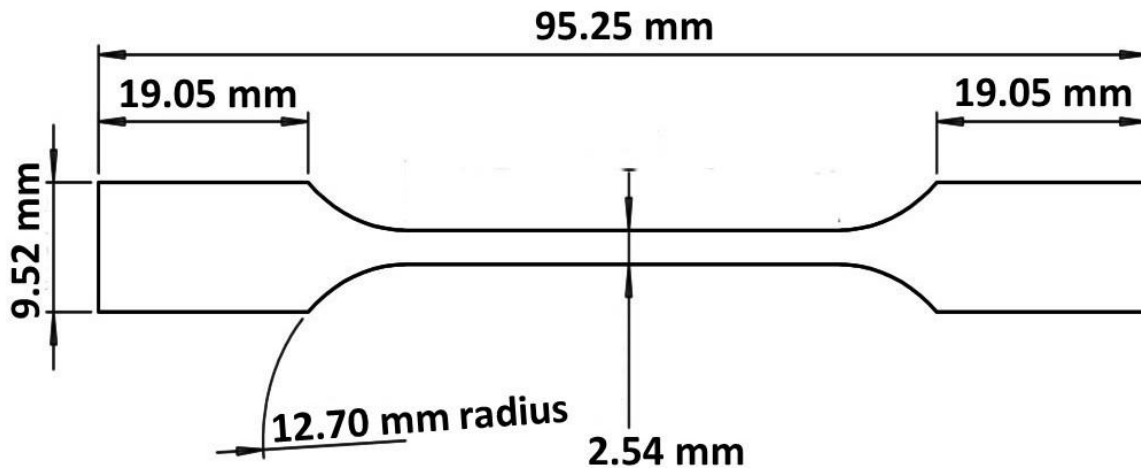


Figure 3.1 Dimensions of the dog-bone shaped fatigue samples of the nano-precipitation hardened $\text{Ni}_{50.3}\text{Ti}_{29.7}\text{Hf}_{20}$ HTSMAs used in this study [161].

Electric current was passed through the specimens to heat them above the austenite finish (A_f) temperature, and cooling down to below martensite finish (M_f) temperature was achieved through convection utilizing a slow speed electric fan. The heating-cooling cycles were induced within the temperature ranges of 40°C to 300°C and 40°C to 350°C . Heating and cooling rates during thermal cycles were kept at approximately 15°C s^{-1} and 8°C s^{-1} , respectively, and with these rates, the fatigue test frame has the capability to

perform about 1,500 thermal cycles per day. The strains were calculated based on the displacements and the reference configuration for the strain measurement was the loaded austenite phase. The measurement of displacements was performed via a linear variable differential transformer (LVDT) sensor attached to the grips. A Micro-Epsilon CTLaser (CTL-CF1-C3) infrared thermometer with an accuracy of smaller than 1 °C was employed to measure the temperature of the specimens at the center of the gage section. The specimens were coated with a high-temperature black paint to prevent changes in the emissivity of the sample surfaces during thermal cycling. The thermal cycling was digitally controlled with a program scripted in LabVIEW, which also collected real-time data, including temperature, displacement, time, peak displacements at the upper and lower cycle temperatures for each cycle, and the number of cycles to failure. The thermo-mechanical loading path for the first cycle of the experiments and the determination of the corresponding austenite, martensite, actuation and irrecoverable strains are schematically shown in Figure 2.2(a).

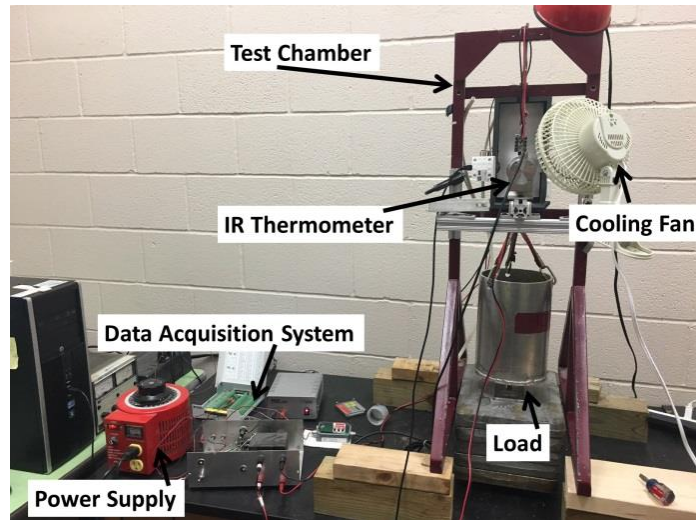


Figure 3.2 Experimental set-up utilized for the actuation fatigue testing of nano-precipitation hardened $\text{Ni}_{50.3}\text{Ti}_{29.7}\text{Hf}_{20}$ HTSMAs. See text for details [161].

3.3 Two-Way Shape Memory Effect Procedure

Thermomechanical training of $\text{Ni}_{50.3}\text{Ti}_{29.7}\text{Hf}_{20}$ and $\text{Ni}_{50.3}\text{Ti}_{29.7}\text{Zr}_{20}$ HTSMAs was conducted using a custom-built actuation fatigue testing setup. Tensile specimens were thermally cycled between 35 °C and 300 °C to ensure that the lower cycle temperature (LCT) stayed below the martensite finish (M_f) temperature and upper cycle temperature (UCT) stayed above the austenite finish temperature (A_f) under the external stress. Temperature of the samples during thermomechanical training was measured using a Micro-Epsilon infrared thermometer with an accuracy of ± 1 °C. Displacement was measured using a linear differential transformer (LVDT). A program scripted in LabVIEW was used to control and record temperature and displacement data during thermomechanical training. Detailed information on how to determine shape memory characteristics such as actuation strain, thermal hysteresis and transformation temperatures from training data can be found elsewhere [50, 161].

The training procedure conducted for nano-precipitation hardened $\text{Ni}_{50.3}\text{Ti}_{29.7}\text{Hf}_{20}$ and $\text{Ni}_{50.3}\text{Ti}_{29.7}\text{Zr}_{20}$ HTSMAs is shown in Figure 3.3. Total number of training cycles was selected as 2000 due to two reasons: compared to precipitation-free NiTi based HTSMAs, precipitation hardened NiTiHf and NiTiZr HTSMAs have higher strength

levels making it more difficult to induce a training effect by the formation of defects [162]; the studies on training of HTSMAs are usually limited to a few hundreds of cycles [110], that do not convey useful information about the changes in the shape memory behavior of the HTSMA for prolonged applications. The training stress was selected as 300 MPa, which induced a reasonable level of martensite reorientation without causing excessive plastic deformation [123]. Actuation behaviour of materials (actuation strain vs. applied stress) was evaluated at certain stages of the training by a running a procedure named "the characterization sequence". Characterization sequence simply consisted of thermally cycling the trained material at the same temperature interval starting at 50 MPa and going up by increments of 50 MPa until 300 MPa, cycling 5 times at each stress, totaling 30 thermal cycles. Loading to the next higher stress level took place when the sample was at the LCT in the martensitic state. Characterization sequence was applied at the 1st, 250th, 500th, 1000th and 2000th training cycles. Two-way shape memory effect (TWSME) characterization at 0 MPa was not carried out due to the limitation of the testing frame, i.e. the smallest load that could be applied on the specimen was around 20 MPa. Thus, actual TWSM strain which is merely the actuation strain at zero stress, was calculated by extrapolating the actuation strains at 50 and 100MPa to 0 MPa. To make a clear distinction between experimental data and estimated data, estimated data were marked with empty markers and connected with dashed lines in the plots.

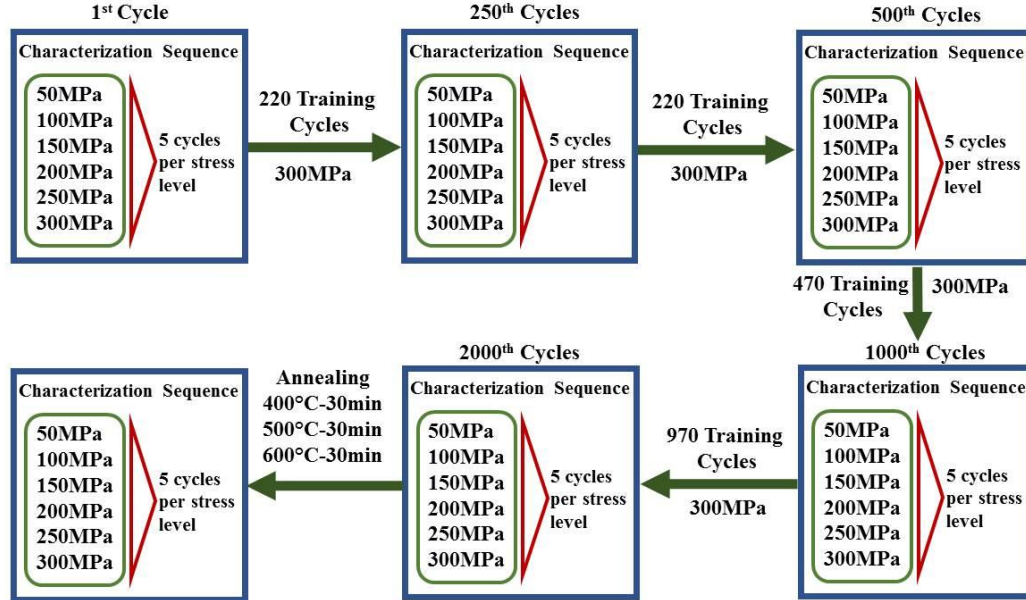


Figure 3.3 Training procedure to obtain TWSME followed by an annealing treatment to evaluate the thermal stability of TWSME right after thermo-mechanical training for nano-precipitation hardened $\text{Ni}_{50.3}\text{Ti}_{29.7}\text{Hf}_{20}$ and $\text{Ni}_{50.3}\text{Ti}_{29.7}\text{Zr}_{20}$ alloys.

3.3.1 Annealing Process

After 2000 training cycles and a total of 5 characterization sequences (Figure 3.3), both alloys were unloaded and annealed successively at three different temperatures well above the operating temperature range of the materials (400 °C, 500 °C and 600 °C) for 0.5h in air atmosphere to quantify the changes in the actuation behavior. After each annealing heat treatment, one characterization sequence, the same used for thermomechanical training procedure, was performed before starting the next heat treatment.

3.4 Microstructural Characterization

3.4.1 Microstructure and Compositional Analysis

In order to understand the roles of microstructure and testing parameters such as upper cycle temperature and applied stress level on the fatigue response, crack formation and the corresponding microstructure evolution, microstructural analysis was performed on the fracture and flat side surfaces using a FEI Quanta 600 scanning electron microscope (SEM) in back scattered electron mode. Electron imaging was carried out using a backscattered electron (BSE) detector. Specimens from the side surfaces were mechanically ground by 1200 grit polishing paper, followed by fine polishing with 6, 3 and 1 μm alumina slurries. Chemical analyses were performed an energy dispersive X-ray spectrometer (EDS) using microanalytical methods and microprobe imaging.

A Tecnai G2 F20 transmission electron microscope (TEM) was employed to determine the size and morphology of the precipitates induced by different heat treatments. Furthermore, effects of temperature and stress on precipitate morphology were investigated through a detailed TEM analysis of both tested and untested samples. For each aging treatment, one sample was mechanically ground down to 80 μm thickness, first, and thereafter, the thin sample was electropolished using a solution of 80 vol.% methanol and 20 vol.% sulfuric acid at 0°C with a Struers Tenupol-5 twin-jet electropolisher [163]. TEM images were collected at room temperature.

3.4.2 Nanoindentation Hardness Testing

Elastic modulus and hardness of materials were evaluated using a Hysitron TI 950 Triboindenter nanomechanical test instrument which was equipped with automated X, Y and Z staging system. Resolution of load, displacement and Z stage is less than 1 nN, 0.0005 nm and 3nm, respectively.

3.4.3 Calorimetry

Stress-free martensitic transformation temperatures (martensite finish, M_f , martensite start, M_s , austenite start, A_s , austenite finish, A_f) and the corresponding heat of transformation, ΔH , were determined using a TA Instruments Q2000 Differential Scanning Calorimeter (DSC) operated at a heating/cooling rate of $10^\circ\text{C min}^{-1}$. The DSC measurement was performed prior to fatigue testing and after fatigue testing completed. All DSC samples were prepared using electrical discharge machining (EDM), which is a stress-free and non-contact technique. Slope line extension technique was used to measure transformation temperatures. The area under DSC peaks represented the amount of heat released (ΔH) during martensitic transformations.

3.4.5 Isothermal Monotonic Loading Tests

A MTS servo-hydraulic testing system was employed to perform the mechanical tests of NiTiHf and NiTiZr for critical parameters including yield strength ductility, elastic modulus and elongation to failure. Tensile tests were carried out at both martensite and austenite states. For tension tests, MTS high-temperature extonsemeter measured the axial strain. Extonsemeter which is made of a pair of ceramic rods with capability of

exerting force of 300 g per rod on a specimen, had a gage length of 12.7mm. Due to gage length of tension samples with 8 mm, the extensometer needs to be attached to samples in a complete compressed mode. Specimens were heated through conduction with heating band in the grips. Liquid nitrogen in copper tubes wrapped around grips to cool samples conductively.

CHAPTER IV
ROLE OF MICROSTRUCTURE ON THE ACTUATION FATIGUE
PERFORMANCE OF NI-RICH NITiHF HIGH TEMPERATURE SHAPE
MEMORY ALLOYS*

The focus of the present study was to systematically investigate the influence of microstructure on the actuation fatigue performance of a Ni-rich NiTiHf high temperature shape memory alloy (HTSMA). Different aging heat treatments led to the formation of H-phase nano-precipitates with different sizes and morphology within the matrix, enhancing thermo-mechanical stability and enabling control of transformation temperatures. Specifically, the actuation fatigue testing of specimens was performed until failure through thermally-induced reversible martensitic transformation under a constant stress level (300 MPa) with two distinct upper cycle temperatures (UCT) of 300°C and 350°C.

There is a need to understand and optimize microstructure to attain best actuation fatigue performance in Ni-rich NiTiHf alloys. It has been recently demonstrated that nano-sized precipitates lead to precise control of transformation temperatures and provide stable shape memory response and high resistance to plastic deformation, as well as excellent superelastic shape recovery in the case of Ni-rich Ni_{50.3}Ti_{29.7}Hf₂₀ [2, 3]. However, the role of different nanoprecipitate sizes and morphologies on the fatigue response of Ni-rich NiTiHf HTSMAs, and which size provides the longest and the most

* Reprinted with permission from “Role of microstructure on the actuation fatigue performance of Ni-rich NiTiHf high temperature shape memory alloys” by O. Karakoc, C. Hayrettin, A. Evirgen, R. Santamarta D. Canadinc^{a,c}, R.W. Wheeler^d, D.C. Lagoudas^{a,d}, I. Karaman, 2019. Acta Materialia, Reference: AM 15323, Copyright 2019 by Acta Materialia Inc. published by Elsevier Ltd.

stable fatigue behavior is not known.

The present study was undertaken with the motivation of addressing this issue, and thereby establishing a thorough understanding of the influence of microstructure on the actuation fatigue performance of Ni-rich $\text{Ni}_{50.3}\text{Ti}_{29.7}\text{Hf}_{20}$. Three heat treatments were selected to form different microstructures: 550°C for 3h (corresponding precipitate size: <20nm in length), 600°C for 10h (precipitate size: 40-80 nm), and furnace cooling from 700 to 100°C in 48h (precipitate size: 70-200nm), following the earlier work of Santamarta et al. [29] on other NiTiHf compositions. After the failure of the specimens, a detailed characterization work was performed using differential scanning calorimetry (DSC) and scanning electron microscopy (SEM) to understand the effects of heat treatments on failure mechanisms as well as the evolution of shape memory response. The primary finding of this study is that shape memory characteristics of nano-precipitation hardened $\text{Ni}_{50.3}\text{Ti}_{29.7}\text{Hf}_{20}$, particularly fatigue life and actuation strain, can be tailored by controlling the precipitate size.

Table 4.1 Martensitic transformation temperatures and transformation heats, determined using DSC, before and after the actuation fatigue tests, with two different upper cycle temperatures (UCT), of the Ni_{50.3}Ti_{29.7}Hf₂₀ HTSMA samples, precipitation heat treated (HT) at three different conditions before the tests. M_s and M_f: Martensite start and finish temperature; A_s and A_f: Austenite start and finish temperatures. FC: Furnace Cooled. Stress-free represents the sample before the fatigue testing. " Reprinted with permission from [164]. "

HT/UCT	Transformation Temperatures (°C)				Hysteresis (A _f -M _s) (°C)	Transformation Heat (J/g)
	M _f	M _s	A _s	A _f		
As-Extruded	63±4	101±3	103±3	133±2	32±2	17±1
Stress Free 550°C-3h	125±3	149±5	153±2	178±4	29±4	18±1
550°C-3h/300°C	105±13	209±13	150±2	251±11	42±12	11±1
550°C-3h/350°C	120±4	167±5	169±8	219±7	52±6	12±1
Stress Free (SF) 600°C-10h	141±2	183±3	185±2	221±4	38±3	18±1
600°C-10h/300°C	142±1	214±2	195±7	251±1	37±2	11.0±1
600°C-10h/350°C	154±3	204±3	203±10	277±8	73±5	14±1
SF FC from 700-100°C	162±4	212±2	214±2	268±3	56±3	19±1
FC from 700°C to 100°C/300°C	140±9	228±6	186±3	277±10	49±8	7±1
FC from 700°C to 100°C/350°C	152±1	216±2	209±2	279±5	63±4	15±2

Table 4.2 Transformation temperatures and thermal hysteresis in the first and last thermo-mechanical cycles of the actuation fatigue experiments, extracted from the strain vs temperature curves of Ni_{50.3}Ti_{29.7}Hf₂₀ HTSMAs heat treated (HT) at different aging times and temperatures. M_s and M_f: Martensite start and finish temperature; A_s and A_f: Austenite start and finish temperatures. $\Delta M_s = M_s^{\text{first}} - M_s^{\text{last}}$, $\Delta A_f = A_f^{\text{first}} - A_f^{\text{last}}$. UCT: Upper Cycle Temperature. " Reprinted with permission from [164]. "

HT/UCT	Trans. Temp. (°C)				Trans.Temp. (°C)				ΔM_s (°C)	ΔA_f (°C)
	First Cycle				Last Cycle					
	M _f	M _s	A _s	A _f	M _f	M _s	A _s	A _f		
550°C- 3h/300°C	158	176	180	191	162	233	181	252	57	61
550°C- 3h/350°C	157	177	176	189	159	213	184	242	36	53
600°C- 10h/300°C	161	182	190	210	171	236	198	256	54	46
600°C- 10h/350°C	164	184	191	211	174	241	206	268	57	57
F.C. from 700°C to 100°C/300°C	186	207	227	249	178	247	207	264	40	15
F.C. from 700°C to 100°C/350°C	190	209	225	252	182	261	219	291	52	39

4.1 Microstructure and Martensitic Transformation Characteristics of the Precipitation Hardened $\text{Ni}_{50.3}\text{Ti}_{29.7}\text{Hf}_{20}$ HTSMA

To provide a baseline behavior and a comparison for the change in shape memory characteristics during actuation fatigue experiments, the samples prior to fatigue tests were characterized using DSC and TEM. The transformation temperatures (TTs) and ΔH of the samples with different microstructures were measured using DSC. Stress free calorimetric responses of the three types of samples and the as-received sample (in as-extruded condition), during three cooling and heating cycles are presented in Figure 4.1. TTs increased concomitant with the aging temperature or duration. This increase is in accord with the formation of Ni-rich precipitates, resulting in Ni depletion in the matrix [29] and the fact that Ni content above 50at.% Ni decreases TTs [165]. Summary of TTs determined from the DSC analysis is presented in Table 4.1. The austenite finish temperature (A_f) of the as-extruded condition was 133°C, and the A_f increased to 178°C after aging at 550°C for 3h. Transformation temperatures of $\text{Ni}_{50.3}\text{Ti}_{29.7}\text{Hf}_{20}$ exhibited a large increase as a consequence of the furnace cooling from 700°C to 100°C. The A_f temperature increased approximately 135°C as compared to the A_f of the as-extruded sample.

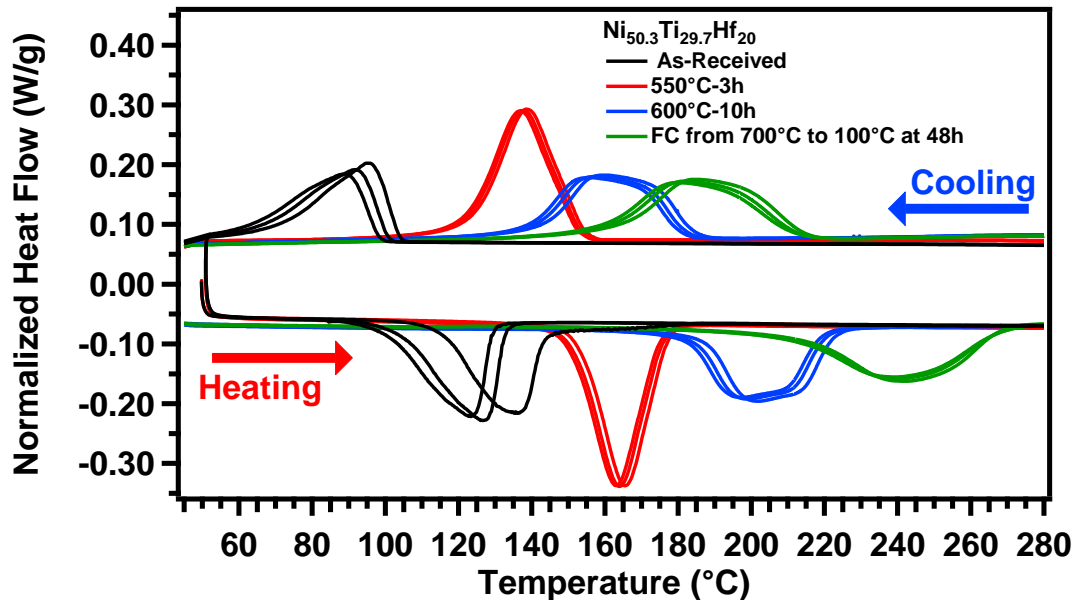


Figure 4.1 DSC results of the $\text{Ni}_{50.3}\text{Ti}_{29.7}\text{Hf}_{20}$ HTSMA specimens in as-extruded condition and after different aging treatments. Three DSC cycles are shown for each sample. " Reprinted with permission from [164]. "

The corresponding bright field TEM images of the aged $\text{Ni}_{50.3}\text{Ti}_{29.7}\text{Hf}_{20}$ specimens are presented in Figure 4.2. Aging at 550°C for 3h led to dense distribution of spindle-like H-phase precipitates, 7-20 nm in length and 4-6 nm in width. The precipitates preserved their spindle-like shapes, but were 40-80 nm in length and 20-40 nm in width after aging at 600°C for 10h. The precipitates were much larger after furnace cooling from 700°C to 100°C in 48 h, reaching to about 70-200 nm in length and 20-70 nm in width. H-phase precipitates are a face-centered orthorhombic lattice with lattice parameter approximately $a=12.56^\circ\text{A}$, $b=8.89^\circ\text{A}$, $c=26.02^\circ\text{A}$ [95]. Generally, H-phase precipitation occurs in Ni-rich (50 at-% <Ni) NiTiHf and NiTiZr alloys within aging temperature of 400°C to 750°C [166]. It is increasingly difficult to form H-phase precipitates at aging temperatures less than 400°C and H-phase precipitates start to dissolve into martensite

matrix at aging temperatures above 750°C. H-phase is richer in Ni and Hf and leaner in Ti relative to martensite microstructure [166]. Precipitation strengthening mechanism can be explained by looping/shearing interaction of dislocations with precipitates in the microstructure [167]. Dislocation shearing mechanism becomes dominant when precipitates size is sufficiently small. In this case, a dislocation cuts through a precipitate since it is energetically favorable. Shearing resistance exhibits an increase as a function of precipitate size due to coherency, ordering, antiphase boundary contributions and modulus. However, at larger precipitates size, dislocation loops dominate interaction mechanism, and interparticle spacing distances [167]. Strengthening decreases as dislocations bypass incoherent precipitates in a microstructure. The details on the crystal structure, compositions, and coherency with the matrix as a function of the size of these precipitates can be found in [2, 4, 29, 124, 168, 169].

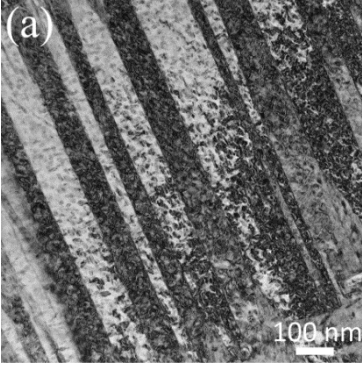
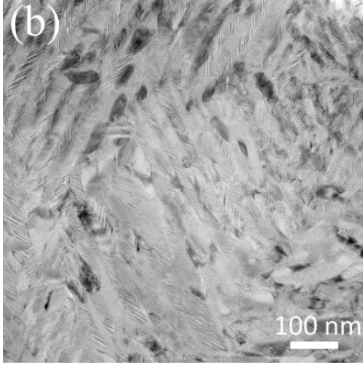
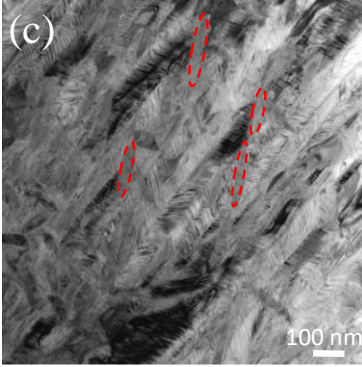
Microstructure 1	Microstructure 2	Microstructure 3
		
550°C 3 h	600°C 10 h	700 to 100°C furnace cooling in 48h
Length 7-20 nm Width 4-6 nm	Length 40-80 nm Width 20-40 nm	Length 70-200 nm Width 20-70 nm
Entire precipitates are absorbed in martensite variants	Some precipitates are absorbed in martensite variants and some are located in between variants	Precipitates are incoherent and act as a barrier to martensite variant growth

Figure 4.2 Bright-field TEM images of the $\text{Ni}_{50.3}\text{Ti}_{29.7}\text{Hf}_{20}$ HTSMA specimens exhibiting different sizes and distribution of H-phase precipitates within martensite variants after aging at (a) 550°C-3h, (b) 600°C-10h and after (c) furnace cooling from 700°C to 100°C in 48h, where the precipitates that are interfering the martensite growth are marked with red dashed ellipsoids. " Reprinted with permission from [164]. "

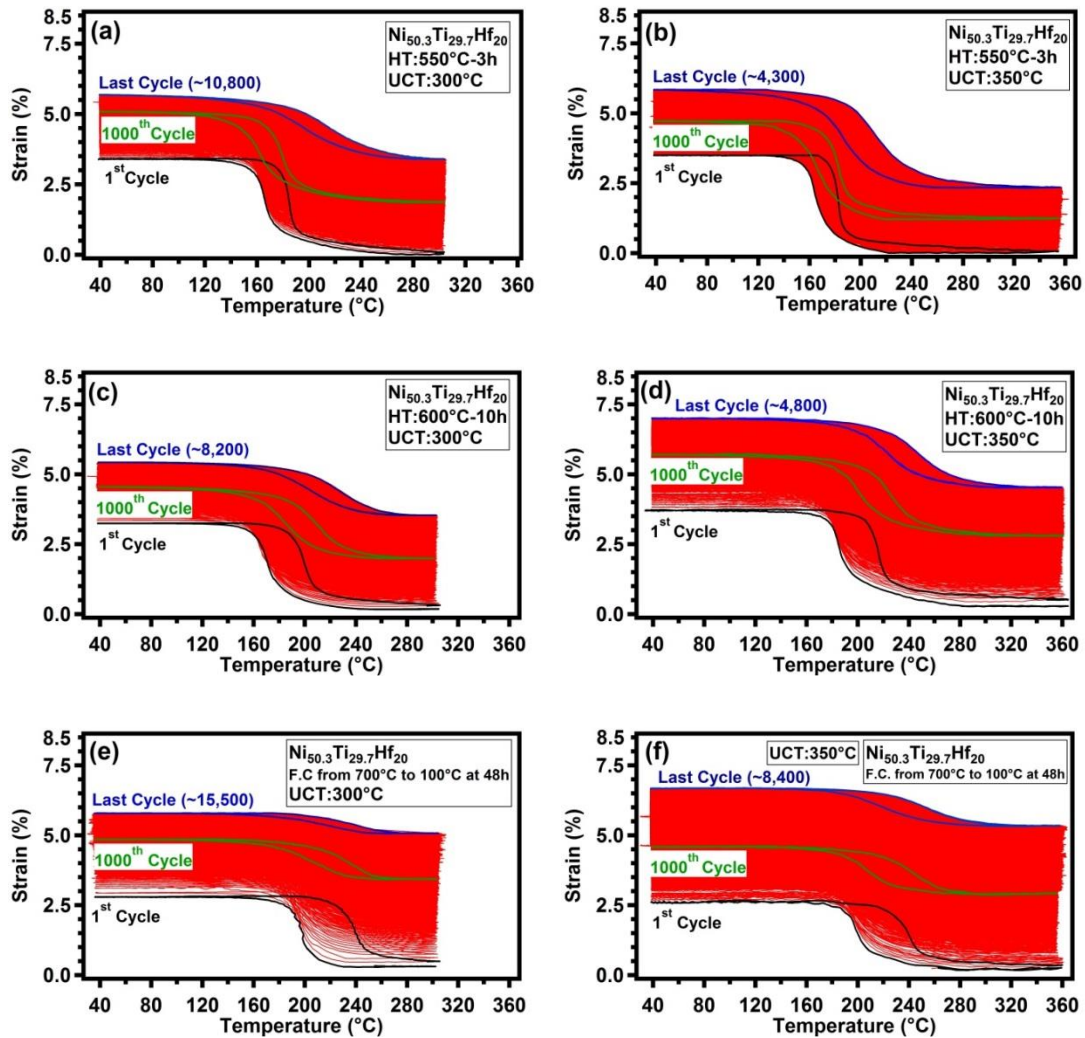


Figure 4.3 Thermal cyclic response of nano-precipitation hardened $\text{Ni}_{50.3}\text{Ti}_{29.7}\text{Hf}_{20}$ HTSMA subjected to 300 MPa. The specimens were exposed to different aging treatments before the tests and then tested up to different UCT: (a) 550°C-3h, 300°C UCT, (b) 550°C-3h, 350°C UCT, (c) 600°C-10h, 300°C UCT, (d) 600°C-10h, 350°C UCT, (e) FC from 700°C to 100°C in 48h, 300°C UCT, and (f) FC from 700°C to 100°C in 48h, 350°C UCT. FC: Furnace Cooling, UCT: Upper Cycle Temperature. " Reprinted with permission from [164]. "

4.2. Actuation Fatigue Experiments

The strain vs. temperature curves, obtained from the actuation fatigue experiments carried out under constant nominal stress of 300 MPa with 300°C and 350°C UCTs until failure, are presented in Figure 4.3 for the specimens with three different heat treatment conditions. Figure 4.4 presents the evolutions of actuation strain, strain in martensite and strain in austenite (i.e. irrecoverable strain) with the number of thermal cycles. Austenite and martensite strains refer to strain levels recorded at the end of each heating and cooling cycles, respectively. The difference between the two extreme strains represents actuation strain (Figure 2.2 (b)). As expected, a large plastic strain was observed during the initial stages of thermal cycles, especially during the first 500 cycles and, thereafter, continued to increase at a slower rate throughout the duration of the fatigue test. Specimens with the largest precipitates upon heat treatment exhibited the largest irrecoverable strains. Actuation strain also decreased throughout the fatigue test for all specimens (i.e. an indication of functional fatigue), with the exception of those heat treated at 550°C for 3h and cycled under 300MPa up to the UCT of 350°C. Specimens with smaller precipitates exhibited larger and more stable average actuation strains (i.e. more stable functional fatigue response) and less irrecoverable strains as compared to those with larger precipitates. As the UCT was increased to 350°C, actuation and irrecoverable strains became larger regardless of the aging treatment.

Specimens with the largest precipitates exhibited a substantial increase in thermo-mechanical fatigue life, such that the failure occurred after 15,500 cycles under 300 MPa with the UCT of 300°C. This is indicative of good structural fatigue response. However,

the longer fatigue life came at the expense of actuation strain, i.e. the actuation strain exhibits large drop from the beginning to end of the fatigue cycling. This behavior is indicative of poor functional fatigue response. The test results also indicated that for microstructures containing smaller precipitates and for experiments with the higher UCT level, fewer thermal cycles were attained before failure. On the other hand, as the UCT decreased and precipitate size increased, fatigue life increased substantially.

Another critical property characteristic for an HTSMA actuator is the actuation work output. Actuation work output is defined as $\sigma_{act} * \epsilon_{act}$ (average actuation strain * applied stress level). Figure 4.5 displays the work output, fatigue life and transformation temperatures of different low temperature NiTi-based SMAs and the present Ni-rich NiTiHf HTSMA samples. The Ni_{50.3}Ti_{29.7}Hf₂₀ samples with the highest transformation temperature (i.e. the furnace cooled samples with large precipitates) among those presented in the figure demonstrated the lowest work output while exhibiting the longest fatigue life amongst others. Even though the transformation temperatures of other Ni-rich NiTiHf HTSMA samples (i.e. those aged at 550°C for 3 h and 600°C for 10 h with relatively small precipitates) are higher than that of low temperature SMAs, their performance in terms of work output and fatigue life is superior or comparable to that of low temperature SMAs. This demonstrates the control of precipitate size help achieve superior actuation fatigue performance in Ni-rich NiTiHf HTSMAs.

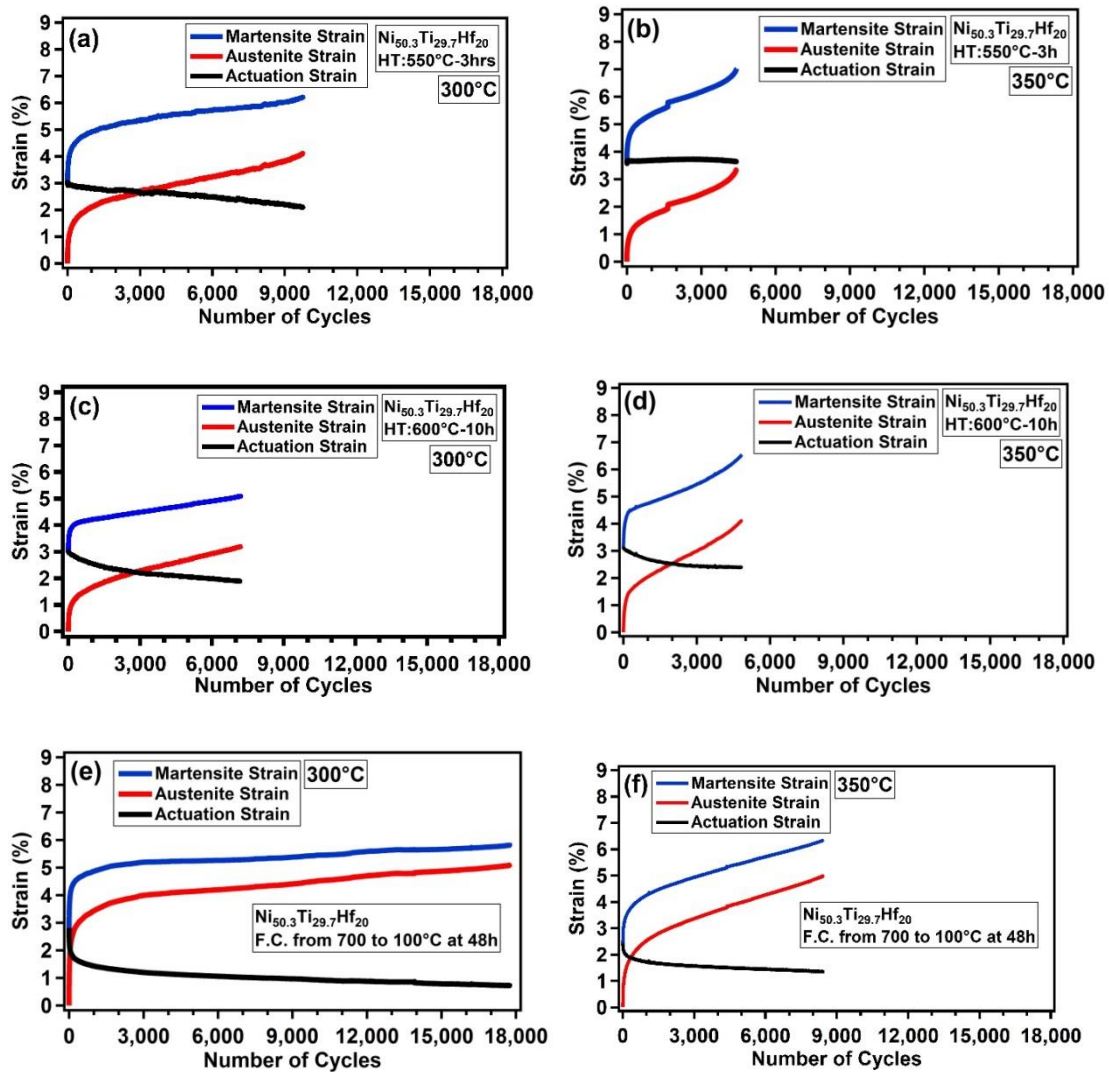


Figure 4.4 Evolution of strain in austenite (i.e. irrecoverable strain), strain in martensite, and actuation strain until failure during thermal cycling tests under constant stress level of 300 MPa for nano-precipitation hardened $\text{Ni}_{50.3}\text{Ti}_{29.7}\text{Hf}_{20}$ HTSMA. The specimens were exposed to different aging treatments before the tests and then tested up to different UCT: (a) 550°C-3h, 300°C UCT, (b) 550°C-3h, 350°C UCT, (c) 600°C-10h, 300°C UCT, (d) 600°C-10h, 350°C UCT, (e) FC from 700°C to 100°C in 48h, 300°C UCT, and (f) FC from 700°C to 100°C in 48h, 350°C UCT. FC: Furnace Cooling, UCT: Upper Cycle Temperature. " Reprinted with permission from [164]. "

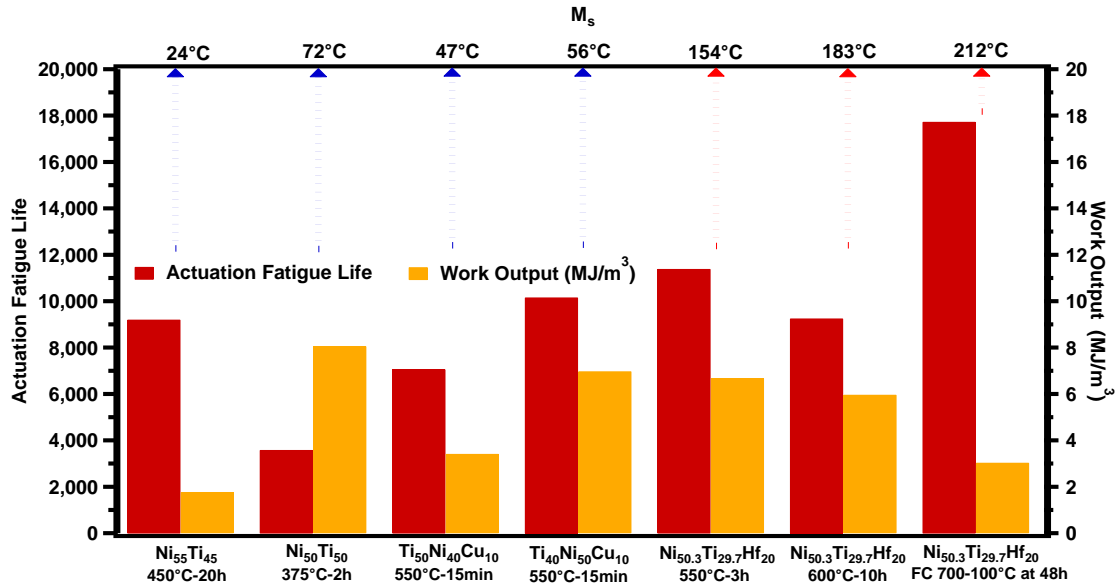


Figure 4.5 A comparison of the work output vs. fatigue life responses of Ni₅₅Ti₄₅[158], Ni₅₀Ti₅₀[128], Ti₅₀Ni₄₀Cu₁₀ [130], Ti₄₀Ni₅₀Cu₁₀ [47] and Ni_{50.3}Ti_{29.7}Hf₂₀ HTSMA heat treated at different aging times and temperatures. The Ti₅₀Ni₄₀Cu₁₀ specimens were in the form of wires whereas all others were in form of flat dog-bone shaped specimens. " Reprinted with permission from [164]. "

4.3. Post-Mortem Martensitic Transformation Characteristics

DSC analysis was performed prior to and following the fatigue tests in order to evaluate the evolution of transformation temperatures and ΔH (Table 4.1). As seen in Figure 4.6, ΔH was reduced by about 40-50 % in the failed specimens, while the transformation temperatures shifted up for the entire batch of the samples. The transformation ranges during cooling and heating cycles ($A_f - A_s$ and $M_s - M_f$) were widened upon actuation fatigue cycling, such that discernible peaks were not prevalent in the failed fatigue samples. Particularly, M_s and A_f temperatures of the failed samples increased as a function of number of cycles to failure for all heat treatment conditions as shown in Figure 4.7, featuring a linear relationship between actuation fatigue life and increase in M_s temperature ($\Delta M_s = M_s^{\text{post-fatigue}} - M_s^{\text{pre-fatigue}}$). Similarly, it is also

possible to find a direct correlation between ΔM_s and average actuation strain. Based on the results presented in Figure 4.5 and Figure 4.7, the higher the average actuation strain is in the fatigue tests, the higher the ΔM_s gets in the failed samples. ΔM_s is usually high when there is an oriented internal stress triggering martensitic transformation at higher temperatures [170, 171]. If there is no oriented internal stress or if the internal stress is more isotropic, then the increase in ΔM_s is not as severe, which is the case for the furnace cooled samples.

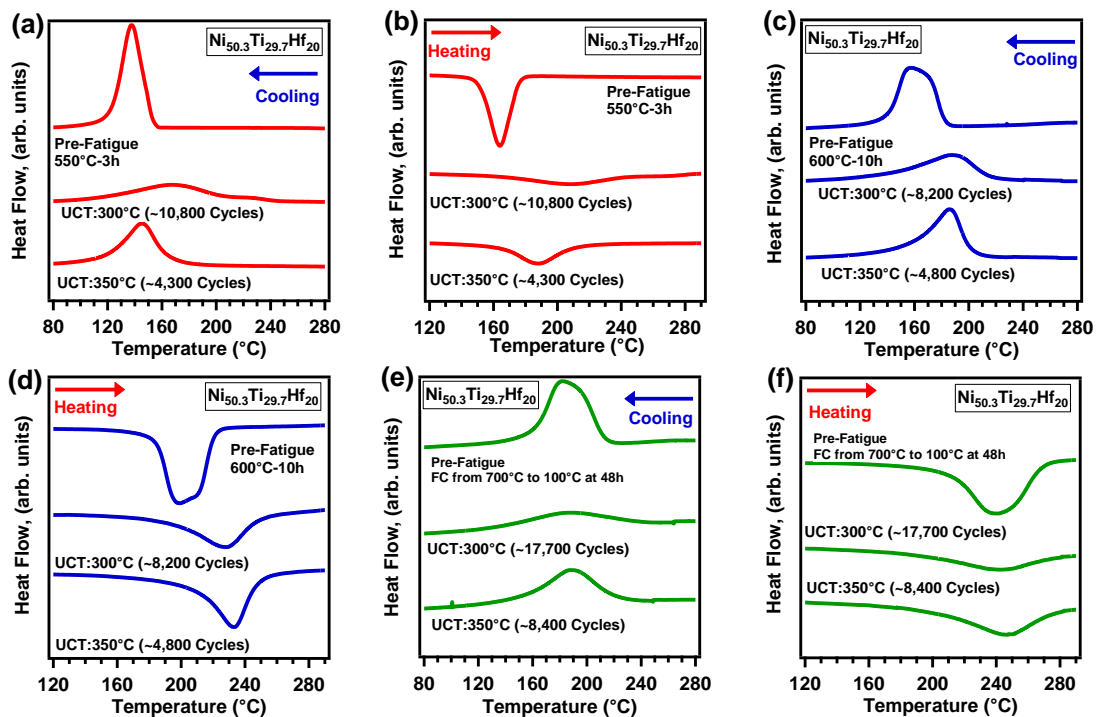


Figure 4.6 Post-mortem DSC results of the nano-precipitation hardened $\text{Ni}_{50.3}\text{Ti}_{29.7}\text{Hf}_{20}$ HTSMA specimens with different aging heat treatments, exhibiting the change in the transformation temperatures and heat of transformation after the actuation fatigue experiments. The figures organized in such a way that (a) and (b) are from the samples aged at 550°C for 3h, (c) and (d) are from the samples aged at 600°C for 10h, and (e) and (f) are from the samples furnace cooled from 700°C to 100°C in 48h. (a), (c), and (e) are for cooling and (b), (d), and (f) are for heating cycles. The numbers in parentheses correspond the fatigue life of those particular samples tested. UCT: Upper Cycle Temperature. " Reprinted with permission from [164].

4.4. Fracture Surface Analysis

SEM investigations of the fracture surfaces of the failed fatigue specimens revealed the fracture modes of the samples with different microstructures and testing conditions, as illustrated in Figure 4.8. Fracture morphology demonstrated that mostly transgranular failure was observed in the specimens containing larger precipitates, particularly in the case of the furnace cooled samples. Transgranular fracture features were also found in the specimens heat treated at 600°C for 10h. The specimens heat treated at 550°C for 3h, on the other hand, exhibited a combination of intergranular and transgranular fracture features. The area percentage of intergranular fracture in the failed specimens containing precipitates with the size of < 20 nm was larger than those containing larger precipitates.

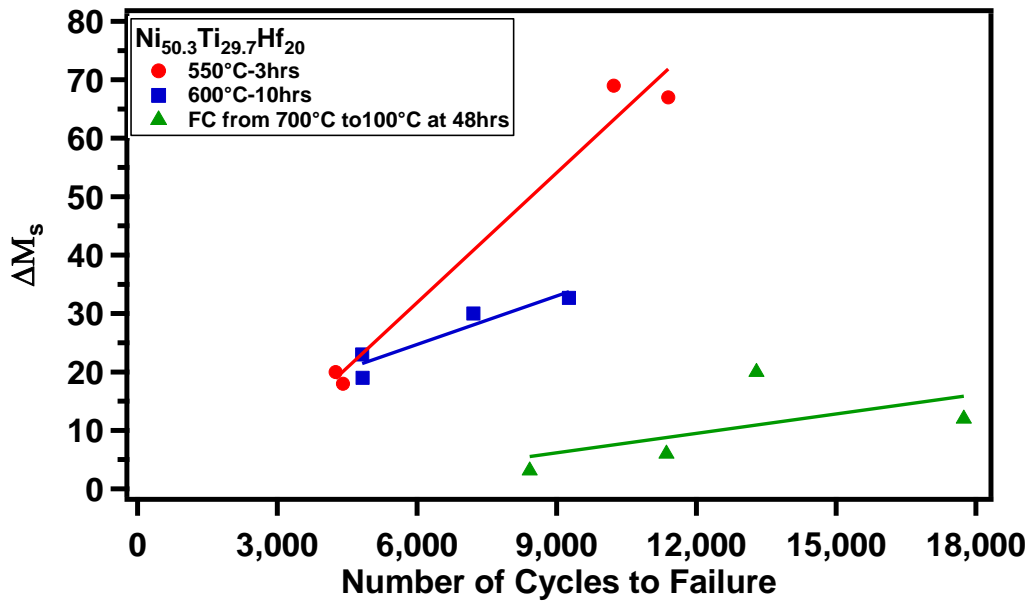


Figure 4.7 Evolution of the M_s temperatures of the actuation fatigue tested $Ni_{50.3}Ti_{29.7}Hf_{20}$ HTSMA specimens with different aging heat treatments as a function of the number of cycles to failure, relative to that of the untested samples (with the same aging heat treatments). $\Delta M_s = M_s^{pro-fatigue} - M_s^{pre-fatigue}$. Reprinted with permission from [164]. "

Figure 4.9 presents the SEM images of the flat side surfaces of the failed fatigue samples after polishing. Randomly distributed microcracks apparently formed perpendicular to the applied stress direction. Higher crack density was observed on the specimens heat treated at 550°C for 3h with the crack lengths ranging between 5 and 400 μm. Cracks in the specimens with largest precipitates were longer and more sparsely distributed with lengths ranging from 40 to 420 μm. For specimens with larger precipitates, however, the crack density seems to be lower. The specimens heat treated at 600°C for 10h had similar crack content to the furnace cooled specimens.

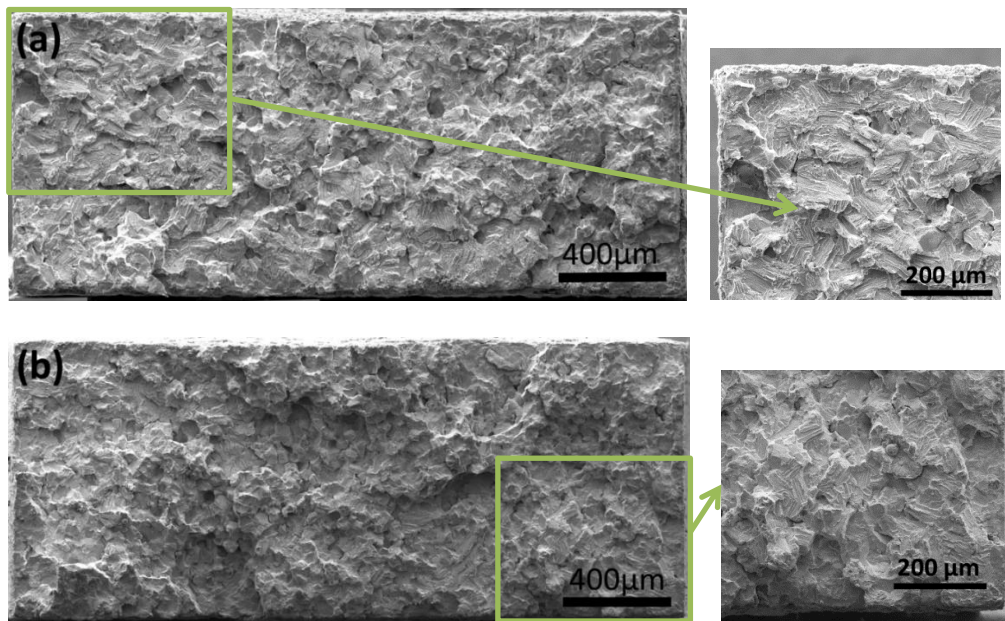


Figure 4.8 SEM micrographs of the fracture surfaces of $\text{Ni}_{50.3}\text{Ti}_{29.7}\text{Hf}_{20}$ HTSMA samples following the failure after the actuation fatigue experiments. The specimens were exposed to different aging treatments before the tests and then tested up to different UCT: (a) 550°C-3h, 300°C UCT, (b) 550°C-3h, 350°C UCT, (c) 600°C-10h, 300°C UCT, (d) 600°C-10h, 350°C UCT, (e) FC from 700°C to 100°C in 48h, 300°C UCT, and (f) FC from 700°C to 100°C in 48h, 350°C UCT. FC: Furnace Cooling, UCT: Upper Cycle Temperature. " Reprinted with permission from [164]. "

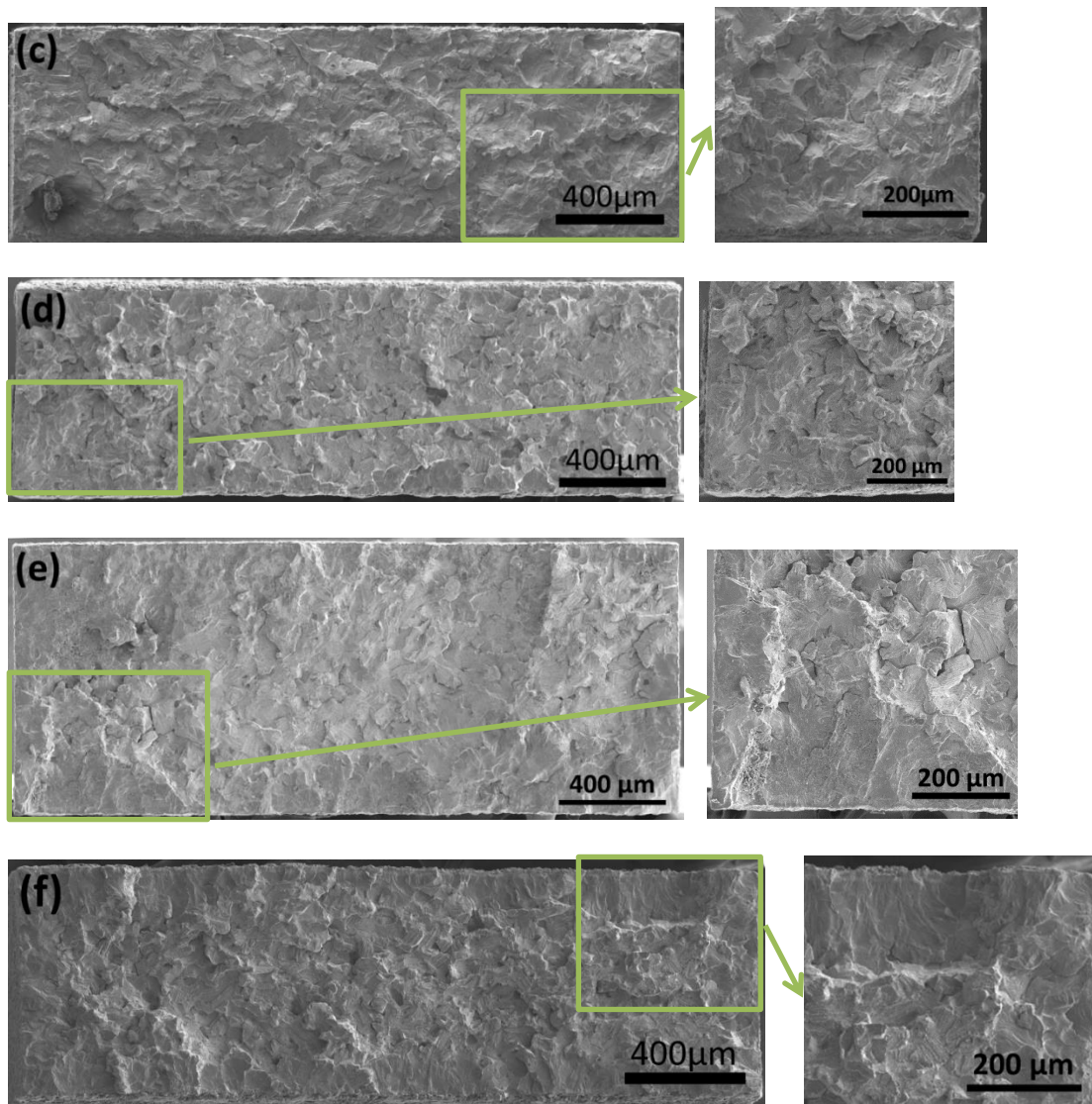


Figure 4.8 Continued. " Reprinted with permission from [164]. "

4.5. Role of Microstructure on the Cyclic Evolution of Actuation Strain, Fatigue Life and Work Output

The role of microstructures, obtained by the three different heat treatments, on the actuation fatigue performance of the $\text{Ni}_{50.3}\text{Ti}_{29.7}\text{Hf}_{20}$ HTSMA was investigated in this study. Aging at 550°C for 3h resulted in nano-sized precipitates 7-20 nm in length and 4-6 nm in width, and the corresponding samples exhibited 2.5 % average actuation strain

when tested under 300 MPa - 300°C stress-UCT combination (Figure 4.10). When UCT was increased to 350°C, average actuation strain increased to 3.6 % under the same stress level. The higher actuation strain in the samples heat treated at 550°C for 3h as compared to the other two microstructures is consistent with the size of the nano-precipitates. Small precipitates impede dislocation motion and allow larger part of the samples transforming into detwinned martensite throughout the actuation fatigue cycling [29, 166]. The actuation strain remained almost constant until the failure in the case of 350°C UCT experiments (Figure 4.10 (b)) while the specimens subjected to 300°C UCT exhibited a gradually declining actuation strain. One reason for the variation in the evolution of actuation strain is the partial transformation occurring during martensitic transformation when UCT is lowered to 300°C. Furthermore, plastic deformation prevalent during repeated thermal cycling under stress induces remnant martensite (and occasionally remnant austenite [119]). Accumulation of remnant martensite for the samples heat treated at 550°C for 3h is more pronounced in the case of 300°C UCT since heating specimens to 350°C UCT leads to the annihilation of more dislocations and other defects, which are responsible for retaining martensite, and this in turn, leads to reverse transformation of stabilized martensite and provides more austenite volume for the reversible transformation. In fact, transformation heat (ΔH) values reported in Table 4.1 clearly indicate that the transforming volume in the 350°C UCT cases is higher than those in the 300°C UCT experiments since ΔH is directly related to the amount of transforming material.

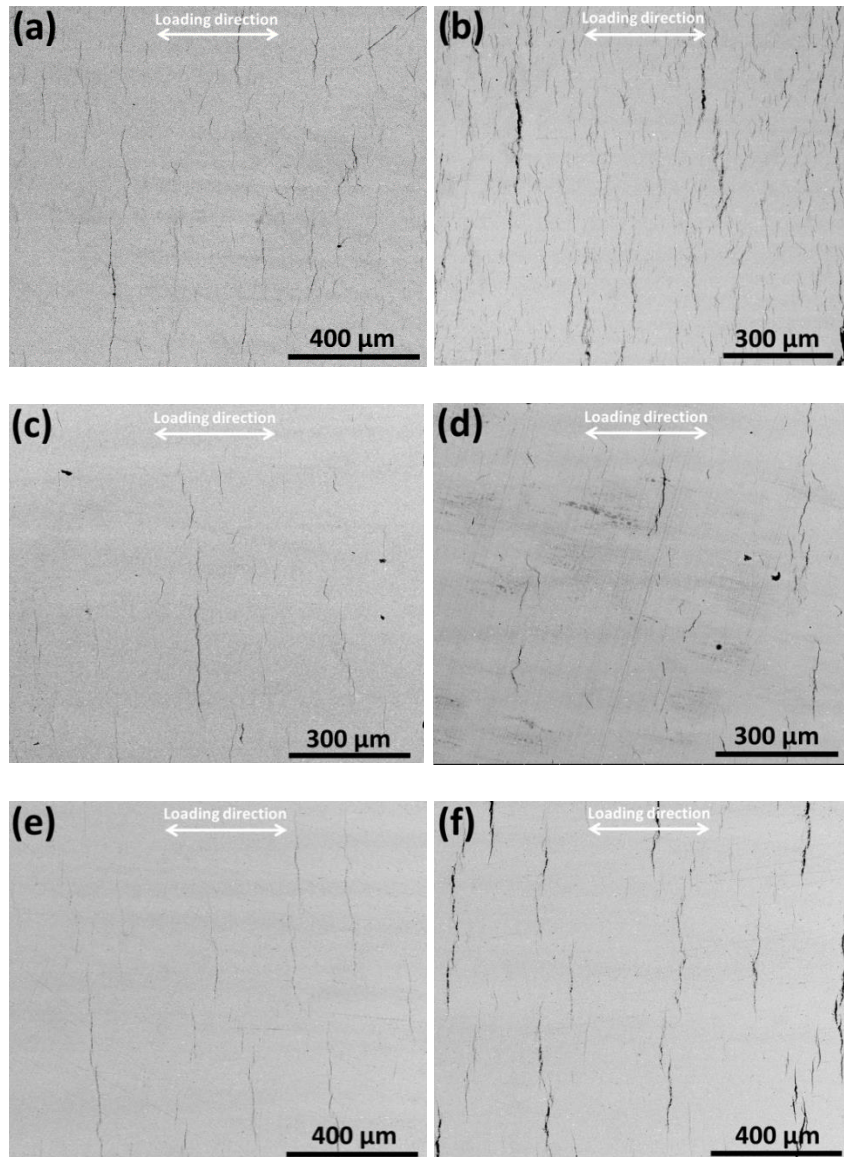


Figure 4.9 Fatigue cracks on the side surface of the failed specimens of $\text{Ni}_{50.3}\text{Ti}_{29.7}\text{Hf}_{20}$ HTSMA samples for different aging treatments/ UCT: **(a)** 550°C-3h, 300°C UCT, **(b)** 550°C-3h, 350°C UCT, **(c)** 600°C-10h, 300°C UCT, **(d)** 600°C-10h, 350°C UCT, **(e)** FC from 700°C to 100°C in 48h, 300°C UCT, and **(f)** FC from 700°C to 100°C in 48h, 350°C UCT. FC: Furnace Cooling, UCT: Upper Cycle Temperature. " Reprinted with permission from [164]. "

The second heat treatment, i.e. 600°C for 10 h, resulted in an increase in transformation temperatures by about 30°C as compared to the 550°C for 3h heat treatment. This heat

treatment led to the formation of nano-sized precipitates which were 40-80 nm in length and 20-40 nm in width. They were slightly larger than the precipitates obtained with the 550°C for 3h heat treatment, but the martensite morphologies in both cases were quite similar; precipitates were mostly absorbed by martensite variant [166]. As it can be seen in Figure 4.10, in contrast to the specimens with the 550 °C-3h heat treatment, the specimens aged at 600°C for 10h showed a faster decrease in actuation strain, exhibiting 2.6 % and 2.0% average actuation strains at 350°C and 300°C UCTs, respectively. The larger precipitates led to a more significant decrease in the actuation strain due to the early initiation of partial transformation and increase in transformation temperatures. When the precipitates get larger with higher temperature or longer aging treatments, their effectiveness in strengthening SMAs and suppressing transformation induced plasticity deteriorates, leading to much faster functional response as in the case of 600°C-10h and furnace cooled samples.

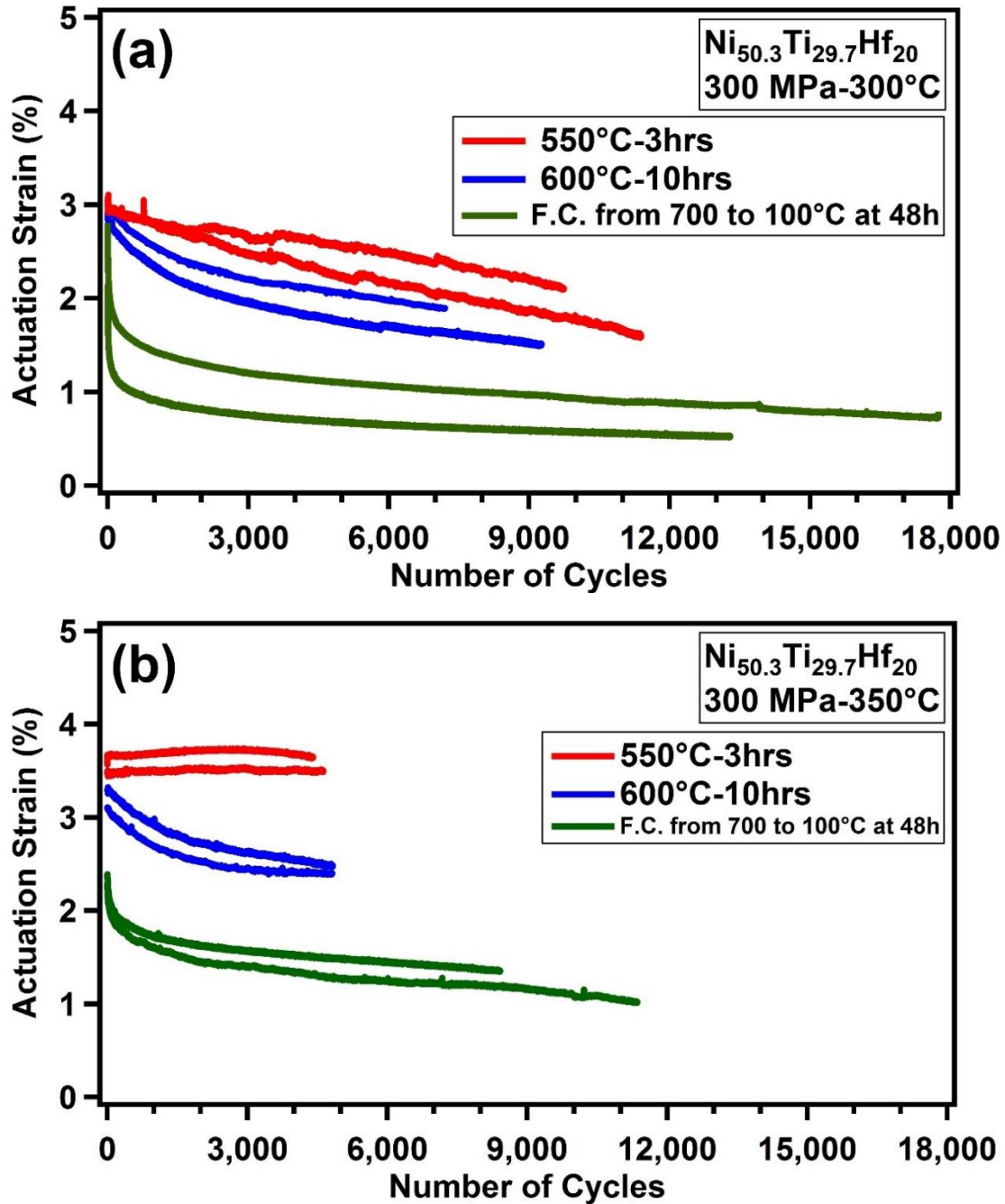


Figure 4.10 Effect of microstructure, obtained with different aging heat treatments, on the actuation fatigue response of the nano-precipitation hardened $\text{Ni}_{50.3}\text{Ti}_{29.7}\text{Hf}_{20}$ HTSMA, thermally cycled up to different Upper Cycle Temperatures (UCT) under 300 MPa: (a) 300°C UCT and (b) 350°C UCT. " Reprinted with permission from [164]. "

The last microstructure studied in this work was the one obtained by furnace cooling, which led to the formation of large incoherent precipitates. Precipitate size was determined to range from 70 to 200 nm in length and 20 to 70 nm in width (Figure 4.2). This increase in the size of H-phase precipitates also manifested itself as a change in martensite morphology. Even though the 550°C-3h and 600°C-10h heat treatments allowed precipitates to be absorbed by martensite plates, the precipitates in furnace cooled samples are not suitable to be absorbed by martensite plates, which interferes with the martensitic transformation [166]. Actuation strain exhibited a preliminary shakedown behavior over few hundred cycles and continued to gradually evolve at a lower rate for both UCTs. Specimens subjected to this heat treatment exhibited an average actuation strain of 1.4 % and 1.0 % for 350°C and 300°C UCTs, respectively. More specifically, the larger precipitates with corresponding higher transformation temperatures eventually led to partial transformation to occur relatively quickly upon cycling, leaving less volume within the matrix to undergo martensitic transformation, and thus, much lower actuation strains.

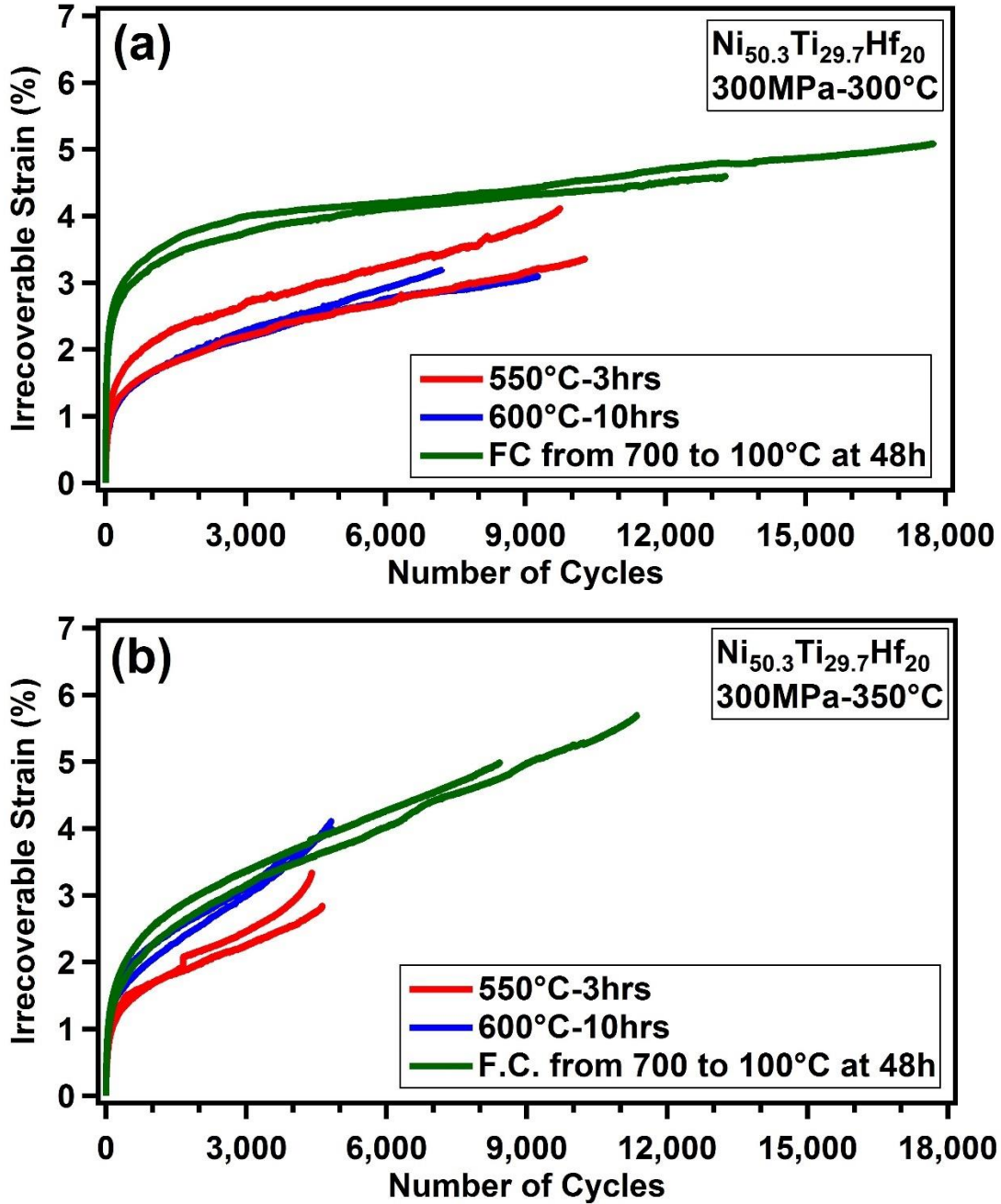


Figure 4.11 Role of microstructure on the evolution of irrecoverable strain (strain in austenite, see Figure 2.2 (b)) during thermal cycling under 300 MPa for nano-precipitation hardened $\text{Ni}_{50.3}\text{Ti}_{29.7}\text{Hf}_{20}$ HTSMA under different upper cycle temperatures (UCT): (a) 300°C UCT and (b) 350°C UCT. " Reprinted with permission from [164]. "

In contrast to actuation strain, larger precipitates in the furnace cooled samples led to an increased actuation fatigue life, due to the decreased actuation strain, and thus, these samples exhibited the longest average fatigue life of 9,800 and 15,500 cycles for 350°C and 300°C UCTs, respectively. In the case of specimens aged at 600°C for 10 h, the average number of cycles to failure dropped to 4,800 and 8,200 cycles for 350°C and 300°C UCTs, respectively. The average number of cycles to failure for the samples heat treated at 550°C for 3h were found to be 4,300 at 350°C UCT and 10,800 at 300°C UCT, which are comparable or better than that of the 600°C-10 h samples, despite the noticeably higher actuation strains in the 550°C-3h samples. Thus, it is concluded that partial transformation cycles consistently improve the number of cycles to failure and changing microstructure through proper aging heat treatments can facilitate such an increase. Accordingly, the fatigue response of NiTiHf HTSMAs is strongly dependent on the microstructure and applied UCT.

Based on the above discussions, the samples of Ni_{50.3}Ti_{29.7}Hf₂₀ HTSMA with nano-precipitate sizes less than 20 nm (i.e. the 550°C-3h samples) clearly provide the best combination of stable actuation strain and actuation fatigue life among the cases investigated in this study. These samples demonstrate higher work output than the specimens aged at 600°C for 10h and the furnace cooled samples. This difference is related to the difference in martensitic transformation temperatures and precipitate sizes. Samples with higher transformation temperatures experience partial transformation more easily due to being closer to UCT. In addition, larger precipitates (observed in the latter two cases) are less effective in suppressing plastic deformation that accompanies

martensitic transformation. Moreover, larger precipitates interfere with martensitic transformation (especially in the furnace cooled samples), resulting in poor cyclic stability, shape memory response and work output.

Actuation fatigue life and corresponding work outputs of low temperature SMAs from the literature and the present HTSMAs were plotted as a function of their M_s in Figure 4.5. The $Ni_{55}Ti_{45}$ alloy aged at $450^\circ C$ for 20h had a work output of $\sim 1.8 J/cm^3$, M_s of $24^\circ C$, and actuation fatigue life of $\sim 9,000$ cycles when tested under 200MPa constant stress [158]. Due to high Ni content, this particular NiTi composition has very high volume fraction of Ni_3Ti precipitates and therefore, the actuation strain and thus the actuation work output is low. The work output increased to $8.5 J/cm^3$ for $Ni_{50}Ti_{50}$ with corresponding fatigue life of $\sim 3,250$ cycles tested under 200MPa constant stress [128]. Even though fatigue life of the $Ti_{40}Ni_{50}Cu_{10}$ alloy was longer than that of $Ti_{50}Ni_{40}Cu_{10}$, the former attained a higher work output than $Ti_{50}Ni_{40}Cu_{10}$. In contrast, the $Ni_{50.3}Ti_{29.7}Hf_{20}$ alloy aged at $550^\circ C$ for 3h, with coherent nano-precipitates smaller than 20 nm in size, appears to be an attractive candidate for HTSMA actuator applications, as it produced a significant work output level ($\sim 7 J/cm^3$) while having a much longer fatigue life ($\sim 10,500$ cycles) than the low temperature SMAs included in Figure 4.5, despite the much higher stress level applied as compared to what low temperature SMA cases in Figure 4.5 were exposed to.

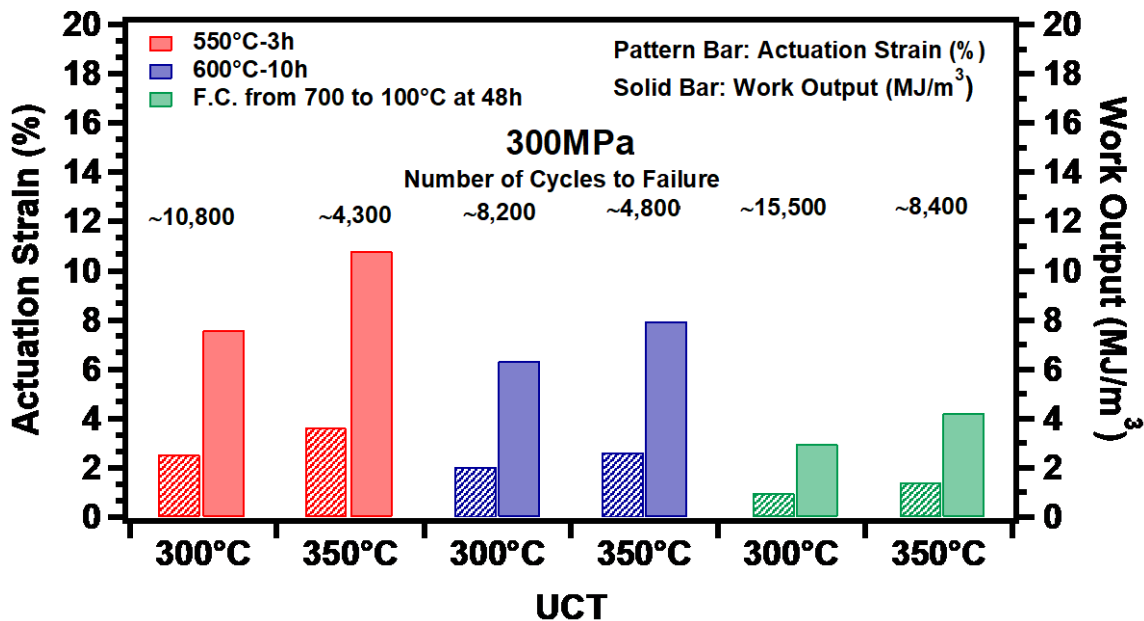


Figure 4.12 Summary of the important actuation fatigue characteristics such as the average actuation strain, work output, and fatigue life of nano-precipitation hardened $\text{Ni}_{50.3}\text{Ti}_{29.7}\text{Hf}_{20}$ HTSMAs aged at 550°C for 3h, 600°C for 10h and FC from 700 to 100°C in 48h. Patterned and solid bars represent the average actuation strain and work output, respectively. FC: Furnace Cooled. UCT: Upper Cycle Temperature. " Reprinted with permission from [164]. "

4.6. Effect of Microstructure on the Cyclic Evolution of Irrecoverable Strain

The strain vs. temperature responses of the aged $\text{Ni}_{50.3}\text{Ti}_{29.7}\text{Hf}_{20}$ samples upon thermal cycling under constant stress and two different UCT levels were studied to assess the evolution of irrecoverable strain, transformation temperatures and thermal hysteresis as a function of the number of cycles to failure. Figure 4.3 shows selected hysteresis curves for 1st, 1000th and last transformation cycles before failure. A comparison of the hysteresis curves for all cases revealed that the transformation temperatures increase concomitant with the number of cycles, which is a consequence of the changes in the microstructure and the accumulation of irrecoverable strain. Figure 4.11 presents the accumulation of irrecoverable strain during thermal cycling until failure for all cases.

Irrecoverable strain increases rapidly during the initial stages of thermal cycling, namely up to 1000 cycles, and then continues to increase more gradually with further cycling until failure. The accumulation of irrecoverable strain does not fully saturate and continues until failure. Furthermore, the rate of accumulation of irrecoverable strain and total accumulated irrecoverable strain increases with increasing precipitate size. The samples with precipitate sizes less than 20 nm result in significant reduction of the irrecoverable strain rate. When the precipitate size gets significantly larger, however, as in the case of the furnace cooled samples, the precipitates do not sufficiently strengthen the matrix against plastic deformation as much as the nano-sized precipitates do [3, 166]. Moreover, when the precipitate size reaches several hundreds of nanometers, the precipitates cannot be absorbed into martensite variants anymore, which, in turn, increases the number of intervariant boundaries, further contributing to the irrecoverable strain [166]. As seen in Figure 4.11, increase in heat treatment temperature and time leads to an increase in irrecoverable strain, where the maximum irrecoverable strains were observed in the furnace cooled samples.

Thermal hysteresis (ΔT) is another crucial parameter for the practical applications of HTSMAs, which is brought about by energy dissipation associated with martensitic transformation. As can be seen in Table 4.2, thermal hysteresis increases with the increase in precipitate size. This is mainly because of the loss of coherency of the precipitates with increasing size and increase in the number of precipitate-martensite variant interfaces in the case of large precipitate sizes. These in turn leads to an increase in energy dissipation and larger thermal hysteresis.

4.7. Evolution of Martensitic Transformation Temperatures

Table 4.1 tabulates the pre-fatigue and post-fatigue transformation heat, ΔH , values and the transformation temperatures. As also seen in Figure 4.6, M_s and A_f temperatures increased as a function of number of cycles to failure. Decrease in ΔH after fatigue test was observed for all specimens regardless of their prior heat treatment. There is a clear trend between fatigue life and increase in M_s and A_f temperatures, which is represented as $\Delta M_s = M_s^{\text{after fatigue}} - M_s^{\text{before fatigue}}$ in Figure 4.7 for all cases. Increase in M_s is due to the inhomogeneous martensitic transformation that develops throughout the actuation fatigue cycling as a result of the plastic deformation and other defect generation, such that the material can no longer transform homogeneously as the number of cycles increases. As a consequence of this partial transformation, in the regions that transforms repeatedly till failure, local oriented internal stress develops. These regions start to undergo martensitic transformation at higher temperatures due to local oriented internal stress, and the rest of the sample would either transform at lower temperatures (due to the inhomogeneous microstructure and internal stress distribution) or not transform at all.

DSC results also indicated that failed fatigue samples exhibited about 40-50 % reduction in their heat of transformation. The reduction in ΔH is a result of the defects forming during thermo-mechanical cycling, which limit the volume of the matrix that can undergo reversible thermally-induced martensitic transformation [4, 46, 119, 172].

4.8. Fractography and Fracture Modes

SEM was carried out to qualitatively evaluate the fracture surface morphologies in failed fatigue specimens. In order to relate topology of the fracture surfaces to fracture mode of failure, it is accepted that transgranular fracture is characterized by feather markings, cleavage steps and river patterns [173]. On the other hand, intergranular fracture is characterized by rock-candy morphology, triple points, and faceted appearances [174]. Generally, the latter occurs when grain boundary is brittle and weak, and cracks spread rapidly with negligible plastic deformation. The typical SEM pictures of the fracture surfaces from failed specimens presented in Figure 4.8 indicate that intergranular fracture was the dominant failure mode in the case of the specimens heat treated at 550°C for 3hrs, while transgranular fracture dominated the fracture surfaces of the furnace cooled samples. It was also observed that the specimens cycled to 350°C UCT had more intergranular fracture morphology than the samples exposed to 300°C UCT, on their fracture surfaces. The largest river pattern regions, indicative of transgranular fracture mode, was observed close to the edge of the specimens with the largest precipitates.

Following the fatigue experiments, SEM micrographs of the sample surfaces were also captured to evaluate surface crack densities. Figure 4.9 shows the room temperature postmortem SEM images. While thermal cycling under stress facilitated formation of a significant number of cracks across entire samples heat treated at 550°C for 3hrs, less cracks were present for specimens with larger precipitates. As the precipitates became larger, corresponding cracks also got larger, more sparse, and less in density. Size of the

cracks ranged from 5 to 400 μm for the specimens aged at 550°C for 3h while the specimens aged at 600°C for 10h and furnace cooled from 700°C to 100°C in 48h contained microcracks with lengths ranging between 20 and 400 μm and 40 and 420 μm , respectively.

4.9. Summary and Conclusions

The main purpose of the work presented herein was to investigate the influence of different microstructures formed by different aging heat treatments on the actuation fatigue performance of the Ni-rich $\text{Ni}_{50.3}\text{Ti}_{29.7}\text{Hf}_{20}$ high temperature shape memory alloy (HTSMA). Particularly, evolution of actuation strain, irrecoverable strain, and number of cycles to failure were reported and compared for different microstructures and upper cycle temperatures (UCT). Microstructural characterization was performed following the failure of the samples to evaluate the associated changes in microstructure and martensitic transformation characteristics before and after actuation fatigue experiments. Primary findings can be summarized as follows:

- Isobaric thermal cycling experiments revealed that different sizes of precipitates after various aging treatments significantly impact actuation strain and irrecoverable strain evolution, and the fatigue life. Even though the largest precipitates induced by furnace cooling from 700°C to 100°C in 48h promoted the longest fatigue life, namely 15,500 cycles under 300MPa for 300°C UCT, the corresponding samples suffered from low average actuation strain of 1.0% and extensive permanent deformation. Specimens heat treated at 550°C for 3h and tested under the same condition are capable of undergoing about 10,800

cycles with an average actuation strain of 2.5%. Since suitability of HTSMA for actuator applications depends on the fatigue life and work output, samples heat treated at 550°C for 3h appear to be promising candidates over those samples subjected to the other two selected heat treatments.

- The durability of Ni-rich Ni_{50.3}Ti_{29.7}Hf₂₀ actuators is improved as a result of the increase in the resistance to plastic deformation with precipitation hardening. Small precipitates (formed after the heat treatment at 550°C for 3h) less than 20 nm in size are fully absorbed in the martensite variants, which do not strongly interfere with the martensite phase front motion. On the other hand, aging heat treatments at higher temperatures and for longer times result in precipitates that are several hundred nanometers in size (furnace cooled from 700 to 100°C in 48 h) and cannot be absorbed by the martensite variants, resulting in poor shape memory recovery and larger irrecoverable strains due to the lower strength against dislocation plasticity as compared to the samples with smaller precipitates. Transformation-induced irrecoverable (plastic) strain evolves continuously as a function of the number of actuation cycles and does not saturate until failure, regardless of the type of microstructure. The samples heat treated at 550°C for 3hr was more stable against plastic deformation as compared to the samples subjected to the other two heat treatments.
- A large reduction in the heat of transformation, ΔH , was detected after fatigue failure due to increased volume fraction of remnant martensite or austenite, i.e. less volume of material participate in reversible phase transformation. Thermal

cycling under constant stress generates dislocations that lock in some of the martensite variant. Therefore, some portion of the microstructure is not able to transform back to austenite, reducing the heat of transformation. This rationalizes the continuous reduction in actuation strain with the number of cycles during actuation fatigue experiments. In addition, M_s experienced an increase concomitant with number of cycles to failure as a result of the oriented internal stresses stored during thermal cycling in the regions of the material that participate in reversible phase transformation until failure.

- Larger precipitates favor transgranular fracture mode as well as long and sparse cracking during repeated transformations. However, smaller precipitates lead to both intergranular and transgranular fracture modes, as well as dense and shorter cracking.
- The current findings demonstrate that thermo-mechanical properties of Ni-rich NiTiHf HTSMAs, such as fatigue life, irrecoverable strain and actuation strain, can be altered by changing precipitate size through aging treatments. Longer fatigue life comes at the expense of actuation strain and is accompanied by significant irrecoverable strain. Experimental observations revealed that nano-precipitation hardened $\text{Ni}_{50.3}\text{Ti}_{29.7}\text{Hf}_{20}$ HTSMAs is a viable choice for high-force actuator applications at elevated temperatures. Overall, nano-precipitation hardened $\text{Ni}_{50.3}\text{Ti}_{29.7}\text{Hf}_{20}$ HTSMA at 550°C for 3h exhibits superior performance as compared to several low temperature SMAs when fatigue life and actuation energy density are considered as the decisive

parameters in determining suitability of candidate materials for actuator application.

CHAPTER V

ROLE OF APPLIED STRESS LEVEL ON THE ACTUATION FATIGUE BEHAVIOR OF NITiHF HIGH TEMPERATURE SHAPE MEMORY ALLOYS*

This study presents the actuation fatigue response of nano-precipitation hardened Ni_{50.3}Ti_{29.7}Hf₂₀ high temperature shape memory alloy (HTSMA) undergoing thermal cycling between martensite and austenite under various tensile stress levels up to 500 MPa. Changes in fatigue life, and actuation and irrecoverable strains were monitored as a function of the number of cycles to failure. As opposed to conventional metals, plastic deformation occurs in SMAs during repeated phase transformation even though applied stress level is often below the yield strength of the alloys [126]. Moreover, the fatigue performance of an SMA is strongly dependent on few parameters such as material composition, test temperatures, heat treatment procedures, and applied stress level [11, 127-135] .

Applied stress level plays a significant role in dictating the cyclic actuation behavior of SMAs [47, 130, 132, 133, 175-177], yet the effects of applied stress on the actuation fatigue of NiTiHf HTSMAs have never been reported before. From an application point of view, it is important to note that SMA actuators need to overcome a constant or variable bias force in many cases, yet there is only a limited number of studies focusing

* Reprinted with permission from “Role of applied stress level on the actuation fatigue behavior of NiTiHf high temperature shape memory alloys” by O. Karakoc, C. Hayrettin, D. Canadinc, I. Karaman, 2018. Acta Materialia, 153, pp.156-168, Copyright 2018 by Acta Materialia Inc. published by Elsevier Ltd.

on the actuation fatigue failure as a function of stress and they are mostly on low temperature SMAs [17, 47, 126, 130, 157]. The present study was undertaken with the motivation of addressing this issue in HTSMAs, and thereby developing a fundamental understanding of the effects of applied stress on the actuation fatigue behavior of the nano-precipitation hardened Ni_{50.3}Ti_{29.7}Hf₂₀ alloy (the most studied NiTiHf composition so far), in terms of the evolution of actuation strain, durability, actuation work output, and the number of cycles to failure. The comprehensive set of experimental results reported herein will contribute to the database for designing HTSMA actuators with improved performance, stability and durability delivering maximum work output at elevated temperatures.

Table 5.1 First and last cycle transformation temperatures obtained from the strain-temperature responses of the Ni_{50.3}Ti_{29.7}Hf₂₀ HTSMA specimens, heat treated at 550°C for 3 hours, for different stress levels during the actuation fatigue experiments. " Reprinted with permission from [50]. "

Stress Level (MPa)	Transformation Temps. (°C)				Transformation Temps. (°C)				ΔM_s (°C)	ΔA_f (°C)
	First Cycle				Last Cycle					
	M _f	M _s	A _s	A _f	M _f	M _s	A _s	A _f		
200	153.5±0.7	160.5±0.7	171.5±0.7	183.5±0.7	152.0±17.6	216.5±4.9	171.5±2.1	249.5±0.7	56	66
300	156.5±2.1	177.0±1.4	182.0±2.8	193.0±2.8	163.5±2.1	237.0±5.6	183.0±2.8	254.0±2.8	60	61
400	160.0±1.4	194.5±7.7	184.0±1.4	209.5±3.5	161.5±0.7	244.0±1.4	186.5±2.1	270.5±0.7	49	61
500	172.5±3.5	208.5±2.1	205.0±4.2	236.5±4.9	168.5±9.1	263.0±2.8	179.5±2.1	286.0±1.4	54	49

Table 5.2 Change in martensitic transformation temperatures and the transformation heat of the Ni_{50.3}Ti_{29.7}Hf₂₀ HTSMA heat treated at 550 °C for 3 hours after failure in the actuation fatigue experiments under different stress levels. DSC was utilized for measuring the transformation temperatures, and the results represent the average of the measurements carried out on two different failed specimens. " Reprinted with permission from [50]. "

Stress Level	Transformation Temperatures (°C)				Hysteresis (A _f -M _s) (°C)	Transformation Heat (J/g)
	M _f	M _s	A _s	A _f		
Initial Material	124.6±0.7	149.7±1.7	153.4±1.4	178.2±0.0	28.5±0.8	18.3±0.8
200MPa	115.5±0.7	184.5±0.7	158.4±6.3	240.3±1.4	55.8±1.0	8.7±0.5
300MPa	122.5±3.5	195.2.3±4.2	168.7±6.8	235.1.±6.3	39.9±5.2	9.4±0.6
400MPa	109.9±0.4	184.8±0.9	160.4.3±7.8	220.2±5.0	35.4±2.9	9.0± 1.2
500MPa	97.9±4.9	167.3±5.2	150.2±1.7	208.6±14.0	41.3±9.6	11.4±0.3

5.1 Initial Material Properties

The samples were characterized prior to the fatigue tests in order to provide baseline data for evaluating the post-mortem experimental results. The transformation temperatures and heat of transformation of Ni_{50.3}Ti_{29.7}Hf₂₀ HTSMA samples heat treated at 550°C for 3 hours were determined using DSC (Figure 5.1 (a)). Corresponding precipitate size and morphology in the heat treated samples were determined using TEM. Figure 5.1 (b) shows coherent and homogeneously distributed nano-sized precipitates (<20 nm in length) in the matrix. Carbide content representing the purity level of the samples was calculated by processing the backscattered electron (BSE) images (Figure 5.1 (c)) with the ImageJ software, and the corresponding area fraction of carbides was estimated as 0.41 ± 0.15 %. The carbide particles appeared as heterogeneously

distributed with $< 3\mu\text{m}$ in size and were determined to be hafnium carbide, through EDS. These carbides stem from the diffusion of carbon atoms from the matrix or from the crucibles used for melting, causing slight loss of hafnium in the matrix from the nominal composition [178].

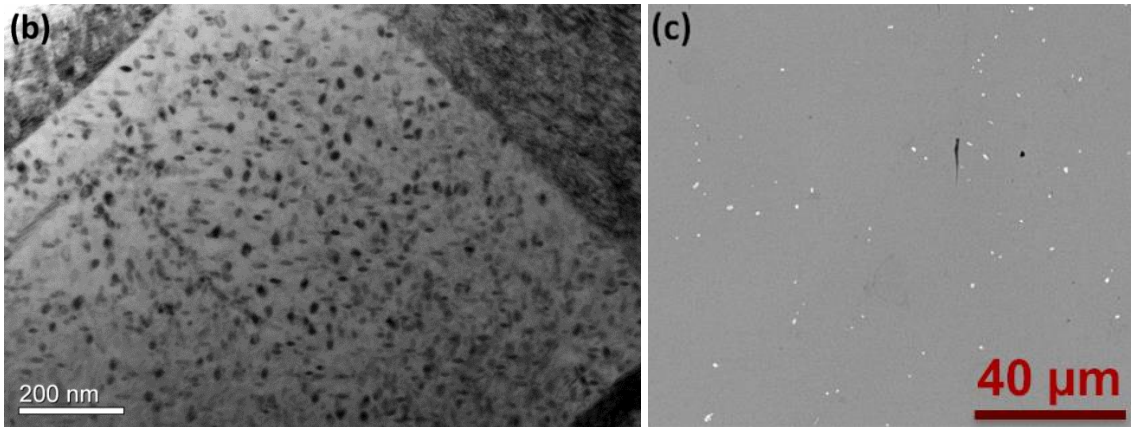
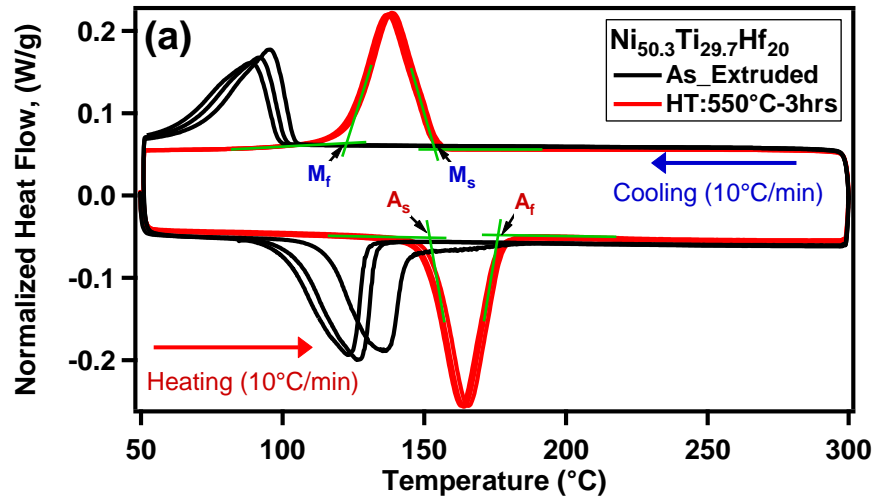


Figure 5.1 (a) Initial DSC results of the $\text{Ni}_{50.3}\text{Ti}_{29.7}\text{Hf}_{20}$ specimen in as extruded and heat treated (HT) at 550°C for 3 hours conditions before the actuation fatigue tests, (b) the corresponding bright field TEM image of the microstructure, showing H-phase nano-precipitates, and (c) representative carbide size and distribution in the microstructure for the same $\text{Ni}_{50.3}\text{Ti}_{29.7}\text{Hf}_{20}$ sample. White particles in (c) are the hafnium carbides. " Reprinted with permission from [50]. "

5.2 Actuation Fatigue Experiments

Actuation fatigue response of the nano-precipitation hardened $\text{Ni}_{50.3}\text{Ti}_{29.7}\text{Hf}_{20}$ HTSMA was investigated through thermal cycling under tensile loads across the martensitic transformation temperatures. Figure 5.2 depicts the representative strain-temperature responses under different stress levels. From these results, the evolutions of strain in martensite, total irrecoverable strain (i.e. austenite strain as described in Figure 2.2 (a) Schematic illustration of the actuation fatigue loading cycles on a stress-temperature phase diagram, and (b) a representative strain-temperature response describing how the relevant shape memory characteristics of the HTSMA actuator are determined from this kind of response. M_f : martensite finish, M_s : martensite start, A_s : austenite start, A_f : austenite finish temperatures [50].), and actuation strain were determined as a function of the number of cycles until failure, and summarized in Figure 5.3 for the cases shown in Figure 5.2. Specifically, the change in the stress level from 200 MPa to 500 MPa leads to an increase in the average actuation strain from 2.15 % to 3.22 %, respectively. In terms of the number of cycles to failure, the samples loaded at 200 MPa experienced ~21,000 cycles while the specimens under 500 MPa lasted only ~2,100 cycles, demonstrating that the longer fatigue lives were attained at the expense of actuation strain.

An important aspect in the selection of HTSMAs for practical applications is improved actuation fatigue performance with minimum amount of total irrecoverable strain, which is a consequence of the stabilized martensite and/or plastic strain due to dislocations and the formation of other defects during actuation cycling. Accordingly, based on the

results shown in Figure 5.3, the stress level has a substantial influence on the irrecoverable strain accumulated during cyclic martensitic transformations. The specimens loaded to 500 MPa had high damage accumulation accompanied by 6.90 % total irrecoverable strain on the average, while the samples tested under 200 MPa exhibited only ~3 % total irrecoverable strain at the failure.

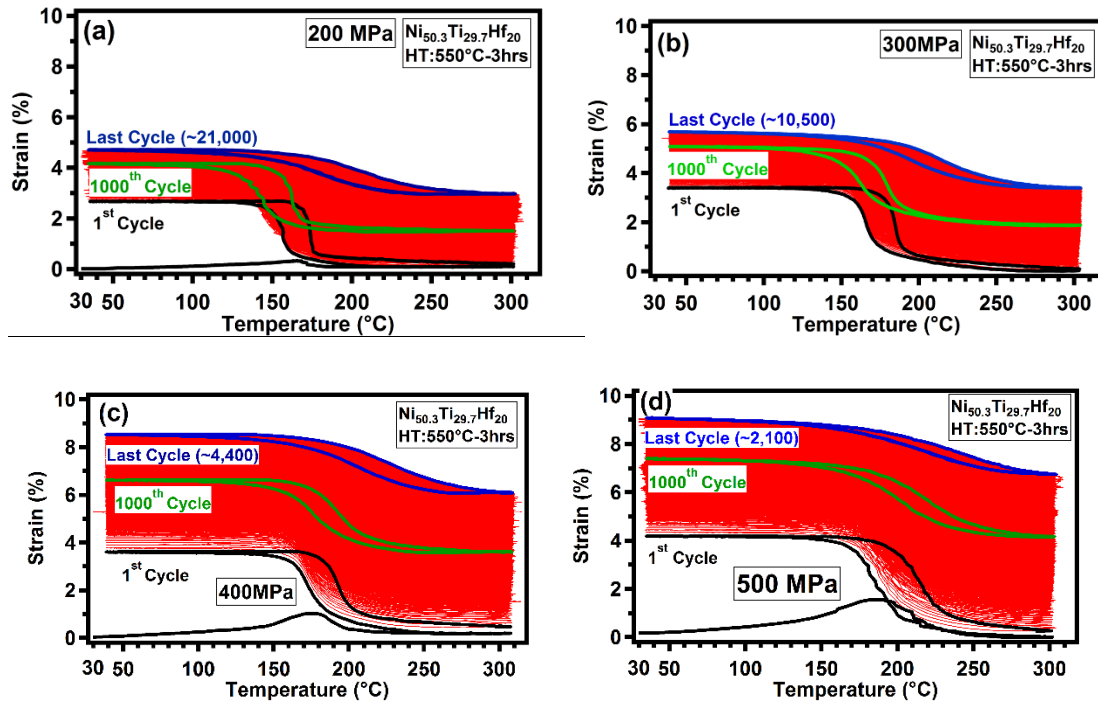


Figure 5.2 Evolution of strain vs. temperature responses with the number of cycles to failure for the nano-precipitation hardened $\text{Ni}_{50.3}\text{Ti}_{29.7}\text{Hf}_{20}$ HTSMA, heat treated (HT) at 550°C for 3 hours, under (a) 200MPa, (b) 300 MPa, (c) 400 MPa, and (d) 500 MPa tensile stresses. Only one representative case for each condition is shown. " Reprinted with permission from [50]. "

From the strain-temperature responses shown in Figure 5.2 and the responses of other samples tested in the same conditions, the transformation temperatures were determined in the first and last cycles of the experiments for each stress level, and the results are

presented in Table 5.1. During actuation cycling, plastic deformation and defect generation lead to accumulation of internal stresses, which in turn contributes to the increase in martensitic transformation temperatures (ΔM_s and ΔA_f in Table 5.1), more than 50°C prior to the fatigue failure. The corresponding evolution of transformation temperatures with the applied stress level for the first and last cycles of the strain vs. temperature responses of the $\text{Ni}_{50.3}\text{Ti}_{29.7}\text{Hf}_{20}$ HTSMA is provided in Figure 5.4. One clear observation in this figure is the large shift in M_s and A_f temperatures during thermal cycling under stress, while M_f and A_s temperatures stay almost constant until failure, indicating that the transformation range (A_f - M_f) extends significantly throughout the cycling. This is the consequence of the localization of internal stress accumulation, i.e. defects that stabilize martensite and lead to internal stress accumulation are localized, and those defect regions are where the austenite to martensite transformation starts and the martensite to austenite transformation ends, due to the local high stress levels.

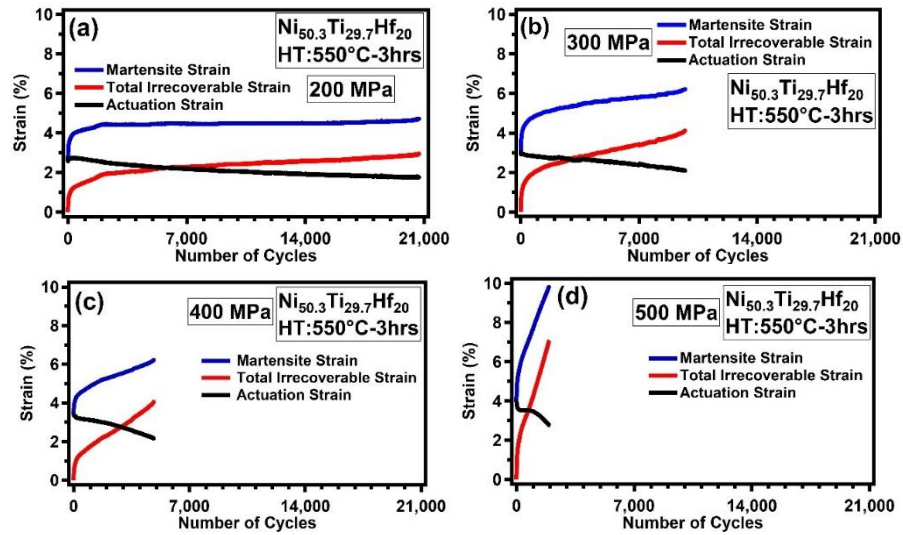


Figure 5.3 Evolution of the martensite strain, total irrecoverable strain, and actuation strain as a function of the number of thermal cycles until failure for the nano-precipitation hardened $\text{Ni}_{50.3}\text{Ti}_{29.7}\text{Hf}_{20}$ HTSMA, heat treated (HT) at 550°C for 3 hours, under (a) 200 MPa, (b) 300 MPa, (c) 400 MPa and (d) 500 MPa tensile stress levels. " Reprinted with permission from [50]. "

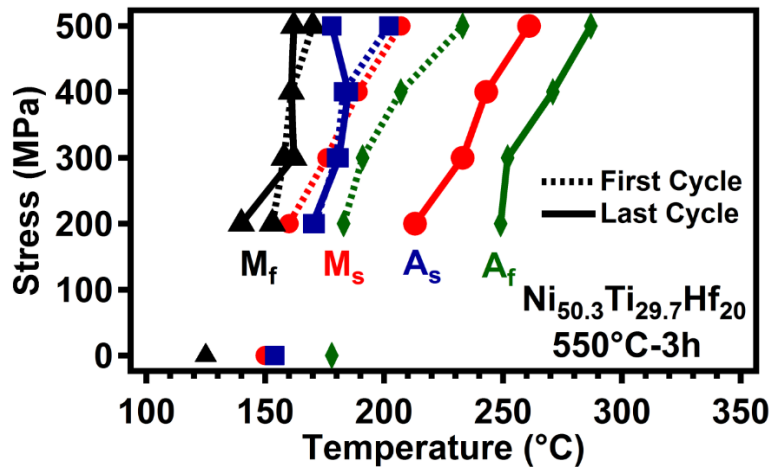


Figure 5.4 Evolution of martensitic transformation temperatures as a function of stress level in the first and last cycles of the actuation fatigue experiments for the nano-precipitation hardened $\text{Ni}_{50.3}\text{Ti}_{29.7}\text{Hf}_{20}$ HTSMA demonstrating large shifts in M_s and A_f temperatures while almost constant M_f and A_s temperatures. " Reprinted with permission from [50]. "

5.3 Post-Mortem Analysis- DSC and SEM Results

Figure 5.5 (a), (b) and (c) illustrate the changes in transformation temperatures and transformation heat of the fatigue specimens prior to and following the actuation fatigue experiments under different stress levels. The corresponding values extracted from the DSC results are summarized in Table 5.2. In order to ensure the reliability of the results, all DSC samples were cut 3 mm away from the fracture surfaces of the failed samples. Large reduction of almost 50 % in latent heat of transformation was observed after the fatigue tests. Transformation temperatures of the failed specimens, particularly M_s and A_f , increased in comparison to the stress-free transformation temperatures prior to the fatigue tests, which was also clearly observed in the strain-temperature responses of the specimens, discussed in the previous section. The results show that the thermal cycling under stress causes the transformation peaks and transformation range to get wider, indicating the evolution of microstructural inhomogeneity. Figure 5.5 (c) demonstrates the difference between pre- and post-fatigue M_s temperatures, where an increasing trend in M_s ($\Delta M_s = M_s^{\text{after fatigue}} - M_s^{\text{before fatigue}}$) was observed with increasing number of cycles to failure for the stress levels ranging from 300 to 500 MPa. The specimens loaded under 200 MPa, however, slightly deviated from this trend since less amount of internal stresses was accumulated compared to the other selected stress levels [46, 66, 179] .

Fracture surfaces of the failed specimens are illustrated in Figure 5.6 (a)-(d), where the failure mode appears to be intergranular fracture for the specimens loaded at 500 MPa and transgranular fracture for the samples under 200 MPa. A mixed fracture mode was

prevalent in the case of 300 MPa. Based on the actuation fatigue and fractography results one can conclude that higher stress levels favor intergranular fracture leading to rapid failure, while transgranular fracture facilitates failure in the case of lower stress levels promoting relatively longer fatigue lives.

Figure 5.6 (e) and (f) present the backscattered scanning electron (BSE) micrographs on the side surfaces near the fracture surface, where many cracks ranging from 5 to 200 μm in size are visible for the two extreme stress cases (200 MPa and 500 MPa). It can be clearly seen that failure occurs when a certain amount of crack density is attained. However, it was noted that the specimens cycled under 500 MPa have slightly larger crack sizes than the samples loaded at 200 MPa. Higher stress level facilitates formation of cracks, which promotes higher irrecoverable strains and shorter fatigue lives.

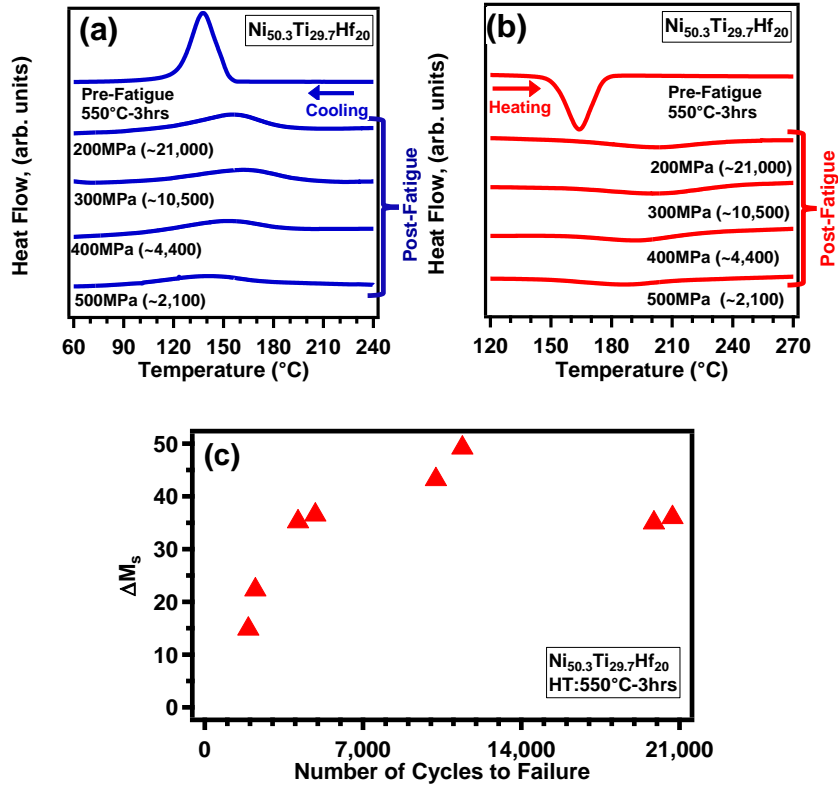


Figure 5.5 Post-mortem DSC results exhibiting changes in transformation heat and martensitic transformation temperatures of the fatigue failed specimens as compared to the initial nano-precipitation hardened Ni_{50.3}Ti_{29.7}Hf₂₀ HTSMA samples: (a) heating and (b) cooling DSC curves of the samples before and after fatigue failure under different stress levels, and (c) the corresponding evolution of M_s temperatures of these fatigue specimens relative to that of an untested specimen. $\Delta M_s = M_s^{after\ fatigue} - M_s^{before\ fatigue}$. " Reprinted with permission from [50]. "

5.4 Discussion of The Results

To better understand the role of applied stress level on the cyclic evolution of the actuation behavior, Figure 5.7 is constructed to present the evolution of actuation strain as a function of the number of thermal cycles under the stress levels ranging from 200 to 500 MPa. The difference between the austenite and martensite strains are defined as the actuation strain for each cycle. As expected in NiTiHf HTSMAs [2, 4], the higher

constant stress levels during actuation cycling result in higher initial actuation strain values since more oriented / detwinned martensite forms under these stresses. Following the high actuation strains of more than 3%, a rapid reduction in actuation strain was observed in the early stages of thermal cycling under 400 and 500 MPa. The specimens loaded under 200 and 300 MPa, on the other hand, exhibited a continuous and almost linear decrease in actuation strain until failure. This discrepancy in the rate of reduction in actuation strain for the two extreme stress cases is related to the difference between their initial martensitic transformation temperatures consistent with the Clausius-Clapeyron (CsCl) relation. According to the CsCl relation, higher stress levels correspond to higher martensitic transformation temperatures [130, 180]. In addition, in most SMAs, higher applied stresses lead to faster increase in transformation temperatures with the number of thermal cycles as compared to the lower stress levels [23, 24, 27, 162]. The combination of these two effects causes the faster onset of partial transformation under higher stress levels during thermal cycling, in the presence of constant upper cycle temperature of cycling, and thus more rapid initial reduction in the actuation strain is observed under 400 and 500 MPa.

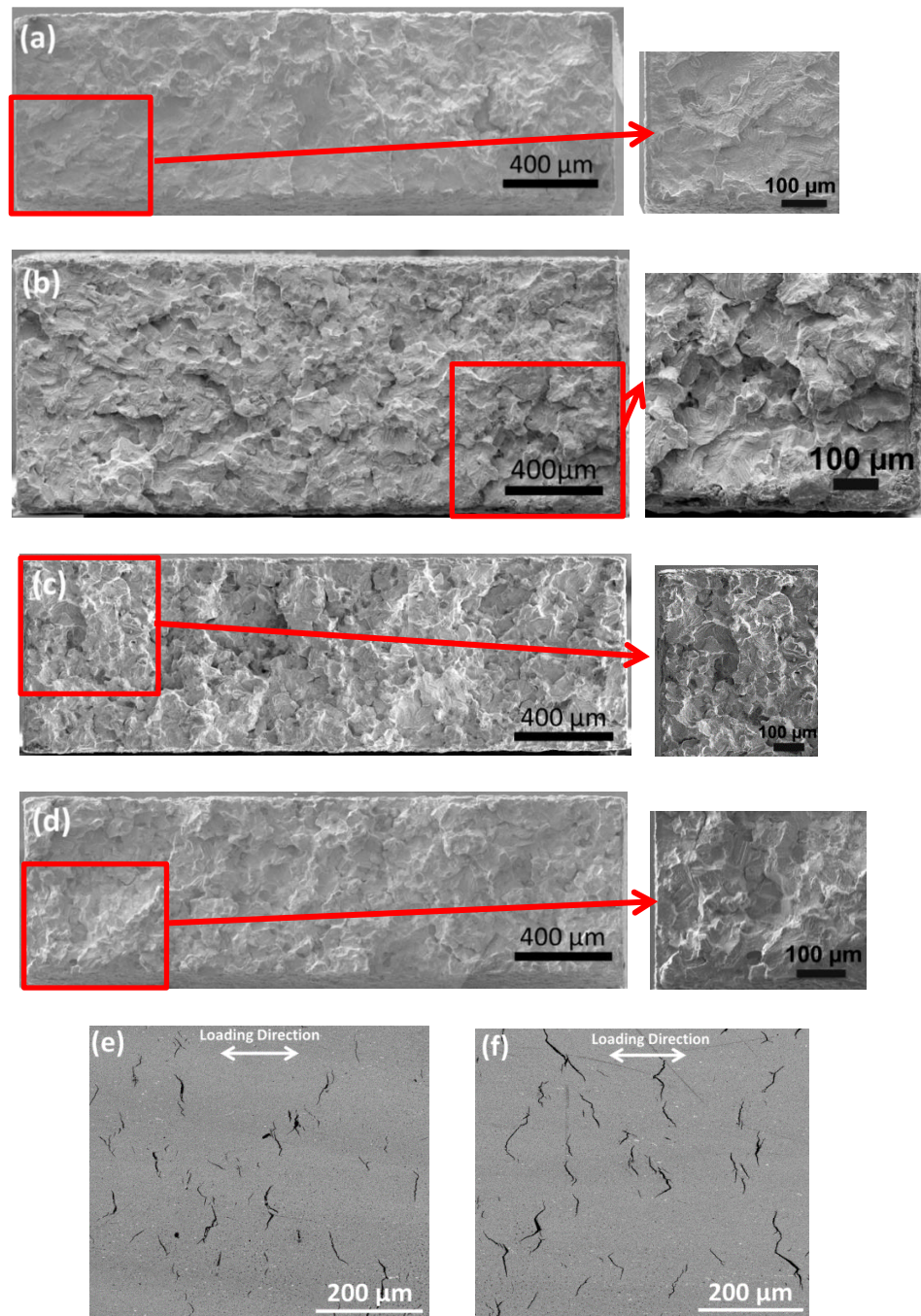


Figure 5.6 Backscattered scanning electron micrographs of the fracture surfaces of the nano-precipitation hardened $\text{Ni}_{50.3}\text{Ti}_{29.7}\text{Hf}_{20}$ HTSMA specimens after failure during the actuation fatigue experiments under (a) 200 MPa, (b) 300 MPa, (c) 400 MPa and (d) 500 MPa. Cracks detected in the interior sections of the failed specimens for (e) 200 MPa and (f) 500 MPa. The arrows in (e) and (f) indicate the loading direction of the specimens. " Reprinted with permission from [50]. "

Relatively slower reduction in actuation strain under 200 and 300 MPa from the onset of thermal cycling, and under 400 and 500 MPa following the rapid initial reduction is a result of the continuous dislocation and other defect generation upon repeated martensitic transformation. These defects lead to oriented internal stress accumulation, which increases the martensite start and austenite finish temperatures in localized regions, as also inferred from the DSC results mentioned above. This eventually brings about more remnant martensite at the upper cycle temperature with further cycling, the reduction in transforming volume in subsequent cycles, and thus, the actuation strain. Higher stresses cause faster accumulation of defects during actuation cycling, as compared to lower stress levels, resulting in a faster reduction in the volume of austenite transforming into martensite. This is why the slope of the reduction in actuation strain in Figure 5.7 is a function of the applied stress level.

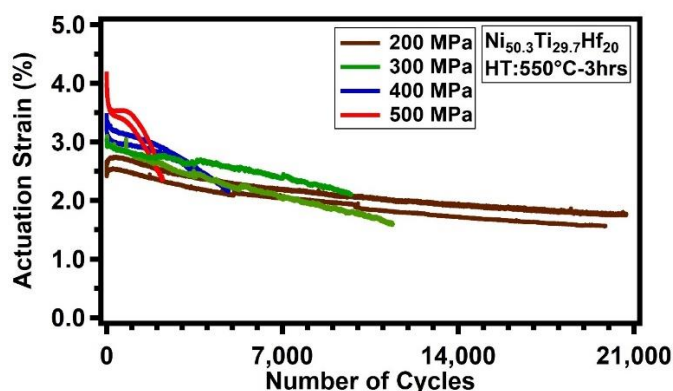


Figure 5.7 Effect of constant tensile stress level on the evolution of actuation strain as a function of the number of thermal cycling in the $\text{Ni}_{50.3}\text{Ti}_{29.7}\text{Hf}_{20}$ HTSMA samples aged at 550°C for 3 hrs during the actuation fatigue experiments. Lower and upper cycling temperatures were 40°C and 300°C , respectively. The results from two different samples are presented here to demonstrate the relatively small sample to sample variation in actuation strains and fatigue lives. " Reprinted with permission from [50]. "

It should be noted here that the effects of applied stress on the evolution of actuation strain and the resulting fatigue lives, presented in Figure 5.7, are reliable since the sample to sample variations were relatively small, as it can be seen in the Figure 5.7 and Figure 5.8. Overall, the current experimental results reveal that applied stress dictates both the number of cycles to failure and the evolution of actuation strain (Figure 5.8) during actuation fatigue experiments for a constant upper cycle temperature of thermal cycling.

The average actuation strain shown in Figure 5.8 was calculated as the sum of actuation strain per cycle divided by the number of cycles to failure. Samples loaded at 200 MPa exhibited 2.15 % average actuation strain while increase in stress level to 500 MPa led to 3.22 % average actuation strain. The actuation strain is the consequence of the strain from detwinning/reorientation of martensite upon the transformation, and it increases as a function of the increase in applied stress due to the higher volume fraction of the reoriented / detwinned martensite. As opposed to binary NiTi, the transformation / actuation strains in NiTiHf HTSMAs do not saturate even under very high stress levels as detwinning / reorientation in these alloys is significantly more difficult than detwinning in NiTi binary SMA compositions [4, 66, 181, 182].

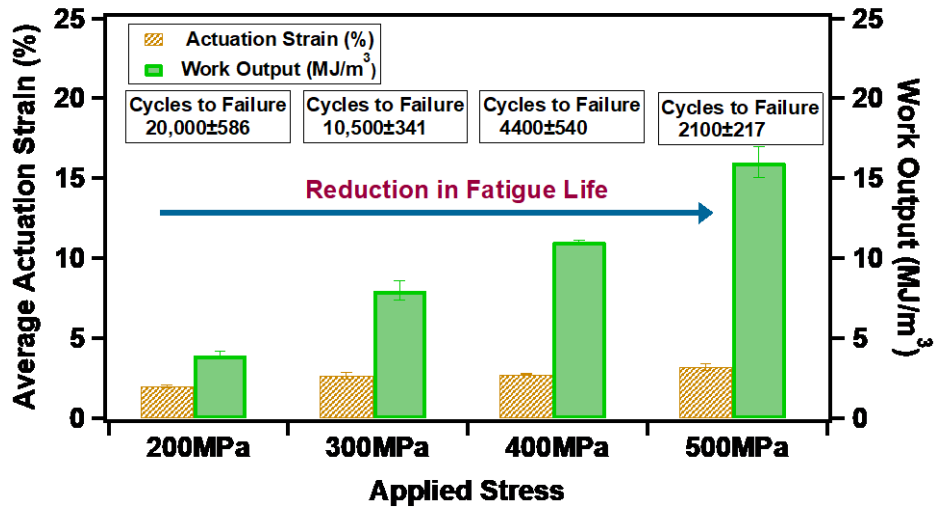


Figure 5.8 Comparison of the average actuation strains, average work output levels, and fatigue lives as a function of the applied tensile stress levels during actuation fatigue experiments on nano-precipitation hardened Ni_{50.3}Ti_{29.7}Hf₂₀ HTSMA, heat treated at 550°C for 3 hrs. The error bars represent the sample to sample variations. " Reprinted with permission from [50]. "

In order to correlate the actuation characteristics and applied loading conditions to the actuation fatigue lives in NiTiHf HTSMAs, and eventually to be able to predict the fatigue lives, a work-based approach has been adopted as an alternative to stress- and strain-based methods to fatigue life estimation. This is because of the fact that neither the strain- nor stress-based fatigue prediction methods properly capture the actuation fatigue behavior of SMAs, as shown by Calhoun *et al.* [129, 175] for low temperature SMAs. Accordingly, the average work output vs. fatigue life data for the present material are shown in Figure 5.9, in comparison with the published actuation fatigue results for low temperature SMAs. In the work-based approach, actuation lifetime (N_f) is correlated with the actuation work output in each actuation fatigue cycle through a power law formulation based on the critical plane model of Smith, Watson and Topper [183]. The

work-based model is described as $\sigma_{act}\epsilon_{act} = aN_f^{-b}$ [129, 175], where the average actuation strain (ϵ_{act}) multiplied by the applied constant stress level (or actuation stress, σ_{act}) from the actuation fatigue experiments represents the average work output for actuation cycles. The model utilizes two empirical fatigue parameters a and b that relate the work output to number of cycles to failure (N_f). In this formulation, an increase in the proportionality constant a corresponds to an increase in the reduction in work output with fatigue life, which refers to cyclic deterioration of the functional properties at a higher rate. Similarly, a higher rate of cyclic deterioration of the work output is implied by an increased power exponent b .

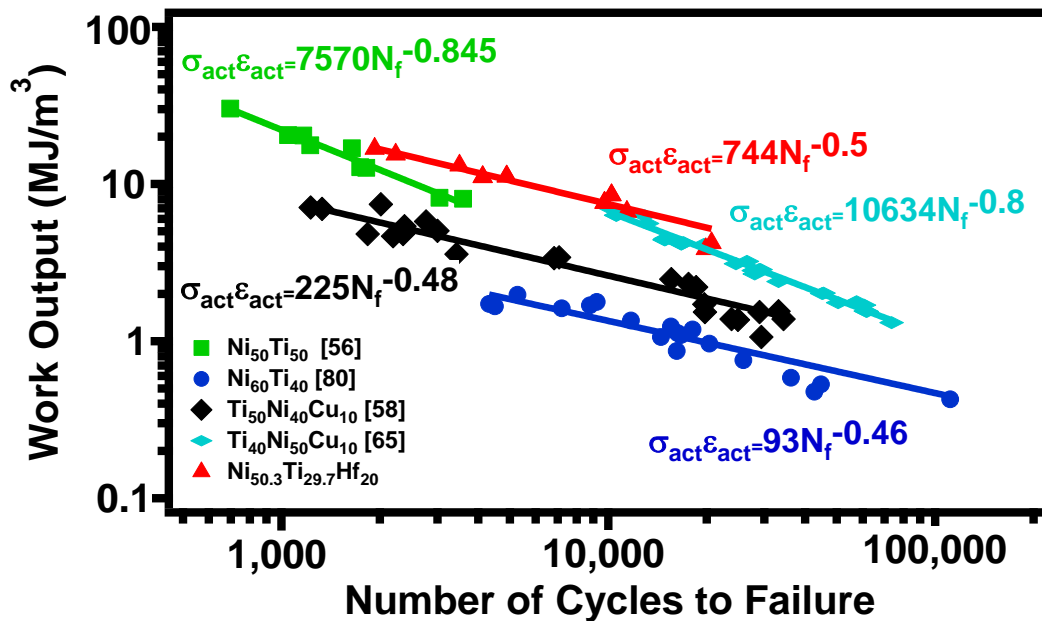


Figure 5.9 A comparison of the work output vs. fatigue life results obtained from $\text{Ti}_{50}\text{Ni}_{40}\text{Cu}_{10}$ wires [130], bulk $\text{Ni}_{50}\text{Ti}_{50}$ [128], bulk $\text{Ni}_{60}\text{Ti}_{40}$ [184], $\text{Ti}_{40}\text{Ni}_{50}\text{Cu}_{10}$ wires [47], and bulk nano-precipitation hardened $\text{Ni}_{50.3}\text{Ti}_{29.7}\text{Hf}_{20}$ HTSMAs. The solid lines and the equations next to them are the best fit lines of the data presented to the power-law relationship $\sigma_{act}\epsilon_{act} = aN_f^{-b}$. " Reprinted with permission from [50]. "

The correlations provided by this method are presented in Figure 5.9 for the present NiTiHf HTSMA data in comparison with the power law fits to the above equation for the actuation fatigue results reported in the literature for low temperature binary NiTi and NiTiX SMAs [47, 128, 130, 158]. The provided results in the literature were obtained from both small wires and dog-bone shaped samples. It is clear from the figure that the work-based model can successfully capture the actuation fatigue response of both low and high-temperature SMAs. Based on these power law fits, the exponent b was determined to be either ~ -0.5 or ~ -0.8 . The physical significance of and the reasons for observing these two discrete values in completely different SMAs are currently unknown. More actuation fatigue experiments are presently being conducted in different SMAs to further investigate the physical significance of these values. However, the fact that there is a very good fit to several experimental data with the same power law exponents, capturing the actuation fatigue behavior of SMAs very well, make us believe that there might be a universal empirical rule for describing the actuation fatigue response of SMAs. We speculate that the fatigue exponent b might be correlated with the resistance to plastic deformation, accompanying martensitic transformation, as the main difference between the alloys having $b \approx -0.8$ and those with $b \approx -0.5$ is the former alloys having lower yield strength against plasticity than the latter alloys. The latter alloys are either strengthened with precipitates or have smaller grain size or strong crystallographic texture.

For the present material, the parameter a and the exponent b were determined to be 744 MJ/m^3 and -0.5 , respectively. Interestingly, the $\text{Ni}_{50.3}\text{Ti}_{29.7}\text{Hf}_{20}$ HTSMA cycled under

500 MPa exhibits outstanding fatigue performance with a 16 MJ/m^3 energy density. The work outputs and fatigue lives attained by the present NiTiHf HTSMA is superior to those exhibited by the several low temperature SMAs, even though the operating temperatures are significantly higher.

5.5 Effects of Stress Level on Irrecoverable Strain

As opposed to conventional metal alloys where they are cyclically loaded to stress levels considerably lower than their yield strengths during fatigue loading, SMA actuators usually operate in an elastic loading range, however, through cyclic martensitic phase transformations. The distinguishing feature of SMAs in comparison to conventional metal alloys is that repeated cyclic martensitic transformation can cause local plastic deformation, even if the stress levels applied can be significantly lower than the stress required for global dislocation plasticity in SMAs. This permanent deformation usually occurs due to the incompatibility between the transforming phases, which causes the inelastic accommodation of the transformation shear. Therefore, the accumulation of plasticity, even it might be very small, is unavoidable in HTSMA actuators. The corresponding irrecoverable strain represents the remnant shape change that cannot be recovered through shape memory effect, upon heating to the selected upper cycle temperature.

To better quantify the role of applied stress on the evolution of irrecoverable strain as a function of the number of cycles and on the level of total irrecoverable strain at failure, Figure 5.10 is constructed to provide a comparison. As it can be seen in the figure, the irrecoverable strain levels increased with each subsequent cycle and attained a maximum

value of 2.96 % and 6.76 % prior to failure at applied stress levels of 200 MPa and 500 MPa, respectively. The irrecoverable strain accumulated quickly within the first few hundred cycles for both extreme cases, and then started to stabilize for specimens under 200 MPa, however, continued to accumulate at a certain rate for specimens subjected to 500 MPa. The accumulation of irrecoverable strain was also observed for other stress levels and did not fully saturate until failure. The rate of accumulation of the irrecoverable strain is notably higher under 400 MPa and 500 MPa as compared to the lower stress levels. Specifically, dislocations and other defects generated during the cycling under high stress levels reduce the amount of austenite transforming into martensite due possibly to remnant martensite, leading to larger irrecoverable strains, and eventually earlier failure.

5.6 Calorimetric Results and Phase Transformation Behavior

Based on the DSC results, the changes in the heat flow curves for the transformation prior to and following the fatigue experiments are provided for different stress levels in Figure 5.5 (a) and (b), and the list of corresponding transformation temperatures and transformation heat values are tabulated in Table 5.2. It can be observed in the figures and the table that the failed samples possess higher M_s and A_f temperatures as compared to the stress-free initial transformation temperatures, regardless of the applied stress level. Furthermore, the reduction of the transformation heat was observed in all failed samples. As seen in the figure, the discernible peaks in the heating and cooling curves almost disappeared following actuation cycling. For example, the transformation heat dropped from 18 Jg^{-1} to about 10 Jg^{-1} for the sample cycled under 400 MPa,

corresponding to a 45 % reduction, which stems from the reduction in the transforming volume at the selected upper cycle temperature, due to the remnant martensite and formation of defects. This is consistent with previous reports on low temperature SMAs by Miller *et al.* [46] and Lim *et al.* [185] that the martensite remains pinned in the microstructure due to the defects generated and internal stresses accumulated during the actuation cycling, resulting in a drop in the latent heat of transformation due to less material undergoing the transformation. Note that as demonstrated in our earlier work [186], the upper cycle temperature of thermal cycles play a significant role in the accumulation of the irrecoverable strain, the amount of transforming volume, and thus, the actuation fatigue lives; therefore, the changing the upper cycle temperature from 300°C of the current study to a higher temperature would influence the most of the actuation characteristics reported here.

Another notable observation in Figure 5.5 is the significant increase in the transformation range, i.e. A_f - M_f . The defects induced and cracks formed towards the later stages of the cycling cause microstructure to heterogeneously undergo martensitic transformation. While part of the microstructure undergoes martensitic transformation at higher temperatures due to localized accumulation of internal stresses, the remainder of the microstructure transforms at colder temperatures, and hence, the calorimetric transformation curves for cooling and heating become broader after the actuation fatigue failure.

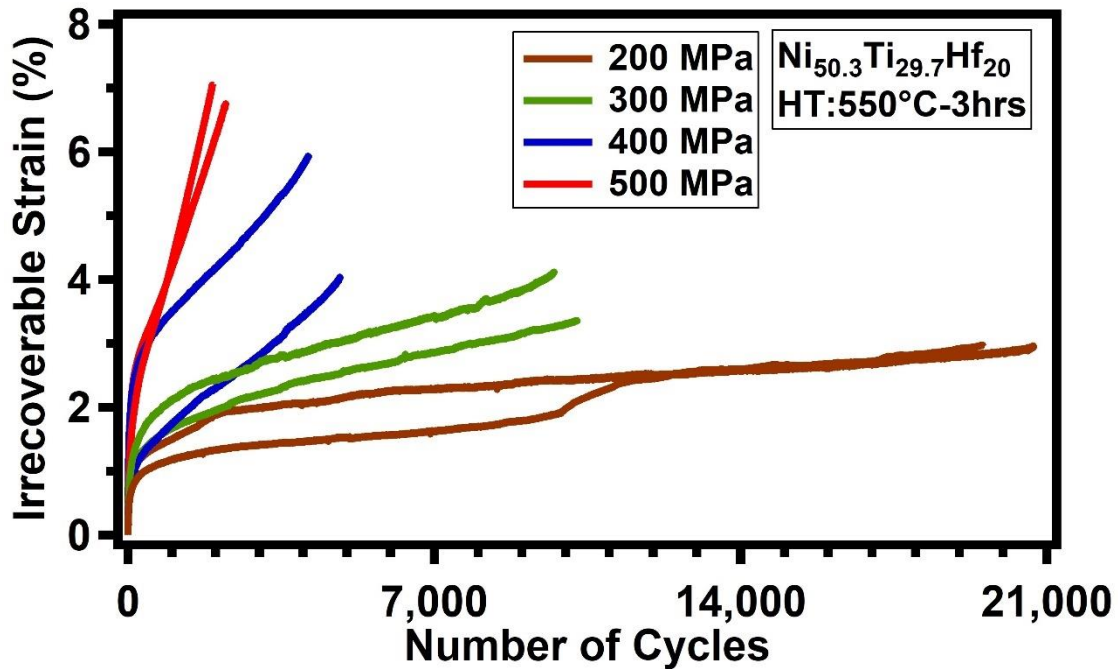


Figure 5.10 Effect of applied stress level on the evolution of the irrecoverable strain until failure upon thermal cycling of the nano-precipitation hardened $\text{Ni}_{50.3}\text{Ti}_{29.7}\text{Hf}_{20}$ HTSMA heat treated at 550°C for 3 hrs. " Reprinted with permission from [50]. "

Figure 5.5 (c) depicts the evolution of M_s temperature comparing pre-test and post-test results, represented as $\Delta M_s = M_s^{\text{after fatigue}} - M_s^{\text{before fatigue}}$: there is a clear trend in the increase of the onset of the transformation with the number of cycles to failure for specimens tested under stresses ranging from 500 MPa to 300 MPa. However, specimens cycled under 200 MPa significantly deviated from the observed trend. This deviation is a consequence of less amount of defects forming under this stress level as compared to the defects generated under 300 MPa. Under 200 MPa, the actuation strain is lower, less oriented martensite forms at each cycle, and thus, lower level of oriented internal stress accumulates leading to the less increase in the M_s temperature despite the higher number of cycles to failure.

5.7 Failure Mechanisms

From the SEM images showing the fracture surfaces of the failed samples in Figure 5.6, it can be seen that the higher stress level (500 MPa) favored intergranular cracking where fracture took place along the grain boundaries, as evidenced by the rock-candy and faceted fracture surface appearance, and apparent triple points [173]. When the samples were cycled under low stress level (200 MPa), transgranular cracking was more favorable, as identified by river patterns, cleavage steps and feather markings (Figure 5.6). Following the failure of specimens cycled under 200 MPa and 500 MPa, specimen surfaces close to fracture zone were polished to remove recast and oxide layer formed upon heat treatment, and thereafter the crack analysis was performed on the specimen surfaces as shown in Figure 5.6 (e) and (f). The SEM images showed that cracks formed perpendicular to applied stress direction and were distributed uniformly across the sample. The corresponding crack size ranged between 5-200 μm . Even though the crack density appears similar just prior to failure for two extreme cases, the specimens cycled under 500 MPa featured slightly wider and longer cracks as compared to the specimens cycled under 200 MPa. It is noted that $\text{Ni}_{50.3}\text{Ti}_{29.7}\text{Hf}_{20}$ material aged at 550 °C for 3 hours are prone to large amount of crack formation prior to failure under all selected stress levels, yet the higher stress levels facilitated formation of longer cracks, leading to earlier failure of specimens.

5.8 Summary and Conclusions

The primary objective of this study was to evaluate the effect of stress level on the cyclic actuation response and fatigue performance of the $\text{Ni}_{50.3}\text{Ti}_{29.7}\text{Hf}_{20}$ high temperature

shape memory alloy (HTSMA). Tensile specimens heat treated at 550 °C for 3 hours were subjected to actuation fatigue experiments, under different constant stress levels ranging from 200 to 500 MPa, while cycling the temperature across the martensitic transformation between 40°C and 300°C. Based on the experimental results presented herein, the main observations and conclusions can be summarized as follows:

- The applied stress level has a significant influence on the actuation response of nano-precipitation hardened HTSMAs, particularly on the actuation strain, fatigue life and irrecoverable strain. Increase in the stress level resulted in a decrease in fatigue life but at the same time an increase in the actuation strain. In particular, the specimens cycled under 200 MPa achieved 21,000 cycles while samples loaded at 500 MPa survive only 2,100 cycles on the average. The experimental results showed that the actuation strain attained a maximum value of 3.22% under 500 MPa, whereas the minimum actuation strain was recorded under 200 MPa, namely 2.15 %, on the average.
- Saturation of irrecoverable strain was not observed during the actuation fatigue experiments up to the failure, regardless of the applied stress level. Substantial irrecoverable strain accumulation was monitored during the cycling. Specifically, the samples cycled under 500 MPa exhibited large irrecoverable strain accumulation (6.76 %) within a relatively short fatigue life. Tensile specimens loaded under 200MPa, on the other hand, experienced irrecoverable strain accumulation of about 2.96 %, and are considered durable against dimensional instability.

- DSC results of the fatigue failed samples displayed a large reduction in the transformation heat. Dislocations and other defects generated during the cycling led to the retention of martensite in the austenite phase at the selected upper cycle temperature, and thus, prevented a portion of the sample undergoing martensitic transformation and resulted in the drop of the transformation heat. Reduction in actuation strain with the number of actuation cycles is also an indication of the reduction in the available volume for the transformation. Therefore, the M_s temperature increased concomitant with the number of cycles to failure as a consequence of oriented internal stresses accumulated during actuation cycling for the stress levels ranging between 300 -500 MPa.
- Transgranular fracture was prevalent when the sample was loaded at 200 MPa, as characterized by river patterns and cleavage steps. However, specimens cycled under 500 MPa exhibited intergranular fracture as identified rock-candy appearance and triple points across the grain boundaries. The SEM images proved that both extreme stress levels of 200 and 500 MPa facilitated the formation of similar volume fractions of cracks throughout the specimens, pointing out that failure takes place only when specimen reaches certain amount of crack density.
- Precipitation hardened $Ni_{50.3}Ti_{29.7}Hf_{20}$ HTSMA aged at 550 °C for 3 hours exhibited a significantly high work output of 16 MJ/m³ when thermally cycled under the stress level of 500 MPa, dimensional stability up to more than

21,000 cycles when cycled under 200 MPa, and an impressive cyclic stability as compared to NiTi binary SMAs. The fact that these outstanding properties were achieved at much higher operating temperatures than the NiTi SMAs, the current $\text{Ni}_{50.3}\text{Ti}_{29.7}\text{Hf}_{20}$ HTSMA emerges as a promising actuator material suitable for service at elevated temperatures.

- In order to accurately capture the actuation fatigue response of HTSMAs in this study, a work-based fatigue life prediction approach was adopted and demonstrated that the actuation fatigue lives of the present HTSMA exhibit an almost perfect power law correlation with average actuation work output. The same work-based power law was shown to successfully capture the fatigue lives of several low temperature SMAs, as well. Surprisingly, the power law exponents for many SMAs were shown to be either ~ -0.5 or ~ -0.8 , which points out the likelihood of the existence of a universal empirical rule for predicting actuation fatigue lives of SMAs. The power law exponent can be correlated with the strength of SMAs against plastic deformation accompanying reversible martensitic transformation.

CHAPTER VI
EFFECTS OF UPPER CYCLE TEMPERATURE ON THE
THERMOMECHANICAL FATIGUE PERFORMANCE OF NITIHf HIGH
TEMPERATURE SHAPE MEMORY ALLOYS*

The present study focuses on the effects of upper cycle temperature (UCT) on thermo-mechanical cyclic behavior and fatigue response of nano-precipitation hardened Ni_{50.3}Ti_{29.7}Hf₂₀ high temperature shape memory alloy (HTSMA). A series of actuation fatigue experiments were conducted under different constant tensile stresses while cycling temperature between two extreme martensitic transformation temperatures. The cyclic evolution of actuation strain and fatigue lives were monitored as a function of UCT and applied stress level.

Despite the aforementioned advantages brought about by nano-precipitation, many of the envisaged applications also require a stable fatigue response and long fatigue lives, and thus, it is of utmost importance to assess the cyclic deformation response of NiTiHf high temperature SMAs (HTSMAs) at elevated temperatures. Even though numerous studies have been conducted on superelastic fatigue properties of SMAs [9-13], only a very few reports are available in the literature addressing their actuation fatigue response [14-17], and to the best of the authors' knowledge, none on the actuation fatigue response of HTSMAs. The present work was undertaken with the motivation of addressing this issue

* Reprinted with permission from “Effect of upper cycle temperature on the actuation fatigue response of NiTiHf high temperature shape memory alloys” by O. Karakoc, C. Hayrettin, M. Bass, S. J. Wang, D. Canadinc, J.H. Mabe, I. Karaman, 2017. Acta Materialia, 138, pp.185-197, Copyright 2017 by Acta Materialia Inc. published by Elsevier Ltd.

and providing the first systematic study on the actuation fatigue response HTSMAs, and more specifically, establishing a thorough understanding of the thermo-mechanical fatigue response of a nano-precipitation hardened NiTiHf HTSMA. In particular, the effects of upper cycle temperature (UCT) and stress level on the thermo-mechanical cyclic response and actuation fatigue life of the Ni-rich Ni_{50.3}Ti_{29.7}Hf₂₀ HTSMA were investigated, where nano-precipitates with sizes less than 50 nm lead to excellent reversibility of martensitic transformation and dimensional stability under thermo-mechanical loading [2-4, 26, 29].

Table 6.1. Evolution of transformation temperatures and enthalpies of nano-precipitation hardened Ni_{50.3}Ti_{29.7}Hf₂₀ HTSMAs following failure in the thermo-mechanical fatigue experiments. The measurements were conducted using DSC. The average values from two or three different failed fatigue samples are provided. DSC samples were cut from a region near the fracture surface. " Reprinted with permission from [161]. "

Stress Level and UCT	Transformation Temperatures (°C)				Hysteresis (A _f -M _s) (°C)	Transformation Enthalpy (J/g)
	M _f	M _s	A _s	A _f		
Initial Material	124.2	149.5	153.1	178.3	28.8	18.3
300MPa -300°C	104.6±12.6	209.3±13.3	150.4±1.7	250.6±11.0	41.3± 2.3	11.0±1.0
300MPa - 350°C	106.3±7.0	168.5±1.4	154.2± 9.9	218.5±0.5	50.0± 1.4	10.9± 0.2
400MPa - 300°C	98.6±4.2	187.3±8.1	145.3±4.0	223.4±4.0	36.1±5.5	10.4± 0.7
400MPa - 350°C	101.1±1.4	156.5±2.1	150.2±0.3	186.2±7.1	29.7±4.9	12.4±0.7

6.1. Initial Material Properties

DSC results and corresponding microstructure for the initial material heat treated at 550°C for 3 hours are shown in Figure 6.1 (a) and (b). This particular heat treatment was selected here because it leads to the best thermo-mechanical stability among many other

heat treatments applied to $\text{Ni}_{50.3}\text{Ti}_{29.7}\text{Hf}_{20}$ composition due to the perfectly coherent nano-precipitates [6, 7, 29, 187, 188]. Transformation temperatures M_f , M_s , A_s and A_f were measured as 124°C, 149°C, 153°C and 178°C, respectively. The heat of transformation was calculated from the area under the heating and cooling cycles, and found as approximately 18.3 J/g. The provided exemplary bright field image in Figure 6.1 (b) demonstrates the size and distribution of the H-phase precipitates [29] within the matrix upon aging the material at 550°C for 3 hours, leading to nano-sized (< 20 nm) and coherent precipitates.

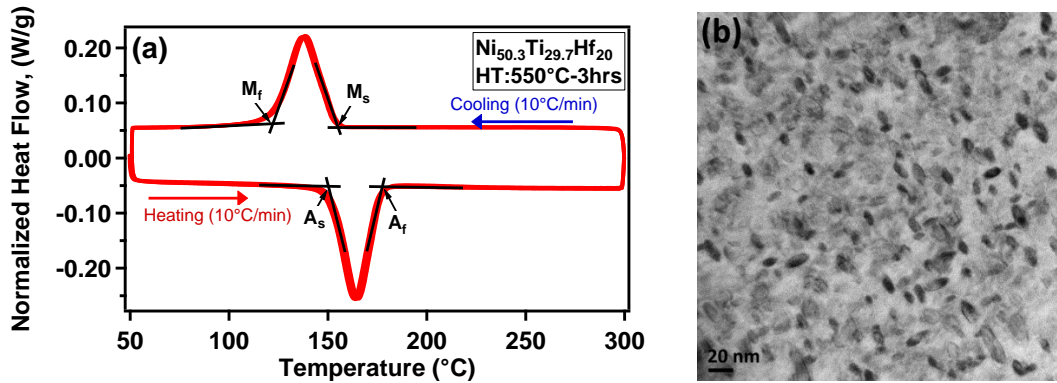


Figure 6.1. (a) DSC result for the $\text{Ni}_{50.3}\text{Ti}_{29.7}\text{Hf}_{20}$ specimen heat treated at 550°C for 3 hours and (b) the corresponding TEM image showing H-phase precipitates. HT:Heat Treatment. " Reprinted with permission from [161]. "

6.2. Thermo-Mechanical Fatigue Experiments

Figure 6.2 (a) and (b) indicate the strain vs. temperature response of the 550°C - 3 hours heat treated $\text{Ni}_{50.3}\text{Ti}_{29.7}\text{Hf}_{20}$ under two extreme conditions: 300 MPa stress - 300°C UCT and 400 MPa stress - 350°C UCT. The loading path shown in Figure 2.2 applied to the samples consisted of thermal cycles through the transformation temperatures, i.e. from $T < M_f$ to $T > A_s$, until fracture. The results exhibit development of plastic strain as

a function of number of cycles. Upon thermo-mechanical cycling, the total irrecoverable strain increased with increasing cycles until failure, and reached a maximum value of 3.39% and 4.11% for samples subjected to 300 MPa - 300°C UCT and 400 MPa - 350°C UCT, respectively. In addition, the hysteresis associated with martensite-austenite transformation is around 12°C for the first cycle and remains constant at failure cycle for 300MPa-300°C while it starts from 7°C and reaches to 18°C prior to failure in the case of 400MPa-350°C. In the figure, it can also be seen that the transformation temperatures evolve with the number of cycles. This change in transformation temperatures manifested itself in form of smaller shifts during 400 MPa - 350°C UCT test, while a more significant increase in the transformation temperatures was observed in the case of 300 MPa - 300°C UCT experiment, especially in the M_s and A_f transformation temperatures.

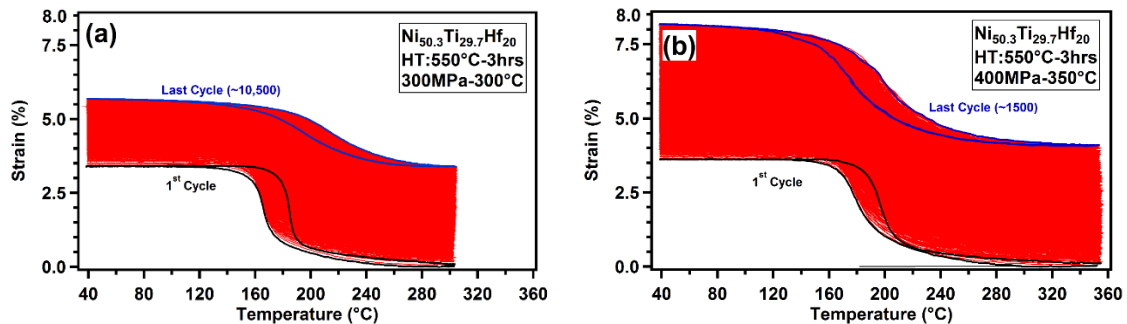


Figure 6.2. Strain vs. temperature curves for the nano-precipitation hardened $Ni_{50.3}Ti_{29.7}Hf_{20}$ HTSMA heat treated at 550°C for 3 hours under (a) 300 MPa with the UCT of 300°C and (b) 400MPa with the UCT of 350°C. UCT: Upper Cycle Temperature. " Reprinted with permission from [161]. "

Figure 6.3 (a) and (b) demonstrate the fatigue response for each specimen, in the form of actuation strain vs. the number of thermo-mechanical cycles. For each test condition,

two or three companion specimens were first mechanically loaded at room temperature, and then thermally cycled between 40°C and the corresponding UCT until the failure. It is immediately noted that the increase of UCT and stress level decreased the fatigue life while leading to larger average actuation strain. The highest number of cycles to failure of about 10,500 cycles was obtained for the specimens tested under 300 MPa - 300°C UCT, where the corresponding lowest average actuation strain was about 2.53%. In contrast, the specimens loaded under 400 MPa - 350°C UCT lasted about 1,530 cycles to failure, exhibiting the highest average actuation strain of 3.92%. The corresponding cyclic evolution of the irrecoverable strain is presented in Figure 6.4. In the figure, increase in stress level and higher UCT promote plastic deformation during thermal cycling, such that the irrecoverable strains, i.e. the strain in austenite state that cannot be recovered, increase concomitant with number of cycles. In order to demonstrate the UCT dependence, additional fatigue tests were carried out at 250 °C and 375°C, and the results are presented in Figure 6.13.

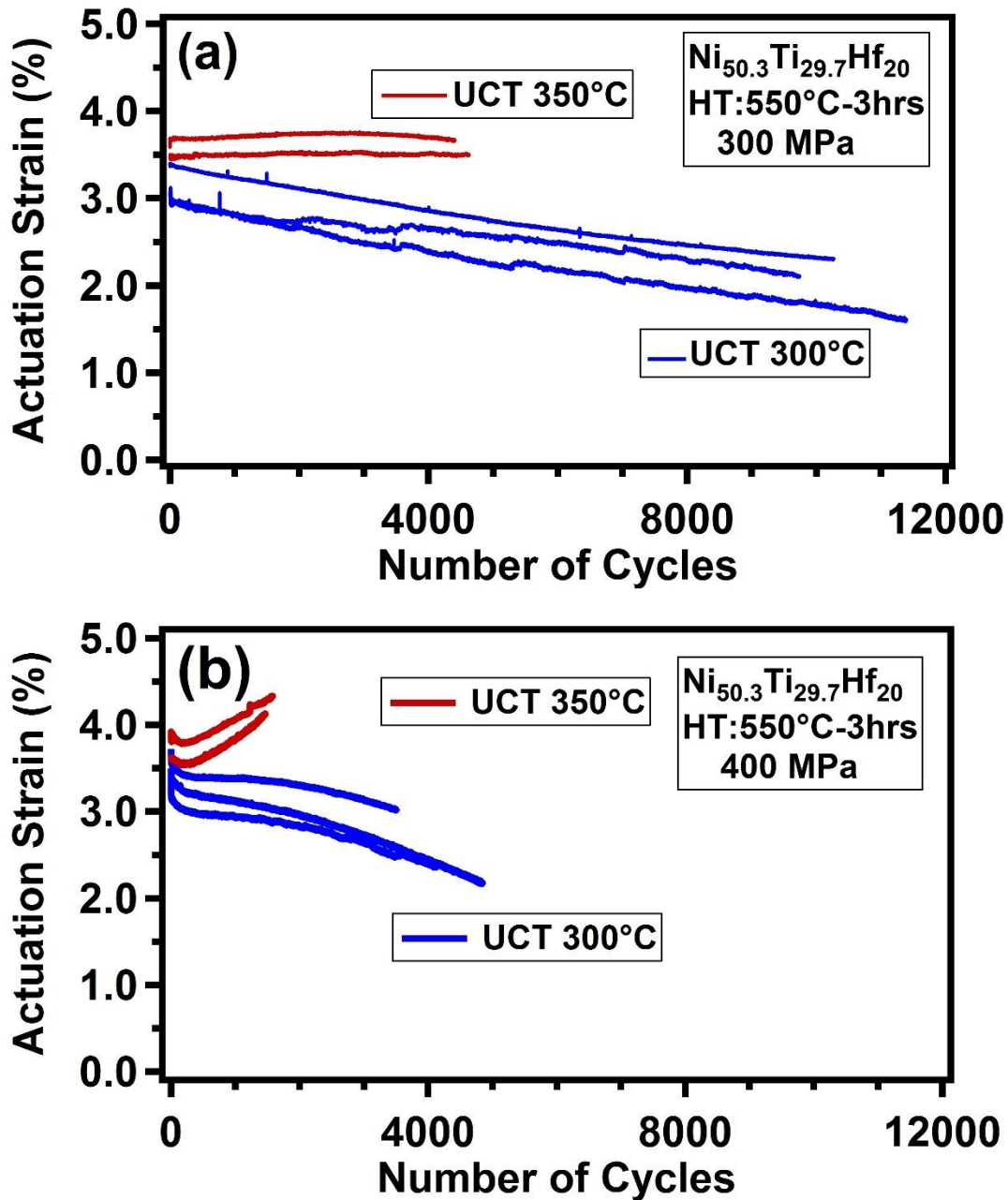


Figure 6.3. Effect of upper cycle temperature (UCT) on the actuation fatigue response of the nano-precipitation hardened $\text{Ni}_{50.3}\text{Ti}_{29.7}\text{Hf}_{20}$ HTSMA heat treated at 550°C for 3 hours under (a) 300 MPa and (b) 400 MPa constant stress levels. HT: Heat Treatment. " Reprinted with permission from [161]. "

6.3. Post-Mortem Characterization – DSC Results

DSC results prior to and following the fatigue experiments are presented in Figure 6.5 (a), (b) and (c) in a comparative manner, demonstrating the evolution of transformation temperatures and latent heat of transformation, which are also summarized Table 1. The DSC samples from the fatigued specimens were cut 3 mm away from the fracture surface for all cases. As seen in Figure 6.5 (a) and (b), and Table 1, the transformation temperatures (M_s and A_f) increased during thermal cycling, while latent heat of transformation decreased. Furthermore, the transformation peaks got broader, such that a discernible peak was not obvious in some cases. As seen in Figure 6.5 (c), the difference between the initial and post-fatigue M_s temperatures increased concomitant with the number of cycles, following a noticeable pattern with the applied stress level and UCT.

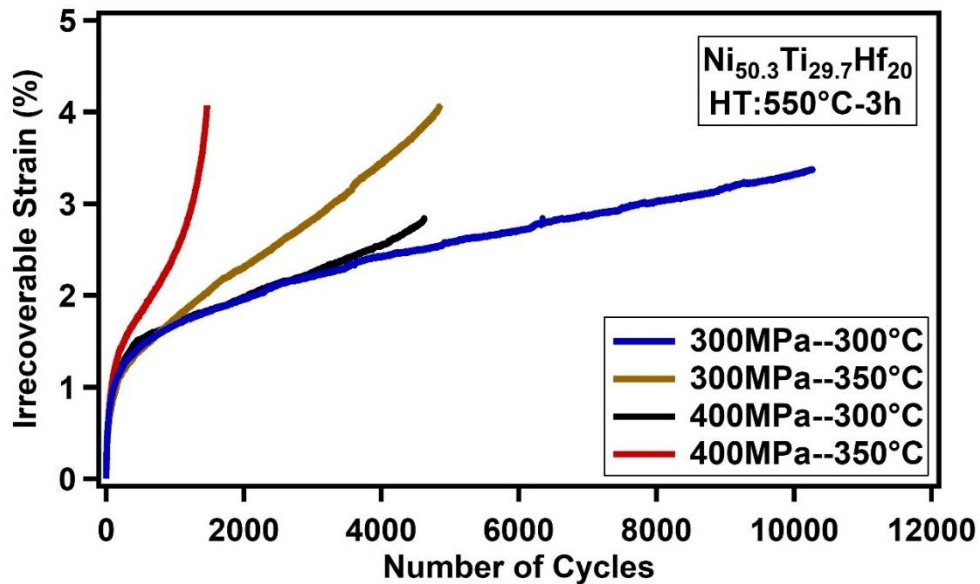


Figure 6.4. Evolution of the irrecoverable strain upon thermo-mechanical cycling of nano-precipitation hardened $Ni_{50.3}Ti_{29.7}Hf_{20}$ HTSMA (heat treated at $550^{\circ}C$ for 3 hours) for the four stress - UCT combinations employed in the current experiments. " Reprinted with permission from [161]. "

6.4. Post-Mortem Characterization – SEM and TEM Results

The post-fatigue failure characterization of the samples involved examination of side surface cracks, fracture surfaces through SEM and evolution of precipitates by TEM. Examination of the fracture surfaces indicated that the crack growth mode was more intergranular for samples with shorter fatigue lives and more transgranular for specimens with longer fatigue lives, as illustrated in Figure 6.6(a), (b), (c) and (d). 400 MPa or 350°C UCT samples demonstrate more intergranular crack mode than the other cases. The side surface analysis revealed a slightly larger crack density for the specimens tested under 400 MPa - 350°C UCT as compared to those tested under 300 MPa - 300°C UCT (Figure 6.6(e) and (f)).

A detailed examination of the TEM results in different foils and images for each tested case indicated that the size and morphology of the H-phase nano-precipitates in the failed specimens are similar regardless of the induced stress -UCT condition during cycling when compared with the untested specimens (Figure 6.7 Figure 6.8). This indicates that the testing conditions did not noticeably change the precipitate size and structure in the fatigued samples, and thus, the change in the precipitates cannot be responsible for the change in the transformation characteristics observed in Figure 6.2 and Figure 6.5. Furthermore, the bright field images and corresponding diffraction patterns in martensite at room temperature demonstrated that all fatigued specimens exhibited (001)-compound twins and (011) Type I twins (Figure 6.10), in various grains, similar to what is observed in the untested specimens [29]. There was not a notable difference in the martensite phase, in terms of the type and amount of twins observed,

between the untested and fatigued samples, other than the fact that the fatigued samples featured more oriented martensite than the untested samples, as expected.

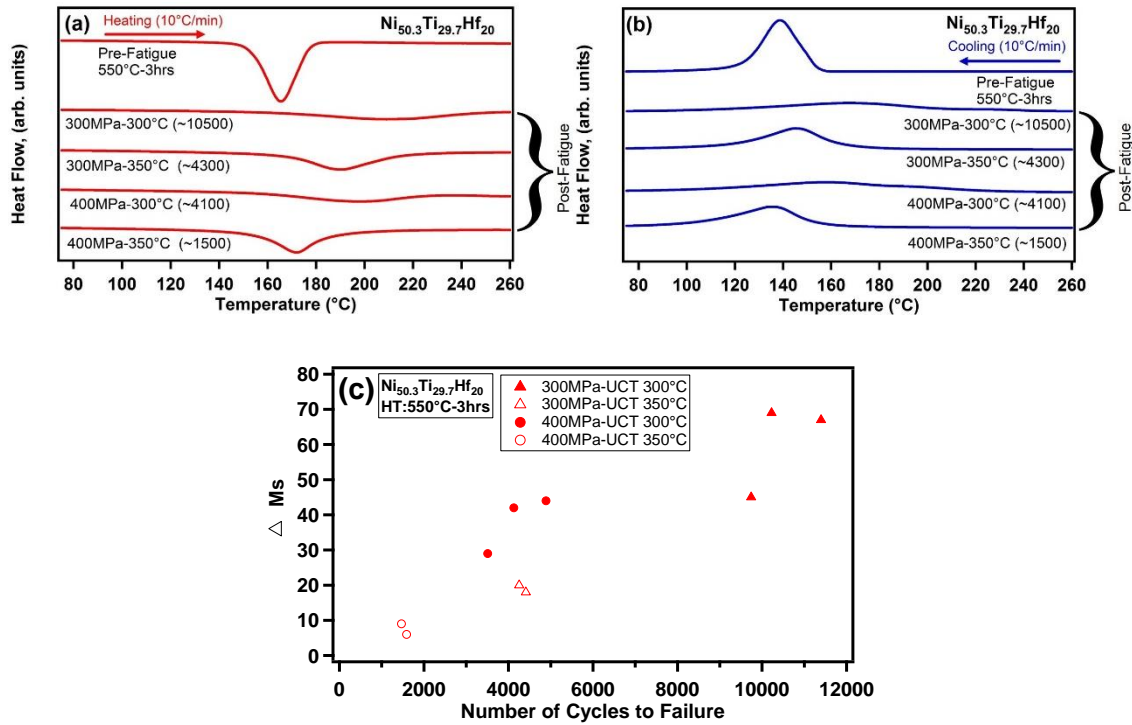


Figure 6.5. Post-mortem DSC results of nano-precipitation hardened $\text{Ni}_{50.3}\text{Ti}_{29.7}\text{Hf}_{20}$ HTSMA specimens, demonstrating the change in the transformation temperatures and heat of transformation after the thermo-mechanical fatigue experiments: (a) heating and (b) cooling DSC curves of pre- and post-fatigue samples, and (c) the corresponding evolution of M_s temperatures of these fatigue specimens relative to that of an untested specimen: $\Delta M_s = M_s^{\text{pro-fatigue}} - M_s^{\text{pre-fatigue}}$. The numbers in parentheses in (a) and (b) correspond the fatigue lives of those particular samples tested. " Reprinted with permission from [161]. "

6.5. Cyclic Evolution of Actuation Strain

Experimental isobaric strain-temperature results are presented for two extreme cases, namely 300 MPa - 300 $^{\circ}\text{C}$ UCT and 400 MPa - 350 $^{\circ}\text{C}$ UCT, in Figure 6.2, where the thermal cycles were applied until failure. While the initial irrecoverable strain response

evolved rapidly with each thermal cycle in both cases, the rate of increase stabilized and the irrecoverable strain continued to increase at a certain rate until failure in the case of 300 MPa - 300°C UCT; however, the samples under 400 MPa - 350°C UCT exhibited faster irrecoverable strain rate over the first few hundreds cycle and continued at increasing irrecoverable strain rate until failure. Specifically, plastic deformation facilitated by increased UCT and applied stress level resulted in earlier failure of the samples. Transformation temperatures (M_s and A_f), on the other hand, increased with each subsequent thermal cycle for both cases: in the case of 300 MPa - 300°C UCT, M_s and A_f temperatures increased from 177°C and 190°C to 236°C and 248°C, respectively. As for the 400 MPa - 350°C UCT experiment, M_s and A_f temperatures increased from 201°C and 208°C to 210°C and 228°C, respectively.

Figure 6.3 (a) and (b) show the evolution of actuation strains for both 300°C and 350°C UCTs under each 300 MPa and 400 MPa. Based on these results, the cycles to failure, average actuation strain, and corresponding work output were determined and are presented in Figure 6.11. Here, the actuation strain is defined as the difference between austenite strain and martensite strain for each cycle, and the average actuation strain is obtained by normalizing the sum of cyclic actuation strains by the number of cycles to failure. The work output is employed for better representing fatigue lives and is quantified as $\sigma_{act}\epsilon_{act}$, actuation strain (ϵ_{act}) multiplied by the applied stress (or actuation stress, σ_{act}) for constant uniaxial loading in the actuation fatigue tests. Calhoun *et al.* [15] demonstrated in several low temperature NiTi and NiTiCu SMAs that the fatigue lives in SMAs are much better correlated with actuation work output than the actuation

stress or actuation strain alone, following the relationship $\sigma_{act}\varepsilon_{act} = aN_f^{-b}$, which is mainly based on the critical plane model of Smith, Watson, and Topper [189] proposed for the low and intermediate-cycle fatigue life of conventional elastic–plastic materials. Below, it will be shown that the same relationship between actuation work output and fatigue lives also holds for NiTiHf HTSMAs.

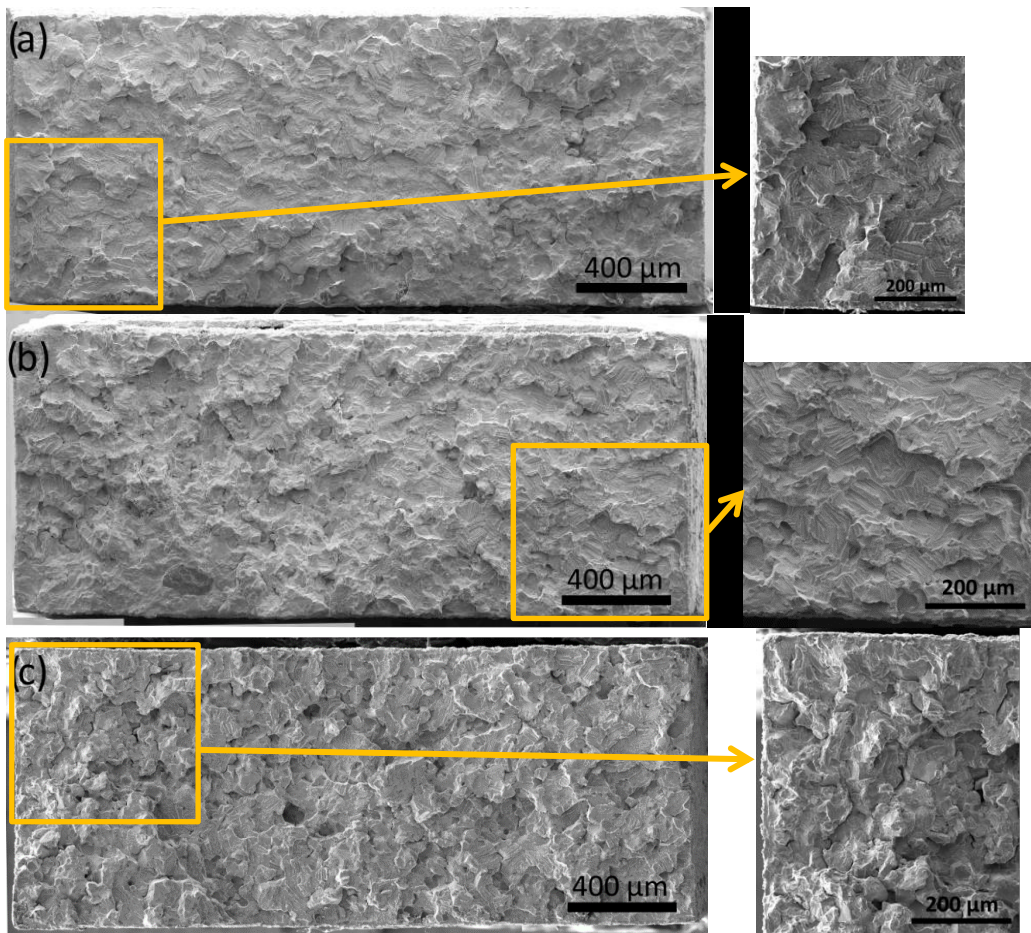


Figure 6.6. SEM micrographs of the fracture surfaces of nano-precipitation hardened $\text{Ni}_{50.3}\text{Ti}_{29.7}\text{Hf}_{20}$ HTSMA specimens following failure after the thermo-mechanical fatigue experiments under (a) 300 MPa with 300°C UCT, (b) 300 MPa with 350°C UCT, (c) 400 MPa with 300°C UCT, and (d) 400 MPa with 350°C UCT. Detected fatigue cracks on the side surface of the failed samples are demonstrated for (e) 300 MPa with 300°C UCT and (f) 400 MPa with 350°C UCT cases. The arrows in (e) and (f) show the loading direction of the samples. " Reprinted with permission from [161]. "

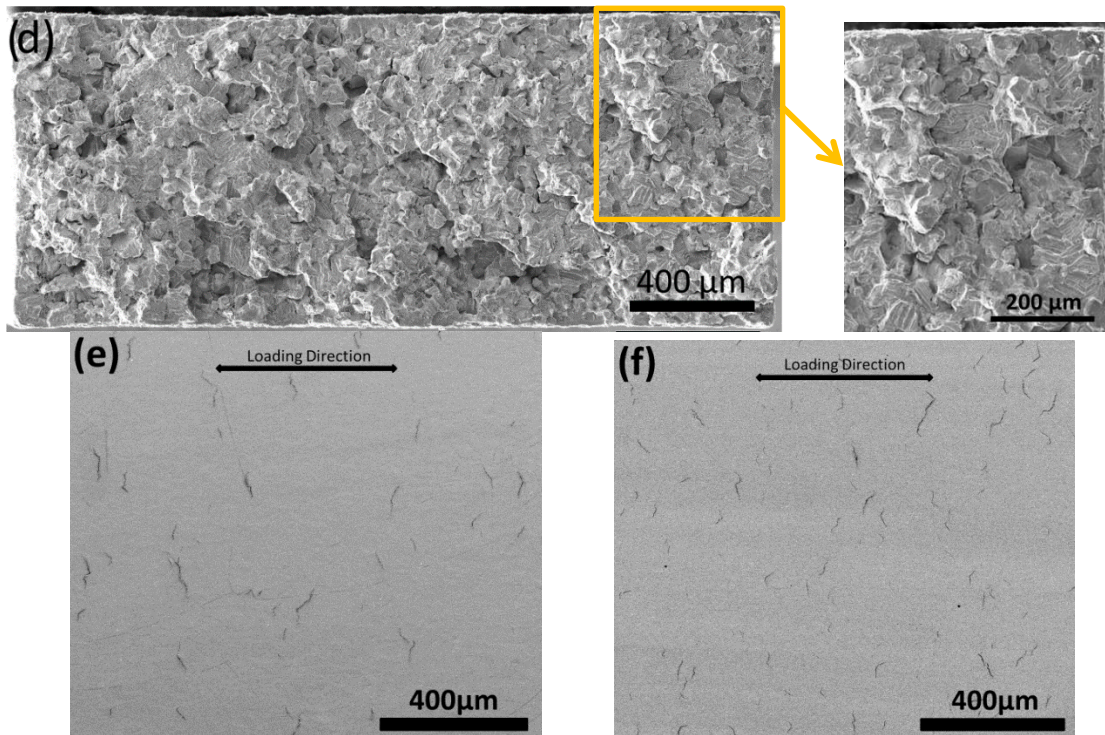


Figure 6.6. Continued [161].

The fatigue experiments shown in Figure 6.2 and Figure 6.3 revealed that the specimens loaded under 300 MPa with a 300°C UCT exhibited an average fatigue life of about 10,500 cycles, while the specimens loaded under the same stress level with a 350°C UCT lasted about 4300 cycles on the average (Figure 6.3 and Figure 6.11). Loading under 400 MPa, however, significantly altered the fatigue lives at both 300°C and 350°C UCTs, such that the samples failed at 4175 cycles and 1530 cycles (on the average), respectively. Note that the sample-to-sample variations in the fatigue lives were relatively and remarkably small indicating that the observed trend on the effect of the stress level is reliable, i.e. the higher the stress level is, the lower the actuation fatigue life becomes. When the UCT was increased to 350°C, for both stresses, the fatigue lives became shorter; however, still the lower stress level resulted in longer

fatigue lives as compared to the higher stress level, similar to the case of the 300°C UCT. This observation, i.e. the shorter fatigue lives in the higher UCT cases independent of the stress level, is expected since it is anticipated that the potential microstructural deformation mechanisms are activated and yield strength decreases at higher UCTs. Two additional UCT levels (250 and 375 °C) were considered under the stress level of 300 MPa in order to verify the UCT dependence trend (Figure 6.13). Due to partial cycling, specimen tested at 250 °C UCT did not fail until 31,000 cycles, and thus, the experiment was stopped at that point. As for the UCT of 375 °C, the actuation strain went up while the sample failed at about 2,500 cycles.

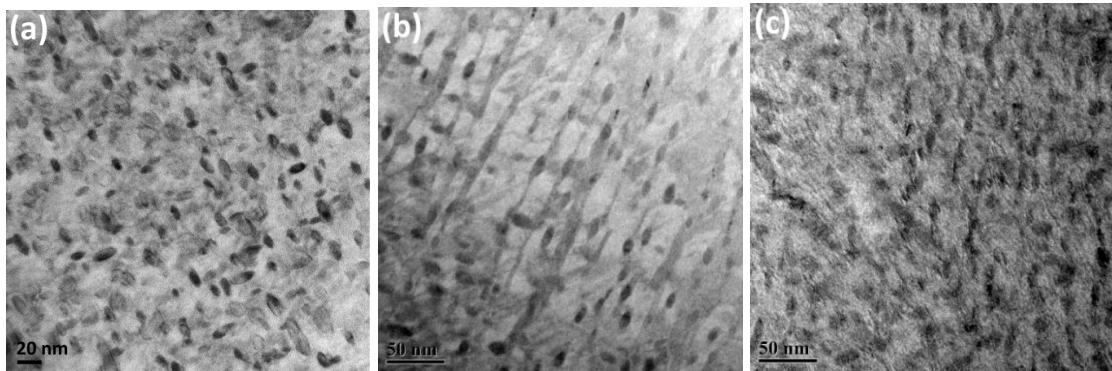


Figure 6.7. Bright field TEM images exhibiting size, volume, and morphology of precipitates in nano-precipitation hardened $\text{Ni}_{50.3}\text{Ti}_{29.7}\text{Hf}_{20}$ HTSMA specimens: (a) the sample heat treated at 550°C for 3 hours prior to fatigue testing, (b) failed sample under 300 MPa stress and an UCT of 300°C, and (c) the failed specimen under 400 MPa stress and an UCT of 350°C. All images were captured at room temperature. " Reprinted with permission from [161]. "

In contrast to the trends in actuation fatigue lives, the average actuation strains were observed to increase with increasing UCT and the applied stress level: the higher the UCT and applied stress levels were, the higher the average actuation strains became (Figure 6.3 and Figure 6.11). This behavior can be attributed to the early onset of partial

martensitic transformation in the lower UCT cases, such that a lower UCT is not sufficient to facilitate a complete martensitic transformation upon temperature cycling, as also evidenced by the results provided in Figure 6.2. This leads to a decrease in the actuation strain concomitant with the number of thermal cycles, which, in turn, brings about an increased fatigue life as compared to that of a sample loaded under the same stress level yet at higher UCT. A similar behavior was also reported for the actuation fatigue experiments on binary $\text{Ni}_{40}\text{Ti}_{50}\text{Cu}_{10}$ wires [130, 180], where higher UCT leads to more actuation strain at the expense of fatigue performance. As for the 350°C UCT case, a complete phase transformation seems likely to occur throughout the cyclic loading as evidenced by the constant (under 300 MPa) or increasing (under 400 MPa) actuation strain. Consequently, one of the reasons for the shorter fatigue lives in the higher (350°C) UCT cases is the nearly complete martensitic transformation as compared to the only partial transformations and lower actuation strains (i.e. lower actuation energy provided at each cycle) in the lower UCT (300°C) cases.

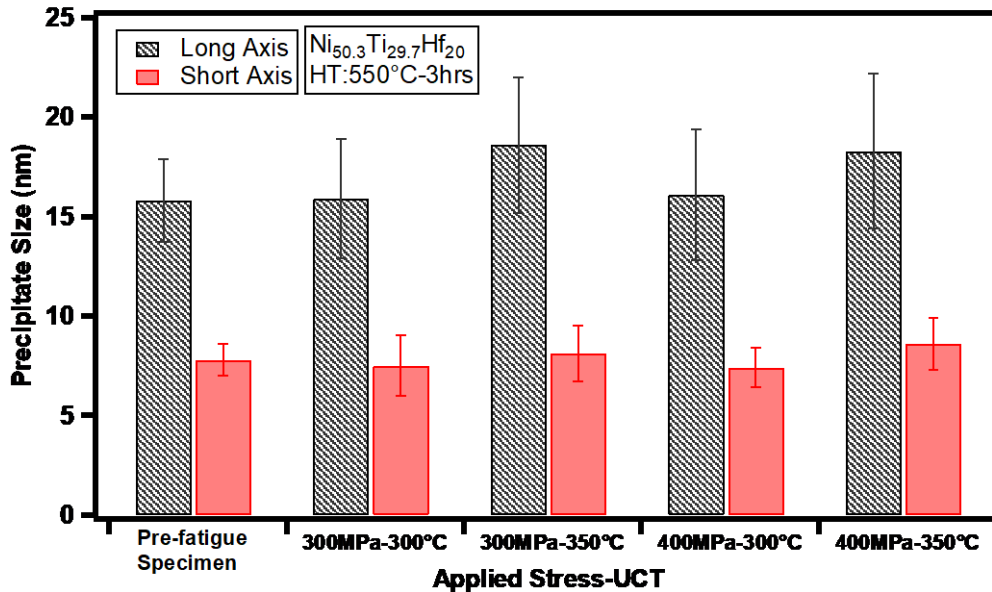


Figure 6.8. Average precipitate size along the long and short axes based on the TEM observations carried out on the $\text{Ni}_{50.3}\text{Ti}_{29.7}\text{Hf}_{20}$ HTSMA samples prior to and following thermo-mechanical cyclic experiments. The error bars indicate the range of the measured lengths for each case. Minimum 20 different TEM images from different locations and more than 500 precipitates were analyzed for each case. " Reprinted with permission from [161]. "

Another possible reason for the increase in actuation strain with the number of cycles in the 350°C UCT case is the fact that higher UCTs accelerate formation of cracks, due to complete transformation of austenite to martensite, which undergo cyclic opening and closing, and thereby propagate, between two different states. This opening and closing of the cracks are expected to contribute to the measured overall actuation strain, such that the complete phase transformation at higher UCT and the higher applied stresses promote an increase in actuation strain at the expense of fatigue performance (Figure 6.9). This argument warrants further investigation of the crack initiation and propagation

behavior utilizing in situ optical microscopy or digital image correlation analysis, which remains beyond the scope of the current work.

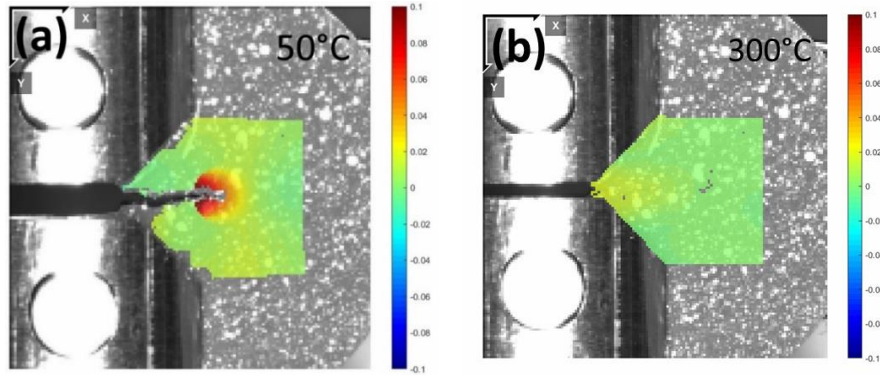


Figure 6.9. (a) Crack opens in the martensite state and (b) closes in the austenite state during thermomechanical cycling. NiTiHf sample was thermally cycled between 50°C-300°C under 545 N [190].

One of the primary objectives of fatigue testing is to generate fatigue life data in order to develop a life prediction design method. Since neither the strain- nor stress-based fatigue prediction methods properly capture the actuation fatigue behavior of SMAs, an alternative work-based formulation has been adopted in the literature, which takes varying stress levels and actuation strains into account [15, 191]. In this context, the change in work output is defined as the work done on the material during each thermo-mechanical cycle, such that

$$\sigma_{act}\varepsilon_{act} = aN_f^{-b} \quad (\text{Equation 1})$$

In Equation 1, σ_{act} and ε_{act} represent actuation stress and actuation strain, respectively, while a and b are the fatigue parameters that relate the work output to the fatigue life (N_f) through a power law formulation (based on the critical plane model of Smith, Watson, and Topper [189]), such that the work output is inversely proportional to the b^{th} power of

fatigue life. From a physical point of view, an increase of the proportionality constant a corresponds to an increase in the reduction in work output, which, in turn, refers to cyclic deterioration of mechanical properties at a higher rate. Similarly, a higher rate of cyclic deterioration of the work output is implied by an increased power exponent b .

In order to verify the suitability of the work-based formulation for the HTSMAs and compare the fatigue response of the NiTiHf HTSMA with that of conventional SMAs, data obtained from fatigue experiments carried out on Ni₆₀Ti₄₀ [192], Ni₅₀Ti₅₀ [128] and NiTiCu [193] were fit to Equation 1 along with the data on the current Ni_{50.3}Ti_{29.7}Hf₂₀ HTSMA (Figure 6.12). The results show that the adopted work-based method can successfully capture the actuation fatigue response of both low and high-temperature SMAs. Moreover, one can conclude that the NiTiHf-based HTSMAs are appropriate when SMA-based actuator design requires high work density. Furthermore, the fatigue response of the present NiTiHf SMA is comparable to, and for some cases better than, the fatigue response of other NiTi-based SMAs reported in Figure 6.12. This finding is remarkable, especially considering the much higher transformation temperatures of the NiTiHf HTSMA.

An analysis of the fatigue parameters (defined in $\sigma_{act}\varepsilon_{act} = aN_f^{-b}$

(Equation 1) for the four different materials compared in Figure 6.12 has important implications regarding the microstructure. In particular, both Ni₆₀Ti₄₀ and Ni_{50.3}Ti_{29.7}Hf₂₀ fit to Equation 1 with significantly lower proportionality constants a , which are at least one order of magnitude smaller as compared to those of the other two materials: about 100 and 250 as opposed to 10630 and 6400. Similarly, the power

coefficients are also smaller in the cases of $\text{Ni}_{60}\text{Ti}_{40}$ and $\text{Ni}_{50.3}\text{Ti}_{29.7}\text{Hf}_{20}$, such that the cyclic change in work output is relatively less for these two materials, as evidenced by the smaller slopes of the fit lines (Figure 6.12). The corresponding stability of $\text{Ni}_{60}\text{Ti}_{40}$ and $\text{Ni}_{50.3}\text{Ti}_{29.7}\text{Hf}_{20}$ can be explained by the nano-precipitation observed in both materials ([54] and Figure 6.7), which enhances the thermo-mechanical fatigue performance of these materials.

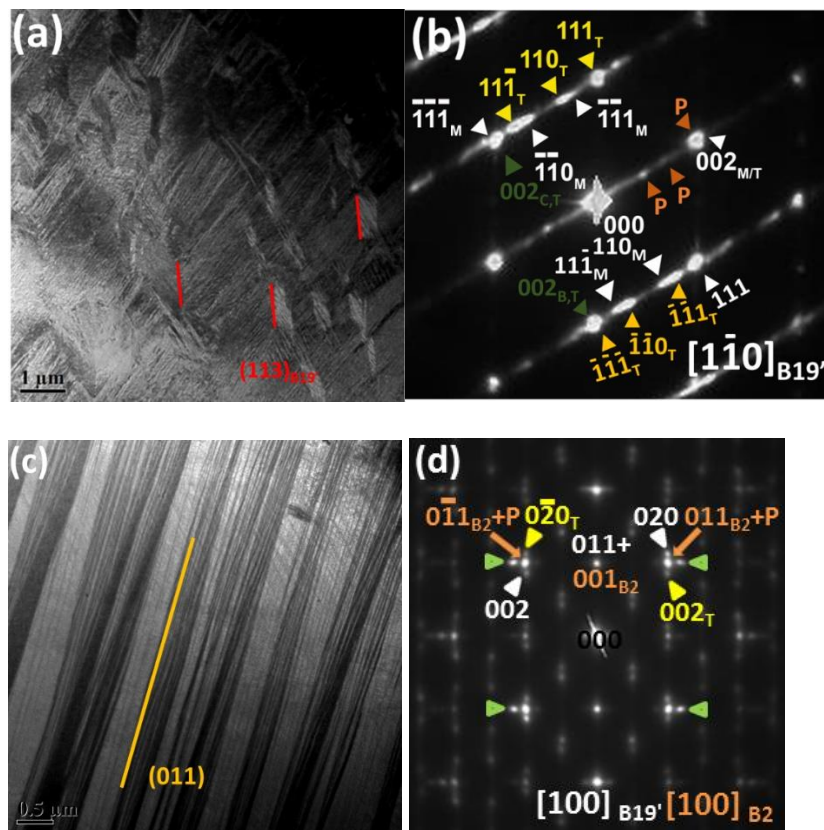


Figure 6.10 (a) An exemplary bright field TEM image of two variants of (001) compound twins observed in the matrices of all failed specimens, (b) the corresponding SAD pattern evidencing the compound twins observed in tested samples, (c) an exemplary bright field TEM image of {011} Type I twins observed in all failed samples, and (d) the corresponding SAD pattern demonstrating two martensite variants on the $(011)_{B_{19}}$ type I twin plane along the $[100]_{B_{19}}$ zone axis, and precipitates. " Reprinted with permission from [161]. "

6.6. Cyclic/Dimensional Stability

Evolution of irrecoverable strain (strain in austenite) upon thermo-mechanical cycling, which is an indication of cyclic and dimensional stability, for stress – UCT combinations employed in the current experiments is presented in Figure 6.4. Accordingly, the irrecoverable strain is dependent on applied stress level, UCT and the number of cycles. An important observation is that, in certain conditions (e.g. 400 MPa – 350°C), the samples exhibited an increasing rate of irrecoverable strain starting in the middle of or toward the end of their life span, which constitutes an unstable cyclic response, where this instability was accompanied by inferior fatigue performance as evidenced by the significantly altered number of cycles to failure (Figure 6.11). Specifically, the samples tested at 350°C exhibited an unstable fatigue response, which is indicative of increased apparent ductility at the higher UCT. While the samples tested under 400 MPa exhibited about 4% irrecoverable strain at 350°C UCT, the samples loaded to 300 MPa exhibited about only 2% irrecoverable strain at the same number of cycles. Consequently, these results imply that higher UCT and stress levels lead to a rapid increase in plastic strain, and thus, promote earlier failure of samples under thermo-mechanical cycling. Based on the irrecoverable strain data, more dislocation storage was expected in the 350°C cases, which should increase the stored internal stresses. However, according to the post-mortem DSC results shown in Figure 6.5, the samples with 350°C UCT do not exhibit large internal stresses since the M_s temperature does not change as much as those with 300°C UCT. This brings about two possibilities: first, specimens tested with a 350°C UCT may exhibit more ductility and enhanced dislocation formation, but the

dislocations may have annihilated or rearranged at this temperature to relax the internal stress. The other possible reason for the higher irrecoverable strain might be the crack formation and higher damage accumulation. When a crack forms, it cannot easily propagate in a transgranular fashion because of the relaxation at higher UCT, but at lower UCT they can propagate easier due to less relaxation and the resulting higher stress concentrations. This, in turn, implies that a relatively larger number of smaller cracks and intergranular fracture are expected at the higher UCT (350°C), as observed in the SEM investigations.

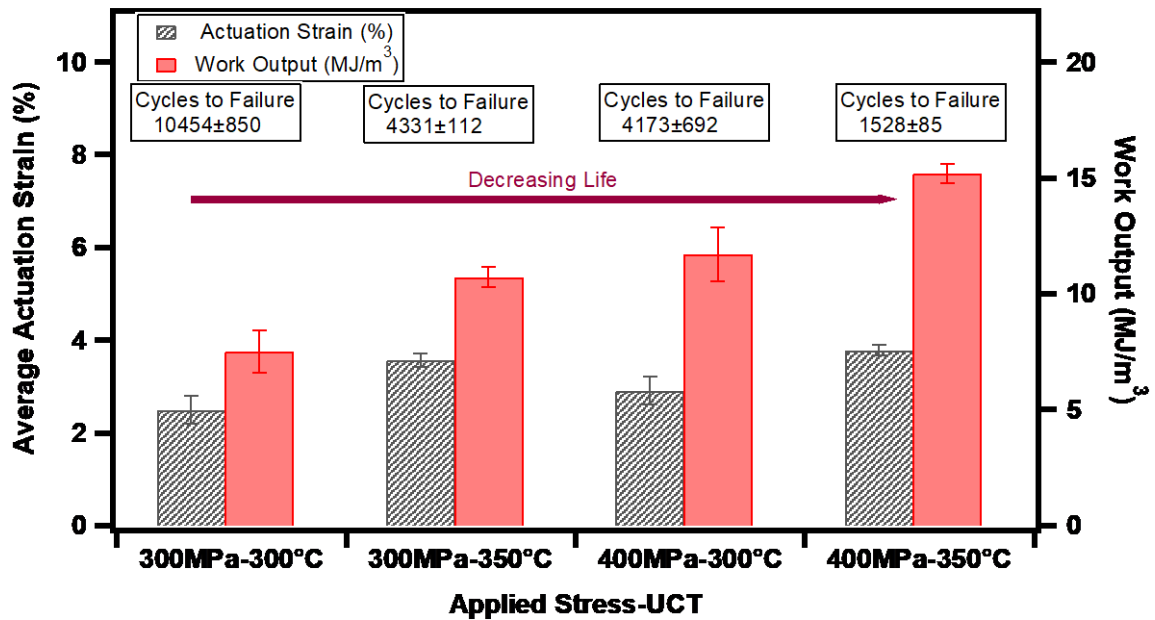


Figure 6.11. Summary of the average actuation strains and actuation fatigue lives observed in the thermo-mechanical fatigue experiments carried out on nano-precipitation hardened $\text{Ni}_{50.3}\text{Ti}_{29.7}\text{Hf}_{20}$ HTSMAs heat treated at 550°C for 3 hours, for the four stress - UCT combinations considered in this work. The error bars were obtained based on the companion experiments conducted for each case. " Reprinted with permission from [161]. "

6.7. Calorimetric Results and Phase Transformation Behavior

Transformation temperatures and enthalpies of each specimen prior to and following (after failure) the fatigue experiments are presented in Table 1 and the corresponding DSC results are demonstrated in Figure 6.5 (a)-(c). Clearly, there are significant changes in both transformation temperatures and enthalpies following thermo-mechanical cycling. Considering that the variation in transformation enthalpies among the failed samples does not exceed 3 J/g, upon thermo-mechanical cycling, the enthalpy of the samples dropped about 45% on the average (from 18 J/g to about 10 J/g). This large reduction in the enthalpy is a consequence of dislocations and other defects that impede the quantity of the material allowed to undergo thermally-induced martensitic phase transformation (Figure 6.5 (a) and (b)). Even though the differences are small, the 300°C UCT samples seem to have lower transformation enthalpies than the 350°C UCT samples following the fatigue failure, indicating that the former may have smaller volume of transforming material towards the end of the fatigue cycling. Indeed, this is in agreement with the lower actuation strains observed in the 300°C UCT cases.

In contrast, the failed samples exhibited a significant increase in M_s and A_f temperatures, and this increase in M_s ($\Delta M_s = M_s^{\text{post-fatigue}} - M_s^{\text{pre-fatigue}}$) showed a remarkable correlation, an almost linear relationship, with the number of cycles to failure (Figure 6.5 (c)). In particular, the 300°C UCT samples exhibited much higher ΔM_s than the 350°C UCT samples for a given stress level while the same trend was observed for the samples tested under 300 MPa, i.e. they exhibited notably higher ΔM_s than the samples tested under 400 MPa. This increase in the transformation temperatures should be a result of

either the internal stresses stored during thermo-mechanical cycling [194], or the growth of existing nano-precipitates or formation of new ones, depleting Ni content of the matrix and thereby increasing the transformation temperatures. If the latter is correct, then one would expect that the 350°C UCT cases should have resulted in higher transformation temperatures than the 300°C UCT cases because of the proximity to the precipitation temperatures. However, the opposite is observed in Figure 6.5 (c). Therefore, the increase in ΔM_s should be a result of the oriented internal stress storage facilitated by dislocations and oriented remnant martensite [25, 120, 162].

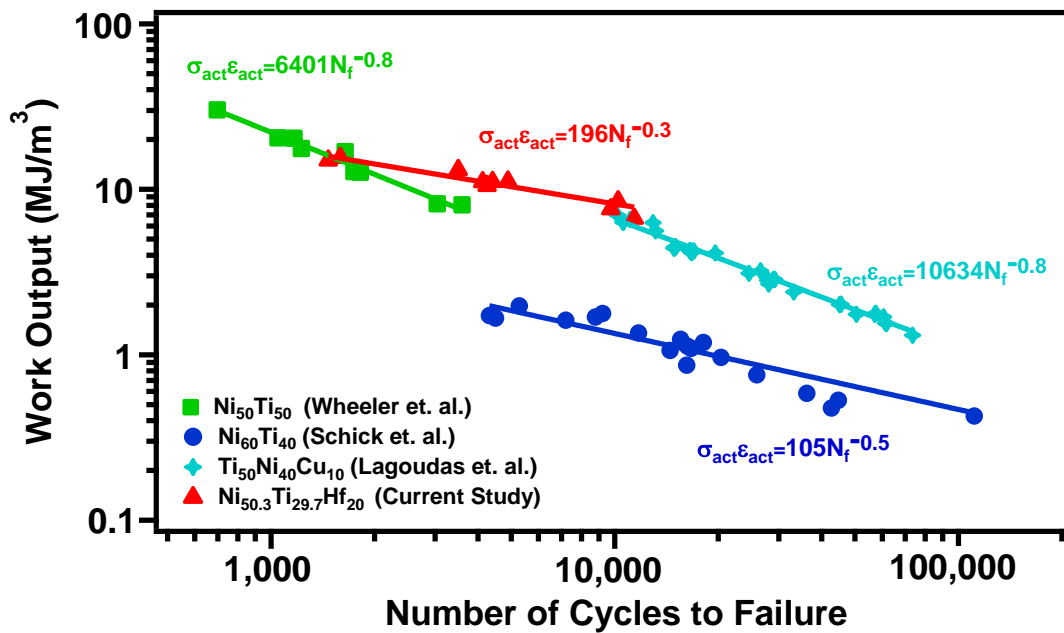


Figure 6.12. A comparison of the work output vs. number of cycles to failure responses of Ni₆₀Ti₄₀ [192], Ni₅₀Ti₁₅₀ [128], Ti₅₀Ni₄₀Cu₁₀ [193] and nano-precipitation hardened Ni_{50.3}Ti_{29.7}Hf₂₀ HTSMA. The Ti₅₀Ni₄₀Cu₁₀ samples were in form of wires whereas all others were in form of dog-bone shaped samples. " Reprinted with permission from [161]. "

6.8. Microstructural Evolution

SEM images of the fracture surfaces of samples failed under different stress – UCT combinations are presented in Figure 6.6, where the observed fracture mode was brittle fracture for all tested specimens. It is noted that thermal cycling under 400 MPa resulted in a significant fracture surface roughness (Figure 6.6 (c)-(d)) as compared to the cases cycled under 300 MPa. For the former, much higher crack density on the fracture surface, especially at triple junctions (shown by arrows), is evident as compared to those samples thermally cycled and failed under 300 MPa. It is known that intergranular cracking is characterized by rock-candy triple points and faceted appearances, while transgranular cracking is characterized by river patterns, cleavage steps and feather markings [173]. Accordingly, in the current study, the crack growth mode was intergranular for specimens with shorter fatigue lives, while samples with longer fatigue lives failed upon transgranular crack propagation based on the fracture surface investigations (Figure 6.3 and Figure 6.6).

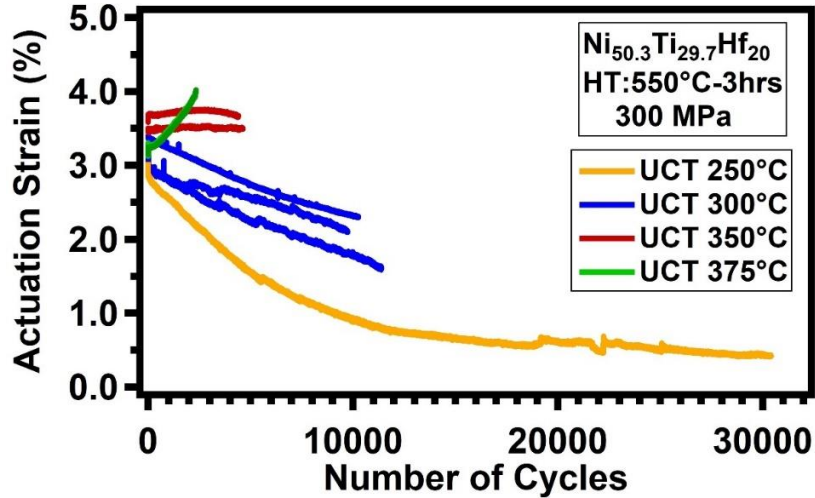


Figure 6.13. Effect of UCT on the actuation fatigue response of the nano-precipitation hardened $\text{Ni}_{50.3}\text{Ti}_{29.7}\text{Hf}_{20}$ HTSMA samples heat treated at 550°C for 3 hours under 300 MPa. The experiment with 250°C UCT did not result in failure of specimen, and the experiment was stopped at about 31,000 cycles. " Reprinted with permission from [161]."

Figure 6.6 (e) and (f) demonstrate the microcracks on the sub-surfaces (roughly $60\ \mu\text{m}$ below the actual surface due to the polishing) of the $\text{Ni}_{50.3}\text{Ti}_{29.7}\text{Hf}_{20}$ HTSMA samples subjected to thermo-mechanical cycling under 300 MPa with 300°C UCT and 400 MPa with 350°C UCT, respectively. Microcrack networks that are randomly distributed cover the entire surfaces of the HTSMA samples, and the lengths of the microcracks vary between $10\ \mu\text{m}$ and $200\ \mu\text{m}$. Furthermore, the microcracks formed mostly parallel to each other and perpendicular to the loading direction, and at the triple junctions. It is noted that the density of cracks is similar for most cases at the point of failure but slightly higher in the case of 400 MPa - 350°C UCT sample, implying that the increases in both the applied stress level and UCT promote faster formation of cracks, and consequently, earlier failure in fatigue experiments. Specifically, higher applied stresses

and UCT promote larger irrecoverable strains (Figure 6.4), such that plastic strains accumulating at a higher rate during cyclic loading lead to earlier failure of the samples loaded under these conditions through intergranular crack propagation (Figure 6.6).

The microstructural evolution upon thermo-mechanical cyclic loading of the $\text{Ni}_{50.3}\text{Ti}_{29.7}\text{Hf}_{20}$ samples heat treated at 550°C for 3 hours was further investigated, both prior to and following the fatigue failure, in order to reveal the evolution of precipitate size and morphology, and other microstructural fatigue features during thermal cycling under different UCT and applied stress levels. In particular, since nano-precipitates start to form above 400°C in $\text{Ni}_{50.3}\text{Ti}_{29.7}\text{Hf}_{20}$ alloys [187] and applied stress may accelerate the precipitation kinetics, it is expected that thermal cycling under stress with UCT of 300°C or 350°C can influence the size and morphology of existing nano-precipitates in the present alloy. If the precipitate size, morphology, and volume fraction evolve during thermo-mechanical cycling, this would substantially affect cyclic evolution of actuation, irrecoverable strains and the fatigue lives, and thus, the precipitates should be carefully monitored before and after the experiments.

The TEM investigations revealed that the precipitates in all $\text{Ni}_{50.3}\text{Ti}_{29.7}\text{Hf}_{20}$ tested samples have similar sizes (maximum 10-15% difference) and morphologies regardless of the different stress – UCT combinations used when compared to the samples prior to testing (Figure 6.7 Figure 6.8). Therefore, the observed dense distribution of nanometer-sized ellipsoidal precipitates is mainly a result of the relatively short heat treatment (3 hours) carried out at 550°C for the present material (Figure 6.7(a)) [29]. It is noted that the specimens tested with a 300°C UCT have an average precipitate size of 16 nm along

the long axis, while the samples tested at 350°C UCT feature slightly larger precipitates with about 18.5 nm average sizes, as indicated in Figure 6.8. This slight increase in the precipitate size could arise from the growth of precipitates during thermo-mechanical cycling with a higher UCT through enhanced diffusion under stress. It is not clear if such a small change in the precipitate size can be responsible for notable differences in the cyclic evolution of the properties as a function of UCT and stress level.

In addition to the morphology and size of the precipitates, the twinning modes active in the B19' martensite were also investigated using TEM (Figure 6.10). Specifically, bright field images and the corresponding diffraction patterns revealed that (001)-compound twins and (011) Type I twins were present in all tested samples. Even though the (011) Type I twins are considered appropriate for lattice invariant shear (LIS) deformation, the (001)-compound twins are regarded as deformation twins due to their incompatibility with LIS deformation [29]. Figure 6.10 (a) shows two sets of twinned variants exhibiting (001)-compound twinning. The main variant and the twins are marked by white and yellow indices on the corresponding selected area diffraction (SAD) pattern, respectively, and the green indices indicate (002) reflections belonging to other variants (Figure 6.10 (b)). In addition, precipitates leading to the $1/3\{110\}$ -type satellites and fundamental reflections due to either retained austenite or precipitates are marked with P labels. Figure 6.10 (c) shows a bright-field image where the boundaries between two martensite variants are indeed (011)_{B19'} common twin plane (type I). Another SAD pattern obtained from the failed samples (Figure 6.10). Figure 6.10 (d) clearly shows the (011)_{B19'} type I twin plane and two martensite variants on the [100]_{B19'}.

In this figure, precipitates are represented by the fundamental reflections, and $\frac{1}{4}(210)B2$ satellites are marked with orange arrow and triangles [29]. All other martensite variants are marked with green triangles. Comparing the present TEM results with our earlier investigations on the same material [29], it was not possible to identify significant differences, in terms of the type of twins and amount of different type twins in martensite, between pre- and post-fatigue samples. Therefore, more detailed TEM investigations are needed at high temperatures in the austenite phase to better understand the dislocation structures in the post-fatigue samples and reveal the fatigue induced microstructural changes. Moreover, high energy synchrotron or neutron diffraction experiments on the post-fatigued or interrupted fatigue samples can help better reveal the microstructural evolution and understand the role of UCT and applied stress level on the microstructural evolution.

6.9. Summary and Conclusions

The effects of applied stress level and upper cycle temperature (UCT) on the thermo-mechanical fatigue performance of nano-precipitation hardened $Ni_{50.3}Ti_{29.7}Hf_{20}$ high-temperature shape memory alloy (HTSMA) were investigated. Fatigue experiments were accompanied by a set of pre- and post-experimental differential scanning calorimetry, scanning electron microscopy, fractography, and transmission electron microscopy (TEM) in order to reveal the microstructural parameters governing the cyclic evaluation of actuation and irrecoverable strains, cyclic stability, and actuation fatigue lives. Based on the results, main findings and conclusions can be summarized as follows:

- As the applied stress level and the UCT increase, the $\text{Ni}_{50.3}\text{Ti}_{29.7}\text{Hf}_{20}$ HTSMA samples exhibit shorter fatigue lives yet higher actuation strains. Specifically, thermo-mechanical cycling under 300 MPa with 300°C UCT leads to a fatigue life of about 10,500 cycles, while the specimens subjected to 400 MPa with 350°C UCT fail at about 1530 cycles.
- Higher stress levels and UCT in general promote the accumulation of higher apparent permanent strains. In particular, the specimens cycled up to 350 °C exhibit larger irrecoverable strains as compared to the samples tested up to 300 °C under the same stress. Similarly, the samples tested under 400 MPa exhibit about twice the irrecoverable strains at a given number of cycles as compared to the samples tested under 300 MPa at the same UCT. Furthermore, the actuation strain remains constant or increases as a function of the number of cycles when the UCT is 350°C; however, the specimens cycled with 300°C UCT exhibit a decreasing trend in terms of actuation strain. This increase in actuation strain is also attributed to the accelerated formation of cracks at higher UCTs, which open and close when the sample reversibly transforms between martensite and austenite, contributing to the apparent actuation strain.
- Fracture surface investigations indicate that higher applied stress levels and increasing UCT lead to a much rougher fracture surface and slightly higher density of microcracks in the samples, signature of intergranular fracture while the lower stress levels and higher UCT result in transgranular fracture. Thus, lower

applied stress – UCT combination should be considered for the safe utility of $\text{Ni}_{50.3}\text{Ti}_{29.7}\text{Hf}_{20}$ HTSMAs for actuator applications.

- TEM analysis revealed that the precipitates observed in the tested and untested $\text{Ni}_{50.3}\text{Ti}_{29.7}\text{Hf}_{20}$ samples exhibit nearly equivalent sizes and morphologies, and thus, UCT and applied stress were concluded not to have a considerable impact on growth of the precipitates during thermo-mechanical fatigue experiments considered in the present work.
- Post-mortem DSC analysis revealed that there is a significant increase in the martensite start temperatures, as high as 80°C, in the fatigued samples. The increase in this temperature show a remarkable correlation with the number of cycles to failure. The possible change in the precipitate size and associated change in the matrix composition was ruled out as a potential reason for this increase due to the insignificant change in precipitate size in the fatigued samples. Therefore, the increase was attributed to the oriented internal stress storage facilitated by dislocations and oriented remnant martensite.
- $\text{Ni}_{50.3}\text{Ti}_{29.7}\text{Hf}_{20}$ HTSMA heat treated at 550°C-3 hours exhibited considerably high work output 16MJ/m³ for 400 MPa-350°C, dimensional stability up to more than 10,000 cycles under condition of 300 MPa-300°C, and impressive cyclic stability as compared to NiTi binary SMAs, and these impressive properties were obtained at much higher operating temperatures than NiTi.

CHAPTER VII
ON THE ROLE OF APPLIED STRESS LEVEL ON THE ACTUATION
FATIGUE PERFORMANCE OF NITIZR HIGH TEMPERATURE SHAPE
MEMORY ALLOYS

This study focuses on the influence of applied stress levels on the actuation fatigue performance of Ni-rich NiTiZr alloys. Aging treatment of Ni-rich NiTiZr alloys forms H-phase precipitates as a superstructure of B2 phase, which not only improves mechanical and shape memory properties of the material, but also yields control of martensitic transformation temperatures by depleting Ni content in the matrix [3, 6, 29]. After this improvement, one constitutive parameter that becomes extremely important for widespread implementation of Ni-rich NiTiZr alloy as a high temperature actuator is understanding of the actuation fatigue properties of these alloys. Even though mechanical fatigue of SMAs are extensively investigated, actuation fatigue behavior of Ni-rich NiTiZr alloys remains relatively unknown or available studies are somewhat limited to a few hundred thermo-mechanical cycles. This study strives to establish the first fundamental understanding on actuation fatigue behavior of nano-precipitation hardened Ni-rich NiTiZr under different stress levels. Precipitation hardened Ni_{50.3}Ti_{29.7}Zr₂₀ was investigated until rupture to examine this behavior with a focus of the effect varying stress levels has on transformation characteristics, such as, actuation strain, irrecoverable strain, and fatigue life. Based on fatigue test results, Ni-rich Ni_{50.3}Ti_{29.7}Zr₂₀ shows potential for use as a high temperature actuator in practical applications due to a significant achievement of 12,600 cycles average fatigue life and only ~0.86% actuation strain under a 200MPa load.

Aging at 550°C-3h introduced densely populated and heterogeneously distributed small H-phase nano-precipitates with a size of 6 to 22nm (measured along the large axis) surrounded by a continuous martensite matrix (Figure 7.1(a)). Figure 7.1(b) and (c) exhibited temperature vs strain graphs for two extreme load cases; 200MPa vs 400MPa. From these results, irrecoverable strain and actuation strain were calculated until sample fractured. Detailed information how to calculate shape memory characteristics can be found in [50, 161]. Figure 7.1(b) and (c) displayed development of plastic deformation as a function of isobaric thermal cycles. Also, transformation temperatures shifted with thermal cycles under constant load levels. More significant increase was observed in the case of 200MPa due to greater number of fatigue life.

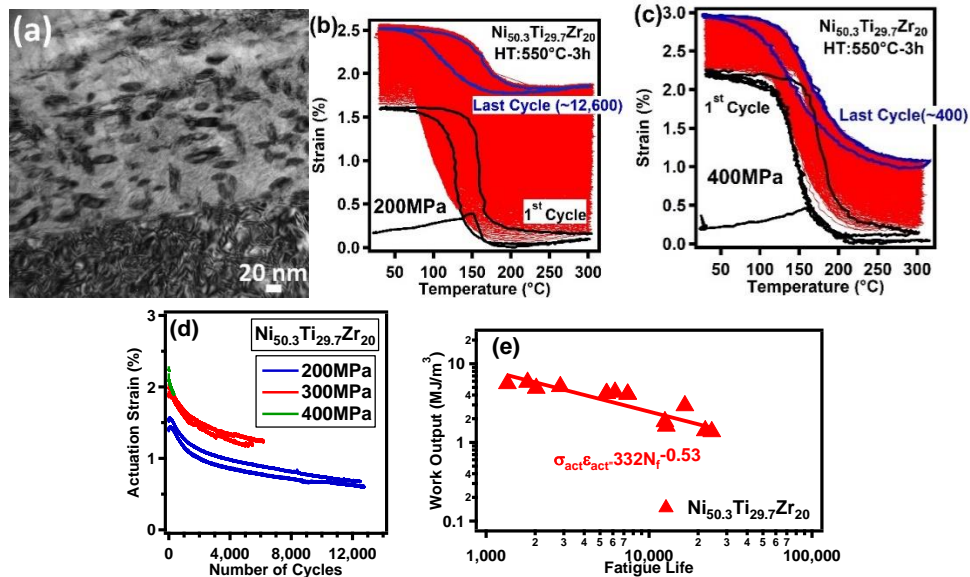


Figure 7.1 (a) Nano-precipitates within the matrix after aging 550°C-3h, temperature vs. strain evolution of nano-precipitation hardened Ni_{50.3}Ti_{29.7}Zr₂₀ alloys until failure under stress level of (b) 200MPa, (c) 400MPa, and effect of applied stress levels on (d) the evolution of actuation (e) work-output of Ni_{50.3}Ti_{29.7}Zr₂₀.

Figure 7.1 (d) presented the influence of applied stress on actuation strain and fatigue life of nano-precipitation hardened Ni-rich NiTiZr alloys during thermally induced transformations. Fatigue life of the specimens decreased as a function of increasing applied stress levels, yet in contrast, the actuation strain level increased. Specimens at 200MPa failed at ~12,600 cycles on average, whereas, at a stress level of 400MPa fatigue life was reduced to an average of only ~180 cycles. As stress levels increased from 200MPa to 400MPa, the average actuation strain increased from 0.86% to 2.10% respectively. Higher fatigue life came at the expense of diminished actuation strain.

Figure 7.1(e) presented the work-output vs. fatigue life of NiTiZr alloy aged at 550°C-3h. The work-based approach was adopted to relate the applied loading conditions to the actuation fatigue life of SMA. The work-based model was expressed as $\sigma_{act}\varepsilon_{act} = aN_f^{-b}$ [129, 175], where applied stress level (σ_{act}) multiplied by average actuation strain (ε_{act}) represented actuation work-output of actuation cycles. Empirical parameters a and b in the work-output model relate work-output to fatigue life (N_f). Experimental data of NiTiZr alloy fitted well with power law formulation of work-based model. Primary aim of this model provides a life prediction method to decrease the number of fatigue testing which is time-consuming and costly.

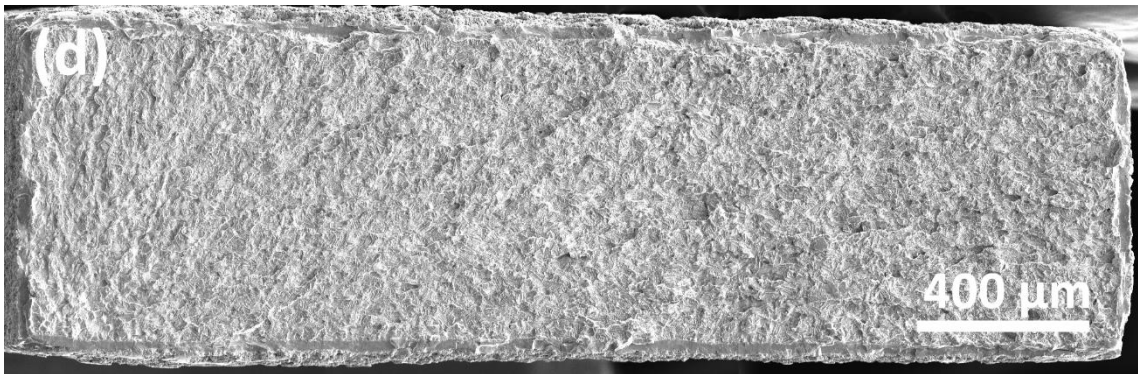
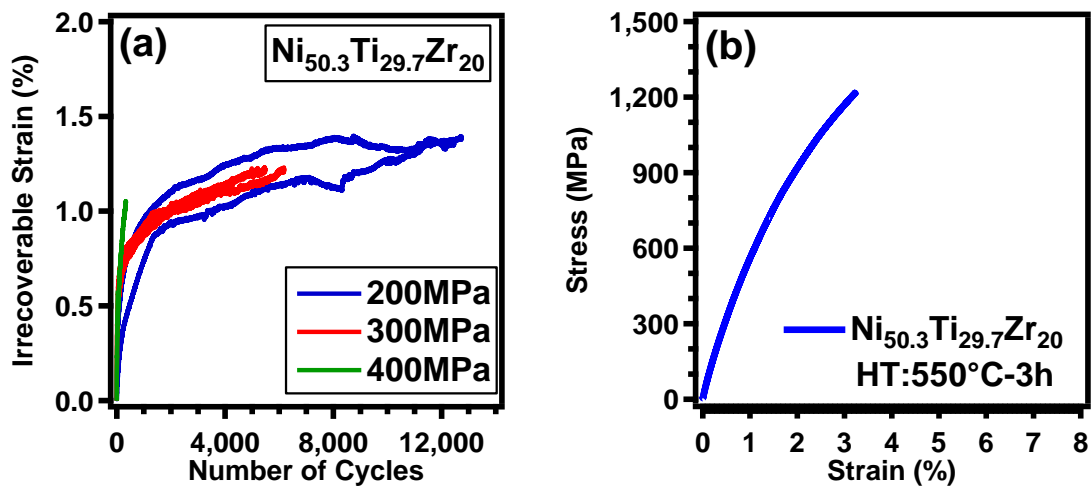


Figure 7.2 (a) Effect of applied stress levels on the evolution of the irrecoverable strain for nano-precipitation strengthened $\text{Ni}_{50.3}\text{Ti}_{29.7}\text{Zr}_{20}$ alloy (b) stress vs. strain graph of $\text{Ni}_{50.3}\text{Ti}_{29.7}\text{Zr}_{20}$ aged at 550°C-3h obtained through servo-hydraulic MTS test frame, and fracture surface of specimens failed at stress level of (c) 200MPa and (d) 400MPa.

Figure 7.2(a) showed the evolution of irrecoverable strain under different applied stress levels. Irrecoverable strain increased rapidly over the first few hundred cycles after which it continued to increase but at a lower rate. The rate of increase in the irrecoverable strain was faster with a larger applied stress. Highest irrecoverable strain was observed at 200MPa and associated with the longest fatigue life. Stress-strain curves profile can explain the reason of earlier failure of samples at 400MPa. As seen in Figure 7.2 (b), nanoprecipitation hardened NiTiZr alloy was brittle with high modulus and exhibits low degree of elongation. NiTiZr alloy attained yield strength of 600MPa and ultimate strength of 1220MPa. Fractography of broken samples at 200MPa and 400MPa were carried out using SEM (Figure 7.2(c) and (d)). Primary predominant fractographic feature in SEM micrograph was brittle fracture associated with flat fracture surface which was in a good agreement with MTS results.

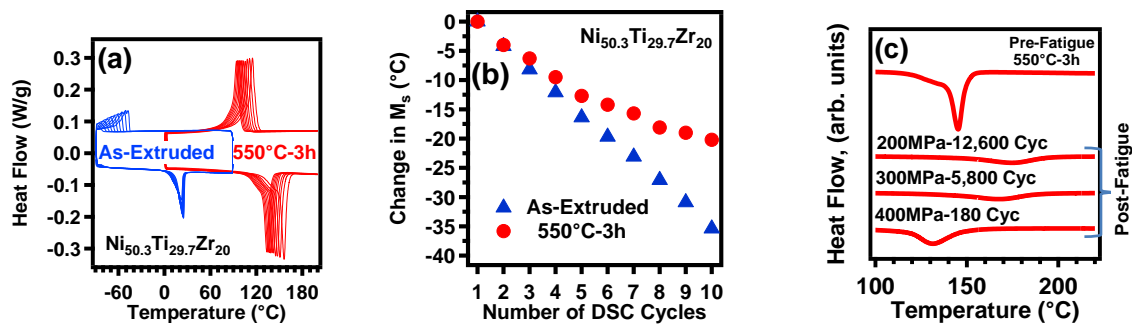


Figure 7.3 (a) Stress-free DSC measurements over ten thermal cycles prior to fatigue testing for Ni_{50.3}Ti_{29.7}Zr₂₀ alloy in the as-extruded condition and aged at 550°C-3h, (b) decrease in the M_s for two conditions (c) post-mortem heating DSC curve of pre- and post-fatigue specimens.

DSC analysis was performed prior to testing and after failure of the samples as shown in Figure 7.3. Aging treatment at 550°C-3h increased M_s of the as-extruded sample from

-45 to 122°C in the first DSC cycle (Figure 7.3(a)). Development of H-phase nano-precipitates after aging treatment at 550°-3h improved thermal stability of alloy (Figure 7.3(b)) and these precipitates act as a barrier dislocation motion. Post-fatigue test results revealed that heat of transformation decreased by more than 50% after failure (Figure 7.3 (c)). Since the increase in the number of thermo-mechanical cycles allowed formation of more internal stresses, specimens with higher fatigue life experienced a greater reduction in the heat of transformation. The reason behind this reduction stemmed from less material being available to undergo martensitic transformation due to the internal stress accumulation during repeated transformation, stabilizing the martensite state. Furthermore, there was a change in A_f temperature of failed specimens compared to those untested sample $\Delta A_f (A_f^{Post-fatigue\ test} - A_f^{Pre-fatigue\ test})$. There were two main competing factors that affected the transformation temperatures of specimens during repeated martensitic transformations. The increase in ΔA_f was a consequence of oriented internal stresses of dislocation arrays piling up during thermo-mechanical cycling[110]. The decrease in ΔA_f has been rationalized by the increasing dislocation density during thermally-driven transformation cycles making it more and more difficult for the martensitic phase to undergo martensitic transformation [195]. From these deductions the higher fatigue life under 200MPa resulted in a larger accumulation of oriented internal stress fields and rise in ΔA_f above 0°C. Earlier failure under 400MPa induced less oriented internal stress fields, hence, the drop in ΔA_f below 0°C.

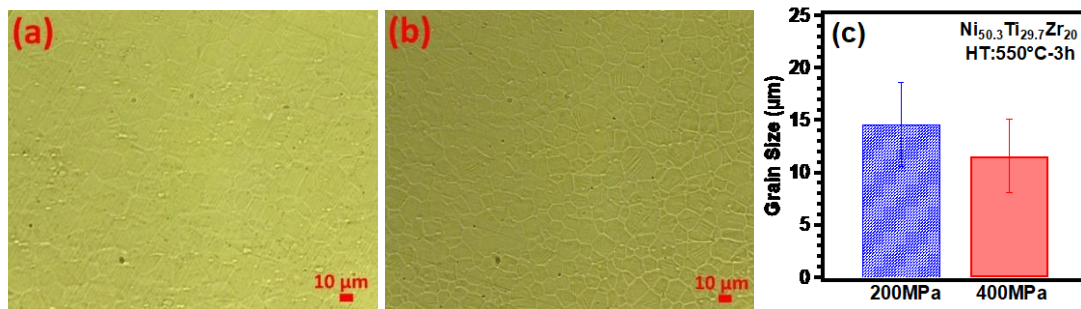


Figure 7.4. Grain size images of failed $\text{Ni}_{50.3}\text{Ti}_{29.7}\text{Zr}_{20}$ samples (a) 200MPa, (b) 400MPa and (c) grain size distribution plots of 200MPa and 400MPa.

Figure 7.4 (a) and (b) displayed the grains after failure of the specimens under 200MPa and 400MPa. Size of average grain was calculated based on randomly selected 30 grains. Specimens under 200MPa had greater average grain size than those under 400MPa. Average grain size was determined to be $\sim 14.8 \pm 4.0 \mu\text{m}$ for specimens under 200MPa after $\sim 12,600$ cycles and $\sim 11.6 \pm 3.5 \mu\text{m}$ for samples under 400MPa after ~ 180 cycles (Figure 7.4 (c)). Due to differences in fatigue life between two cases, specimens under 200MPa were exposed to heat for a longer period of time as compared to those under 400MPa. Expectedly, grain growth increases as a function of the period of time spent at higher temperatures increases.

The focus of this study was centered on establishing a fundamental understanding of reliability, durability, mechanical test data, and the work attributes for the nano-precipitation hardened Ni-rich $\text{Ni}_{50.3}\text{Ti}_{29.7}\text{Zr}_{20}$ alloy. Actuation fatigue test results revealed that the increase in stress levels decreased fatigue life, yet in contrast, resulted in a rise in actuation strain. In other words, a higher fatigue life came at the cost of

diminished actuation strain. With a fatigue life as high as ~12,600 cycles and a considerable amount of actuation strain of ~0.86%, nano-precipitation hardened $\text{Ni}_{50.3}\text{Ti}_{29.7}\text{Zr}_{20}$ HTSMAs are viable candidates for use as actuators in high temperature applications.

CHAPTER VIII
EFFECTS OF UPPER CYCLE TEMPERATURE ON THE ACTUATION
FATIGUE PERFORMANCE OF NITIZR HIGH TEMPERATURE SHAPE
MEMORY ALLOYS

This study focuses on the role of upper cycle temperature (UCT) on the actuation fatigue performance of nano-precipitation hardened Ni-rich NiTiZr alloys by studying loaded cyclic thermally-induced martensitic transformations to fracture.

H-phase precipitates in Ni-rich NiTiZr alloys do not only strengthen the matrix against plastic deformation, but also modifies transformation temperatures by depleting Ni content within the matrix [3, 6, 29, 62, 196]. These developments stimulate growing interest towards understanding the actuation fatigue behavior of Ni-rich NiTiZr which remains unknown. Widespread implementation of this alloy as a high-temperature actuator depends on fatigue performance under various application parameters. Since there is no study concerning the influence of upper cycle temperature on actuation fatigue response of nano-precipitation hardened Ni-rich NiTiZr alloys (and available works are only to investigate several hundred cycles), this work establishes first fundamental understanding of transformation characteristics and actuation fatigue life of these alloys under thermal cycling at different upper cycle temperatures until failure [3, 6, 166].

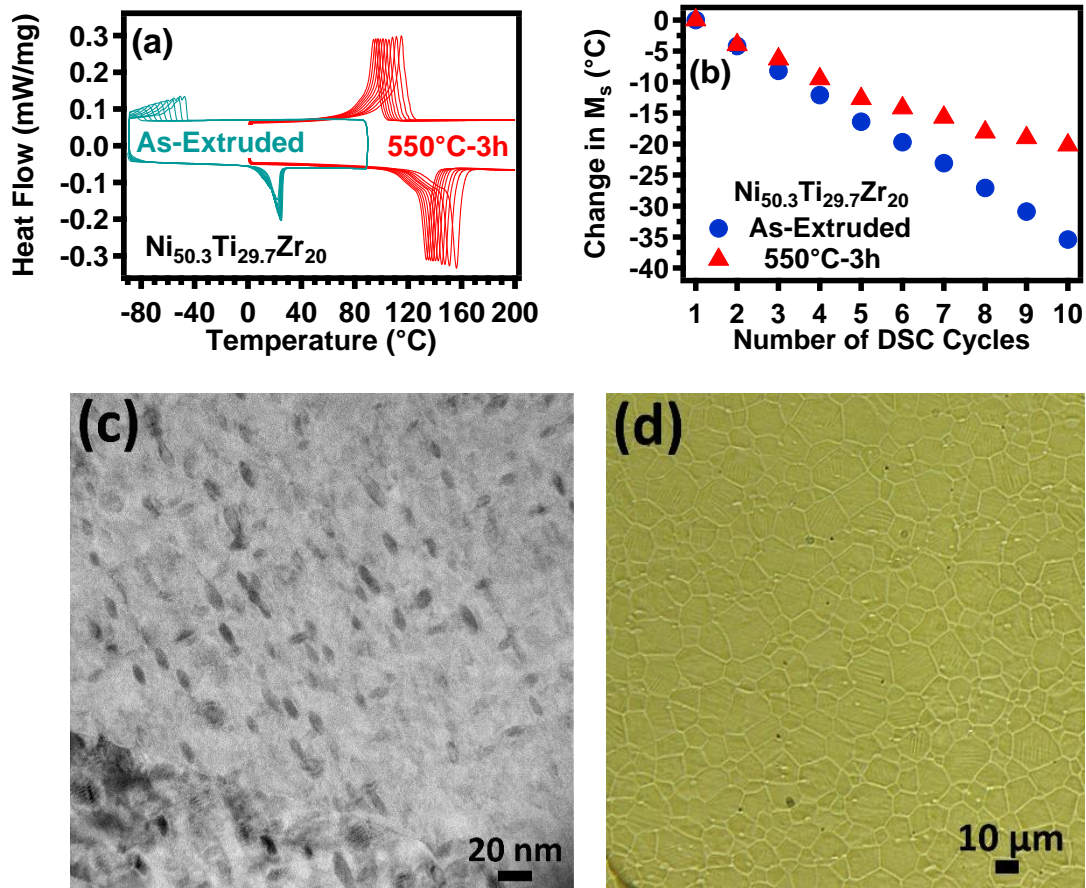


Figure 8.1. Initial material properties of nano-precipitation hardened $\text{Ni}_{50.3}\text{Ti}_{29.7}\text{Zr}_{20}$ alloy before the actuation fatigue testing (a) transformation temperatures of specimens in as-extruded condition and aged at 550°C -3h, (b) decrease in the M_s of specimen as a function of DSC cycles under stress free conditions for as-extruded condition and aged at 550°C -3h, (c) bright field TEM micrograph of microstructure after aging at 550°C -3h, (d) grain size analysis in the optical microscopy for sample aged at 550°C -3h.

A sample of $\text{Ni}_{50.3}\text{Ti}_{29.7}\text{Zr}_{20}$ alloy was produced by induction melting and subsequently homogenized in vacuum at 1050°C -72h. The ingots were then extruded at 900°C with area reduction ratio of 7:1. The as-extruded rod was machined into dog-bone shaped specimens that were aged at 550°C for 3h. Finally, specimens were thermo-mechanically

cycled until fracture at different UCT levels, specifically 250, 300, 350 and 400°C in custom-built constant load fatigue test frames.

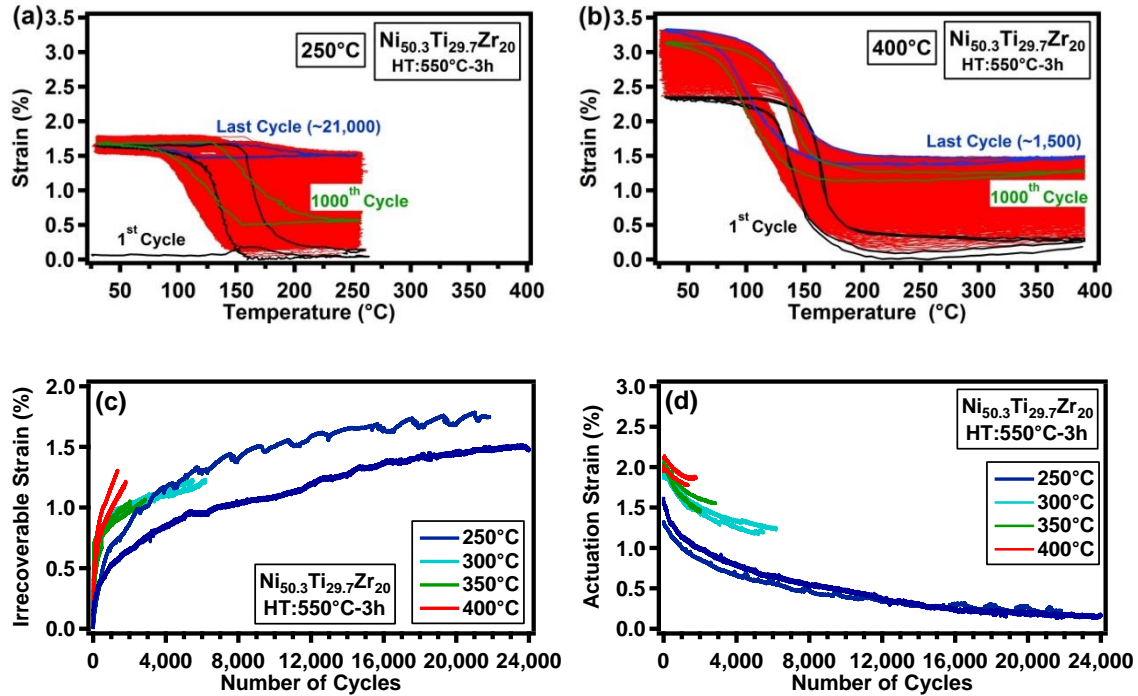


Figure 8.2 Effect of UCT levels on the actuation fatigue performance of nano-precipitation hardened $\text{Ni}_{50.3}\text{Ti}_{29.7}\text{Zr}_{20}$ alloys, temperature vs. strain vs evolution until failure of specimens at (a) 250°C UCT, (b) 400°C UCT and evolution of (c) actuation strain and (d) irrecoverable strain for various UCT levels.

Prior to fatigue testing, initial material characteristics were determined using DSC, TEM and optical microscopy to evaluate the evolution of microstructure and thermal behavior after the failure of the specimen (Figure 8.1). Examination of the first stress-free DSC cycle showed as-extruded samples having a M_s of -45°C, whereas, 550°C-3h aged samples had a M_s of 122°C (Figure 8.1 (a)). After ten DSC cycles M_s reduced by 35°C for the as-extruded specimens, and 20°C for the specimens aged at 550°C -3h (Figure 8.1 (b)). The change in transformation temperatures was significantly affected by

aging treatment as is evident from the large differences between these values. Aged samples reached a more stable condition faster than the as-extruded specimens. The TEM micrograph shows that aging at 550°C-3h resulted in a homogeneous distribution of densely populated H-phase nano-precipitates throughout the martensite matrix and are ~10-20nm in length and ~3-7nm in width (Figure 8.1 (c)). Grain sizes were measured using optical microscopy and were between 3-30 μ m (Figure 8.1 (d)).

Figure 8.2 (a) and (b) show the strain vs. temperature evolution with thermal cycling under stress level of 300MPa for two extreme UCT levels of 250°C and 400°C. Irrecoverable strain progressively increased throughout the life of the actuator for all selected UCT levels (Figure 8.2 (c)). A large accumulation of irrecoverable strain was observed over the first few hundred cycles and continued to increase at a lower rate until fracture. The rapid increase of irrecoverable strain in the early cycles was more prominent at the higher UCTs as the amount of permanent strain increases more rapidly at higher operating temperatures. Thermal hysteresis shifted to the right during thermomechanical cycling, signifying increased transformation temperatures as a function of thermal cycles. Actuation fatigue testing revealed that UCT played an important role in determining the durability of specimens and their corresponding actuation strain (Figure 8.2 (d)). When comparing the fatigue test results from distinct applied UCT levels, it was found that as UCT was increased, so did actuation strain, however, fatigue life decreased. UCT of 250°C resulted in a fatigue life of ~21,000, however, increased UCT levels reduced fatigue life to ~1,500 at 400°C. These results demonstrate that average fatigue life for specimens at 250°C UCT is fourteen times

longer than that of samples at 400°C UCT. Unlike the fatigue life trend, increase in UCT improved reversibility of actuation strain, hence, the largest actuation strain was obtained at the highest applied UCT. Less actuation strain during repeated transformations at an UCT of 250°C is an indication of the material undergoing partial transformation during cycling. Actuation strain decreased continuously throughout the life of the actuator for all UCT levels. Specimens with an UCT of 400°C had ~1.9% actuation strain, and those with an UCT of 250°C resulted in ~0.47% actuation strain.

Microstructural characterization after failure was aimed to relate the evolution in the microstructure, thermal and mechanical properties to shape memory performance of nano-precipitation hardened Ni-rich NiTiZr. The DSC curves in Figure 8.3 (a) demonstrate the change in heat flow during cooling of the tested and untested samples. Broadening of the cooling curve is an indication of heterogeneous transformation due to defects and cracks in the material. Stabilization of martensite, caused by internal stresses accumulated during repeated transformations, reduced the amount of material available to undergo martensitic transformation which significantly reduced the heat of transformation. The reduction in the heat of transformation was more pronounced in the test with an UCT 250°C. Figure 8.3 (b) displays the differences between tested and untested fatigue M_s temperatures of the samples ($\Delta M_s = M_s^{\text{after fatigue}} - M_s^{\text{before fatigue}}$). There was a almost linear relationship between increase in fatigue life and ΔM_s . From this experimentation, it was observed that thermomechanical cycling during repeated transformations increased transformation temperatures, as can be seen by the increase in

M_s temperature after cycling. The largest increase in transformation temperature was observed at 250°C and is associated with the highest fatigue life.

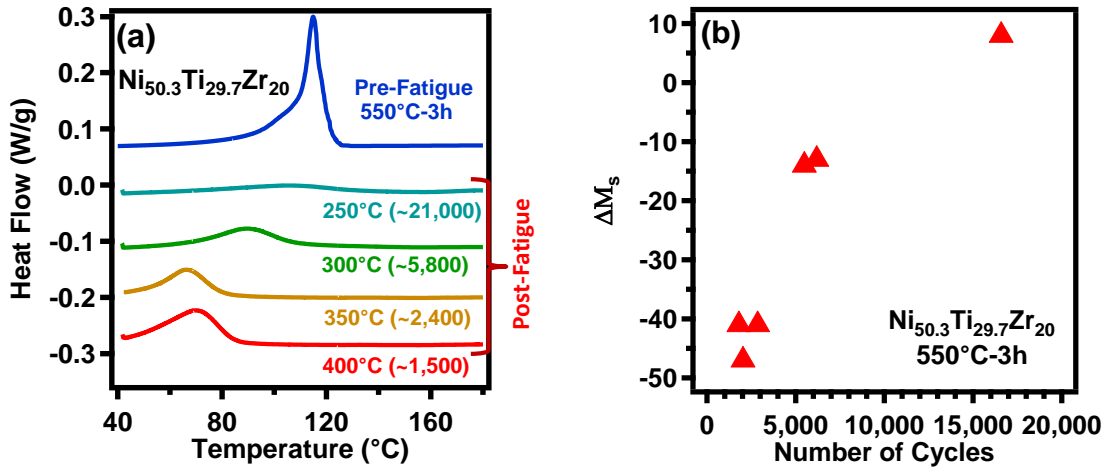


Figure 8.3. Post- mortem analysis through DSC after failure of samples (a) heat of transformation of failed samples at different UCT levels as compared to untested sample in the stress free condition during cooling, (b) evolution of M_s temperature of failed samples relative to an untested sample. $\Delta M_s = M_s^{after\ fatigue} - M_s^{before\ fatigue}$.

The SEM micrographs in Figure 8.4 show the cross-sectional fatigue fracture morphologies for the two extreme UCT conditions of 250°C and 400°C. Higher applied UCT level promoted mostly intergranular cracking (Figure 8.4 (b)), whereas lower applied UCT level mostly favored transgranular cracking (Figure 8.4(a)). It is assumed that continual void formation weakened the samples during the extended period of repeated martensitic transformation. Upon further examination of the cross-section of the samples (Figure 8.4 (c and d)), it appears that a low crack density formed during repeated cycling and propagated perpendicular to the applied stress. These cracks appeared similarly in all samples and so were identified as a likely cause of fracture.

Increased UCT levels caused faster defect formation, hence, shorter fatigue life. Cracks ranged from 100 μm to 500 μm in size.

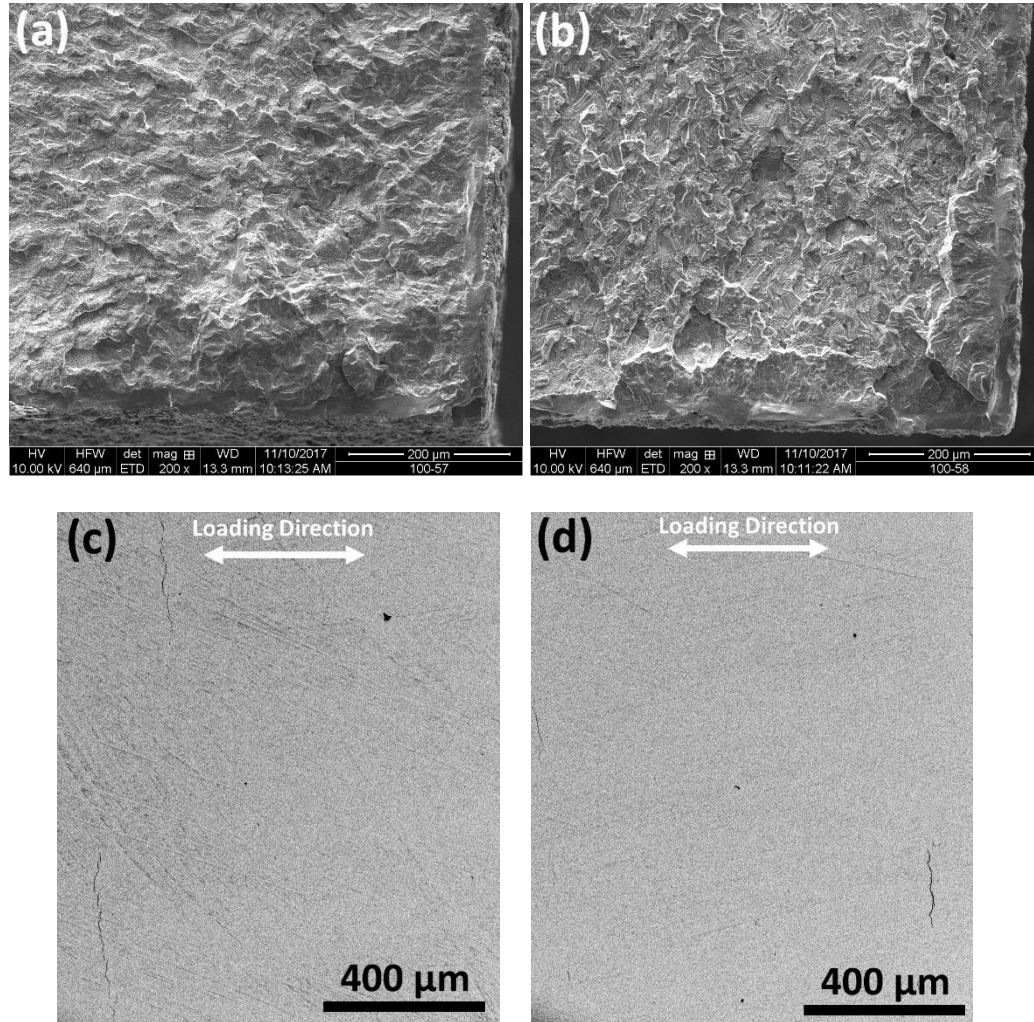


Figure 8.4. Secondary electron images of the fracture surfaces of nano-precipitation hardened $\text{Ni}_{50.3}\text{Ti}_{29.7}\text{Zr}_{20}$ HTSMA specimens after failure at (a) 250°C-UCT and (b) 400°C-UCT, backscattered electron micrographs of microstructure examined in the interior section of broken samples at (c) 250°C-UCT and (d) 400°C-UCT.

This first comprehensive thermally activated actuation fatigue study of nano-precipitation hardened $\text{Ni}_{50.3}\text{Ti}_{29.7}\text{Zr}_{20}$ alloy was conducted under different applied UCT levels. Fatigue tests and microstructural observation show that having an UCT above

300°C results in a drastically reduced fatigue life performance, however, actuation strain increases at a higher applied UCT. NiTiZr alloys demonstrate a reasonable fatigue life of ~21,000 at 250°C associated with ~0.47% actuation strain. Higher UCT yields poorer mechanical stability, resulting in earlier failure and larger permanent strain over fewer cycles. The microstructure of post-failure specimens revealed crack formation during repeated transformation ultimately leading to the failure of the samples. This crack initiation was accelerated at a higher UCT and these cracks then propagated through the thickness of the specimens promoting earlier fracture. This work has demonstrated that nano-precipitation strengthened Ni_{50.3}Ti_{29.7}Zr₂₀ can be a viable actuator material in high-temperature applications provided the UCT is maintained $\leq 300^\circ\text{C}$.

CHAPTER IX

COMPARISON OF ACTUATION FATIGUE PERFORMANCE FOR NI-RICH NITiHF AND NITiZR HIGH TEMPERATURE SHAPE MEMORY ALLOYS

The focus of this study is centered on investigation of actuation fatigue performance of Ni-rich NiTiHf and NiTiZr alloys. After proper heat treatment, Ni-rich NiTiHf and NiTiZr alloys exhibit reasonable shape memory properties due to formation of nano-scale H-phase precipitates. But prior to widespread implementation of these promising alloys in high temperature applications, characterization and a detailed understanding of the actuation fatigue performance of these alloys is needed. Consequently, thermomechanical fatigue testing through the thermally induced phase transformation under constant loads from 200 to 500 MPa is performed until failure.

To our knowledge, comprehensive study in Hf- and Zr-based HTSMAs is still lacking in the literature. Available comparative studies are mostly limited to transmission electron microscopy (TEM) and calorimetry investigation. This study constitutes the first systematic comparative investigation on actuation fatigue properties of Ni-rich NiTiHf and NiTiZr. Comparing Hf and Zr addition at same stoichiometric composition will provide a better assessment of actuation fatigue performance of these alloys under different stress levels. Additionally, precise characterization through microstructure (precipitates size, morphology and volume fraction), mechanical testing (stress vs. strain evolution) and thermal analysis will provide a better understanding on actuation fatigue life and strain differences between two alloys. In summary, with larger actuation strain, higher fatigue life and work-output, nano-precipitation hardened $\text{Ni}_{50.3}\text{Ti}_{29.7}\text{Hf}_{20}$ alloy demonstrates extraordinary promise. Consequently, utilization of this class of alloys in

elevated temperature applications occurs where high work-output density and high fatigue life are desired.

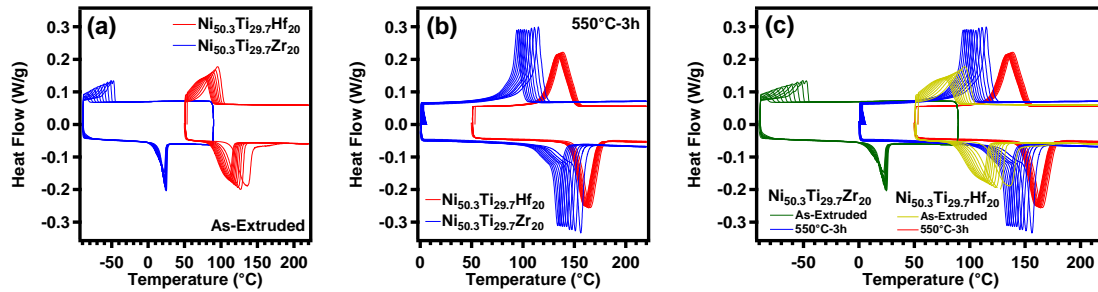


Figure 9.1. Comparison of transformation temperatures for $\text{Ni}_{50.3}\text{Ti}_{29.7}\text{Hf}_{20}$ and $\text{Ni}_{50.3}\text{Ti}_{29.7}\text{Zr}_{20}$ alloys in the condition of (a) As-Extruded (b) 550°C-3h and (c) both As-Extruded and 550°C-3h.

9.1. Stress-Free Martensitic Transformation Temperature and Thermal Stability

As it is known, aging treatment plays significant role in enhancing mechanical and shape memory properties of SMAs. Nano-precipitation hardening at 550°C-3h was shown to be effective heat treatment in improving actuation fatigue response of HTSMAs. The present study has started on the basis of this scenario where as-extruded NiTiHf and NiTiZr alloys were heat treated at 550°C-3h to modify transformation temperatures and strengthen the thermal and mechanical stability. Ten consecutive DSC cycles were performed on as-extruded and aged samples to examine improvement in the thermal properties of HTSMAs samples.

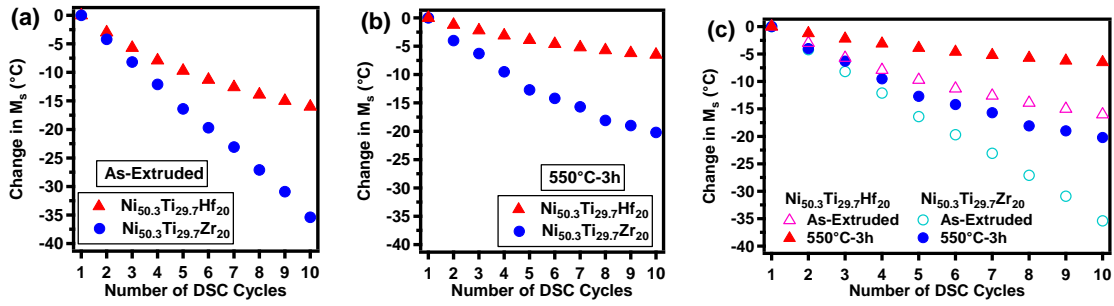


Figure 9.2. Decrease in the M_s temperatures of $Ni_{50.3}Ti_{29.7}Hf_{20}$ and $Ni_{50.3}Ti_{29.7}Zr_{20}$ alloys due to stress free thermal cycling through DSC in the condition of (a) As-Extruded (b) 550°C-3h and (c) both As-Extruded and 550°C-3h.

Figure 9.1 compared the DSC results for $Ni_{50.3}Ti_{29.7}Hf_{20}$ and $Ni_{50.3}Ti_{29.7}Zr_{20}$ alloys in both as-extruded and 550°C-3h cases. DSC results indicated that Hf addition instead of Zr to binary NiTi alloy is much more effective in increasing transformation temperatures in as-extruded (precipitate-free). The transformation temperatures of materials aged at 550°C-3h were higher than as-extruded condition due to formation of H-phase precipitates within the microstructure (Figure 9.1. (a) and (b)). H-phase precipitates are relatively Ni-rich compared to microstructure of alloy. Thus, the increase in the transformation temperatures after aging was rationalized on the basis of nickel loss in the matrix due to creation of Ni-rich H-phase precipitates. Besides, $Ni_{50.3}Ti_{29.7}Hf_{20}$ alloy exhibited higher transformation temperatures than $Ni_{50.3}Ti_{29.7}Zr_{20}$ counterpart in both as-extruded and aging at 550°C cases. However, precipitation hardening led to higher transformation temperature rise in Zr-based alloy which is consistent with TEM observation, indicating that size of H-phase precipitates was bigger in Zr-based alloy than that in Hf-based alloy (Figure 9.1). While the difference in M_s was 150°C in as-extruded case, nano-precipitation hardening reduced this difference to 30°C. Sluggish

diffusivity of Hf as compared to Zr was the main reason in the reduction of difference in M_s , indicating faster coarsening kinetics for Zr.

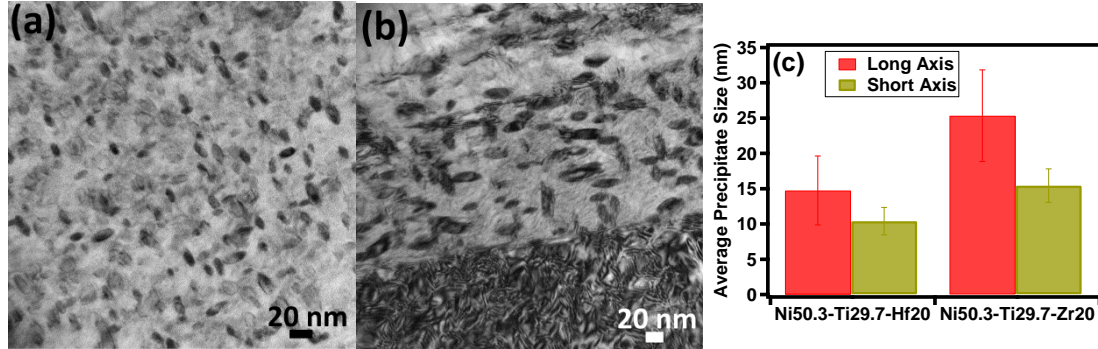


Figure 9.3. Comparison of morphology, size and distribution of precipitates after aging at 550°C-3h for (a) Ni_{50.3}Ti_{29.7}Hf₂₀ (b) Ni_{50.3}Ti_{29.7}Zr₂₀ and (c) comparison of size of precipitates along long axis and short axis for Ni_{50.3}Ti_{29.7}Hf₂₀ and Ni_{50.3}Ti_{29.7}Zr₂₀ alloys.

Thermal hysteresis is calculated as $(\Delta T: A_f - M_s)$. Thermal hysteresis was considerably smaller in Hf-based alloy than Zr-based alloy in as-extruded condition. In both alloys, aging at 550°C-3h decreased the thermal hysteresis in comparison to as-extruded case as a result of precipitation strengthening (Figure 9.2). Change in first M_s temperature with respect to following subsequent stress-free thermal cycles represents thermal stability of alloy ($\Delta M_s: M_s^{first} - M_s^{tenth}$). Nano-precipitation hardening improved thermal stability of both alloys. The shifts in M_s decreased after 3 or 4 consecutive cycles due to formation precipitates as compared to as-extruded case in both alloys since precipitation hardening generated fewer amounts of defects during stress-free transformation. The shift in M_s was smaller in Hf-based alloy than Zr-based alloy, indicating that Hf-based alloy has stronger resistance to formation of defects.

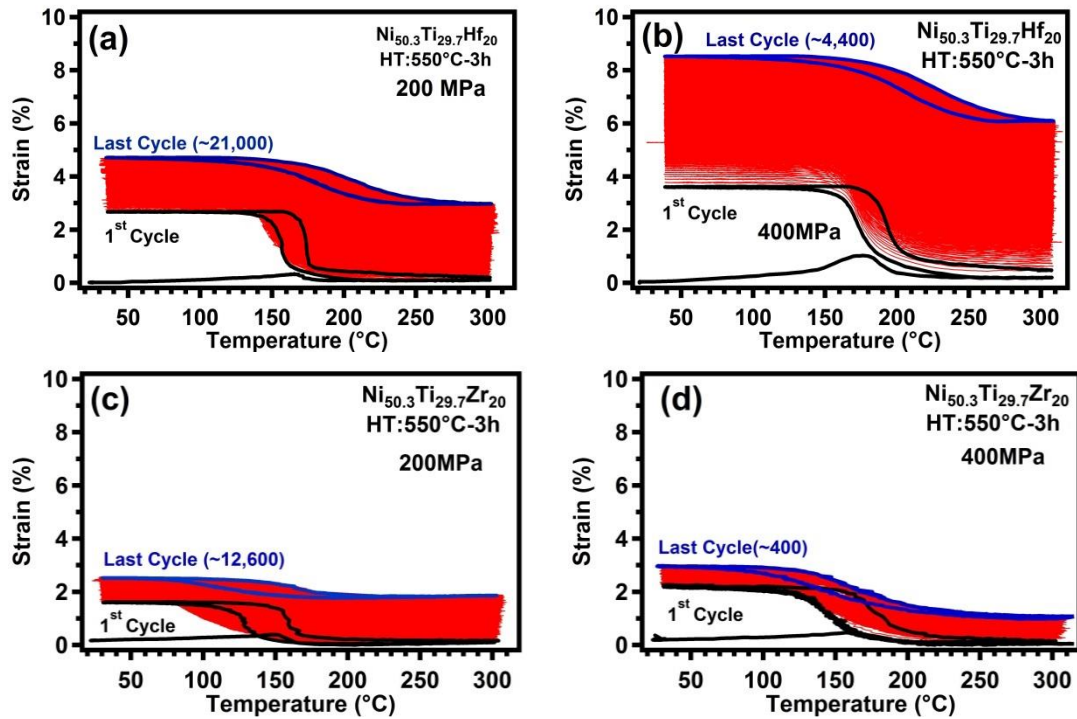


Figure 9.4. Strain vs. temperature response of nano-precipitation hardened $\text{Ni}_{50.3}\text{Ti}_{29.7}\text{Hf}_{20}$ loaded at (a) 200MPa, (b) 400MPa and $\text{Ni}_{50.3}\text{Ti}_{29.7}\text{Zr}_{20}$ loaded at (c) 200MPa, (d) 400MPa.

9.2. Microstructure of NiTiHf and NiTiZr Alloys

Figure 9.3 (a) and (b) showed bright field TEM images to compare the size, morphology and distribution of precipitates in the $\text{Ni}_{50.3}\text{Ti}_{29.7}\text{Hf}_{20}$ and $\text{Ni}_{50.3}\text{Ti}_{29.7}\text{Zr}_{20}$ alloys aged at 550°C-3h. Morphology of precipitates was same and spindle like in shape for both alloys. The comparison of precipitate sizes was summarized in Figure 9.3 (c). Aging treatment at 550°C-3h resulted in larger precipitates in NiTiZr material than NiTiHf alloy for the same stoichiometric composition. This was attributed to faster coarsening kinetics in $\text{Ni}_{50.3}\text{Ti}_{29.7}\text{Zr}_{20}$ alloy due to increased mobility at elevated temperature since faster diffusivity of Zr as compared to Hf was readily apparent. After aging at 550°C-3h,

size of average precipitates was in 14.7nm in length along long axis in the NiTiHf alloy, while average precipitate size reached to 25.3nm in length in the NiTiZr alloy.

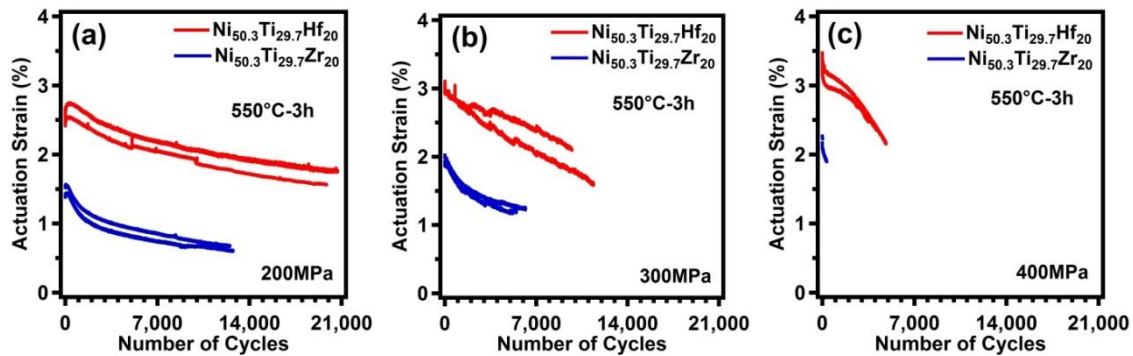


Figure 9.5. Evolution of actuation strain until failure of specimens for nano-precipitation hardened $\text{Ni}_{50.3}\text{Ti}_{29.7}\text{Hf}_{20}$ and $\text{Ni}_{50.3}\text{Ti}_{29.7}\text{Zr}_{20}$ materials under (a) 200MPa, (b) 300MPa and (c) 400 MPa.

9.3. Strain vs. Temperature of NiTiHf and NiTiZr alloys

Strain vs. temperature fatigue tests were carried out on $\text{Ni}_{50.3}\text{Ti}_{29.7}\text{Hf}_{20}$ and $\text{Ni}_{50.3}\text{Ti}_{29.7}\text{Zr}_{20}$ alloys aged at 550°C-3h as a method to evaluate actuation strain, dimensional stability and work-output under various stress levels. In the present study, specimens were loaded under constant stress levels through a series of ascending load levels (200MPa, 300MPa, 400MPa and 500MPa) and thermally cycled twice through transformation regime at each applied load levels.

Figure 9.4 illustrated strain vs. temperature evolution of both alloys until fracture of samples under stress levels of 200 and 400MPa. Actuation strain, irrecoverable strain, work output and fatigue life were derived from these data and compiled in Figure 9.5 Figure 9.6, Figure 9.7 and Figure 9.8. Fatigue test on NiTiZr alloy at 500MPa was not performed due to poor mechanical properties of this alloy at that stress level. Irrecoverable strain is the displacement that alloy can no longer recover through shape

memory effect. Irrecoverable strain was generated in each load-biased thermal cycling. Irrecoverable strain reached to maximum value at highest applied load levels for NiTiHf alloy, but NiTiZr alloy attained similar amount of irrecoverable strain at all stress level before failure. Shape of hysteresis loop in the 1st and last cycles in both alloys was different due to microstructural change during repeated transformations. Each load-biased thermal cycling contributed to plastic deformation through accumulation of dislocations and other type of defects that led to change in the microstructure of alloy.

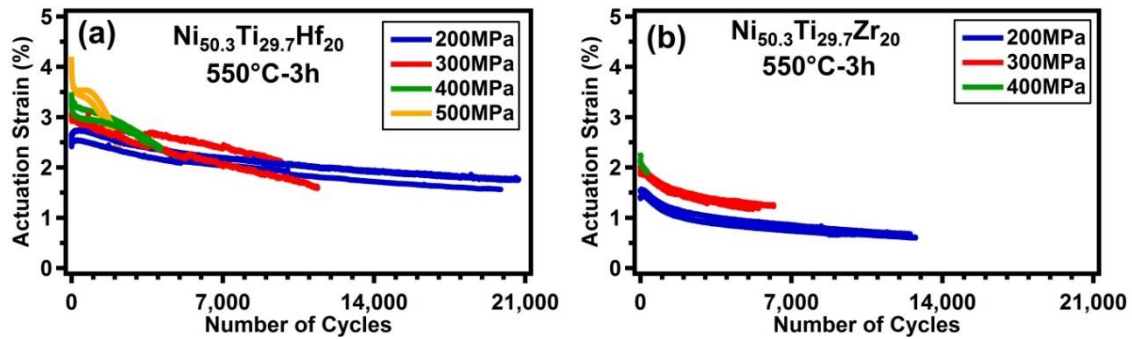


Figure 9.6. Effect of stress levels on the evolution of actuation strain for nano-precipitation hardened (a) Ni_{50.3}Ti_{29.7}Hf₂₀ and (b) Ni_{50.3}Ti_{29.7}Zr₂₀ alloys.

9.4. Actuation Fatigue Properties of NiTiHf and NiTiZr alloys

Nano-precipitation hardened Ni_{50.3}Ti_{29.7}Hf₂₀ and Ni_{50.3}Ti_{29.7}Zr₂₀ alloys were subject to isobaric thermal cycles until specimen fractured to evaluate their actuation fatigue properties. Stress levels were increased from 200MPa in 100 increments up to 400MPa and 500MPa. Figure 9.5 compared evolution of actuation strain at different applied stress levels. Ni_{50.3}Ti_{29.7}Hf₂₀ alloys had considerably higher actuation strain than Ni_{50.3}Ti_{29.7}Zr₂₀ counterpart at all applied stress levels. For instance, NiTiHf alloy were capable of generating 2.01% at 200MPa, while NiTiZr alloy can induce lower actuation strain of 0.86% on the average. This study suggested that addition of Hf to NiTi instead

of Zr element results in greater recoverable strain. The difference in the actuation strain may be rationalized that thickness of martensite plate in the NiTiHf material, is much smaller than that in NiTiZr material for similar precipitate sizes. Santamarta attributed this observation as an evidence for easier accommodation of transformation strain in NiTiZr materials than NiTiHf, which in turn resulted in lower transformation strain in the NiTiZr materials. Furthermore, NiTiHf alloy exhibited greater number of fatigue life over broad range of stress level than NiTiZr alloy. Average fatigue life was obtained as 20,200 for NiTiHf alloy loaded at 200MPa, while NiTiZr alloy can only withstand up to 12,600 isobaric thermal cycles. These observations revealed that neither actuation strain nor fatigue life of NiTiZr alloys is comparable with its NiTiHf counterpart.

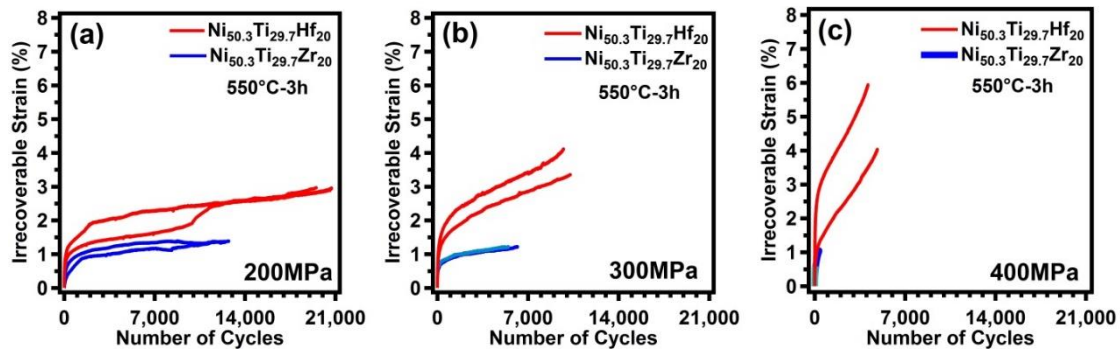


Figure 9.7. Evolution of irrecoverable strain until failure of specimens for nano-precipitation hardened $\text{Ni}_{50.3}\text{Ti}_{29.7}\text{Hf}_{20}$ and $\text{Ni}_{50.3}\text{Ti}_{29.7}\text{Zr}_{20}$ materials under (a) 200MPa, (b) 300MPa and (c) 400 MPa.

Figure 9.6 illustrated the influence of applied stress level on the actuation fatigue performance of NiTiHf and NiTiZr alloys. Actuation strain increased with increasing stress levels, reaching to peak value of 3.22% at 500MPa and 2.10% at 400MPa for Hf-based and Zr-based alloys, respectively (Figure 9.6). Higher applied stress levels

resulted in more martensite twin variants to reorient towards an orientation during cooling, thus inducing more transformation strain available to be recovered during subsequent heating sample above A_f temperature. Unlike the trend in actuation strain, fatigue life of specimen reduced while increasing applied stress level in both alloy. For instance, NiTiHf specimen under 200MPa lasted 20,200 cycles to failure, whereas same specimen was only capable of performing 4,100 cycles. NiTiZr alloy also experienced similar drop in fatigue life as applied stress level increased. Increase stress level from 200MPa to 400MPa reduced average fatigue life from 12,600 to 180 cycles. Rate of decrease was much faster with Zr-alloy, indicating Zr-alloy more sensitive to load level applied.

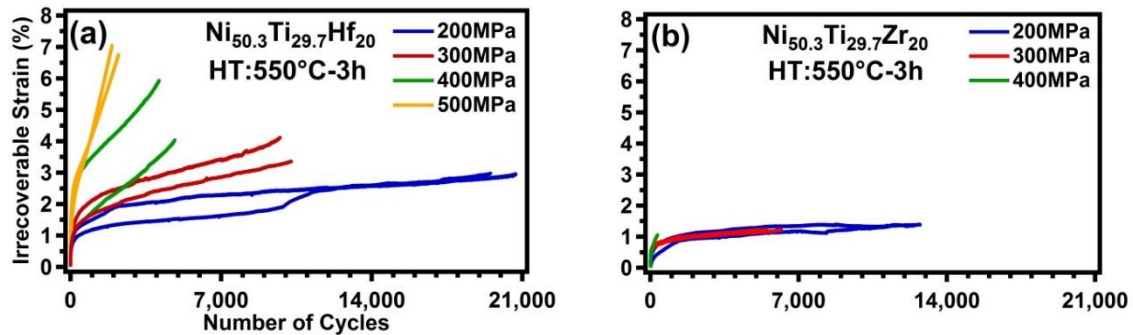


Figure 9.8. Effect of stress levels on the evolution of irrecoverable strain for nano-precipitation hardened (a) $\text{Ni}_{50.3}\text{Ti}_{29.7}\text{Hf}_{20}$ and (b) $\text{Ni}_{50.3}\text{Ti}_{29.7}\text{Zr}_{20}$ alloys.

Figure 9.7 represents comparison of irrecoverable strain for nano-precipitation hardened $\text{Ni}_{50.3}\text{Ti}_{29.7}\text{Hf}_{20}$ and $\text{Ni}_{50.3}\text{Ti}_{29.7}\text{Zr}_{20}$ alloys at different stress levels. Irrecoverable strain until failure of specimens is lower for the Zr-based alloy than Hf-based alloy at all stress levels. Increasing applied stress levels promoted plastic deformation, in a way that irrecoverable strain increased concomitant with isobaric

thermal cycles. In the early stage of thermal cycling, high amount of dislocations was generated. Consequently, all Hf- and Zr-based samples exhibited faster irrecoverable strain evolution rate over few hundred thermo-mechanical cycles. Afterwards, it started to continue at lower rate until failure of specimens.

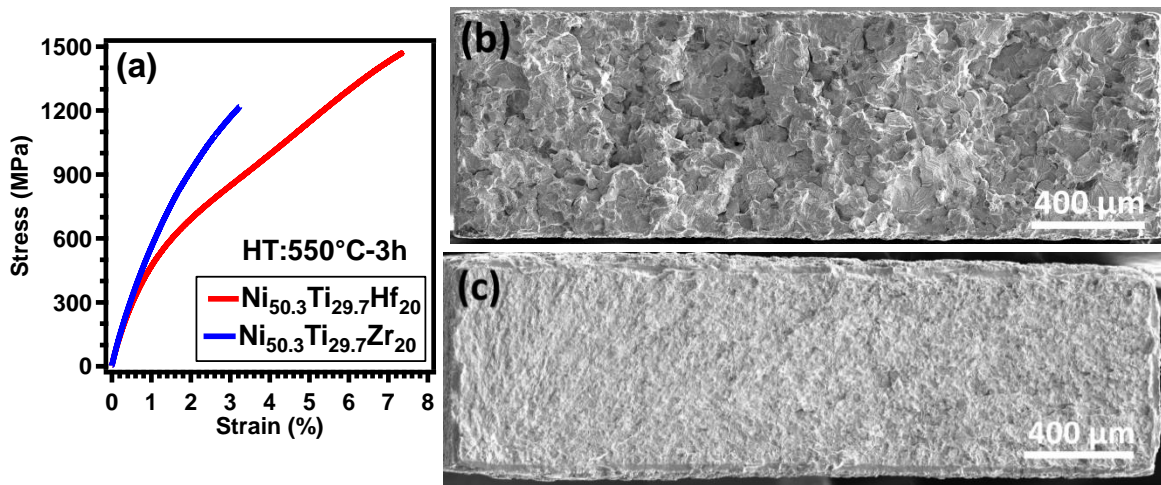


Figure 9.9. Comparison of uniaxial stress vs. strain curves of Ni_{50.3}Ti_{29.7}Hf₂₀ and Ni_{50.3}Ti_{29.7}Zr₂₀ material aged at 550°C-3h

Nano-precipitation hardened Ni_{50.3}Ti_{29.7}Zr₂₀ alloy appeared improved resistance against plasticity than Ni_{50.3}Ti_{29.7}Hf₂₀ alloy at all stress levels (Figure 9.8). However, when magnitude of actuation strain was taken into account, their irrecoverable strains were comparable since Hf-based alloy had greater actuation strain that may induce larger irrecoverable strain. Ratio of irrecoverable strain to actuation strain was 1.5 for NiTiHf alloy under 200MPa, while this ratio reached to 2.1 for NiTiZr alloy under the same stress level. The amount of irrecoverable strain or open-loop increased during each thermal cycle. Some unrecovered strain occurred at all stress levels applied, indicating

dimensional stability problem in both alloys even at relatively low stress level of 200MPa. Increased stress levels facilitated formation of irrecoverable strain, which peaked at 500MPa for NiTiHf alloy and at 400MPa for NiTiZr alloy.

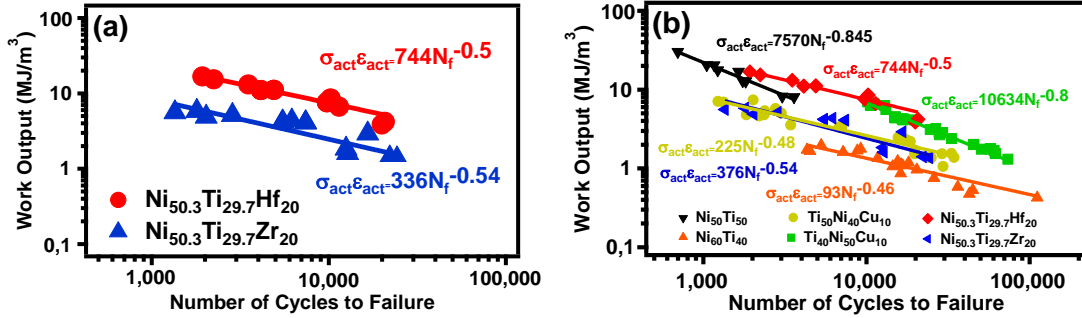


Figure 9.10. Comparison of work-output vs. number of cycles to failure of (a) Ni_{50.3}Ti_{29.7}Hf₂₀ vs. Ni_{50.3}Ti_{29.7}Zr₂₀ alloys and (b) high temperature shape memory alloys (HTSMAs) vs. low temperature shape memory alloys (LTSMAs) including Ti₄₀Ni₅₀Cu₁₀ wires, bulk Ni₅₀Ti₅₀, Ti₅₀Ni₄₀Cu₁₀ wires, bulk Ni₆₀Ti₄₀. The equations and solid lines are obtained through power-law relationship $\sigma_{act}\epsilon_{act} = aN_f^{-b}$.

9.5. Stress-Strain Behaviour of NiTiHf and NiTiZr Alloys

Figure 9.9 displayed the stress-strain curves of nano-precipitation hardened NiTiHf and NiTiZr alloy at the room temperature. The initial slope was higher in NiTiZr alloy than NiTiHf alloy. The stress-strain curves profile of Zr-based alloy was indication of hard and brittle sample with high modulus and low degree of elongation. Consequently, it fractured at a much lower strain. This observation supported the idea that addition of Hf produced low modulus sample, resulting in increase in the degree of elongation with low modulus. It is hard to define yield point of both alloys. Thus, offset yield point was set at 0.2% plastic strain. While yield strength of NiTiHf was 435MPa, ultimate strength was approximately 1470MPa. NiTiZr alloy had yield strength of 600MPa and ultimate strength of 1220MPa.

Fractography of failed samples at 300MPa was performed by means of SEM microscopy. SEM micrographs of fractures surfaces demonstrated that the most predominant fractographic features in NiTiZr was brittle fracture since the fracture surface was flat and smooth, suggesting rapid initial crack growth in a brittle mode. NiTiHf alloy promoted moderately ductile fracture which was consistent with the results of stress vs. strain curve. Brittle fracture mode in NiTiZr is up to debate. It might be intrinsic property of this alloy or sample might contain higher amount carbide and oxide content than Hf-based alloy.

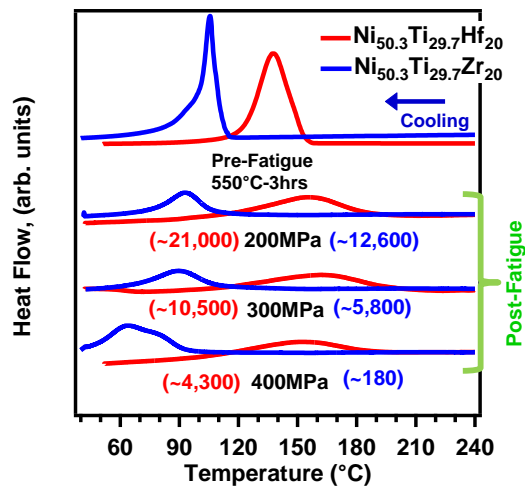


Figure 9.11. Changes in the transformation temperatures and transformation heat of the fatigue failed $\text{Ni}_{50.3}\text{Ti}_{29.7}\text{Hf}_{20}$ and $\text{Ni}_{50.3}\text{Ti}_{29.7}\text{Zr}_{20}$ samples during heating at different stress levels as compared to the untested and aged $\text{Ni}_{50.3}\text{Ti}_{29.7}\text{Hf}_{20}$ and $\text{Ni}_{50.3}\text{Ti}_{29.7}\text{Zr}_{20}$ samples at 550°C-3h.

9.6. Stress-Free Transformation Heat and Temperatures of Failed Samples

DSC measurement was performed on failed samples to observe the change in the transformation heat and temperatures of untested and failed samples during cooling process as seen in Figure 9.11 for both alloys. Clearly, significant changes were observed in both transformation temperatures and transformation heat following

actuation fatigue cycling. The area under curve represents transformation heat during cooling process. Failed NiTiHf specimens experienced large reduction almost 50% (from 18J/g to 9J/g) as compared to untested sample, while larger reduction nearly 70% (from 15J/g to 5J/g) in the transformation heat was observed for failed NiTiZr alloy at 200MPa and 300MPa with exception of the stress level at 400MPa where NiTiZr exhibited lower reduction in transformation heat due to shorter fatigue life ~180 cycles. Thermomechanical cycling also led to transformation peaks and range to get wider, implying the inhomogeneous microstructure. It indicated that some part of samples started to transform earlier than others due to microstructural inhomogeneity generated by dislocations and other type of defects during repeated transformations. Decrease in heat of transformation was a consequence of accumulation of plastic deformation that stabilizes the martensite phase and allows fewer regions to undergo martensitic transformation. The decrease in the transformation heat was consistent with decrease in the actuation strain, implying less smaller volume of transforming microstructure at the end of the actuation fatigue cycling.

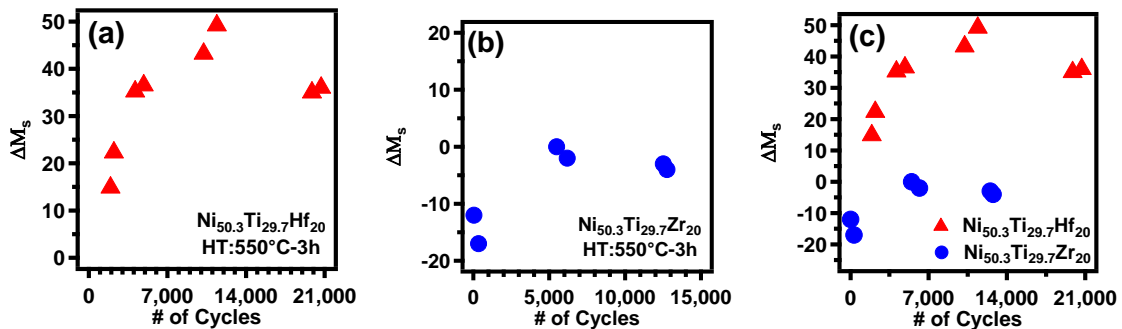


Figure 9.12. Post-mortem DSC results demonstrating evolution of the M_s temperatures of the fatigue failed specimens as compared to the untested nano-precipitation hardened (a) $Ni_{50.3}Ti_{29.7}Hf_{20}$ (b) $Ni_{50.3}Ti_{29.7}Zr_{20}$ (c) both $Ni_{50.3}Ti_{29.7}Hf_{20}$ and $Ni_{50.3}Ti_{29.7}Zr_{20}$. $\Delta M_s = M_s^{after\ fatigue} - M_s^{before\ fatigue}$.

Figure 9.12 displayed the difference between pre- and post-fatigue M_s temperatures ($\Delta M_s = M_s^{\text{after fatigue}} - M_s^{\text{before fatigue}}$) of nano-precipitation hardened NiTiHf and NiTiZr alloys. NiTiHf alloys exhibited notably much higher ΔM_s than NiTiZr alloys. The increase in ΔM_s is result of oriented internal stress fields or growth of precipitates during repeated transformations. NiTiHf alloy exhibited an increasing trend in M_s concomitant with increase in fatigue life for the applied stress levels ranging from 300MPa to 500 MPa. The samples at 200 MPa, however, slightly deviated from this increasing trend since less quantity of internal stress was stored than those of the other selected stress levels. Interestingly, almost entire NiTiZr alloy attained ΔM_s below 0°C , indicating lack of preferred oriented martensite by oriented internal stress fields. Increase in transformation temperatures appears independent from growth of precipitates since H-phase precipitates grow faster in NiTiZr alloys due to faster diffusivity of Zr, but failed NiTiZr alloys had ΔM_s below 0°C . Consequently, the increase in ΔM_s should be a consequence of oriented internal stress fields generated by oriented martensite and dislocations.

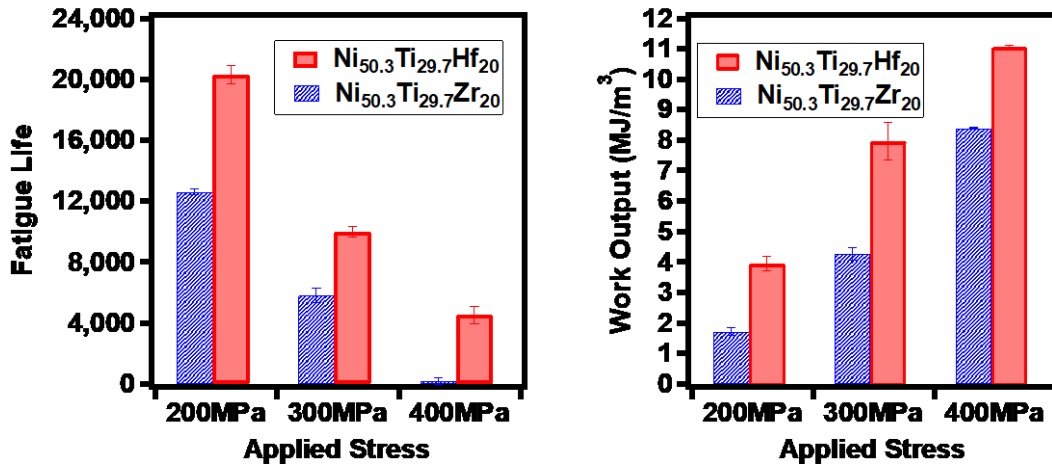


Figure 9.13. Comparison of nano-precipitation hardened $\text{Ni}_{50.3}\text{Ti}_{29.7}\text{Hf}_{20}$ and $\text{Ni}_{50.3}\text{Ti}_{29.7}\text{Zr}_{20}$ materials at different stress levels in terms of (a) fatigue life (b) work output.

9.7. Work-Based Model

Main interest in HTSMAs is their potential for use as a solid-state actuator and being a major component in adaptive structures. One of the primary aims of actuation fatigue testing is to develop a life prediction method by generating fatigue life data. Prediction methods will reduce the iterative process of fatigue testing that is expensive and time-consuming.

Stress-based and strain-based methods have been proposed to predict actuation fatigue life under constant stress. However, as it was presented by Calhoun *et al* for low temperature SMAs, neither the stress nor strain methods have successfully predicted actuation fatigue life of specimens. As an alternative to strain or stress based methods, a work-based method has been adopted to make fatigue life-prediction that accounts both varying actuation strain and stress levels. In the work-based method, actuation lifetime (N_f) has a correlation with work-output of specimen in each isobaric thermal cycle. Work-based method was established on the critical plane model of Smith, Watson and

Topper. Work-output at each stress level was measured by multiplying average actuation strain (ϵ_{act}) by constant stress level applied (σ_{act}). Power law formulation of work-based model is expressed as $\sigma_{act}\epsilon_{act} = aN_f^{-b}$, where two empirical actuation fatigue parameters a and b relate the work output to actuation lifetime of alloys (N_f). Based on work-based model formulation, decrease in fatigue parameter a leads to reduction in work-output, implying cyclic degradation of shape memory properties at a high rate. Inversely, increase in power exponent b refers to faster deterioration of samples, resulting in reduction in work-output along with number of cycles to failure.

Isobaric thermally cycled tests were carried out on nano-precipitation hardened Hf and Zr based alloys to evaluate their work-output potential which is one of the most critical factor in determining suitability of actuator in practical applications. Samples were subject to a series of increasing stress levels; 200MPa, 300MPa, 400MPa and 500MPa. The results showed that increasing stress levels increased the work-output, but decreased fatigue life. Adding Hf instead of Zr to NiTi alloy produced higher work-output.

Figure 9.10(a) exhibited work-output vs fatigue life data of NiTiHf and NiTiZr alloys that fit to power law equation of work-based model. NiTiHf alloy acquired greater value proportionality constant a than that of NiTiZr alloy, implying that NiTiHf is a promising candidate with higher work-output potential. Based on this observation and MTS results, it may be concluded that brittle samples promote lower proportionality constant a . Interestingly, both alloys attained similar value of $b \sim 0.5$. Figure 9.10(b) presented actuation fatigue data of high temperature SMAs and low temperature SMAs which were obtained from literature. Low temperature SMA consisted of dogbone shaped

specimens and small wires. The figure demonstrated that work-based model has properly predicted the actuation fatigue properties of either high and low temperature SMAs. Experimental data of different materials either low temperature or high temperature SMA have fitted well to same power exponent b . Interestingly, power exponent b became either ~ 0.5 or ~ 0.8 , pointing out that there is a mathematical law between physical and mechanical properties of SMA and power exponent b . In this study, mechanical properties of NiTiHf and NiTiZr was extracted, but to find a mathematical law, further mechanical analysis is required on one of low temperature SMA such as equiatomic NiTi which has power exponent of ~ 0.8 .

Based on observation captured from Figure 9.10, it was concluded that although operating temperatures of HTSMAs is relatively higher than low temperature SMAs, nanoprecipitation hardened NiTiHf alloys exhibited superior shape memory response than low temperature SMAs since suitability and performance of SMAs was determined in having high magnitude of work-output and fatigue life. Actuation fatigue performance of Ni-rich NiTiZr alloys are inferior to that of Ni-rich NiTiHf alloys. Brittle materials appear inappropriate for use as an actuator in the adaptive structures.

Figure 9.13 demonstrated the applied stress levels and resulting fatigue life and work-output in both alloys. Summary plot did not include work-output data at 500MPa for Zr-based alloy since this alloy is able survive up to several hundred cycles at 400MPa. Magnitude of work-output increased in a consistent with increasing applied stress levels, reaching a maximum value at 400MPa in both alloys. In contrast, fatigue life decreased with increasing stress level, reaching a peak at 200MPa.

9.8. Conclusions

The focus of the present study was centred on comparison of thermal, mechanical, microstructural and actuation fatigue behaviour of Ni-rich $\text{Ni}_{50.3}\text{Ti}_{29.7}\text{Hf}_{20}$ and $\text{Ni}_{50.3}\text{Ti}_{29.7}\text{Zr}_{20}$ alloys. Nano-precipitation hardened specimens at 550°C -3h were thermally cycled at different stress levels until fracture of specimens. Main findings are the as follows:

Transformation temperatures are 150°C higher in $\text{Ni}_{50.3}\text{Ti}_{29.7}\text{Hf}_{20}$ than $\text{Ni}_{50.3}\text{Ti}_{29.7}\text{Zr}_{20}$ in as-extruded condition. Precipitate hardening by aging at 550°C -3h reduced this difference 30°C due to formation of larger precipitate sizes in the Zr-based alloys. Hf addition is more effective to increase transformation temperature as compared to its counterpart Zr element. Furthermore, thermal stability is improved after nano-precipitation hardening in both alloys. After ten consecutive stress-free thermal cycles, reduction in M_s is 6.5°C for NiTiHf alloy, while NiTiZr alloy experiences 20°C drop in M_s ($^\circ\text{C}$), indicating Hf-based alloy more stable.

Aging at 550°C -3h introduced densely populated small nano-precipitates surrounded by a continuous martensite matrix. $\text{Ni}_{50.3}\text{Ti}_{29.7}\text{Zr}_{20}$ alloy has larger H-phase precipitate sizes than $\text{Ni}_{50.3}\text{Ti}_{29.7}\text{Hf}_{20}$, indicating faster precipitate-coarsening kinetics in the NiTiZr alloy for same stoichiometric composition.

Nano-precipitation hardened $\text{Ni}_{50.3}\text{Ti}_{29.7}\text{Zr}_{20}$ HTSMA specimens showed lower irrecoverable at all stress levels than its NiTiHf counterpart, indicating greater resistance to plastic deformation during repeated transformation.

NiTiHf alloy demonstrated higher fatigue life and larger actuation strain than NiTiZr alloy at all stress levels applied. Hence, NiTiZr systems have inferior shape memory properties to Hf alloyed NiTi ternary alloys. Besides, increase in stress level reduced fatigue life yet increase actuation strain in both alloys. Higher actuation strain came at the expense of diminished number of cycles to failure.

Stress vs. strain graph indicated that nano-precipitation strengthened NiTiZr alloy is found to be somewhat brittle than Ni-rich NiTiHf counterpart with lower degree of elongation which is supported by SEM micrograph which surface is smooth for Zr-based alloy while it is rough for Hf-based alloy.

Work-based model successfully captured actuation fatigue response of HTSMAs and LTSMAs. Both alloys contained almost equivalent power exponent $b \sim 0.5$ and different proportionality constant a . NiTiHf alloy produced greater work-output than NiTiZr alloy. Even though operating temperature is higher, NiTiHf alloy exhibited superior actuation fatigue response than LTSMA.

Precipitation hardened $\text{Ni}_{50.3}\text{Ti}_{29.7}\text{Hf}_{20}$ HTSMA produced attained higher amount of work-output, actuation fatigue life and actuation strain as compared to its precipitation hardened $\text{Ni}_{50.3}\text{Ti}_{29.7}\text{Hf}_{20}$ HTSMA counterpart. The current $\text{Ni}_{50.3}\text{Ti}_{29.7}\text{Hf}_{20}$ HTSMA exhibited great potential as an actuator in the high temperature applications.

CHAPTER X

TWO-WAY SHAPE MEMORY EFFECT IN THE NITIHf AND NITiZr HIGH TEMPERATURE SHAPE MEMORY ALLOYS

In the current study, the effect of constant load thermal cycles (training) on the thermomechanical behavior of nano-precipitation strengthened $\text{Ni}_{50.3}\text{Ti}_{29.7}\text{Hf}_{20}$ (NiTiHf) and $\text{Ni}_{50.3}\text{Ti}_{29.7}\text{Zr}_{20}$ (NiTiZr) high temperature shape memory alloys (HTSMAs) was compared. Thermomechanical properties were determined as a function of the number of training cycles, which consisted of up to 2000 isobaric thermal cycles at 300 MPa, between lower and upper cycle temperatures of 35 and 300 °C, respectively. In addition, the stability of the trained alloys was determined after exposing them to thermal treatments at temperatures above the upper cycle training temperature. Training at 300 MPa significantly improved the actuation strain capability of the NiTiHf HTSMA at low stresses (i.e., 50 MPa) and resulted in an extrapolated two-way shape memory strain (TWSMS) of 1.9%, but essentially had no effect on the 300 MPa response. Training had much lower benefits in the case of the NiTiZr, producing negligible TWSMS, and resulting in a decrease in actuation strain capability at 300 MPa with repeated cycling. Any benefits of training to the NiTiHf HTSMA were mostly maintained after aging at 400 °C but were lost after exposure to 500 °C and above. Since training was not very beneficial to the NiTiZr alloy and resulted in a loss in strain capability at 300 MPa, the high temperature annealing treatment actually recovered strain capability in the alloy.

Although there are several studies in literature about thermomechanical training of binary NiTi SMA and associated changes in shape memory characteristics [107, 114-118], limited studies are available for NiTi based HTSMAs [5, 108, 110, 119]. Training

procedures employed in these studies usually comprise a relatively low number of thermal cycles, i.e. up to a few hundred thermal cycles targeted to achieve a stable shape memory behavior in the HTSMA. A significant difficulty to obtain a stable response in HTSMAs is the recovery of the thermally cycled microstructure, either by the reversal of the retained martensite or relaxation of the defect structure due to the necessity to heat up to elevated transformation temperatures. For instance, Atli et. al [110, 120, 121] reported a near-perfect two-way shape memory effect (TWSME) stability in a $\text{Ti}_{50.5}\text{Ni}_{24.5}\text{Pd}_{25}$ HTSMA characterized by minimal shape changes during stress-free thermal cycling, but no significant TWSME in $\text{Ti}_{50.5}\text{Ni}_{28.5}\text{Pt}_{21}$ due to its relatively high transformation temperatures relaxing any training induced defects during thermal cycling. Applied stress during training cycles is another important parameter that defines the overall shape memory behavior of the trained material. A low stress may not be enough to fully reorient martensite variants during thermal cycling, and thus not induce a strong training effect; while high stresses may cause plastic deformation and martensite stabilization, essentially reducing the amount of transforming volume [123]. The effects of training stress magnitude and number of cycles on the resulting actuation behavior have recently been studied in $\text{Ni}_{50.3}\text{Ti}_{29.7}\text{Hf}_{20}$ torque tubes [119]. It was reported that an actuation shear strain of about 3%, independent of the applied stress, can be obtained in nano-precipitation hardened $\text{Ni}_{50.3}\text{Ti}_{29.7}\text{Hf}_{20}$ HTSMAs. The training effect got even better after a short term annealing heat treatment at 350 °C. However, increasing annealing temperatures, especially above 450 °C, started to degrade the training affected microstructure, decreasing the actuation strain.

While there are limited studies on the thermomechanical training behavior of NiTiHf HTSMAs, to our knowledge, there is no study conducted on the training behavior of Ni-rich NiTiZr HTSMAs and their thermal stability at elevated temperatures. Therefore, the first objective of the present study is to investigate the evolution of thermomechanical properties of nano-precipitation hardened $\text{Ni}_{50.3}\text{Ti}_{29.7}\text{Zr}_{20}$ (at. %) HTSMA during a training procedure consisting of 2000 thermal cycles at 300 MPa and compare with a baseline $\text{Ni}_{50.3}\text{Ti}_{29.7}\text{Hf}_{20}$ (at. %) HTSMA (Figure 3.3). Additionally, this study aims to understand the degradation of the actuation strain in both trained alloys after stress-free heat treatment at temperatures above their operating temperatures (>300 °C). The purpose here is to establish a fundamental understanding on the thermal stability of training induced dislocations and defects, and a systematic comparison of shape memory properties of these alloys. Trends in actuation strain, two-way shape memory strain and safe operation temperature ranges for these particular HTSMAs are finally reported.

10.1. Calorimetric results of Ni-rich $\text{Ni}_{50.3}\text{Ti}_{29.7}\text{Hf}_{20}$ and $\text{Ni}_{50.3}\text{Ti}_{29.7}\text{Zr}_{20}$ alloys

Figure 10.1(a) presents ten cycle DSC response of $\text{Ni}_{50.3}\text{Ti}_{29.7}\text{Hf}_{20}$ and $\text{Ni}_{50.3}\text{Ti}_{29.7}\text{Zr}_{20}$ HTSMAs heat treated at 550 °C for 3h. Both materials exhibit a single-stage transformation without any evidence of R-phase transformation. First cycle M_f , M_s , A_s and A_f temperatures of $\text{Ni}_{50.3}\text{Ti}_{29.7}\text{Hf}_{20}$ were measured as 125 °C, 155 °C, 152 °C and 178 °C, respectively, using the tangent intersection method. Transformation temperatures of $\text{Ni}_{50.3}\text{Ti}_{29.7}\text{Zr}_{20}$ in the first DSC cycle were found as 108 °C, 123 °C, 149 °C and 162 °C for M_f , M_s , A_s and A_f , respectively. Transformation enthalpy was 17.8 J/g

and 15.3 J/g for $\text{Ni}_{50.3}\text{Ti}_{29.7}\text{Hf}_{20}$ and $\text{Ni}_{50.3}\text{Ti}_{29.7}\text{Zr}_{20}$, respectively, measured as the area under the forward transformation peak (cooling cycle).

Figure 10.1(b) demonstrates the change in M_s temperature during ten consecutive stress-free DSC cycles for heat treated $\text{Ni}_{50.3}\text{Ti}_{29.7}\text{Hf}_{20}$ and $\text{Ni}_{50.3}\text{Ti}_{29.7}\text{Zr}_{20}$ alloys. Change in M_s temperature as a function of stress-free thermal cycles represents the cyclic stability of alloys ($\Delta M_s: M_s^{\text{first}} - M_s^{\text{tenth}}$). For $\text{Ni}_{50.3}\text{Ti}_{29.7}\text{Hf}_{20}$, there was a drop of 6.5 °C in M_s after ten DSC cycles, while for $\text{Ni}_{50.3}\text{Ti}_{29.7}\text{Zr}_{20}$, the same value was 20.2 °C. As it is well known, the decrease in transformation temperatures with stress-free thermal cycling may be attributed to the accommodation of the transformation shape change with defects during the repetitive motion of transforming phase interfaces [21]. The drop rate in M_s for $\text{Ni}_{50.3}\text{Ti}_{29.7}\text{Hf}_{20}$ decreased after four consecutive thermal cycles and the transformation temperature got almost stabilized after eight DSC cycles, whereas M_s of $\text{Ni}_{50.3}\text{Ti}_{29.7}\text{Zr}_{20}$ continued decreasing steadily throughout the ten cycles.

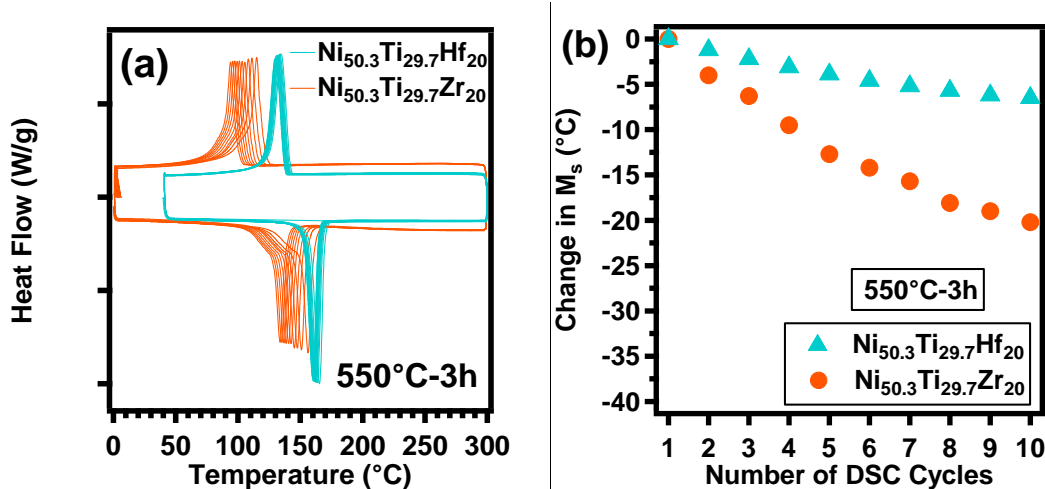


Figure 10.1 DSC results of $\text{Ni}_{50.3}\text{Ti}_{29.7}\text{Hf}_{20}$ and $\text{Ni}_{50.3}\text{Ti}_{29.7}\text{Zr}_{20}$ alloys aged at 550°C-3h (a) transformation temperatures and transformation heat (b) decrease in the M_s temperature representing cyclic instability of materials during stress-free thermal cycling across martensite and austenite phases.

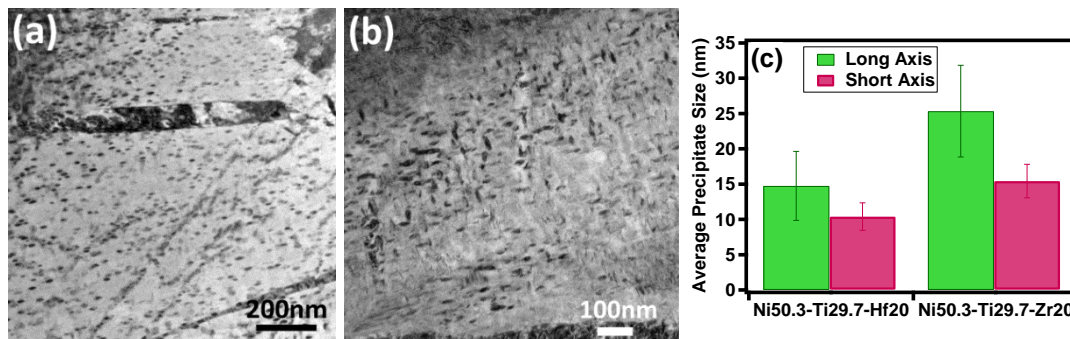


Figure 10.2 Bright field TEM images after aging at 550°C for 3h (a) Ni_{50.3}Ti_{29.7}Hf₂₀ (b) Ni_{50.3}Ti_{29.7}Zr₂₀ and (c) comparison of size of precipitates along long axis and short axis for Hf- and Zr- based alloys.

10.2. Electron microscopy results

Figure 10.2 (a) and (b) show the backscattered electron micrographs of as-extruded Ni_{50.3}Ti_{29.7}Hf₂₀ and Ni_{50.3}Ti_{29.7}Zr₂₀ HTSMAs, respectively. White particles (A) with sizes ranging from 0.4 to 3 μm were identified as HfC through EDS in NiTiHf, while dark gray second phases (B) with size of 2-5μm were of (Ti/Zr)₂Ni type with a measured composition of Ni₃₉Ti₃₅Zr₂₆ (at. %). Volume fraction of HfC is 0.17% in Ni_{50.3}Ti_{29.7}Hf₂₀, whereas second phases occupied a volume fraction of 0.95% in Ni_{50.3}Ti_{29.7}Zr₂₀. It is likely that HfC particles formed in Ni_{50.3}Ti_{29.7}Hf₂₀ due to the reaction of hafnium with carbon in the graphite crucible during melting.

Volume fraction and size of second phase are much greater in Ni_{50.3}Ti_{29.7}Zr₂₀ than Ni_{50.3}Ti_{29.7}Hf₂₀. Second phases were associated with low strength, poor reversibility, large thermal hysteresis in NiTiHf HTSMAs [24, 34, 70]. Thus, microstructural investigation results support the DSC and isothermal monotonic failure testing results (See Section 3.4) of NiTiHf and NiTiZr alloys. For this reason, NiTiZr might have

higher detwinning stress, lower ductility and poor reversibility than NiTiHf. Additionally, poor TWSME properties could be the consequence of higher volume fraction of second phases in NiTiZr.

Figure 10.2 (a) and (b) are the bright field TEM images showing the morphology, size and distribution of precipitates in aged $\text{Ni}_{50.3}\text{Ti}_{29.7}\text{Hf}_{20}$ and $\text{Ni}_{50.3}\text{Ti}_{29.7}\text{Zr}_{20}$ HTSMAs. Precipitate phase corresponded to the H-phase, a face-centered orthorhombic structure with $F 2/d 2/d 2/d$ space group described in [29, 95, 124]. Nanometer sized spindle-shaped precipitates were observed for both HTSMA compositions (Figure 10.2(c)). It can be inferred that aging at 550 °C for 3h led to a more pronounced coarsening effect for the precipitates in $\text{Ni}_{50.3}\text{Ti}_{29.7}\text{Zr}_{20}$ than $\text{Ni}_{50.3}\text{Ti}_{29.7}\text{Hf}_{20}$. The difference in precipitate size may be rationalized with faster coarsening kinetics in $\text{Ni}_{50.3}\text{Ti}_{29.7}\text{Zr}_{20}$ alloy due to increased mobility of Zr element at high aging temperatures since Zr is lighter than Hf. $\text{Ni}_{50.3}\text{Ti}_{29.7}\text{Zr}_{20}$ provides at least 20% weight reduction than $\text{Ni}_{50.3}\text{Ti}_{29.7}\text{Hf}_{20}$ [197]. Therefore, after aging at 550 °C for 3h, average long axis length of H-phase precipitates was measured as 14.7 nm and 25.3 nm in $\text{Ni}_{50.3}\text{Ti}_{29.7}\text{Hf}_{20}$ and $\text{Ni}_{50.3}\text{Ti}_{29.7}\text{Zr}_{20}$ HTSMA, respectively.

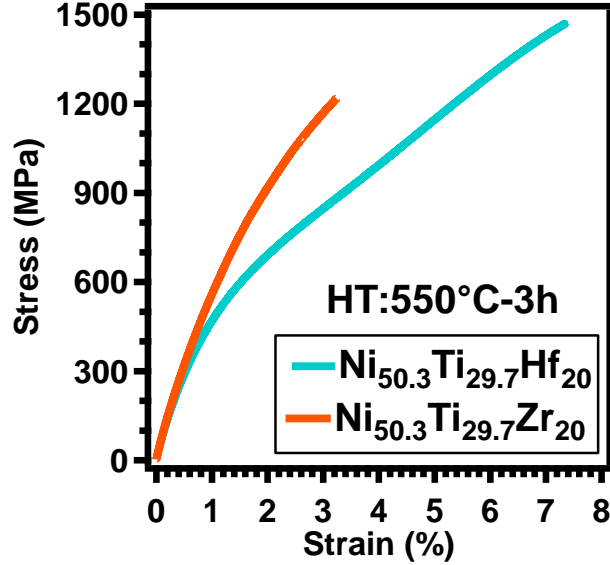


Figure 10.3 Comparison of uniaxial stress vs. strain curves of nano-precipitation hardened Ni_{50.3}Ti_{29.7}Hf₂₀ and Ni_{50.3}Ti_{29.7}Zr₂₀ HTSMAs.

10.3. Isothermal Monotonic Stress-Strain Response

Isothermal monotonic tensile tests were performed to compare the room temperature strength levels of nano-precipitation strengthened Ni_{50.3}Ti_{29.7}Hf₂₀ and Ni_{50.3}Ti_{29.7}Zr₂₀ HTSMAs. Figure 10.3 demonstrates the complete deformation behaviour of both materials to failure. It is observed that ultimate stress to fracture was 1470 MPa in NiTiHf with a ductility of 7.3%, while NiTiZr fractured at 1220 MPa at a much lower strain of 3.2%. The reorientation stress of NiTiHf and NiTiZr HTSMAs were recorded as 435 MPa and 600 MPa, respectively. Isothermal monotonic failure results of the materials will be useful in the following sections to elucidate the evolution behavior of the actuation strain as a function of training cycles.

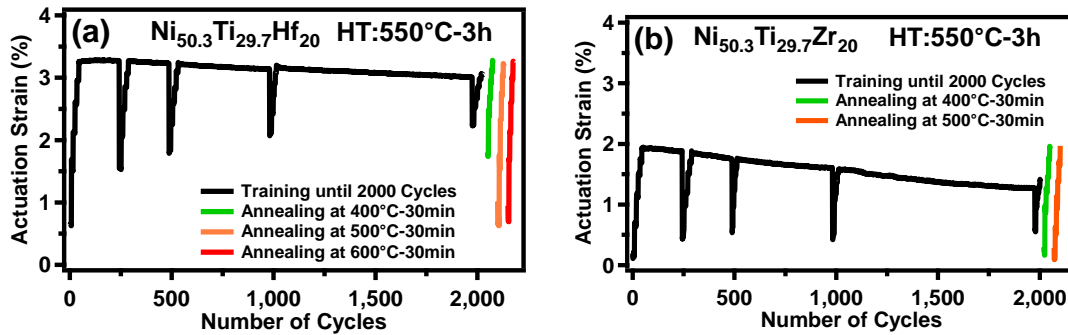


Figure 10.4 Evolution of actuation strain during thermomechanical training procedure employed in this study and subsequent effect of annealing treatment on the actuation strain of material previously trained for 2000-cycles isobaric thermal cycling. The results are for nano-precipitation hardened $\text{Ni}_{50.3}\text{Ti}_{29.7}\text{Hf}_{20}$ and $\text{Ni}_{50.3}\text{Ti}_{29.7}\text{Zr}_{20}$ alloys.

10.4. Evolution of the Actuation Strain and Generation of TWSME

To provide a fundamental understanding on the evolution of actuation strain and generation of TWSME as a result of thermomechanical training, key parameters that have influence on the magnitude and stability of the actuation strain and TWSME will be briefly introduced. During thermomechanical training of SMAs, transformation-induced plasticity (TRIP) is the most prominent deformation mechanism, which takes place during martensitic transformation due to volume mismatch between martensite and austenite phases, resulting in the formation of dislocations at the phase interfaces [110, 198]. Furthermore, general plasticity and creep deformation may occur due to formation of local stress concentrations above the critical resolved shear stress, which is strongly affected by the magnitude of the upper cycle temperature during thermomechanical training. Defects generated during training may also induce nucleation of preferred oriented martensite (OM) through oriented internal stress fields which is a source for generation of TWSME, yet excessive plasticity results in a reduction in the actuation strain [110, 120, 162, 199, 200]. For the NiTiHf HTSMA of the current study, three

possible mechanisms have recently been proposed by Hayrettin et al. [119] for the generation of the TWSME, which were remnant martensite, aligned nano-precipitates and dislocations and other defects or combination of these mechanisms. In the same study, TEM analysis showed that no significant change was observed in size and orientation of the precipitates after training, concluding that possible internal stress fields around aligned nano-precipitates could not be a reason for the TWSME. Based on his observation, it may be postulated that stability of the actuation strain and TWSME in NiTiHf and NiTiZr HTSMAs tested in the current study originates from dislocations and other defects.

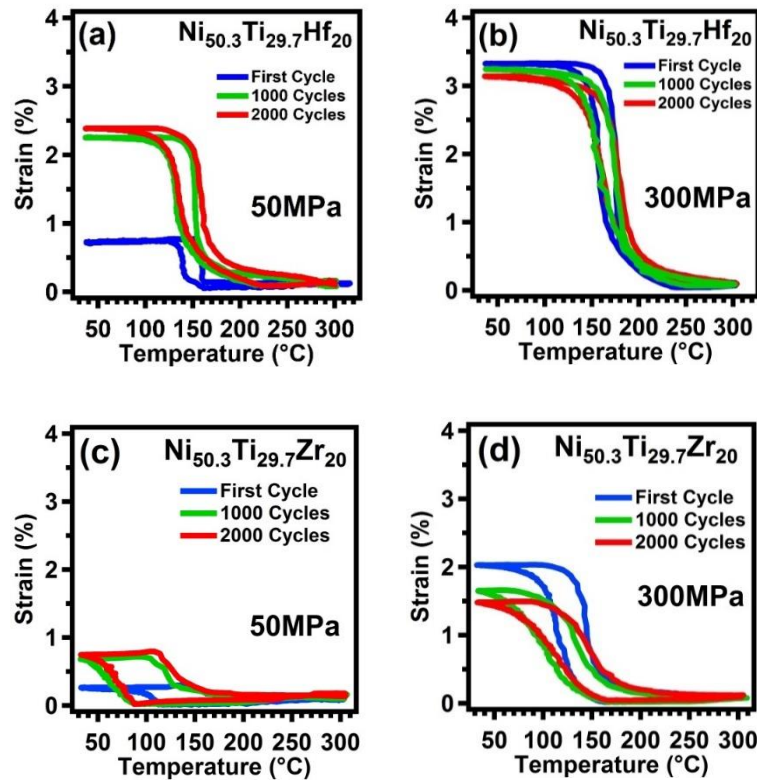


Figure 10.5 Evolution of strain vs. temperature response at 1st, 1000th and 2000th training cycles for nano-precipitation hardened Ni_{50.3}Ti_{29.7}Hf₂₀ under (a) 50MPa, (b) 300MPa and Ni_{50.3}Ti_{29.7}Zr₂₀ under (c) 50MPa, (d) 300MPa.

10.5. Thermomechanical training and evolution of actuation strain and TWSME

Figure 10.4 illustrates the evolution of actuation strain for nano-precipitation hardened $\text{Ni}_{50.3}\text{Ti}_{29.7}\text{Hf}_{20}$ and $\text{Ni}_{50.3}\text{Ti}_{29.7}\text{Zr}_{20}$ during the 2000 cycle thermomechanical training and the subsequent effect of annealing heat treatments on the evolution of actuation strain generated through the training procedure. It is observed for both HTSMAs that after the 1st characterization sequence, actuation strain reaches its maximum value. This value is 3.25% and 1.93% for NiTiHf and NiTiZr, respectively. As training cycles commence, the actuation strain starts declining at a steady rate of 10^{-4} % and 3×10^{-4} % per cycle for NiTiHf and NiTiZr, respectively, which clearly shows the superior actuation strain stability in the NiTiHf HTSMA. At the end of 2000 thermal cycles, the actuation strain of NiTiHf drops by a total 0.24% to 3.01%, while the decrease of actuation strain is by 0.67% in NiTiZr to 1.26%.

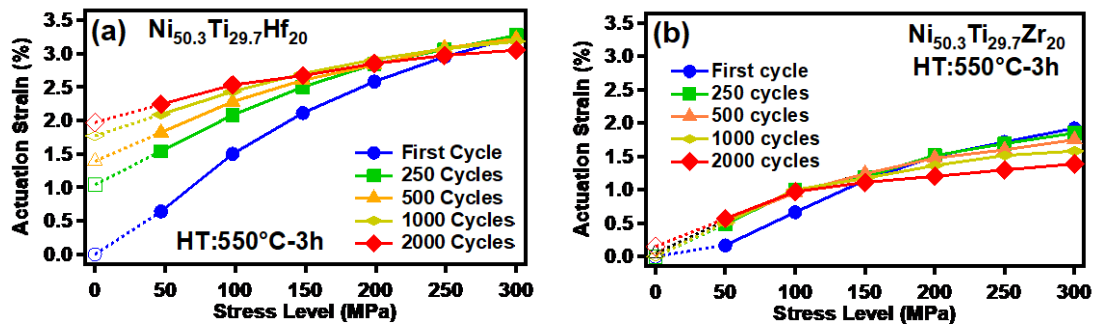


Figure 10.6 Evolution of actuation strain as a function of applied stress levels at various training cycles for nano-precipitation hardened $\text{Ni}_{50.3}\text{Ti}_{29.7}\text{Hf}_{20}$ and $\text{Ni}_{50.3}\text{Ti}_{29.7}\text{Zr}_{20}$.

Figure 10.5 illustrates the 1st, 1000th and 2000th training cycle strain vs. temperature responses of age-hardened $\text{Ni}_{50.3}\text{Ti}_{29.7}\text{Hf}_{20}$ and $\text{Ni}_{50.3}\text{Ti}_{29.7}\text{Zr}_{20}$ HTSMAs under different stress levels. For $\text{Ni}_{50.3}\text{Ti}_{29.7}\text{Hf}_{20}$ loaded at 50MPa, 1st training cycle was completed with

a relatively low actuation strain as compared to the 1000th and 2000th training cycles, which can be attributed to the lack of oriented internal stress fields in the early training cycles (Figure 10.5 a and c)). Larger values of actuation strain were recorded in 1000th and 2000th cycles due to the presence of oriented internal stress fields. Similar to $\text{Ni}_{50.3}\text{Ti}_{29.7}\text{Hf}_{20}$, $\text{Ni}_{50.3}\text{Ti}_{29.7}\text{Zr}_{20}$ loaded at 50 MPa exhibited the smallest actuation strain at the 1st training cycle while obtaining largest actuation strain at the 2000th training cycle (Figure 10.5 (c)). At 300MPa, $\text{Ni}_{50.3}\text{Ti}_{29.7}\text{Hf}_{20}$ had almost the same value of actuation strain irrespective of the number of training cycles, where 2000th cycle had slightly lower actuation strain compared to 1st cycle (Figure 10.5(b)). For $\text{Ni}_{50.3}\text{Ti}_{29.7}\text{Zr}_{20}$, the difference in actuation strain between 1st and 2000th cycle at 300MPa was more apparent (Figure 10.5 (d)). Decrease in actuation strain was most likely a result of accumulation of plastic deformation and formation of retained martensite, resulting in decrease in the volume fraction of transforming microstructure during martensitic transformation.

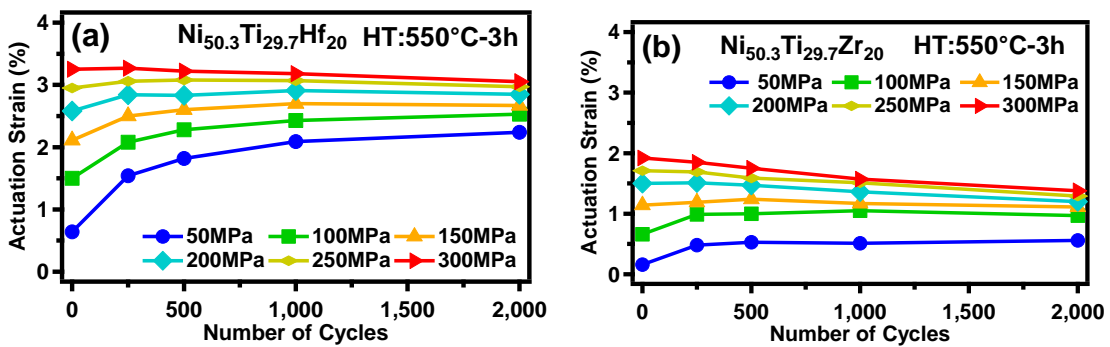


Figure 10.7 Evolution of actuation strain as a function of number of cycles under various applied stress levels for nano-precipitation hardened $\text{Ni}_{50.3}\text{Ti}_{29.7}\text{Hf}_{20}$ and $\text{Ni}_{50.3}\text{Ti}_{29.7}\text{Zr}_{20}$.

Figure 10.6 displays a summary of the actuation strain vs. applied stress levels during each characterization sequence of the thermomechanical training process for both materials. Overall, a trend of increasing actuation strain with increasing stress level is observed for both materials. For $\text{Ni}_{50.3}\text{Ti}_{29.7}\text{Hf}_{20}$, below 250 MPa, an increase in actuation strain with increasing number of training cycles was recorded at a constant applied stress, while this value was 150 MPa for $\text{Ni}_{50.3}\text{Ti}_{29.7}\text{Zr}_{20}$. Above these threshold stress values, an increase in the number of training cycles reduced the actuation strain of both HTSMAs which was obtained in 1st characterization sequence. As mentioned previously, this decrease is attributed to the stabilization of martensite and a reduction in the transforming volume. From Figure 10.6, two-way shape memory strain (TWSMS) was calculated by extrapolating the actuation strain values of 50MPa and 100MPa to 0MPa. Although this method only gives a rough estimate of the actual value of the TWSMS, it is convenient for comparison purposes. Before the commencement of training cycles (i.e. 300 MPa cycles), extrapolation of strains at two lowest applied stress levels (50MPa and 100MPa) demonstrated that NiTiHf and NiTiZr at zero stress had no TWSMS before thermomechanical training, while actuation strain at 300MPa was 3.15% for NiTiHf and 1.92% for NiTiZr. After 250 training cycles, TWSMS reached to 0.85 % for NiTiHf, while actuation strain increased to 3.25 % at 300MPa with the ratio of TWSMS to actuation strain of approximately 26%. As the number of training cycles increased, the variation in actuation strain became less sensitive to the applied stress level. After 2000 training cycles, the ratio of TWSMS to actuation strain at 300 MPa increased to 62%. For NiTiZr, there was almost no TWSMS during isobaric thermal

cycling regardless of the number of training cycles or the applied stress, with the only exception of after 2000 training cycles, where the alloy exhibited a relatively small TWSMS of 0.15%. The reason for the low actuation strain as well as the TWSMS in NiTiZr alloy can be attributed to the higher detwinning stress of this material (Figure 10.3). It is harder to reorient martensite variants and induce a large shape change in NiTiZr. Therefore, transformation induced defects are harder to be introduced to bring about the training effect.

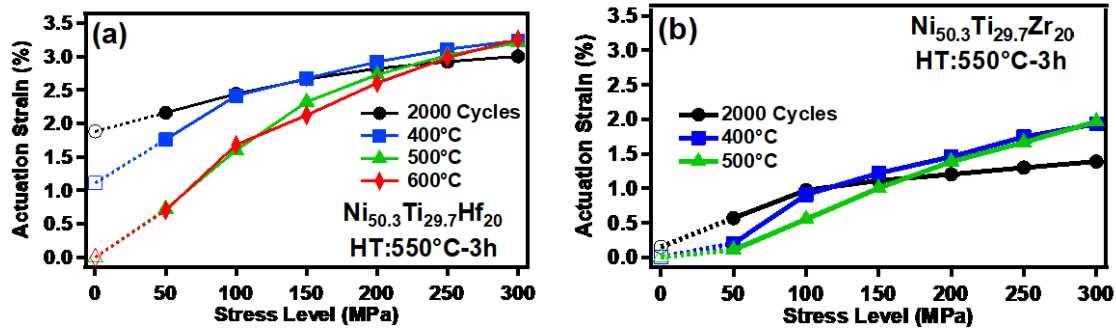


Figure 10.8 Effect of annealing treatment on the evolution of actuation strain and TWSMS stored after 2000th training cycles.

Figure 10.7 presents the evolution of actuation strain as a function of training cycles at different applied stress levels for Ni_{50.3}Ti_{29.7}Hf₂₀ and Ni_{50.3}Ti_{29.7}Zr₂₀ HTSMAs. For both alloys, increasing training cycles led to increased actuation strain at 50 MPa, while increasing number of training cycles adversely affected the actuation strain above 250MPa and 200 MPa for Ni_{50.3}Ti_{29.7}Hf₂₀ and Ni_{50.3}Ti_{29.7}Zr₂₀ respectively, where there was a slight decrease in actuation strain from first cycle to 2000th cycle. For Ni_{50.3}Ti_{29.7}Hf₂₀, difference in actuation strain between 50MPa and 300MPa decreased from 2.61% to 0.81% from 1st training cycle to 2000th cycles. Same value in

Ni_{50.3}Ti_{29.7}Zr₂₀ was 1.76% at 1st training cycle and 0.82% at 2000th cycles. This reduction was attributed to formation of oriented internal stress fields, which promoted formation of favorable martensite variants, while inhibiting non-favorable ones.

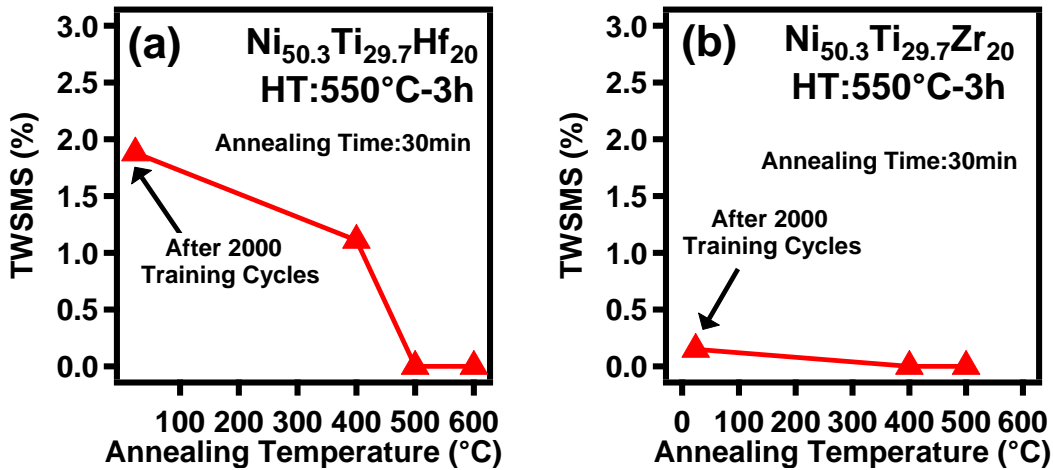


Figure 10.9 Change in the TWSMS obtained right after 2000th training cycles as a function of annealing treatment for nano-precipitation hardened (a) Ni_{50.3}Ti_{29.7}Hf₂₀ and (b) Ni_{50.3}Ti_{29.7}Zr₂₀.

10.6. Effect of annealing on the stability and magnitude of TWSMS

Since dislocations, other defects and oriented internal stress fields are the origin of a stabilized actuation strain and TWSME in HTSMAs, it is crucial to determine their stability as a function of temperature, especially above 0.4T_H (T_H: homologous temperature), where diffusional mechanisms play an important role in determining alloy response. Unlike conventional SMAs, HTSMAs may be utilized at temperatures reaching 500 °C, which result in greater involvement of thermally-induced mechanisms in shape memory response of material. To address these challenges, following the 2000 cycle training process, annealing heat treatment procedures were carried out to quantify the stability of TWSMS and actuation strain. Selected annealing temperatures were 400

°C, 500 °C and 600 °C for 0.5h. For $\text{Ni}_{50.3}\text{Ti}_{29.7}\text{Hf}_{20}$, these temperatures corresponded to $0.43T_H$, $0.49T_H$ and $0.55T_H$, respectively. Figure 10.8 illustrates the evolution of actuation strain and TWSMS as a function of different annealing heat treatments for nano-precipitation hardened $\text{Ni}_{50.3}\text{Ti}_{29.7}\text{Hf}_{20}$ and $\text{Ni}_{50.3}\text{Ti}_{29.7}\text{Zr}_{20}$. For $\text{Ni}_{50.3}\text{Ti}_{29.7}\text{Hf}_{20}$, at a first glance, it was clear that annealing led to a decreased TWSMS and actuation strain below 250 MPa, yet increased the actuation strain at 300 MPa. TWSMS right after training dropped from 1.88% to 1.11% as a result of annealing at 400 °C, whereas annealing heat treatments at 500 °C and 600 °C resulted in a complete annihilation of the defect structure and relaxation of all oriented internal stress fields which was responsible for the TWSME. Although a microstructural observation is not presented in the current study, it is well known that the annealing process changes the post-training by forming more self-accommodated martensite instead of heterogenous single-variant martensite [110]. Based on this observation, $\text{Ni}_{50.3}\text{Ti}_{29.7}\text{Hf}_{20}$ can be considered as inappropriate for TWSME applications at temperatures greater than 400 °C. On the other hand, the slight increase in actuation strain at 300 MPa after annealing as compared to actuation strain right after training was likely the result of reverse transformation of retained martensite at high temperature back to austenite, resulting in much more available transforming microstructure. Also, another possible reason behind this increase might be relaxation of back stresses generated through dislocation structures during training procedure [110]. In a sense, annealing heat treatments at 500 °C and 600 °C have a resetting effect on the microstructure of NiTiHf, i.e. plots with triangle (500 °C) and diamond (600 °C) markers are almost the same as the initial material behavior before training in Figure

10.5(a). For $\text{Ni}_{50.3}\text{Ti}_{29.7}\text{Zr}_{20}$, the magnitude of TWSMS was already close to zero even before any annealing heat treatments. Annealing at 400 °C for 0.5h was sufficient to relieve all internal stress fields accumulated during isobaric thermal training procedure resetting the material back to its pre-training state. Similar to $\text{Ni}_{50.3}\text{Ti}_{29.7}\text{Hf}_{20}$, annealing treatment increased the actuation strain of NiTiZr due to recovery of some remnant martensite back to austenite at elevated temperatures, resulting in increasing transforming volume. Although the material behaves similar to its pre-training state at the end of 500 °C annealing heat treatment, there should be enough damage accumulated, that it did not survive the last 300 MPa cycle of the characterization sequence after 500 °C annealing. Overall, annealing heat treatments at and above 500 °C completely erased the effects of training in both alloys. However, it can be concluded that NiTiHf has a superior TWSME performance since it exhibits a significant TWSM after training and this TWSM is only partially destroyed if the HTSMA is overheated to 400 °C, 100 °C above its anticipated operating temperature (Figure 10.9).

10.7. Summary and conclusions

In the present work, magnitude and stability of Two-Way Shape Memory Effect (TWSME) for nano-precipitation hardened $\text{Ni}_{50.3}\text{Ti}_{29.7}\text{Hf}_{20}$ and $\text{Ni}_{50.3}\text{Ti}_{29.7}\text{Zr}_{20}$ were characterized. TWSME was induced during isobaric thermal cycling by developing an oriented dislocation structure in the austenitic matrix [201]. Annealing treatment procedure was performed at set of temperatures to determine stability of ϵ_{TWSM} which obtained right after 2000-cycles thermo-mechanical training. Significant findings and conclusions are determined as follows:

- For a fixed Ni and Ti contents, coarsening of precipitate phase is faster when ternary element is Zr since lighter Zr has faster precipitate coarsening kinetics as compared to relatively heavier Hf. Thus, after aging at 550°C-3h, $\text{Ni}_{50.3}\text{Ti}_{29.7}\text{Zr}_{20}$ contained larger H-phase precipitates in the microstructure. Precipitate morphology is same and spindle-like shape in both alloys.
- Hf addition is more effective in increasing transformation temperatures of NiTi alloy. Nano-precipitation hardened $\text{Ni}_{50.3}\text{Ti}_{29.7}\text{Hf}_{20}$ at 550°C exhibited higher transformation temperatures and better cyclic stability than its $\text{Ni}_{50.3}\text{Ti}_{29.7}\text{Zr}_{20}$ counterpart.
- Training procedure developed an oriented dislocation structure and corresponding internal stress fields which guides the formation of preferential orientation of certain martensite variants in relation to the deformation adopted during thermo-mechanical training, hence leading to a macroscopic shape change. During thermo-mechanical training process, ϵ_{TWSM} increases as a consistent with increase of training cycles. TWSME behaviour of $\text{Ni}_{50.3}\text{Ti}_{29.7}\text{Hf}_{20}$ is better than its $\text{Ni}_{50.3}\text{Ti}_{29.7}\text{Zr}_{20}$ counterpart with higher ϵ_{TWSM} after 2000 training cycles.
- Annealing treatment has an obvious effect on the TWSME in both $\text{Ni}_{50.3}\text{Ti}_{29.7}\text{Hf}_{20}$ and $\text{Ni}_{50.3}\text{Ti}_{29.7}\text{Zr}_{20}$. During the course of annealing process, decrease in ϵ_{TWSM} was encountered and attributed to reduction in the amount oriented internal stress fields generated during training process. For Hf-based

alloy, TWSME is not stable at any annealing temperature. At 400°C for 30min reduced to ϵ_{TWSM} 1.88% to 1.11%, whereas further annealing at 500°C caused complete annihilation of ϵ_{TWSM} in the material. For Zr-based alloy, annealing at 400°C is sufficient to annihilate all ϵ_{TWSM} . Thermal stability of TWSME for $\text{Ni}_{50.3}\text{Ti}_{29.7}\text{Zr}_{20}$ are inferior to that of $\text{Ni}_{50.3}\text{Ti}_{29.7}\text{Hf}_{20}$. The decrease in TWSMS at temperature above service temperature (300°C) may be the consequence of insufficient training cycles.

- $\text{Ni}_{50.3}\text{Ti}_{29.7}\text{Zr}_{20}$ is more brittle than $\text{Ni}_{50.3}\text{Ti}_{29.7}\text{Hf}_{20}$ with low degree of elongation at the room temperature. It is more difficult to obtain TWSME in brittle materials due lack of sufficient plastic deformation introduced by dislocations and other defects. This might be main reason why TWSME behaviour is poor for $\text{Ni}_{50.3}\text{Ti}_{29.7}\text{Zr}_{20}$.
- Nano-precipitation hardened $\text{Ni}_{50.3}\text{Ti}_{29.7}\text{Hf}_{20}$ is shown to be viable candidate for TWSME applications at high temperatures. It exhibited large amounts of ϵ_{TWSM} after 2000th training cycles. Large amount of ϵ_{TWSM} was maintained until annealing temperature of 400°C.

CHAPTER XI

MAIN CONCLUSIONS AND FUTURE DIRECTIONS

Actuation fatigue properties of $\text{Ni}_{50.3}\text{Ti}_{29.7}\text{Hf}_{20}$ and $\text{Ni}_{50.3}\text{Ti}_{29.7}\text{Zr}_{20}$ HTSMAs were studied in terms of number of cycles to failure, level of actuation strain, reversibility and functional stability. Different heat treatments were applied to identify optimum microstructure to enhance shape memory response of material. Microstructural characterization was employed to identify underlying mechanism for property improvement and deterioration.

Functional instability lies in the fact that repeated transformations generate lattice defects mostly dislocations. Additionally, increasing UCT and stress level were found to accelerate formation of dislocations and caused earlier failure and functional instability. Based on experimental results, ideal conditions were determined for NiTiHf and NiTiZr alloys which are potential actuator candidates in the aerospace industry as a viable alternative to pneumatic and hydraulic actuators.

As a result of intensive microstructural investigation, processing studies and failure analysis performed throughout this study, ideal testing parameters and underlying mechanism responsible for ideal shape memory response and actuation fatigue performance of NiTiHf and NiTiZr alloys are evaluated. Based on the experimental results of the present investigation, following findings and conclusion can be made:

1. Heat treatments resulted in H-phase precipitates in both Ni-rich NiTiHf and NiTiZr alloys. H-phase is superstructure of B2 austenite phase. The crystallography of the twinning modes in Ni-rich NiTiHf remained unchanged after formation of H-phase precipitates.

2. Increase in aging temperature and time led to larger precipitates within microstructure. H-phase precipitates enhanced cyclic stability of materials against plastic deformation and provided control of transformation temperature by changing size of precipitates. There was no R-phase transformation during reverse and forward transformations. Ni-rich NiTiHf and NiTiZr underwent single-step transformation.
3. Thermomechanical tests indicated that different size of precipitates after various heat treatments and the corresponding microstructures considerably have influence on actuation strain, plastic strain and fatigue life of Ni-rich NiTiHf and NiTiZr. Even though the largest precipitates obtained by FC from 700°C to 100°C within 48h resulted in the longest number of cycles to failure in NiTiHf alloy, namely 15,500 cycles under 300MPa-300°C, the corresponding specimens suffered from poor level actuation strain of 1.01% and substantial plasticity. NiTiHf alloy aged at 550°C-3h tested under the same condition survived until 10,800 cycles with an average actuation strain level of 2.53%. Since suitability of HTSMA for actuator applications is depending on work output and fatigue life, specimens heat treated at 550°C-3h seem to be viable candidates over those specimens subjected to the other two selected heat treatments, namely FC from 700°C to 100°C at 48h and 600°C-10h.
4. Higher stress levels and UCT in general led to the accumulation of higher apparent permanent strains. In particular, the samples cycled up to 350 °C demonstrated larger irrecoverable strains as compared to the specimens tested up

to 300 °C under the same stress. Similarly, the specimens loaded at 400 MPa demonstrated about twice the irrecoverable strains at a given number of cycles as compared to the specimens tested under 300 MPa at the same UCT. Additionally, the actuation strain remained constant or increased as a function of the number of cycles when the UCT is 350°C; however, the samples cycled with 300°C UCT exhibited a decreasing trend in terms of actuation strain. This increase in actuation strain was also attributed to the accelerated formation of cracks at higher UCTs, which opened and closed when the specimen reversibly transformed between martensite and austenite phases, contributing to the apparent actuation strain.

5. In order to accurately capture the actuation fatigue response of HTSMAs in this study, a work-based fatigue life prediction approach was implemented and showed that the actuation fatigue lives of the present HTSMA exhibited an almost perfect power law correlation with average actuation work output. The same work-based power law was demonstrated to successfully capture the fatigue lives of several low temperature SMAs, as well. Interestingly, the power law exponents for many SMAs were exhibited to be either ~ -0.5 or ~ -0.8 , which pointed out the likelihood of the existence of a universal empirical rule for predicting actuation fatigue lives of SMAs. The power law exponent can be correlated with the strength of SMAs against plastic deformation accompanying reversible martensitic transformation.

6. Experimental observations demonstrated that nano-precipitation hardened $\text{Ni}_{50.3}\text{Ti}_{29.7}\text{Hf}_{20}$ HTSMA is a viable choice for high-force actuator applications at elevated temperatures as compared to $\text{Ni}_{50.3}\text{Ti}_{29.7}\text{Zr}_{20}$ counterpart. Overall, nano-precipitation hardened $\text{Ni}_{50.3}\text{Ti}_{29.7}\text{Hf}_{20}$ HTSMA at 550°C -3h that operated at elevated temperatures exhibited superior performance as compared to several low temperature SMAs when fatigue life and actuation energy density were considered as the decisive parameters in determining suitability of candidate materials for actuator applications.

Overall, the Ni-rich NiTiHf was shown to exhibit better actuation fatigue performance than NiTiZr counterpart for actuator application. The current findings constitute the first systematically obtained set of results demonstrating the microstructure dependence of actuation strain, irrecoverable strain, thermal hysteresis, transformation temperatures and fatigue performance of the Ni-rich $\text{Ni}_{50.3}\text{Ti}_{29.7}\text{Hf}_{20}$ $\text{Ni}_{50.3}\text{Ti}_{29.7}\text{Zr}_{20}$ HTSMA, demonstrating the importance of controlling H-phase precipitate size.

As a future work, more research is necessary to increase strength levels against plastic deformation. Nanoprecipitation strengthening improved cyclic and functional stability of material but there is still decrease in actuation strain during isobaric thermal cycling. Another major problem in Ni-rich NiTiHf materials is batch to batch variation. Preliminary investigation on different batches with same nominal composition ($\text{Ni}_{50.3}\text{Ti}_{29.7}\text{Hf}_{20}$) exhibited different transformation temperatures, actuation strain level, fatigue life and irrecoverable strain. Reproducibility is a key factor in manufacturing process. Even though nano-precipitation strengthened Ni-rich NiTiHf shows great

potential with outstanding shape memory properties, batch to batch variations still remain one of the biggest unsolved challenge in mass production of Ni-rich NiTiHf HTSMAs.

REFERENCES

- [1] Ma J, Karaman I, Noebe RD. High temperature shape memory alloys. *International Materials Reviews*. 2010;55:257-315.
- [2] Evirgen A, Basner F, Karaman I, Noebe RD, Pons J, Santamarta R. Effect of aging on the martensitic transformation characteristics of a Ni-rich NiTiHf high temperature shape memory alloy. *Functional Materials Letters*. 2012;5:1250038.
- [3] Evirgen A, Karaman I, Noebe R, Santamarta R, Pons J. Effect of precipitation on the microstructure and the shape memory response of the $\text{Ni}_{50.3}\text{Ti}_{29.7}\text{Zr}_{20}$ high temperature shape memory alloy. *Scripta Materialia*. 2013;69:354-7.
- [4] Evirgen A, Karaman I, Santamarta R, Pons J, Noebe R. Microstructural characterization and shape memory characteristics of the $\text{Ni}_{50.3}\text{Ti}_{34.7}\text{Hf}_{15}$ shape memory alloy. *Acta Materialia*. 2015;83:48-60.
- [5] Meng X, Cai W, Fu Y, Li Q, Zhang J, Zhao L. Shape-memory behaviors in an aged Ni-rich TiNiHf high temperature shape-memory alloy. *Intermetallics*. 2008;16:698-705.
- [6] Evirgen A, Karaman I, Pons J, Santamarta R, Noebe R. Role of nano-precipitation on the microstructure and shape memory characteristics of a new $\text{Ni}_{50.3}\text{Ti}_{34.7}\text{Zr}_{15}$ shape memory alloy. *Materials Science and Engineering: A*. 2016;655:193-203.
- [7] Karaca H, Acar E, Tobe H, Saghaian S. NiTiHf-based shape memory alloys. *Materials Science and Technology*. 2014;30:1530-44.
- [8] Saghaian S, Karaca H, Souri M, Turabi A, Noebe R. Tensile shape memory behavior of $\text{Ni}_{50.3}\text{Ti}_{29.7}\text{Hf}_{20}$ high temperature shape memory alloys. *Materials & Design*. 2016;101:340-5.

- [9] Pelton A. Nitinol fatigue: a review of microstructures and mechanisms. *Journal of Materials Engineering and Performance*. 2011;20:613-7.
- [10] Pelton A, Schroeder V, Mitchell M, Gong X-Y, Barney M, Robertson S. Fatigue and durability of Nitinol stents. *Journal of the mechanical behavior of biomedical materials*. 2008;1:153-64.
- [11] Eggeler G, Hornbogen E, Yawny A, Heckmann A, Wagner M. Structural and functional fatigue of NiTi shape memory alloys. *Materials Science and Engineering: A*. 2004;378:24-33.
- [12] Robertson SW, Ritchie RO. In vitro fatigue–crack growth and fracture toughness behavior of thin-walled superelastic Nitinol tube for endovascular stents: a basis for defining the effect of crack-like defects. *Biomaterials*. 2007;28:700-9.
- [13] Duerig T, Pelton A, Stöckel D. An overview of nitinol medical applications. *Materials Science and Engineering: A*. 1999;273:149-60.
- [14] McNichols Jr J, Brookes P, Cory J. NiTi fatigue behavior. *Journal of Applied Physics*. 1981;52:7442-4.
- [15] Calhoun C, Wheeler R, Baxevanis T, Lagoudas D. Actuation fatigue life prediction of shape memory alloys under the constant-stress loading condition. *Scripta Materialia*. 2015;95:58-61.
- [16] Bhaumik S, Ramaiah K, Saikrishna C. Nickel–Titanium Shape Memory Alloy Wires for Thermal Actuators. *Micro and Smart Devices and Systems*: Springer; 2014. p. 181-98.

- [17] Fumagalli L, Butera F, Coda A. SmartFlex® NiTi wires for shape memory actuators. *Journal of Materials Engineering and Performance*. 2009;18:691-5.
- [18] Otsuka K, Ren X. Physical metallurgy of Ti–Ni-based shape memory alloys. *Progress in Materials Science*. 2005;50:511-678.
- [19] Van Humbeeck J. Shape memory alloys: a material and a technology. *Advanced Engineering Materials*. 2001;3:837-50.
- [20] Padula S, Qiu S, Gaydos D, Noebe R, Bigelow G, Garg A, et al. Effect of upper-cycle temperature on the load-biased, strain-temperature response of NiTi. *Metallurgical and Materials Transactions A*. 2012;43:4610-21.
- [21] Otsuka K, Wayman CM. *Shape memory materials*: Cambridge university press; 1999.
- [22] Kockar B, Karaman I, Kim J, Chumlyakov Y, Sharp J, Yu C-JM. Thermomechanical cyclic response of an ultrafine-grained NiTi shape memory alloy. *Acta Materialia*. 2008;56:3630-46.
- [23] Kockar B, Karaman I, Kulkarni A, Chumlyakov Y, Kireeva I. Effect of severe ausforming via equal channel angular extrusion on the shape memory response of a NiTi alloy. *Journal of nuclear materials*. 2007;361:298-305.
- [24] Kockar B, Karaman I, Kim J, Chumlyakov Y. A method to enhance cyclic reversibility of NiTiHf high temperature shape memory alloys. *Scripta Materialia*. 2006;54:2203-8.
- [25] Atli K, Karaman I, Noebe R, Garg A, Chumlyakov Y, Kireeva I. Improvement in the shape memory response of Ti_{50.5}Ni_{24.5}Pd₂₅ high-temperature shape memory alloy

with scandium microalloying. *Metallurgical and Materials Transactions A*. 2010;41:2485-97.

[26] Kockar B, Atli K, Ma J, Haouaoui M, Karaman I, Nagasako M, et al. Role of severe plastic deformation on the cyclic reversibility of a $\text{Ti}_{50.3}\text{Ni}_{33.7}\text{Pd}_{16}$ high temperature shape memory alloy. *Acta Materialia*. 2010;58:6411-20.

[27] Atli K, Karaman I, Noebe R. Work output of the two-way shape memory effect in $\text{Ti}_{50.5}\text{Ni}_{24.5}\text{Pd}_{25}$ high-temperature shape memory alloy. *Scripta Materialia*. 2011;65:903-6.

[28] Kumar PK, Desai U, Monroe JA, Lagoudas DC, Karaman I, Bigelow G, et al. Experimental investigation of simultaneous creep, plasticity and transformation of $\text{Ti}_{50.5}\text{Pd}_{30}\text{Ni}_{19.5}$ high temperature shape memory alloy during cyclic actuation. *Materials Science and Engineering: A*. 2011;530:117-27.

[29] Santamarta R, Arróyave R, Pons J, Evirgen A, Karaman I, Karaca H, et al. TEM study of structural and microstructural characteristics of a precipitate phase in Ni-rich Ni-Ti-Hf and Ni-Ti-Zr shape memory alloys. *Acta Materialia*. 2013;61:6191-206.

[30] Pérez-Sierra A, Pons J, Santamarta R, Karaman I, Noebe R. Stability of a Ni-rich Ni-Ti-Zr high temperature shape memory alloy upon low temperature aging and thermal cycling. *Scripta Materialia*. 2016;124:47-50.

[31] Rios O, Noebe R, Biles T, Garg A, Palczer A, Scheiman D, et al. Characterization of ternary NiTiPt high-temperature shape memory alloys. *Smart Structures and Materials: International Society for Optics and Photonics*; 2005. p. 376-87.

- [32] Yang F, Kovarik L, Phillips PJ, Noebe RD, Mills M. Characterizations of precipitate phases in a Ti–Ni–Pd alloy. *Scripta Materialia*. 2012;67:145-8.
- [33] Namigata Y, Hattori Y, Khan MI, Kim HY, Miyazaki S. Enhancement of shape memory properties through precipitation hardening in a Ti-Rich Ti-Ni-Pd high temperature shape memory alloy. *Materials Transactions*. 2016.
- [34] Meng X-L, Zheng Y-F, Wang Z, Zhao L. Shape memory properties of the $Ti_{36}Ni_{49}Hf_{15}$ high temperature shape memory alloy. *Materials Letters*. 2000;45:128-32.
- [35] Liu M, Zhang X, Li Y, Chen J, Tu M. High-resolution transmission electron microscope (HRTEM) study of the transformation interface and substructure in $NiTiHf_{40}$ melt–spun ribbons. *Journal of Alloys and Compounds*. 2002;334:147-53.
- [36] Wojcik CC. Properties and Heat Treatment of High Transition Temperature Ni-Ti-Hf Alloys. *Journal of Materials Engineering and Performance*. 2009;18:511-6.
- [37] Bucsek AN, Hudish GA, Bigelow GS, Noebe RD, Stebner AP. Composition, compatibility, and the functional performances of ternary nitix high-temperature shape memory alloys. *Shape Memory and Superelasticity*. 2016;2:62-79.
- [38] Wu Y, Patriarca L, Li G, Sehitoglu H, Soejima Y, Ito T, et al. Shape memory response of polycrystalline $NiTi_{12.5}Hf$ alloy: transformation at small scales. *Shape Memory and Superelasticity*. 2015;1:387-97.
- [39] Wang Y, Zheng Y, Cai W, Zhao L. The tensile behavior of $Ti_{36}Ni_{49}Hf_{15}$ high temperature shape memory alloy. *Scripta Materialia*. 1999;40:1327-31.
- [40] Thompson S. An overview of nickel–titanium alloys used in dentistry. *International endodontic journal*. 2000;33:297-310.

- [41] Miura F, Mogi M, Ohura Y, Hamanaka H. The super-elastic property of the Japanese NiTi alloy wire for use in orthodontics. *American Journal of Orthodontics and Dentofacial Orthopedics*. 1986;90:1-10.
- [42] Pelton A, Stöckel D, Duerig T. Medical uses of nitinol. *Materials Science Forum: Trans Tech Publ*; 2000. p. 63-70.
- [43] Stoeckel D. Shape memory actuators for automotive applications. *Engineering Aspects of Shape Memory Alloys*. 1990:283.
- [44] Williams E, Elahinia MH. An automotive SMA mirror actuator: modeling, design, and experimental evaluation. *Journal of Intelligent Material Systems and Structures*. 2008;19:1425-34.
- [45] Hartl DJ, Lagoudas DC. Aerospace applications of shape memory alloys. *Proceedings of the Institution of Mechanical Engineers, Part G: Journal of Aerospace Engineering*. 2007;221:535-52.
- [46] Miller DA, Lagoudas DC. Thermomechanical characterization of NiTiCu and NiTi SMA actuators: influence of plastic strains. *Smart Mater Struct*. 2000;9:640.
- [47] Lagoudas DC, Miller DA, Rong L, Kumar P. Thermomechanical fatigue of shape memory alloys. *Smart Mater Struct*. 2009;18:085021.
- [48] Monroe J, Karaman I, Lagoudas D, Bigelow G, Noebe R, Padula S. Determining recoverable and irrecoverable contributions to accumulated strain in a NiTiPd high-temperature shape memory alloy during thermomechanical cycling. *Scripta Materialia*. 2011;65:123-6.
- [49] Lagoudas DC. *Shape memory alloys*. Science and Business Media, LLC. 2008.

- [50] Karakoc O, Hayrettin C, Canadinc D, Karaman I. Role of applied stress level on the actuation fatigue behavior of NiTiHf high temperature shape memory alloys. *Acta Materialia*. 2018;153:156-68.
- [51] Duerig T, Zadno R. An engineer's perspective of pseudoelasticity. *Engineering aspects of shape memory alloys*. 1990:369-93.
- [52] Recarte V, Perez-Landazabal J, Rodríguez P, Bocanegra E, Nó M, San Juan J. Thermodynamics of thermally induced martensitic transformations in Cu–Al–Ni shape memory alloys. *Acta Materialia*. 2004;52:3941-8.
- [53] George E, Liu C, Horton J, Sparks C, Kao M, Kunsmann H, et al. Characterization, processing, and alloy design of NiAl-based shape memory alloys. *Materials characterization*. 1994;32:139-60.
- [54] Noebe R, Biles T, Padula S. NiTi-based high-temperature shape-memory alloys: properties, prospects, and potential applications. *Materials Engineering-Newyork*. 2006;32:145.
- [55] Yang J, Simpson J. Stress-induced transformation and superelasticity in Ni-Ti-Nb alloys. *Journal de Physique iv*. 1995;5:C8-771-C8-6.
- [56] Atli KC, Karaman I, Noebe RD, Bigelow G, Gaydosh D. Work production using the two-way shape memory effect in NiTi and a Ni-rich NiTiHf high-temperature shape memory alloy. *Smart Mater Struct*. 2015;24.
- [57] Bigelow GS, Padula SA, Garg A, Gaydosh D, Noebe RD. Characterization of Ternary NiTiPd High-Temperature Shape-Memory Alloys under Load-Biased Thermal Cycling. *Metall Mater Trans A*. 2010;41A:3065-79.

- [58] Casalena L, Bigelow GS, Gao YP, Benafan O, Noebe RD, Wang YZ, et al. Mechanical behavior and microstructural analysis of NiTi-40Au shape memory alloys exhibiting work output above 400 degrees C. *Intermetallics*. 2017;86:33-44.
- [59] Hornbuckle BC, Sasaki TT, Bigelow GS, Noebe RD, Weaver ML, Thompson GB. Structure-property relationships in a precipitation strengthened Ni-29.7Ti-20Hf (at%) shape memory alloy. *Mat Sci Eng a-Struct*. 2015;637:63-9.
- [60] Monroe JA, Karaman I, Lagoudas DC, Bigelow G, Noebe RD, Padula S. Determining recoverable and irrecoverable contributions to accumulated strain in a NiTiPd high-temperature shape memory alloy during thermomechanical cycling. *Scripta Materialia*. 2011;65:123-6.
- [61] Stebner AP, Bigelow GS, Yang J, Shukla DP, Saghaian SM, Rogers R, et al. Transformation strains and temperatures of a nickel-titanium-hafnium high temperature shape memory alloy. *Acta Materialia*. 2014;76:40-53.
- [62] Evirgen A, Karaman I, Santamarta R, Pons J, Hayrettin C, Noebe R. Relationship between crystallographic compatibility and thermal hysteresis in Ni-rich NiTiHf and NiTiZr high temperature shape memory alloys. *Acta Materialia*. 2016;121:374-83.
- [63] Shirakawa Y, Morizono Y, Nishida M. New precipitate phase in Pd and Ni rich Ti-Pd-Ni shape memory alloys. *Proceedings of the 1999 International Symposium and Exhibition on Shape Memory Materials (SMM'99)*: Trans Tech Publ; 2000.
- [64] Nagasako M, Nishida M. Phase transformations in Pd-and Ni-rich Ti-Pd-Ni alloys. *Journal de Physique IV (Proceedings)*: EDP sciences; 2003. p. 1043-6.

- [65] Hosoda H, Tsuji M, Takahashi Y, Inamura T, Wakashima K, Yamabe-Mitarai Y, et al. Phase stability and mechanical properties of Ti-Ni shape memory alloys containing platinum group metals. *Materials Science Forum: Trans Tech Publ*; 2003. p. 2333-8.
- [66] Benafan O, Garg A, Noebe R, Bigelow G, Padula S, Gaydos D, et al. Mechanical and functional behavior of a Ni-rich $\text{Ni}_{50.3}\text{Ti}_{29.7}\text{Hf}_{20}$ high temperature shape memory alloy. *Intermetallics*. 2014;50:94-107.
- [67] Benafan O, Garg A, Noebe R, Bigelow G, Padula S, Gaydos D, et al. Thermomechanical behavior and microstructural evolution of a Ni (Pd)-rich $\text{Ni}_{24.3}\text{Ti}_{49.7}\text{Pd}_{26}$ high temperature shape memory alloy. *Journal of Alloys and Compounds*. 2015;643:275-89.
- [68] Bigelow G, Garg A, Padula S, Gaydos D, Noebe R. Load-biased shape-memory and superelastic properties of a precipitation strengthened high-temperature $\text{Ni}_{50.3}\text{Ti}_{29.7}\text{Hf}_{20}$ alloy. *Scripta Materialia*. 2011;64:725-8.
- [69] Padula S, Bigelow G, Noebe R, Gaydos D, Garg A. Challenges and progress in the development of high-temperature shape memory alloys based on NiTiX compositions for high-force actuator applications. 2006.
- [70] Besseghini S, Villa E, Tuissi A. NiTiHf shape memory alloy: effect of aging and thermal cycling. *Materials Science and Engineering: A*. 1999;273:390-4.
- [71] Olier P, Brachet J, Bechade J, Foucher C, Guenin G. Investigation of transformation temperatures, microstructure and shape memory properties of NiTi, NiTiZr and NiTiHf alloys. *Journal de Physique IV*. 1995;5:C8-741-C8-6.

- [72] Mulder J. Investigation on high temperature shape memory alloys using Ni-Ti-Zr and Ni-Ti-Hf system. University of Twente, Enschede, The Netherlands,. 1994.
- [73] Hsieh S, Wu S. Martensitic transformation of quaternary $Ti_{50.5-x}Ni_{49.5}Zr_{x/2}Hf_{x/2}$ (X= 0–20 at.%) shape memory alloys. *Materials Characterization*. 2000;45:143-52.
- [74] Thoma PE, Boehm JJ. Effect of composition on the amount of second phase and transformation temperatures of $Ni_xTi_{90-x}Hf_{10}$ shape memory alloys. *Materials Science and Engineering: A*. 1999;273:385-9.
- [75] Frenzel J, Wiczorek A, Opahle I, Maaß B, Drautz R, Eggeler G. On the effect of alloy composition on martensite start temperatures and latent heats in Ni–Ti-based shape memory alloys. *Acta Materialia*. 2015;90:213-31.
- [76] Angst D, Thoma P, Kao M. The Effect of hafnium content on the transformation temperatures of $Ni_{49}Ti_{51-x}Hf_x$ shape memory alloys. *Journal de Physique IV*. 1995;5:C8-747-C8-52.
- [77] Abujudom D, Kao M-Y, Thoma PE, Angst D. High transformation temperature shape memory alloy. Patent Number EP 0484805. 1992.
- [78] Dalle F, Perrin E, Vermaut P, Masse M, Portier R. Interface mobility in $Ni_{49.8}Ti_{42.2}Hf_8$ shape memory alloy. *Acta Materialia*. 2002;50:3557-65.
- [79] Han X, Zou W, Wang R, Zhang Z, Yang D. Structure and substructure of martensite in a $Ti_{36.5}Ni_{48.5}Hf_{15}$ high temperature shape memory alloy. *Acta Materialia*. 1996;44:3711-21.

- [80] Russell SM, Sczerzenie F. Engineering Considerations in the Application of Nitihf and Nial as Practical High-Temperature Shape Memory Alloys. *Mater Res Soc Symp P*. 1995;360:455-60.
- [81] Thoma PE, Boehm JJ. The effect of hafnium and thermal cycling on the transformation temperatures of NiTi-based shape memory alloys. *Materials of Smart Systems Iii*. 2000;604:221-6.
- [82] Eckelmeyer K. The effect of alloying on the shape memory phenomenon in nitinol. *Scripta Metallurgica*. 1976;10:667-72.
- [83] Firstov G, Van Humbeeck J, Koval YN. High-temperature shape memory alloys: some recent developments. *Materials Science and Engineering: A*. 2004;378:2-10.
- [84] Meng X, Cai W, Zheng Y, Tong Y, Zhao L, Zhou L. Stress-induced martensitic transformation behavior of a Ti–Ni–Hf high temperature shape memory alloy. *Materials Letters*. 2002;55:111-5.
- [85] Meng X, Zheng Y, Wang Z, Zhao L. Effect of aging on the phase transformation and mechanical behavior of $Ti_{36}Ni_{49}Hf_{15}$ high temperature shape memory alloy. *Scripta Materialia*. 2000;42:341-8.
- [86] Santamarta R, Segui C, Pons J, Cesari E. Martensite stabilisation in $Ni_{50}Ti_{32.2}Hf_{17.7}$. *Scripta Materialia*. 1999;41:867-72.
- [87] Javadi MM, Belbasi M, Salehi MT, Afshar MR. Effect of aging on the microstructure and shape memory effect of a hot-rolled NiTiHf alloy. *Journal of Materials Engineering and Performance*. 2011;20:618-22.

- [88] Meng X, Cai W, Fu Y, Zhang J, Zhao L. Martensite structure in Ti–Ni–Hf–Cu quaternary alloy ribbons containing (Ti, Hf)₂Ni precipitates. *Acta Materialia*. 2010;58:3751-63.
- [89] Tong Y, Chen F, Tian B, Li L, Zheng Y. Microstructure and martensitic transformation of Ti₄₉Ni_{51-x}Hf_x high temperature shape memory alloys. *Materials Letters*. 2009;63:1869-71.
- [90] Dalle F, Kolomytsev V, Ochin P, Portier R. Melt-spun ribbons of Ti-Hf-Ni-Re shape memory alloys: Annealing above crystallisation temperature. *Scripta Materialia*. 2001;44:929-34.
- [91] Acar E, Karaca H, Tobe H, Noebe R, Chumlyakov Y. Characterization of the shape memory properties of a Ni_{45.3}Ti_{39.7}Hf₁₀Pd₅ alloy. *Journal of Alloys and Compounds*. 2013;578:297-302.
- [92] Karaca H, Acar E, Ded G, Saghaian S, Basaran B, Tobe H, et al. Microstructure and transformation related behaviors of a Ni_{45.3}Ti_{29.7}Hf₂₀Cu₅ high temperature shape memory alloy. *Materials Science and Engineering: A*. 2015;627:82-94.
- [93] Atli K, Karaman I, Noebe R. Influence of tantalum additions on the microstructure and shape memory response of Ti_{50.5}Ni_{24.5}Pd₂₅ high-temperature shape memory alloy. *Materials Science and Engineering: A*. 2014;613:250-8.
- [94] Canadinc D, Trehern W, Ozcan H, Hayrettin C, Karakoc O, Karaman I, et al. On the deformation response and cyclic stability of Ni₅₀Ti₃₅Hf₁₅ high temperature shape memory alloy wires. *Scripta Materialia*. 2017;135:92-6.

- [95] Han X, Wang R, Zhang Z, Yang D. A new precipitate phase in a TiNiHf high temperature shape memory alloy. *Acta materialia*. 1998;46:273-81.
- [96] Coughlin DR, Phillips PJ, Bigelow GS, Garg A, Noebe RD, Mills MJ. Characterization of the microstructure and mechanical properties of a 50.3Ni-29.7Ti-20Hf shape memory alloy. *Scripta Materialia*. 2012;67:112-5.
- [97] Karaca HE, Saghaian SM, Ded G, Tobe H, Basaran B, Maier HJ, et al. Effects of nanoprecipitation on the shape memory and material properties of an Ni-rich NiTiHf high temperature shape memory alloy. *Acta Materialia*. 2013;61:7422-31.
- [98] Saghaian SM, Karaca HE, Tobe H, Pons J, Santamarta R, Chumlyakov YI, et al. Effects of Ni content on the shape memory properties and microstructure of Ni-rich NiTi-20Hf alloys. *Smart Mater Struct*. 2016;25.
- [99] Saghaian S, Karaca H, Tobe H, Souri M, Noebe R, Chumlyakov Y. Effects of aging on the shape memory behavior of Ni-rich Ni_{50.3}Ti_{29.7}Hf₂₀ single crystals. *Acta Materialia*. 2015;87:128-41.
- [100] Saghaian SM, Karaca HE, Tobe H, Turabi AS, Saedi S, Saghaian SE, et al. High strength NiTiHf shape memory alloys with tailorable properties. *Acta Materialia*. 2017;134:211-20.
- [101] Patriarca L, Sehitoglu H, Panchenko EY, Chumlyakov Y. High-temperature functional behavior of single crystal Ni_{51.2}Ti_{23.4}Hf_{25.4} shape memory alloy. *Acta Materialia*. 2016;106:333-43.

- [102] Meng X, Cai W, Chen F, Zhao L. Effect of aging on martensitic transformation and microstructure in Ni-rich TiNiHf shape memory alloy. *Scripta Materialia*. 2006;54:1599-604.
- [103] Sandu A, Tsuchiya K, Yamamoto S, Todaka Y, Umemoto M. Influence of isothermal ageing on mechanical behaviour in Ni-rich Ti–Zr–Ni shape memory alloy. *Scripta Materialia*. 2006;55:1079-82.
- [104] Sandu AM, Tsuchiya K, Tabuchi M, Yamamoto S, Todaka Y, Umemoto M. Microstructural evolution during isothermal aging in Ni-rich Ti-Zr-Ni shape memory alloys. *Materials Transactions*. 2007;48:432-8.
- [105] Meng X, Cai W, Zheng Y-F, Zhao L-C. Phase transformation and precipitation in aged Ti–Ni–Hf high-temperature shape memory alloys. *Materials Science and Engineering: A*. 2006;438:666-70.
- [106] Davidson FM, Liang C, Lobitz DW. Investigation of torsional shape memory alloy actuators. *Smart Structures and Materials 1996: Smart Structures and Integrated Systems: International Society for Optics and Photonics*; 1996. p. 672-83.
- [107] Liu Y, Liu Y, Van Humbeeck J. Two-way shape memory effect developed by martensite deformation in NiTi. *Acta Materialia*. 1998;47:199-209.
- [108] Meng X, Cai W, Zheng Y, Rao Y, Zhao L. Two-way shape memory effect induced by martensite deformation and stabilization of martensite in $\text{Ti}_{36}\text{Ni}_{49}\text{Hf}_{15}$ high temperature shape memory alloy. *Materials Letters*. 2003;57:4206-11.
- [109] Tadaki T, Otsuka K, Shimizu K. Shape memory alloys. *Annual Review of Materials Science*. 1988;18:25-45.

- [110] Atli K, Karaman I, Noebe R, Gaydos D. The effect of training on two-way shape memory effect of binary NiTi and NiTi based ternary high temperature shape memory alloys. *Materials Science and Engineering: A*. 2013;560:653-66.
- [111] Perkins J. Residual stresses and the origin of reversible (two-way) shape memory effects. *Scripta Metallurgica*. 1974;8:1469-76.
- [112] Guilemany J, Fernandez J. On the mechanism of two way shape memory effect obtained by stabilized stress induced martensite. *Scripta Metallurgica et Materialia;(United States)*. 1994;30.
- [113] Guilemany J, Fernández J. Mechanism of two way shape memory effect obtained by stabilised stress induced martensite J. *Journal de Phys IV Coll C*. 1995;5:355.
- [114] Nishida M. All-round shape memory effect in Ni-rich TiNi alloys generated by constrained aging. *Scripta Metallurgica*. 1984;18:1293-8.
- [115] Lahoz R, Gracia-Villa L, Puértolas JA. Training of the two-way shape memory effect by bending in NiTi alloys. *Journal of Engineering Materials and Technology*. 2002;124:397-401.
- [116] Maletta C, Falvo A, Furgiuele F. A Phenomenological approach for real-time simulation of the two-way shape memory effect in NiTi alloys. *Journal of Engineering Materials and Technology*. 2008;130:011003.
- [117] Urbina C, De la Flor S, Ferrando F. TWSME improvement by thermal cycling at zero stress in NiTi shape memory alloys. *Second International Conference on Smart Materials and Nanotechnology in Engineering: International Society for Optics and Photonics*; 2009. p. 74930L.

- [118] Chang C-Y, Vokoun D, Hu C-T. Two-way shape memory effect of NiTi alloy induced by constraint aging treatment at room temperature. *Metallurgical and Materials Transactions A*. 2001;32:1629-34.
- [119] Hayrettin C, Karakoc O, Karaman I, Mabe J, Santamarta R, Pons J. Two way shape memory effect in NiTiHf high temperature shape memory alloy tubes. *Acta Materialia*. 2019;163:1-13.
- [120] Atli K, Karaman I, Noebe R. Work output of the two-way shape memory effect in $Ti_{50.5}Ni_{24.5}Pd_{25}$ high-temperature shape memory alloy. *Scripta Materialia*. 2011;65:903-6.
- [121] Atli K, Karaman I, Noebe R, Maier H. Comparative analysis of the effects of severe plastic deformation and thermomechanical training on the functional stability of $Ti_{50.5}Ni_{24.5}Pd_{25}$ high-temperature shape memory alloy. *Scripta Materialia*. 2011;64:315-8.
- [122] Benafan O, Gaydosh D. High temperature shape memory alloy $Ni_{50.3}Ti_{29.7}Hf_{20}$ torque tube actuators. *Smart Mater Struct*. 2017;26:095002.
- [123] Benafan O, Gaydosh DJ. Constant-torque thermal cycling and two-way shape memory effect in $Ni_{50.3}Ti_{29.7}Hf_{20}$ torque tubes. *Smart Mater Struct*. 2018;27:075035.
- [124] Yang F, Coughlin D, Phillips PJ, Yang L, Devaraj A, Kovarik L, et al. Structure analysis of a precipitate phase in an Ni-rich high-temperature NiTiHf shape memory alloy. *Acta Materialia*. 2013;61:3335-46.

- [125] Mahtabi M, Shamsaei N, Mitchell M. Fatigue of Nitinol: The state-of-the-art and ongoing challenges. *Journal of the Mechanical Behavior of Biomedical Materials*. 2015;50:228-54.
- [126] Lagoudas DC, Li C, Miller DA, Rong L. Thermomechanical transformation fatigue of SMA actuators. *SPIE's 7th Annual International Symposium on Smart Structures and Materials: International Society for Optics and Photonics*; 2000. p. 420-9.
- [127] Casati R, Tuissi A. Effect of current pulses on fatigue of thin NiTi wires for shape memory actuators. *Journal of materials engineering and performance*. 2012;21:2633-7.
- [128] Wheeler R, Santa-Cruz J, Hartl D, Lagoudas DC. Effect of processing and loading on equiatomic NiTi fatigue life and localized failure mechanisms. *ASME 2013 Conference on Smart Materials, Adaptive Structures and Intelligent Systems: American Society of Mechanical Engineers*; 2013. p. V002T02A10-VT02A10.
- [129] Calhoun CA. Actuation fatigue of shape memory alloys. College Station, USA: Texas A&M University; 2012.
- [130] Bertacchini OW, Lagoudas DC, Patoor E. Thermomechanical transformation fatigue of TiNiCu SMA actuators under a corrosive environment—Part I: Experimental results. *International Journal of Fatigue*. 2009;31:1571-8.
- [131] Tobushi H, Hachisuka T, Yamada S, Lin P-H. Rotating-bending fatigue of a TiNi shape-memory alloy wire. *Mechanics of Materials*. 1997;26:35-42.
- [132] Bo Z, Lagoudas DC. Thermomechanical modeling of polycrystalline SMAs under cyclic loading, Part III: Evolution of plastic strains and two-way shape memory effect. *International Journal of Engineering Science*. 1999;37:1175-203.

- [133] Bertacchini OW, Lagoudas DC, Calkin F, Mabe JH. Transformation induced cyclic behavior and fatigue properties of nickel rich NiTi shape memory alloy actuators. Proceedings of the ICOMAT2008.
- [134] Grossmann C, Frenzel J, Sampath V, Depka T, Oppenkowski A, Somsen C, et al. Processing and property assessment of NiTi and NiTiCu shape memory actuator springs. *Materialwissenschaft und Werkstofftechnik*. 2008;39:499-510.
- [135] Frenzel J, Burow JA, Payton EJ, Rezanka S, Eggeler G. Improvement of NiTi Shape Memory Actuator Performance Through Ultra-Fine Grained and Nanocrystalline Microstructures. *Advanced Engineering Materials*. 2011;13:256-68.
- [136] Calkins FT, Mabe JH, Butler GW. Boeing's variable geometry chevron: Morphing aerospace structures for jet noise reduction. *Smart Structures and Materials 2006: Industrial and Commercial Applications of Smart Structures Technologies: International Society for Optics and Photonics*; 2006. p. 61710O.
- [137] Mabe J. Variable area jet nozzle for noise reduction using shape memory alloy actuators. *Journal of the Acoustical Society of America*. 2008;123:3871-.
- [138] Elahinia MH. Shape memory alloy actuators: design, fabrication, and experimental evaluation: John Wiley & Sons; 2016.
- [139] Hornbogen E, Bunk W. *Advanced structural and functional materials*. Springer-Verlag, Heidelberg; 1991.
- [140] Tobushi H, Nakahara T, Hashimoto T, Shimeno Y, Tanaka K. Fatigue properties of TiNi shape memory alloy and applications to a heat engine and an actuator. *Archives of Mechanics*. 1999;51:833-45.

- [141] Hornbogen E. Some effects of martensitic transformation on fatigue resistance. *Fatigue & Fracture of Engineering Materials & Structures*. 2002;25:785-90.
- [142] Miyazaki S, Mizukoshi K, Ueki T, Sakuma T, Liu Y. Fatigue life of TiNi₅₀ at.% and TiNi₄₀Cu₁₀ (at.%) shape memory alloy wires. *Materials Science and Engineering: A*. 1999;273:658-63.
- [143] Maletta C, Sgambitterra E, Furgiuele F, Casati R, Tuissi A. Fatigue of pseudoelastic NiTi within the stress-induced transformation regime: a modified Coffin–Manson approach. *Smart Mater Struct*. 2012;21:112001.
- [144] Miyazaki S, Imai T, Igo Y, Otsuka K. Effect of cyclic deformation on the pseudoelasticity characteristics of Ti-Ni alloys. *Metallurgical Transactions A*. 1986;17:115-20.
- [145] Predki W, Klönne M, Knopik A. Cyclic torsional loading of pseudoelastic NiTi shape memory alloys: damping and fatigue failure. *Materials Science and Engineering: A*. 2006;417:182-9.
- [146] Sawaguchi TA, Kausträter G, Yawny A, Wagner M, Eggeler G. Crack initiation and propagation in 50.9 at. pct Ni-Ti pseudoelastic shape-memory wires in bending-rotation fatigue. *Metallurgical and Materials Transactions A*. 2003;34:2847-60.
- [147] Delaey L, Janssen J, Van de Mosselaer D, Dullenkopf G, Deruyttere A. Fatigue properties of pseudoelastic Cu-Zn-Al alloys. *Scripta Metallurgica*. 1978;12:373-6.
- [148] Melton K, Mercier O. Fatigue life of CuZnAl alloys. *Scripta Metallurgica*. 1979;13:73-5.

- [149] Melton K, Mercier O. Fatigue of NiTi thermoelastic martensites. *Acta Metallurgica*. 1979;27:137-44.
- [150] Dowling NE. Engineering methods for deformation, fracture and fatigue. *Mechanical Behavior of Materials*. 2007:152-4.
- [151] Figueiredo AM, Modenesi P, Buono V. Low-cycle fatigue life of superelastic NiTi wires. *International Journal of Fatigue*. 2009;31:751-8.
- [152] Furuichi Y, Tobushi H, Ikawa T, Matsui R. Fatigue properties of a TiNi shape-memory alloy wire subjected to bending with various strain ratios. *Proceedings of the Institution of Mechanical Engineers, Part L: Journal of Materials: Design and Applications*. 2003;217:93-9.
- [153] Siredey-Schwaller N, Eberhardt A, Bastie P. Parameters influencing the fatigue life of a Cu–Al–Be single-crystal shape memory alloy under repeated bending. *Smart Mater Struct*. 2009;18:025014.
- [154] Tobushi H, Nakahara T, Shimeno Y, Hashimoto T. Low-cycle fatigue of TiNi shape memory alloy and formulation of fatigue life. *Journal of Engineering Materials and Technology*. 2000;122.
- [155] Arockiakumar R, Takahashi M, Takahashi S, Yamabe-Mitarai Y. Microstructure, mechanical and shape memory properties of Ti–55Pd–5x (x= Zr, Hf, V, Nb) alloys. *Materials Science and Engineering: A*. 2013;585:86-93.
- [156] McKelvey A, Ritchie R. Fatigue-crack growth behavior in the superelastic and shape-memory alloy Nitinol. *Metallurgical and Materials Transactions A*. 2001;32:731-43.

- [157] Bignon M, Morin M. Thermomechanical study of the stress assisted two way memory effect fatigue in TiNi and CuZnAl wires. *Scripta materialia*. 1996;35:1373-8.
- [158] Schick JR. Transformation induced fatigue of Ni-rich NiTi shape memory alloy actuators. College Station, USA: Texas A&M University; 2009.
- [159] Ramaiah K, Saikrishna C, Ranganath V, Buravalla V, Bhaumik S. Fracture of thermally activated NiTi shape memory alloy wires. *Materials Science and Engineering: A*. 2011;528:5502-10.
- [160] Evirgen A, Karaman I, Santamarta R, Pons J, Noebe R. Microstructural characterization and superelastic response of a $\text{Ni}_{50.3}\text{Ti}_{29.7}\text{Zr}_{20}$ high-temperature shape memory alloy. *Scripta Materialia*. 2014;81:12-5.
- [161] Karakoc O, Hayrettin C, Bass M, Wang S, Canadinc D, Mabe J, et al. Effects of upper cycle temperature on the actuation fatigue response of NiTiHf high temperature shape memory alloys. *Acta Materialia*. 2017;138:185-97.
- [162] Atli K, Karaman I, Noebe R, Bigelow G, Gaydos D. Work production using the two-way shape memory effect in NiTi and a Ni-rich NiTiHf high-temperature shape memory alloy. *Smart Mater Struct*. 2015;24:125023.
- [163] Simka W, Kaczmarek M, Baron-Wiecheć A, Nawrat G, Marciniak J, Żak J. Electropolishing and passivation of NiTi shape memory alloy. *Electrochimica Acta*. 2010;55:2437-41.
- [164] Karakoc O, Hayrettin C, Evirgen A, Santamarta R, Canadinc D, Wheeler R, et al. Role of Microstructure on the Actuation Fatigue Performance of Ni-Rich NiTiHf High Temperature Shape Memory Alloys. *Acta Materialia*. 2019.

- [165] Umale T, Salas D, Tomes B, Arroyave R, Karaman I. The effects of wide range of compositional changes on the martensitic transformation characteristics of NiTiHf shape memory alloys. *Scripta Materialia*. 2019;161:78-83.
- [166] Evirgen A. Microstructural characterization and shape memory response of Ni-rich NiTiHf and NiTiZr high temperature shape memory alloys, Ph.D. Dissertation. College Station, USA: Texas A&M University; 2014.
- [167] Frankel DJ, Olson GB. Design of Heusler precipitation strengthened NiTi- and PdTi-base SMAs for cyclic performance. *Shape Memory and Superelasticity*. 2015;1:162-79.
- [168] Coughlin D, Phillips P, Bigelow G, Garg A, Noebe R, Mills M. Characterization of the microstructure and mechanical properties of a $\text{Ni}_{50.3}\text{Ti}_{29.7}\text{Hf}_{20}$ shape memory alloy. *Scripta Materialia*. 2012;67:112-5.
- [169] Hornbuckle B, Sasaki T, Bigelow G, Noebe R, Weaver M, Thompson G. Structure–property relationships in a precipitation strengthened Ni–Ti_{29.7}–Hf₂₀ (at%) shape memory alloy. *Materials Science and Engineering: A*. 2015;637:63-9.
- [170] Xu L, Solomou A, Baxevanis T, Lagoudas DC. A Three-Dimensional constitutive modeling for shape memory alloys considering two-way shape memory effect and transformation-induced plasticity. *AIAA Scitech 2019 Forum* 2019. p. 1195.
- [171] Xu L, Baxevanis T, Lagoudas D. A finite strain constitutive model considering transformation induced plasticity for shape memory alloys under cyclic loading. 1812-05695. 2018.

- [172] Miller DA, Lagoudas DC. Influence of cold work and heat treatment on the shape memory effect and plastic strain development of NiTi. *Materials Science and Engineering: A*. 2001;308:161-75.
- [173] Koneti SR, Gokhale SR, Wadsworth TM. Intergranular cracking of oil field tubular components resulting from the tempering process. *SPE/IADC Drilling Conference and Exhibition: Society of Petroleum Engineers*; 2011.
- [174] Koneti S, Gokhale S, Wadsworth T. Tubular cracking: Pinpointing the cause. *Drilling Contractor*. 2012;68.
- [175] Calhoun C, Wheeler R, Baxevanis T, Lagoudas DC. Actuation fatigue life prediction of shape memory alloys under the constant-stress loading condition. *Scripta Materialia*. 2015;95:58-61.
- [176] Phillips FR, Lagoudas DC. Influence of stress concentrations on failure of shape memory alloy actuators. *Behavior and Mechanics of Multifunctional Materials and Composites 2017: International Society for Optics and Photonics*; 2017. p. 101650D.
- [177] Kumar PK, Caer C, Atkinson G, Patoor E, Lagoudas DC. The influence of stress and temperature on the residual strain generated during pseudoelastic cycling of NiTi SMA wires. *Behavior and Mechanics of Multifunctional Materials and Composites 2011: International Society for Optics and Photonics*; 2011. p. 79781E.
- [178] Evirgen A. Ph.D Thesis. College Station, USA: Texas A&M University; 2014.
- [179] Lagoudas DC, Miller DA. Experiments of thermomechanical fatigue of SMAs. *Smart Structures and Materials 1999: Smart Materials Technologies: International Society for Optics and Photonics*; 1999. p. 275-83.

- [180] Bertacchini OW, Lagoudas DC, Patoor E. Fatigue life characterization of shape memory alloys undergoing thermomechanical cyclic loading. *Smart Structures and Materials: International Society for Optics and Photonics*; 2003. p. 612-24.
- [181] Benafan O, Noebe R, Padula II S, Vaidyanathan R. Microstructural response during isothermal and isobaric loading of a precipitation-strengthened Ni-Ti_{29.7}Hf₂₀ high-temperature shape memory alloy. *Metallurgical and Materials Transactions A*. 2012;43:4539-52.
- [182] Saghaian S, Karaca H, Tobe H, Pons J, Santamarta R, Chumlyakov Y, et al. Effects of Ni content on the shape memory properties and microstructure of Ni-rich Ni-Ti-Hf₂₀ alloys. *Smart Mater Struct*. 2016;25:095029.
- [183] Smith K, Topper T, Watson P. A stress-strain function for the fatigue of metals (Stress-strain function for metal fatigue including mean stress effect). *Journal of materials*. 1970;5:767-78.
- [184] Schick JR. Transformation induced fatigue of Ni-rich NiTi shape memory alloy actuators, M.S. Thesis. College Station, USA: Texas A&M University; 2009.
- [185] Lim JT, McDowell DL. Degradation of an Ni-Ti alloy during cyclic loading. 1994 North American Conference on Smart Structures and Materials: International Society for Optics and Photonics; 1994. p. 326-41.
- [186] Karakoc O, Hayrettin C, Bass M, Wang S, Canadinc D, Mabe J, et al. Effects of upper cycle temperature on the actuation fatigue response of NiTiHf high temperature shape memory alloys. *Acta Materialia*. 2017;138:185-97.

- [187] Karaca H, Saghaian S, Ded G, Tobe H, Basaran B, Maier H, et al. Effects of nanoprecipitation on the shape memory and material properties of an Ni-rich NiTiHf high temperature shape memory alloy. *Acta Materialia*. 2013;61:7422-31.
- [188] Bigelow G, Garg A, Padula S, Gaydos D, Noebe R. Load-biased shape-memory and superelastic properties of a precipitation strengthened high-temperature Ni 50.3 Ti 29.7 Hf 20 alloy. *Scripta Materialia*. 2011;64:725-8.
- [189] Smith K, Topper T, Watson P. A stress-strain function for the fatigue of metals(Stress-strain function for metal fatigue including mean stress effect). *Journal of materials*. 1970;5:767-78.
- [190] Young B. Stable crack growth in NiTiHf alloys. College Station, USA. 2020;Texas A&M University.
- [191] Calhoun CA. M.S. Thesis. College Station, USA: Texas A&M University; 2012.
- [192] Schick JR. M.S. Thesis. College Station, USA: Texas A&M University; 2009.
- [193] Lagoudas D, Miller D, Rong L, Kumar P. Thermomechanical fatigue of shape memory alloys. *Smart Mater Struct*. 2009;18:085021.
- [194] Moumni Z, Van Herpen A, Riberty P. Fatigue analysis of shape memory alloys: energy approach. *Smart Mater Struct*. 2005;14:S287.
- [195] Zhang J, Somsen C, Simon T, Ding X, Hou S, Ren S, et al. Leaf-like dislocation substructures and the decrease of martensitic start temperatures: A new explanation for functional fatigue during thermally induced martensitic transformations in coarse-grained Ni-rich Ti–Ni shape memory alloys. *Acta Materialia*. 2012;60:1999-2006.

- [196] Santamarta R, Evirgen A, Perez-Sierra AM, Pons J, Cesari E, Karaman I, et al. Effect of thermal treatments on Ni–Mn–Ga and Ni-Rich Ni–Ti–Hf/Zr high-temperature shape memory alloys. *Shape Memory and Superelasticity*. 2015;1:418-28.
- [197] Evirgen A. Microstructural characterization and shape memory response of Ni-rich NiTiHf and NiTiZr high temperature shape memory alloys. College Station, USA: Texas A&M University; 2014.
- [198] Perkins J, Sponholz R. Stress-induced martensitic transformation cycling and two-way shape memory training in Cu-Zn-Al alloys. *Metallurgical Transactions A*. 1984;15:313-21.
- [199] Contardo L, Guenin G. Training and two way memory effect in CuZnAl alloy. *Acta Metallurgica et Materialia*. 1990;38:1267-72.
- [200] Stalmans R, Van Humbeeck J, Delaey L. The two way memory effect in copper-based shape memory alloys—thermodynamics and mechanisms. *Acta Metallurgica et Materialia*. 1992;40:2921-31.
- [201] Meng X, Chen F, Cai W, Wang L, Zhao L. Two-way shape memory effect and its stability in a Ti–Ni–Nb wide hysteresis shape memory alloy. *Materials Transactions*. 2006;47:724-7.